MINIATURIZATION OF MICROWAVE TO MILLIMETER-WAVE INTEGRATED WAVEGUIDES AND THEIR APPLICATIONS

by

THOMAS ROBERT JONES

A thesis submitted in partial fulfillment of the requirements for the degree of

Doctor of Philosophy

in

Electromagnetics and Microwaves

Department of Electrical and Computer Engineering
University of Alberta

Abstract

The integration of waveguide technology at the planar level has been a crucial development for the successful realization of 5G, the future fifth generation cellular network. The demand for mobile networks with faster speeds, lower latencies, and denser connectivity scenarios continues to drive the development of microwave systems with increased integration without sacrificing performance. Over the last two decades, substrate integrated waveguides (SIW) have emerged as a promising technology for 5G, offering a low-cost, high performance alternative to traditional planar systems. However, the need for smaller form factors limits their application in certain situations, where their overall size becomes a challenge.

Much progress has been made in the miniaturization of SIW, taking advantage of the unique opportunities of waveguides integrated inside a substrate, such as high aspect ratios and multilayer fabrication technologies. However, even greater miniaturizations remain both possible and essential for increased integration and performance, while reducing both the cost and size of 5G systems.

In this thesis, a new type of miniaturized integrated waveguide platform is investigated. Through the effective combination of different SIW miniaturization techniques, the realization of several ultra-compact integrated waveguide systems are presented.

First, the combination of ridged and half-mode SIW technologies are explored, producing broadside miniaturizations up to 75% compared to standard SIW.

Furthermore, by reducing radiation losses closer to cutoff, the performance compared to half-mode SIW is also improved. Applications of the proposed technology are explored, including high density interconnects, hybrid couplers, bandpass filters, and passive non-contact sensors.

Next, folded waveguide techniques are applied to the ridged half-mode SIW to reduce its broadside width by an additional 50%, thus resulting in a total miniaturization of 88% compared to standard SIW. Furthermore, application of the proposed technique in the design of miniaturized SIW cavity is shown to reduce the footprint up to 98%, producing transverse dimensions of approximately $\lambda/16$, while also increasing spurious-mode bandwidth more than 200%. Applications in tunable and reconfigurable bandpass and bandstop filters are then explored.

As the need for more bandwidth pushes 5G systems up into the millimeter-wave frequency spectrum, the integration of waveguides at the wafer-level becomes increasingly important. Thus, a flexible and low-cost CMOS compatible microfabrication process is developed, and the first realization of a miniaturized monolithic wafer-level air-filled integrated waveguide platform for millimeter-wave 5G communication systems is presented. Fabricated prototypes employing ridged half-mode and folded ridged half-mode waveguide techniques are demonstrated, achieving broadside miniaturizations of 66% and 73% compared to standard rectangular waveguide, respectively. The results demonstrate the potential of the proposed miniaturized monolithic integrated waveguide platform for low-loss high-density millimeter-wave interconnects for 5G communication systems.

Preface

This thesis is an original work by Thomas R. Jones.

Portions of Chapter 3 and Chapter 4 have been published as T. R. Jones and M. Daneshmand, "The characterization of a ridged half-mode substrate-integrated waveguide and its application in coupler design," *IEEE Trans. Microw. Theory Tech.*, vol. 64, no. 11, pp. 3580–3591, Nov. 2016, © 2016 IEEE, T. R. Jones and M. Daneshmand, "Miniaturized slotted bandpass filter design using a ridged half-mode substrate integrated waveguide," *IEEE Microw. Wirel. Compon. Lett.*, vol. 26, no. 5, pp. 334–336, May 2016, © 2016 IEEE, and T. R. Jones, M. H. Zarifi, and M. Daneshmand, "Miniaturized quarter-mode substrate integrated cavity resonators for humidity sensing," *IEEE Microw. Wirel. Compon. Lett.*, vol. 27, no. 7, pp. 612–614, July 2017, © 2017 IEEE.

Portions of Chapter 5 and Chapter 6 have been published as T. R. Jones and M. Daneshmand, "Miniaturized folded ridged half-mode and quarter-mode substrate integrated waveguides for filter design," *IEEE Trans. Microw. Theory Tech.*, vol. 67, no. 8, pp. 3414–3426, Aug. 2019, © 2019 IEEE, and T. R. Jones and M. Daneshmand, "Miniaturized reconfigurable dual-band bandstop filter with independent stopband control using folded ridged quarter-mode substrate integrated waveguide," in *IEEE MTT-S Int. Microw. Symp. Dig.*, Boston, MA, June 2019, pp. 102–105, © 2019 IEEE. Another portion of Chapter 6 has been communicated as T. R. Jones and M. Daneshmand, "Miniaturized folded ridged

quarter-mode substrate integrated waveguide RF MEMS tunable bandpass filters," (submitted to *IEEE Access*; revision requested on July 7, 2019).

A portion of Chapter 7 has been published as T. R. Jones and M. Daneshmand, "The microfabrication of monolithic miniaturized ridged half-mode waveguides for 5G millimeter-wave communication systems," in *IEEE MTT-S Int. Microw. Symp. Dig.*, Philadelphia, PA, June 2018, pp. 323–326, © 2018 IEEE, and another portion has been communicated as T. R. Jones and M. Daneshmand, "Microfabrication of a monolithic wafer-level air-filled half-mode waveguide for millimeter-wave applications," (submitted to *IEEE Microw. Wirel. Compon. Lett.*; revision requested on August 28, 2019).

For all the above publications, I was responsible for the concept formation, theoretical analysis, fabrication, and characterization as well as the manuscript composition. Prof. Daneshmand was the supervisory author and was involved with concept formation and manuscript edits. For publication Jones et al., "Miniaturized quarter-mode substrate integrated cavity resonators for humidity sensing," *IEEE MWCL*, 2018, Dr. Zarifi provided support in the concept formation, experimental setup, and manuscript edits.

Dedication

To my wife.

Acknowledgments

First, I would like to extend my sincerest gratitude to my advisor Professor Mojgan Daneshmand. Her belief and confidence in my research potential made my PhD possible. I am extremely grateful for her sense of humor, patience, guidance, mentorship, and support throughout my many struggles.

I would also like to thank Professor Dimitrios Peroulis, Professor Ashwin Iyer, Professor Vien Van, and Professor Douglas Barlage for serving on my committee and for taking the time to provide constructive criticisms to help improve this dissertation.

Completing this work would not have been possible without the financial support provided by the Canadian Research Chair Program, the National Science and Engineering Research Council of Canada, Alberta Innovates Technology Futures, CMC Microsystems, IEEE Microwave Theory and Techniques Society, and IEEE Antennas and Propagation Society. Their support is greatly appreciated.

A big thanks goes out to the staff of the nanoFAB facility located at the University of Alberta for their kind support, fabrication advice, and friendship throughout this project, including Steph, Scott, Les, Aditi, Aaron, and Melissa. I would also like to thank Herb, Reiner, and Terry for allowing me to mess around in their machine shop, and Rick McGregor for making sure all my product orders actually arrived. Many thanks to Eric Carty from Analog Devices, Inc. for providing the RF MEMS SP4T switches, Ron Eakin from Integrated Micro

Materials for his insightful discussions on AZ 40XT-11D processing, Adhesives Research, Inc. for providing the EL-7876 adhesive tape, Brad Chamberlain from Circuit Graphics for providing PCB bonding services, and Paul Jamiel and Rogers Corporation for their generous donation of the substrates and bonding materials used in this research.

A special thanks to my best friend and colleague Dr. Sanghamitro Das, without whose help I would not have finished this dissertation on time. A big thanks also to my friends and colleagues including Dr. Vahabisani, Dr. Zarifi, Stuart, Saeed, Chris, Vivian, Sabreen, Mohammad, Dr. Nosrati, Dr. Moghadas, Zahra, Sameir, Navid, Eric, Dr. Baghelani, and the rest of the team at M2M. I will miss all of our conversations and time spent in the lab.

Lastly, but certainly most importantly, I would like to thank my wife Corinne for her endless love and support. This thesis would not exist if it was not for your patience and commitment to our family, putting up with my long hours and stressful workload. You cared for our incredible son Rowan when I could not. My heartfelt thanks go out to my Mum, whose unconditional love and sacrifice throughout my life helped get me to where I am today, to my Dad, for teaching me to work hard to reach my goals, and to my brothers James and Gavan, who remind me of what truly matters. I would like to thank all my family and friends for their support and kindness throughout my PhD program.

Table of Contents

List of Tables

List of Figures

List of Symbols and Acronyms

α	Attenuation Constant
β	Propagation (or Phase) Constant
γ	Complex Propagation Constant
c_0	Speed of Light in Vacuum
ε	Permittivity
ε_0	Permittivity of Free-Space
ε_r	Relative Permittivity
f	Frequency
f_0	Resonance Frequency
f_c	Waveguide Cutoff Frequency
f_e	Odd-Mode (Electric Wall) Resonance Frequency
f_m	Even-Mode (Magnetic Wall) Resonance Frequency
k	Wave Number
k_c	Cutoff Wave Number
k_x	Mode Wave Number in the x-direction
k_y	Mode Wave Number in the y-direction
λ	Wavelength of a Plane Wave Propagating in a Dielectric Medium
λ_0	Wavelength in Free-Space
λ_c	Waveguide Cutoff Wavelength
λ_g	Guided Wavelength
μ	Permeability
μ_0	Permeability of Free-Space
μ_r	Relative Permeability
Q	Quality Factor
Q_c	Unloaded Quality Factor due only to Conductor Losses
Q_d	Unloaded Quality Factor due only to Dielectric Losses
Q_e	External Quality Factor
Q_u	Unloaded Quality Factor
σ	Conductivity
$tan\delta$	Loss Tangent
τ	Group Delay
ω	Radian Frequency
5G	Fifth Generation Cellular Network Technology
BPF	Bandpass Filter
BSF	Bandstop Filter

BW	Bandwidth
CMOS	Complementary Metal-Oxide-Semiconductor
CPW	Coplanar Waveguide
CW	Continuous Wave
DI	Deionized Water
DRIE	Deep Reactive Ion Etching
DUT	Device Under Test
EFAB	Electrochemical Fabrication
EM	Electromagnetic
EMSIW	Eighth-Mode Substrate Integrated Waveguide
FBW	Fractional Bandwidth
FESEM	Field-emission scanning electron microscope
FMWG	Full-Mode Waveguide
FRHMSIW	Folded Ridged Half-Mode Substrate Integrated Waveguide
FRHMWG	Folded Ridged Half-Mode Waveguide
FRQMSIW	Folded Ridged Quarter-Mode Substrate Integrated Waveguide
FRSIW	Folded Ridged Substrate Integrated Waveguide
FSIW	Folded Substrate Integrated Waveguide
HMSIW	Half-Mode Substrate Integrated Waveguide
HMWG	Half-Mode Waveguide
IC	Integrated Circuit
IPA	Isopropyl Alcohol
LIGA	Lithography, Electroplating, and Molding (*English Translation*)
LTCC	Low Temperature Co-Fired Ceramic
MEMS	Microelectromechanical Systems
MFC	Mass Flow Controller
MIC	Microwave Integrated Circuit
MIMO	Multiple-Input Multiple-Output
MMIC	Monolithic Microwave Integrated Circuit
MS	Microstrip
NRN	Nonresonating Node
PCB	Printed Circuit Board
PEB	Post Exposure Bake
PEC	Perfect Electric Conductor
PECVD	Plasma-Enhanced Chemical Vapour Deposition
PMC	Perfect Magnetic Conductor
QMSIW	Quarter-Mode Substrate Integrated Waveguide
RF	Radio Frequency

RFID	Radio Frequency Identification
RH	Relative Humidity
RHMSIW	Ridged Half-Mode Substrate Integrated Waveguide
RHMWG	Ridged Half-Mode Waveguide
RIE	Reactive-Ion Etching
RQMSIW	Ridged Quarter-Mode Substrate Integrated Waveguide
RSIW	Ridged Substrate Integrated Waveguide
RWG	Rectangular Waveguide
SDR	Software Defined Radio
SIW	Substrate Integrated Waveguide
SMA	SubMiniature Version A
SoC	System-on-Chip
TE	Transverse Electric
TL	Transmission Line
TM	Transverse Magnetic
TRL	Thru, Reflect, Line
VNA	Vector Network Analyzer
WG	Waveguide
UV	Ultraviolet Light
UWB	Ultra-Wideband

Chapter 1

Introduction

1.1 Motivation

Integration of microwave components remains critical for the successful implementation of the future fifth generation (5G) cellular network, where spectral efficiency and bandwidth have become the principle bottlenecks to achieve 5G's vision of wireless data rates on the order of gigabits per second [1]–[3]. Over the last two decades, substrate integrated waveguides (SIW) have emerged as a promising technology for 5G systems up to and including millimeter-wave (mm-wave) frequencies. This is due to their advantages including high quality factor (Q), high power handling, convenient integration with planar technology, and simple low-cost fabrication using conventional printed circuit board (PCB), low temperature co-fired ceramic (LTCC), or monolithic microwave integrated circuit (MMIC) techniques [4], [5]. However, due to a wavelength dependent width, where the fundamental $TE_{1,0}$ mode is half a wavelength in its transverse dimension, the large overall size of SIW presents a challenge for use in applications requiring high density signal routing, e.g., large filters banks or switch networks.

Many strategies have been presented in the literature for the miniaturization of SIW. One popular technique cuts the waveguide along the planes of symmetry of the fundamental $TE_{1,0}$ mode, and due to the high aspect (width to height) ratios of SIW, maintains the propagation or resonant characteristics of the mode with

reduced size. Technologies employing this method have been well studied and include half-mode (HMSIW), quarter-mode (QMSIW), and eighth-mode (EMSIW) interconnects and resonant cavities [6]–[10]. While significant miniaturization is possible, increases in radiation losses limit their applicability. Employing multilayer fabrication technology, the incorporation of ridged structures inside SIW channels (RSIW) have been presented in [11]–[13]. By reducing the cutoff frequency of the fundamental $TE_{1,0}$ mode, experimental demonstrations of RSIW have shown broadside miniaturizations of 40%, while also improving monomode bandwidth by 168%. Another multilayer strategy for SIW miniaturization folds the fundamental $TE_{1,0}$ mode between two or more substrates, producing a folded SIW (FSIW), reducing the broadside width up to 50% or more [14]. FSIW has been combined with other technologies such as ridged (FRSIW) [15] and half-mode (FHMSIW) [16] to further increase the amount of miniaturization.

The methods so far discussed have indeed shown promising potential for miniaturized integrated waveguide solutions. However, further miniaturization of SIW remains essential to meet the demand for increased integration and performance, while reducing both the overall cost and size, of advanced 5G wireless systems for both communication and sensing. Through the effective combination of the techniques discussed above, significant miniaturization of SIW-based systems is still possible. Therefore, it is the motivation of this thesis to develop a new type of miniaturized integrated waveguide platform, with the goal of producing one of the most compact single conductor transmission lines in the present literature.

1.2 Objectives

The main goal of this thesis is to introduce a new design platform for the miniaturization of integrated waveguides for 5G wireless communication and sensing. To achieve this goal, a miniaturized waveguide platform utilizing ridged, half-mode, and folded waveguide techniques is proposed. Applications including high-density interconnects, couplers, sensors, and filters operating from sub-6 GHz frequencies up to mm-waves are then investigated.

The objectives of this thesis can be summarized as the following: (1) combine the benefits of ridged and half-mode techniques into a single waveguide structure to develop a miniaturized waveguide platform; (2) utilizing SIW technology, apply the miniaturized waveguide platform to improve the performance of microwave components including couplers, bandpass filters, and environmental sensors; (3) combine folded and quarter-mode techniques to achieve further miniaturization of the waveguide platform; (4) apply the improved waveguide platform to develop miniaturized tunable and reconfigurable filter technologies; (5) develop a miniaturized monolithic wafer-level waveguide platform for low-loss integrated wireless communications technology at mm-wave frequencies. The work of this thesis has a high potential for future expansion into miniaturized monolithic wafer-level waveguide switches and switch matrices, along with reconfigurable diplexers and multiplexers. The work of this thesis will be key to developing miniaturized systems that will lay the foundation for an entirely new generation of integrated waveguide technology.

1.3 Structure of the Thesis

The thesis is structured into eight main chapters as follows:

Chapter 1 discusses the motivation and research objectives of the thesis.

Chapter 2 presents a literature survey on the topics related to the thesis, beginning with a summary of the electromagnetic (EM) theory of rectangular waveguides, along with a review of the state-of-the-art in integrated waveguides including SIW and microfabricated monolithic wafer-level waveguides. Finally, the state-of-the-art in miniaturization techniques of SIW including ridged SIW, half-mode SIW, quarter-mode SIW cavity, and folded SIW technologies are presented.

Chapter 3 develops the theory and provides the characterization and measurement of a miniaturized waveguide design platform by combining the benefits of ridged and half-mode technology to produce the first ridged half-mode substrate integrated waveguide (RHMSIW), yielding a 75% reduction in broadside width compared to standard SIW, while reducing the radiation losses closer to cutoff frequency compared to HMSIW.

In Chapter 4, a variety of applications of RHMSIW technology are presented, including the design and experimental results of a Riblet short-slot hybrid coupler, two and four-pole slotted bandpass filters, and quarter-mode cavity humidity sensors.

In Chapter 5, the combination of folded and ridged half-mode technology is presented, producing further miniaturization of the broadside width of standard SIW up to 87.5% or more. The theory, characterization, and experimental results of the folded ridged half-mode substrate integrated waveguide (FRHMSIW) are discussed, along with a study of the structure's monomode bandwidth.

In Chapter 6, the design and experimental results of high-performance microwave filters using folded ridged half-mode and folded ridged quarter-mode miniaturized SIW cavities are provided, including tunable and reconfigurable bandpass and bandstop filters.

Chapter 7 presents the first successful realization and characterization of fully monolithic wafer-level air-filled half-mode, ridged half-mode, and folded ridged half-mode waveguides, where a CMOS compatible microfabrication process is developed using thick sacrificial layers to build and release 3D structures on-wafer.

Finally, in Chapter 8, a summary of the major results from the thesis, along with future work and suggestions for continuation of the project, are presented.

Chapter 2

Background

This chapter presents a literature survey on the topics related to the thesis. Section 2.1 provides a summary of the electromagnetic theory of rectangular waveguides, along with a description of the transverse resonance technique used to calculate the cutoff frequency and propagation constant of waveguides with more complex transverse geometries. Next, in Section 2.2, a detailed review of the state-of-the-art in integrated waveguides including SIW and microfabricated monolithic wafer-level waveguides is provided. Finally, in Section 2.3, the state-of-the-art in miniaturization techniques of SIW including ridged SIW, half-mode SIW, quarter-mode SIW, and folded SIW technologies are presented.

2.1 Rectangular Waveguide Theory

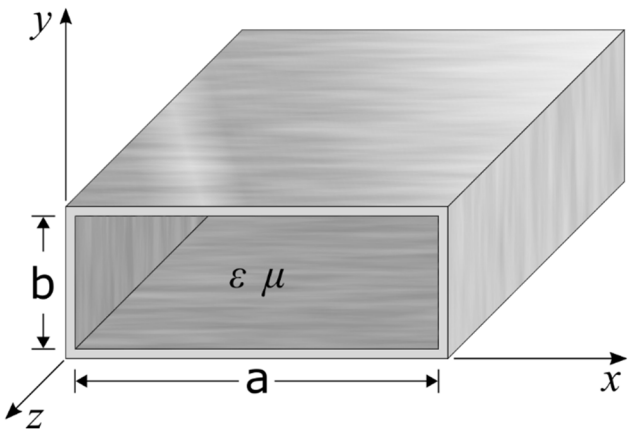

Fig. 2.1. The geometry of a conventional rectangular waveguide of width *a* and height *b*, assumed to be filled with a material of permittivity ($\varepsilon = \varepsilon_r\varepsilon_0$) and permeability ($\mu = \mu_r\mu_0$).

Rectangular waveguides (RWGs) are used throughout the microwave industry for applications requiring high power handling or low attenuation loss, including high power communication links, satellite networks, and mm-wave systems [17]–[19]. Due to the presence of only a single conductor, transverse electric and magnetic (TEM) modes are not supported by such structures. However, the propagation of higher order transverse electric (TE) or transverse magnetic (TM) modes are supported. As such, electromagnetic power can be transmitted through a RWG above a particular waveguide mode's cutoff frequency, below which the modes are termed evanescent, and decay very rapidly along their propagation direction. In Fig. 2.1, the geometry of a conventional RWG is shown, with width a and height b. According to standard convention, the largest dimension ($a > b$) is oriented in the x-direction, while wave propagation is in the z-direction. To decrease loss, RWGs are typically empty of material (relative permittivity (ε_r) and permeability (μ_r) equal to unity). However, dielectric-filled RWGs including SIW are used in industry for improved integration with planar technology [20].

In general, TE and TM modes are characterized by having their electric (and magnetic) field components in the propagation direction (z-direction) equal to zero, respectively. To determine the cutoff frequency $f_{c_{m,n}}$ of a particular waveguide mode, the following equation can be used

$$k_c = \sqrt{k_x^2 + k_y^2} = \sqrt{\left(\frac{m\pi}{a}\right)^2 + \left(\frac{n\pi}{b}\right)^2} \tag{2.1}$$

$$f_{c_{m,n}} = \frac{k_c}{2\pi\sqrt{\mu\epsilon}} \tag{2.2}$$

where m and n are the mode indexes (or half sine wave variations in field components) in the x- and y-direction, respectively, k_x and k_y the mode wave numbers in the x- and y-direction, respectively, and k_c the cutoff wave number [17]–[19]. The propagation constant of the waveguide mode can then be calculated as

$$\beta_{m,n} = \sqrt{k^2 - k_c^2} \tag{2.3}$$

where the wave number $k = \omega(\mu\varepsilon)^{1/2}$ [17]–[19]. For conventional RWGs with $a = 2b$, the $TE_{1,0}$ mode has the lowest cutoff frequency and is called the fundamental mode. The bandwidth between the fundamental and the next higher order mode is called the monomode region of the waveguide, which in a large number of cases is used as the operational range of the RWG due to power spread across multiple modes at higher frequencies [19]. Typically, the next higher order mode is the $TE_{2,0}$ mode, with cutoff frequency $f_{c2,0} \approx 2 \times f_{c1,0}$. Therefore, the fundamental $TE_{1,0}$ mode is the only mode supported by a RWG which can propagate by itself. The monomode bandwidth of a waveguide is approximately the same as its fundamental $TE_{1,0}$ mode cutoff frequency, with a monomode bandwidth ratio (fundamental to next higher order mode) of ~1:2.

2.1.1 Transverse Resonance Technique

In order to determine the cutoff frequency and propagation constant of waveguides with more complex transverse profiles, the transverse resonance technique can be used [17]–[19], [21]. The transverse resonance technique allows the representation of a composite waveguide with a transmission line model in the transverse plane. When a waveguide is at cutoff, the fields inside the waveguide

form standing waves in the transverse plane. This situation can be modelled with an equivalent circuit operating at resonance. A condition of a resonant circuit is that the input impedances (or admittances) looking to either side at any point along the transverse plane of the waveguide must sum to zero [19]. Using this condition, the equivalent circuit model can be solved for the cutoff frequency and propagation constant of the waveguide structure.

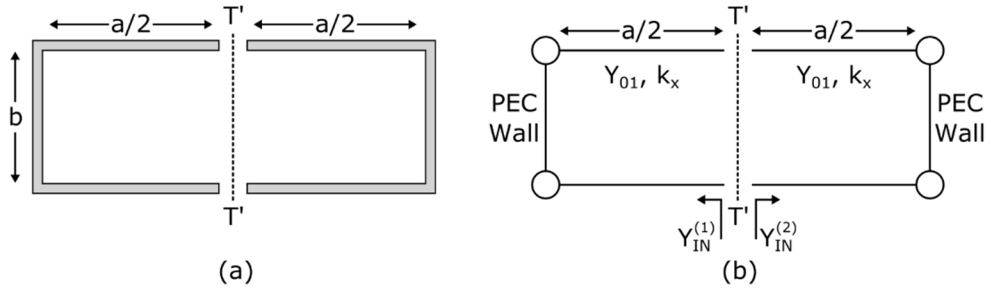

Fig. 2.2. (a) Cross-section of a RWG and (b) equivalent transverse circuit model.

In Fig. 2.2(a), the cross-section of a RWG is shown, where plane T' has been inserted down the center of the waveguide. An equivalent transverse circuit model of the RWG is shown in Fig. 2.2(b). The two halves of the waveguide are modelled as parallel-plate waveguides shorted at their ends [18]. Based on the transverse resonance technique, by summing the two input admittances to zero, the cutoff wave number, and therefore cutoff frequency and propagation constant, for the $TE_{m,0}$ modes of the waveguide can be determined by

$$Y_{IN}^{(1)} + Y_{IN}^{(2)} = 0 \tag{2.4}$$

which is simplified to

$$\cot\left(\frac{k_x a}{2}\right) = 0. \tag{2.5}$$

$$k_x = m\pi/a \tag{2.6}$$

for m = 1, 3, 5, … Likewise, for even m modes, the input impedance is used. Thus, the transverse resonance technique solves for the cutoff frequency as shown in (2.2) and propagation constant as shown in (2.3).

2.1.2 Rectangular Waveguide Cavity Resonators

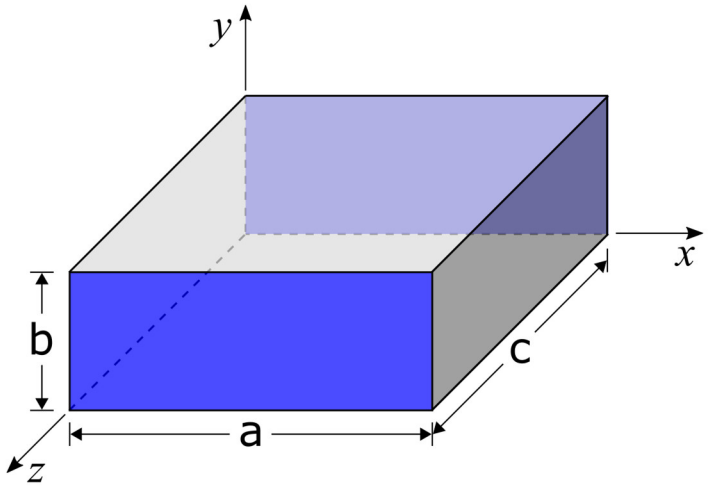

Fig. 2.3. The geometry of a conventional rectangular waveguide cavity, with width a, height b, and length c.

For microwave and mm-wave filtering applications, RWG cavity resonators offer superior performance due to their high power handling capability, low loss, and very high Q [22]. As shown in Fig. 2.3, a RWG cavity is constructed by inserting short circuit walls in the xy-plane at locations $z = 0$ and $z = c$. By bounding the waveguide in the z-direction, resonant modes are generated within the cavity, and the wave number and cutoff frequency of each resonant mode can be calculated using

$$k_{m,n,l} = \sqrt{\left(\frac{m\pi}{a}\right)^2 + \left(\frac{n\pi}{b}\right)^2 + \left(\frac{l\pi}{c}\right)^2} \tag{2.7}$$

$$f_{m,n,l} = \frac{k_{m,n,l}}{2\pi\sqrt{\mu\epsilon}} \tag{2.8}$$

where l is the mode index (or half sine wave variation of the field component) in the z-direction [17]–[19].

An important characteristic of microwave and mm-wave resonators in the design of filters is their spurious performance, which is the bandwidth between neighboring resonant modes and the desired operating mode [22]. For typical waveguide cavity applications with dimensions $b < a < c$, the resonant mode with lowest cutoff frequency is the $TE_{1,0,1}$ mode, also known as the fundamental mode [17]–[19]. The next higher order mode then forms the upper boundary of the spurious-free region of the resonator, which for typical waveguide cavity is ~1:2 (a ratio of the fundamental to first higher order mode). Generally, large spurious-free regions are desired in filter design in order to improve out-of-band rejection and limit the interference of spurious modes with the filters performance [22].

2.2 Integrated Rectangular Waveguides

Conventional RWGs have been used extensively in the microwave industry, and are often the best candidates for mm-wave applications. This is due to their advantageous properties such as high Q, low attenuation, high power handling, and ease of manufacturing. Yet, for integration with planar level microwave components and integrated circuit (IC) design, the overall size of conventional

RWGs is too large due to their significant height compared to their width. Integrated RWGs have been used to combine the benefits of RWGs with planar level microwave integrated circuits (MIC). Although their reduced height lowers the power handling and increases the conductor losses, the advantages of integrated RWGs, such as lower impedance and higher Q compared to coplanar waveguide or microstrip, still make them an excellent choice for MIC design in the mm-wave regime. A variety of integrated RWG platforms have been reported in the literature, including substrate integrated waveguides, hybrid micro-machined waveguides, and monolithic wafer-level waveguides. In this section, a review of the literature will be presented on the current state-of-the-art in integrated RWG design, outlining the advantages and limitations of each technology.

2.2.1 Substrate Integrated Waveguides

Substrate integrated waveguides (SIW) have become an attractive solution to the problem of integrating RWGs with planar technology, including both MICs and monolithic microwave integrated circuits (MMIC) [5], [23]–[27]. Using standard printed circuit board (PCB), low temperature co-fired ceramic (LTCC), or integrated circuit (IC) fabrication techniques, depending upon the application, a waveguide is integrated into the substrate using rows of periodically spaced metalized through vias for the waveguide's electric sidewalls. With this topology, SIW combines the benefits of RWGs, such as good power handling and high Q, with the added benefit of low-cost and low profile for planar integration.

The general layout of an SIW is shown in Fig. 2.4, highlighting the important design dimension along with an equivalent RWG for comparison [5]. Due to their

truncated nature, the sidewalls of the SIW channel do not support longitudinal currents. Furthermore, $TE_{m,n}$ modes for n > 0 are pushed up to very high frequency due to the relatively thin substrate compared to width. Therefore, only $TE_{m,0}$ modes are of interest in SIW [27]. The pitch between vias must also be chosen carefully to ensure low radiation leakage, and that no electromagnetic bandgaps exist in the operational bandwidth of the SIW component [26]. Due to the periodic nature of the via arrays, bandgap phenomena occur when the following condition is satisfied

$$\beta p = n\pi \tag{2.9}$$

where β is the phase constant of the SIW in the direction of propagation, with the first bandgap appearing when $n = 1$ [28].

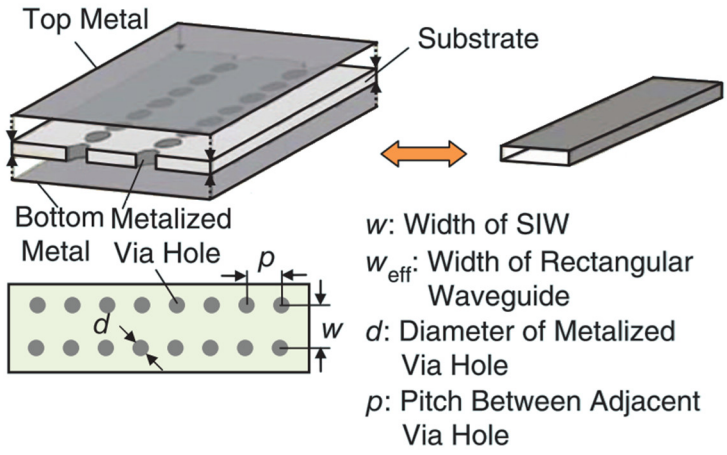

Fig. 2.4. General layout of an SIW and equivalent RWG [5] © 2014 IEEE.

Considering the above performance constraints, a set of SIW design rules have been developed for monomode propagation of the fundamental $TE_{1,0}$ mode, which are

$$p > d \tag{2.10}$$

$$p/\lambda_c < 0.25 \tag{2.11}$$

$$\alpha/k_0 < 1 \times 10^{-4} \tag{2.12}$$

$$p/\lambda_c > 0.05 \tag{2.13}$$

where λ_c is the cutoff wavelength of the fundamental $TE_{1,0}$ mode, α the total loss, and k_0 the wave number in free-space [26]. The condition in (2.10) makes the SIW physically realizable, while (2.11) keeps any periodic bandgaps outside the operational bandwidth. The condition in (2.12) is to make radiation losses negligible, with a more stringent requirement of $p \leq 2d$ recommended, while (2.13) limits the over-perforation of the SIW by vias for mechanical rigidity. The via diameter is generally chosen comparable to the substrate thickness. Finally, the effective width can be approximated using the simple relation [29]

$$W_{eff} = W - \frac{d^2}{0.95p}. \tag{2.14}$$

In Fig. 2.5, the region of interest for monomode propagation of the fundamental $TE_{1,0}$ mode for via diameter d and pitch spacing p normalized to cutoff wavelength λ_c is shown [5], summarizing the above SIW design rules.

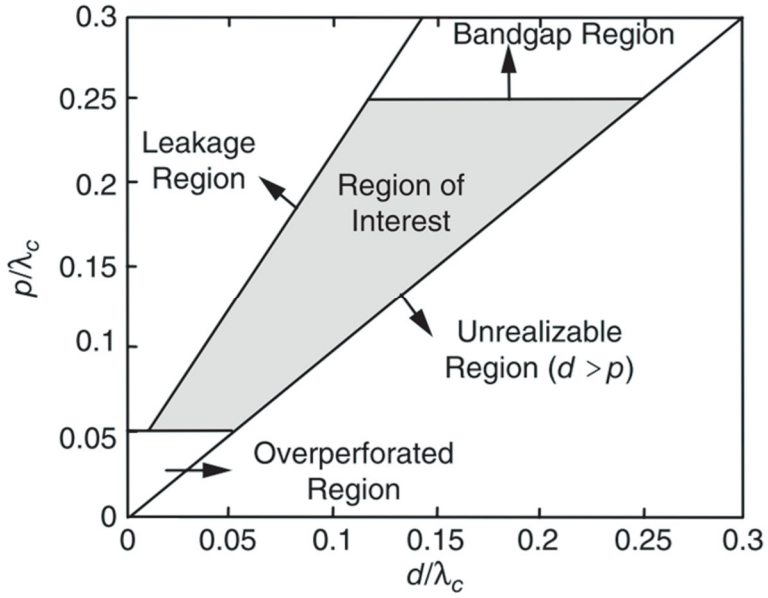

Fig. 2.5. Region of interest for monomode propagation of SIW fundamental $TE_{1,0}$ mode with normalized via diameter d/λ_c and pitch spacing p/λ_c [5] © 2014 IEEE.

A large diversity of microwave components have been successfully designed using SIW, including directional couplers [30], slot array and leaky-wave antennas [31], [32], and filters [33]–[36]. However, as demand increases for circuits with smaller footprints, SIW fall short due to the $\lambda_c/2$ restriction of their broadside width.

2.2.2 Monolithic Wafer-Level Rectangular Waveguides

As frequencies move into the mm-wave regime, conventional PCB and machine-milling techniques no longer offer the miniaturized dimensions required for cost effective waveguide fabrication. Fortunately, the extensive progress made in microfabrication technology offers a variety of state-of-the-art techniques for the fabrication of mm-wave waveguides at the wafer-level, as reported in the literature. The microfabrication of waveguides at the wafer-level also allows for their monolithic integration with silicon-based IC design, and microfabrication

techniques allow for the mass production of microwave components with relatively low cost.

For the microfabrication of waveguides, a number of innovative techniques exist in the literature. Fabrication techniques such as LIGA (Lithography, Electroplating, and Molding – *English translation*) [37], [38] and EFAB (Electrochemical Fabrication) [39], [40] have been successfully used to create high aspect ratio, free standing structures, yet their substantial prototyping cost and large number of process steps has led researchers to more cost effective solutions using photolithography. Methods combining bulk micromachining with hybrid integration techniques have found many uses in the fabrication of waveguides [41]–[45]. Although these techniques have shown great potential, wafer bonding requires extremely high precision with high planarity, reducing the repeatability and introducing error [46]. The Deep Reactive Ion Etching (DRIE) process also offers high aspect ratio features, but has increased surface resistivity due to the scalloping effect, impacting the waveguide attenuation [47].

In [48], one of the first examples of a fully monolithic dielectric-filled metal-pipe RWG is reported. These laminated, or "photoimageable" dielectric-filled waveguides have been further developed in [49], [50], where a low-loss photoimageable dielectric paste is successively deposited and fired, creating a waveguide channel. Silver conductive paste is used for metallization. In Fig. 2.6, the process flow for the photoimageable waveguide in [50] is shown, along with a cross-section of the monolithic waveguide. In Fig. 2.7, the attenuation constant is extracted across V-band (40 – 75 GHz) and W-band (75 – 110 GHz), showing

losses as low as 0.2 dB/mm at 100 GHz. While this technology has shown good performance, its main limitation is with the constraint imposed by the small dielectric thickness of 10 – 15 μm for each printed layer. As such, many layers are required to achieve waveguide heights of 50 – 100 μm, increasing error due to alignment and resolution [51]. High process temperatures due to the firing of the paste (850°C) introduce fabrication issues including shrinkage and cracking, while also limiting compatibility with IC design.

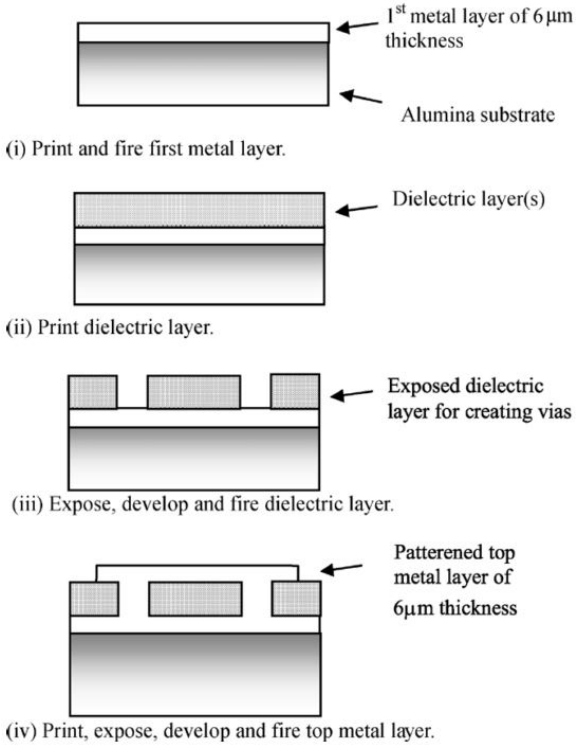

(a)

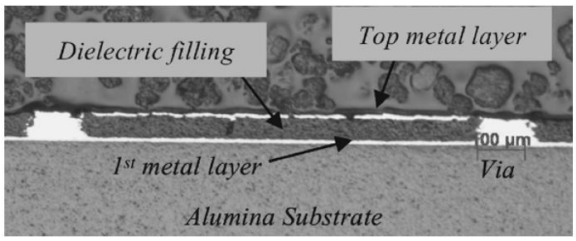

(b)

Fig. 2.6. (a) Process flow and (b) cross-section of a photoimageable waveguide [50] © 2005 IEEE.

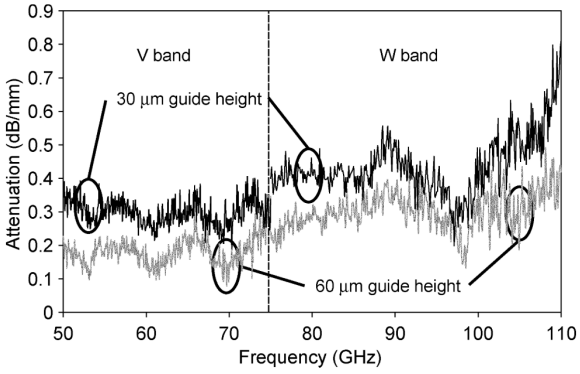

Fig. 2.7. Measured extracted attenuation constant for the monolithic photoimageable waveguide for operation in V-band and W-band with channel heights 30 µm and 60 µm [50] © 2005 IEEE.

Sacrificial layers using thick photoresists are becoming a popular choice among researchers to develop relatively inexpensive high aspect ratio structures. One such popular negative photoresist is SU-8, used in many microfabrication applications requiring good mechanical stability [52], thick layers with high aspect ratios [53], and stable RF properties [54]. Although SU-8 has many benefits, it has shown problems with its use as a sacrificial layer due to difficulties dissolving the cross-linked polymer, with material being left behind after the stripping process [55]–[57]. This becomes a problem for proper release of microelectromechanical system (MEMS) structures integrated within the proposed waveguide channel, as well as affecting final device performance.

THB-151N is another negative photoresist which has been explored as a thick sacrificial layer for applications such as air-filled half-coax and RWG [58], [59]. It also allows for thick layers with high aspect ratios and improved RF performance over SU-8, where monolithic THB-filled RWGs have shown attenuation losses down to 0.21 dB/mm at V-band [60]. However, wet chemical stripping of either SU-8 or THB-151N to improve attenuation loss causes swelling of the photoresist, possibly destroying the structure above [61]. Stripping THB-151N using dry oxygen ashing has shown good results [62], [63], but accumulates heat due to the high temperatures (over 300°) and long process times, impacting the stresses of any integrated MEMS beams, and also being undesirable for integrated circuit (IC) fabrication. Therefore, an alternative thick photoimageable polymer is required for complete removal of the sacrificial layer within the waveguide channel.

In [64], a monolithic wafer-level air-filled RWG is presented using MicroChemicals chemically amplified thick positive photoresist AZ 40XT-11D [65]. With advantageous properties including single coat layers up to 60 μm thick, high aspect ratios, low exposure doses, and standard wet stripping processes, the design shows that AZ 40XT-11D has considerable potential for use as a sacrificial layer for wafer-level waveguide microfabrication. In Fig. 11, a SEM picture of the waveguide is shown, along with the measured performance in Fig. 12, where the extracted attenuation constant achieves less than 0.1 dB/mm across V-band.

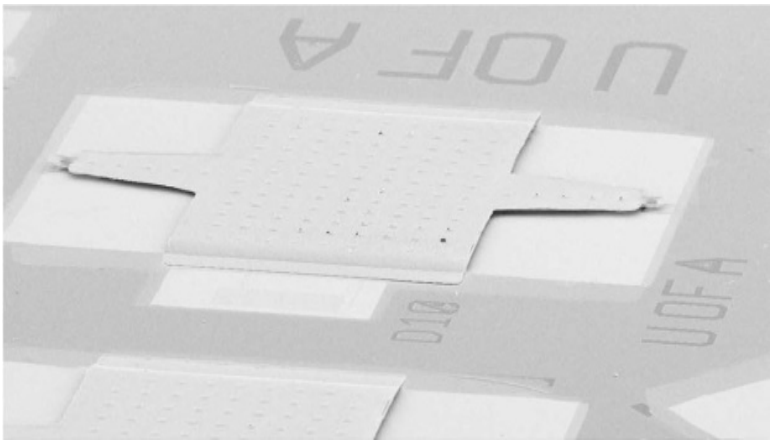

Fig. 2.8. SEM picture of a monolithic wafer-level air-filled RWG using AZ 40XT-11D chemically amplified thick positive photoresist as a sacrificial layer [64] © 2015 IEEE.

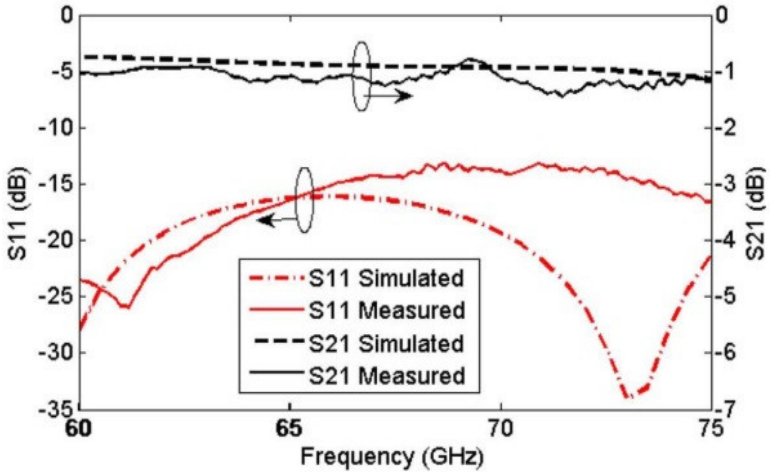

Fig. 2.9. Scattering parameters of the monolithic wafer-level air-filled RWG [64] © 2015 IEEE.

In Table 2.1, a performance comparison of monolithic wafer-level RWGs is summarized. While showing excellent results, highlighting the potential capabilities of monolithic wafer-lever waveguides, the footprint of the RWG used is still quite large, due to the $\lambda_c/2$ broadside width condition, and further miniaturization would be beneficial for more realistic integration with IC.

Waveguide Technology	Waveguide Channel Material	Waveguide Channel Empty?	Attenuation Constant (dB/mm)	Ref.
Dielectric-Filled RWG	Polymide	No	8.5 (W-band)	[48]
Photoimageable RWG	Dielectric Paste	No	0.2 – 0.4 (W-band)	[50]
THB-Filled RWG	THB N151 – Thick Negative Photoresist	No	0.21 (V-band)	[60]
Air-Filled RWG	THB N151 – Thick Negative Photoresist	Yes	Not Reported	[63]
Air-Filled RWG	AZ 40XT-11D Thick Positive Photoresist	Yes	< 0.1 (V-band)	[64]

Table 2.1. Comparison of Monolithic Wafer-Level RWG Performance

2.3 Miniaturization of Substrate Integrated Waveguides

The integration of waveguides in the substrate and at the wafer-level have shown promising results for 5G radio systems from microwaves up to mm-wave frequencies. However, as previously discussed, their size is still too large for high-density applications including switch matrices or filter banks due to their broadside half-wavelength width dependency. Furthermore, with a growing need for greater integration of high performance microwave devices, their size remains a challenge for true integration with IC. Therefore, miniaturization of integrated waveguides remains essential. Research into the miniaturization of SIW has produced a number of notable technologies in the literature. In this section, the state-of-the-art in miniaturization techniques of SIW including half-mode SIW, ridged SIW, and folded SIW technologies are presented.

2.3.1 Half-Mode Substrate Integrated Waveguides

Half-mode technology realizes a simple solution for reducing the broadside width of SIW by approximately 50% [6]. As shown in Fig. 2.10, a half-mode substrate integrated waveguide (HMSIW) is created by essentially splitting the waveguide down its center, leaving one side open and the other side shorted by periodic vias. Due to the symmetrical field configuration of the fundamental $TE_{1,0}$ mode of SIW, and large width to height ratios owing of the use of relatively thin substrates, this open side can be represented by an effective PMC wall, with low radiation loss above a certain critical frequency, as illustrated in Fig. 2.11.

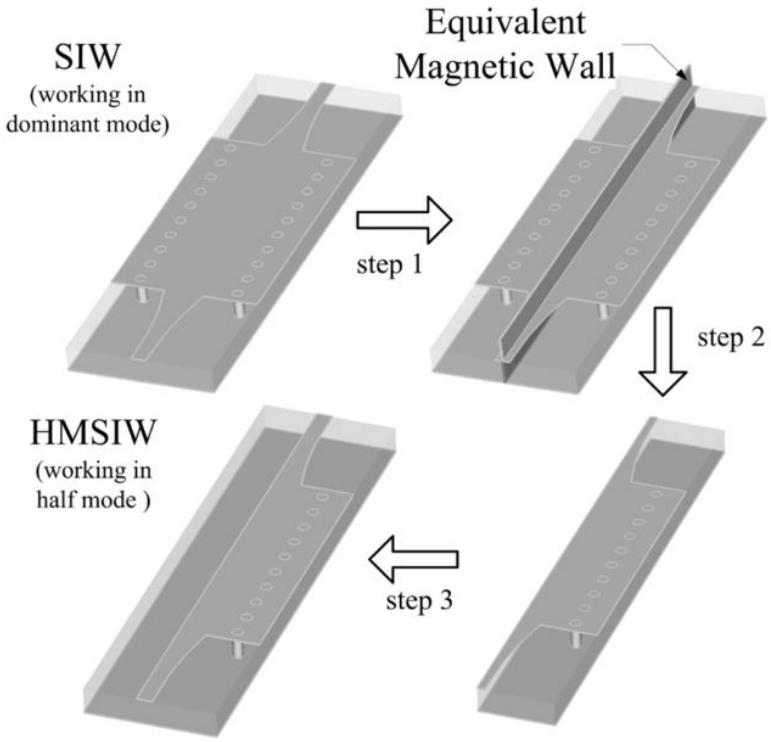

Fig. 2.10. Evolution of HMSIW by cutting SIW down the middle of the channel [66] © 2007 IEEE.

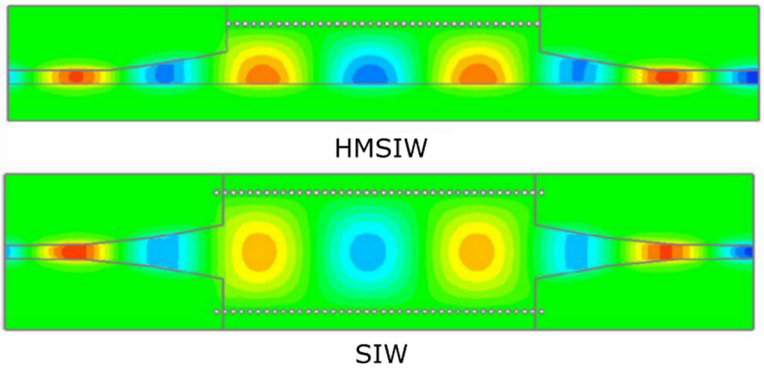

Fig. 2.11. Fundamental mode electric field distributions of the HMSIW and SIW with microstrip transitions [6] © 2006 IEEE.

The propagation properties of the HMSIW have been well characterized in [7]. An additional benefit of HMSIW compared to SIW structures is an increase in the monomode bandwidth of its fundamental quasi-$TE_{0.5,0}$ mode. Due to the PMC condition of the open sided structure, $TE_{m,0}$ modes with *m* even are not supported, thus the next higher order mode is the quasi-$TE_{1.5,0}$ mode (~3 times higher than the

fundamental) [7]. Fig. 2.12 shows a comparison of the attenuation constants of SIW and HMSIW with the same cutoff frequency. A microstrip line is also included to compare HMSIW performance with typical planar technology. At approximately 35 GHz, the attenuation loss in the HMSIW is equivalent to SIW, while both waveguides show lower attenuation loss than microstrip [7]. Below 35 GHz, the radiation losses of the HMSIW become more substantial due to its radiating behaviour closer to the cutoff frequency, where a study of the near-field radiation pattern determining the transition from radiating to guiding behavior is presented [67].

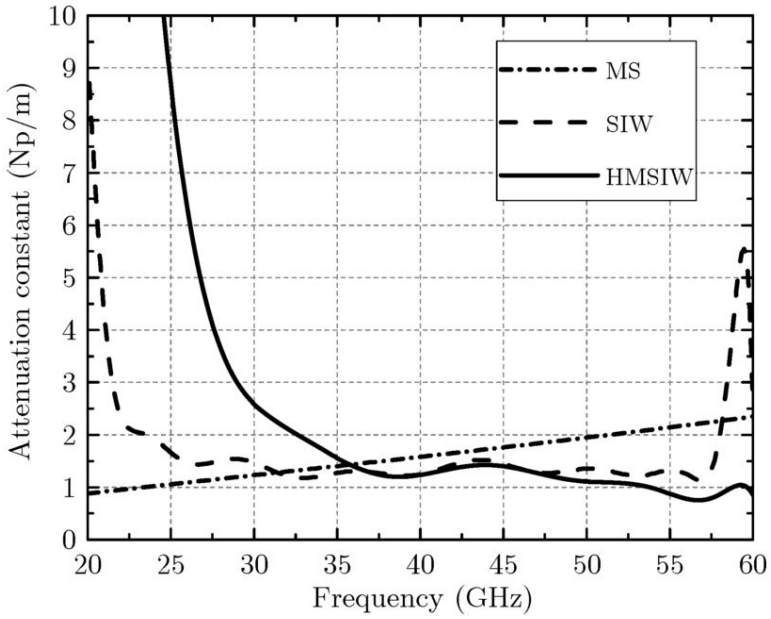

Fig. 2.12. Attenuation constants of HMSIW and SIW with similar cutoff [7] © 2009 IEEE.

Many devices using HMSIW technology have been characterized in the literature. These include couplers, filters, and leaky wave antennas [66], [68]–[71], as well as investigations into the use of HMSIW for high speed and high density interconnect applications such as antenna array feed networks [72]–[75].

Explorations into periodically loading the open side of the HMSIW with lumped elements and electronic bandgap (EBG) structures have shown the ability to create tunable monomode regions and controllable cutoff frequencies. This has led to the design of tunable filters, phase shifters, and electronically controlled leaky wave antennas [76], [77]. Implementation of buried corrugated vias along the electric wall has allowed for the biasing of active components, separating the top conductor from the ground plane [78]. Although the HMSIW has shown excellent potential, its broadside width is still large compared to conventional planar transmission lines, which remains a problem. Therefore, the study into further miniaturization of the HMSIW would be extremely beneficial.

2.3.2 Quarter-Mode Substrate Integrated Waveguide

As the building blocks of filters, SIW cavity resonators offer improvements over the performance of conventional planar resonator technology, including higher Q and greater power handling [5], [35], [36]. In Fig. 2.13, a comparison of the size, cost, and performance (unloaded quality factor Q_u) between the more common microwave and mm-wave resonators used in industry is shown. It is noted that SIW cavities fill the gap between small, low-cost, low Q_u planar resonators with good integration, and large, high cost, high Q_u dielectric and waveguide resonators with poor integration. However, for applications requiring high-density hardware integration, including massive multiple-input multiple-output (MIMO) wireless communication systems for 5G, the overall footprint of SIW cavity remains large.

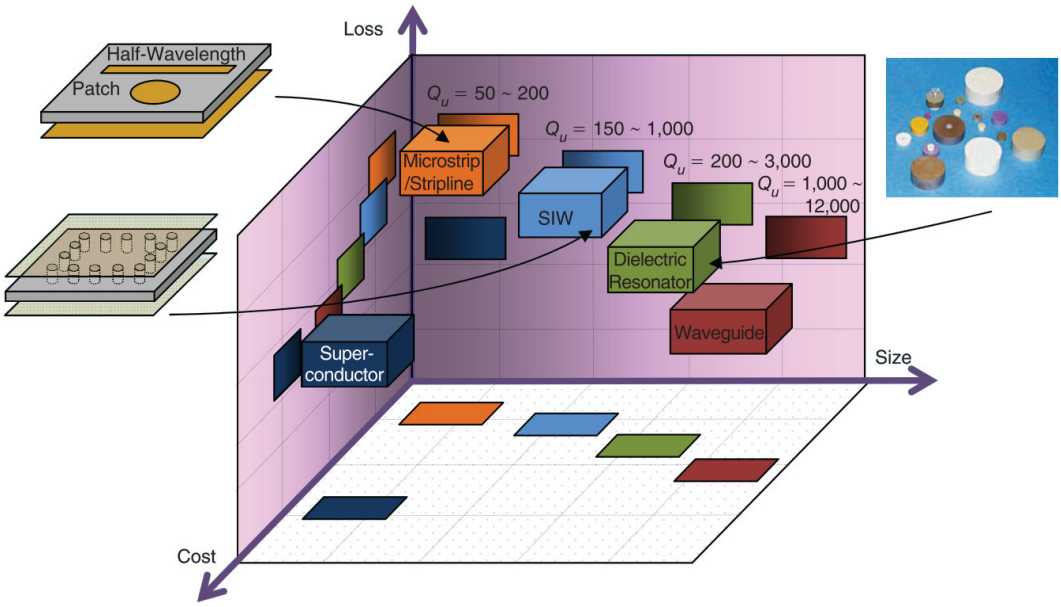

Fig. 2.13. Comparison showing the relative size, cost, and performance of different microwave resonators [5] © 2014 IEEE.

The half-mode technique discussed in the previous section has also been applied to the miniaturization of SIW cavity resonators [10], [79], [80]. In Fig. 2.14, a standard SIW cavity is cut along planes of symmetry in its fundamental $TE_{1,0,1}$ resonant mode, where due to the high aspect ratio of the SIW structure, the open sides behave as equivalent magnetic walls preserving the field configuration of the original resonant mode. As shown, both HMSIW and quarter-mode SIW (QMSIW) cavities are created, reducing the area of SIW cavity by approximately 50% and 75%, respectively.

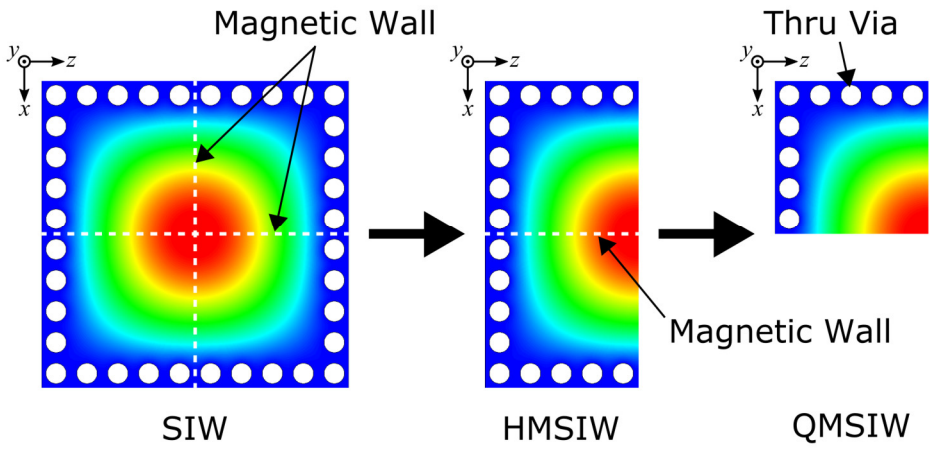

Fig. 2.14. Top view of a standard SIW cavity cut into a HMSIW cavity and then again into a QMSIW cavity due to field symmetry of the fundamental $TE_{1,0,1}$ resonant mode.

Applications of HMSIW and QMSIW cavities include filters [10], [79]–[84], sensors [85], [86] and filtering power dividers [87]. While increased radiation losses due to the open side of the QMSIW slightly lowers the cavities Q_u, further still by cutting the QMSIW one more time into an eighth-mode SIW (EMSIW) cavity, this characteristic has been successfully utilized in the design of leaky-wave antennas [88], [89]. Shielding techniques have also recently been applied to QMSIW cavity to improve radiation losses [84], [87]. However, their size remains relatively unchanged, and further miniaturization would still be beneficial.

2.3.3 Ridged Substrate Integrated Waveguides

Ridge waveguides were first introduced to increase the monomode region of the fundamental $TE_{1,0}$ mode of RWGs by introducing a continuous axial ridge along the center of the waveguide channel [90], [91]. By essentially acting like a distributed loading, the capacitive ridge lowers the phase velocity of the fundamental $TE_{1,0}$ mode decreasing its cutoff frequency, while leaving the TE_{20} mode relatively unaffected. This not only increases the monomode bandwidth, but

also allows for substantial miniaturizations of the RWG up to 50% or more due to the lower cutoff.

The ridge concept has also been incorporated into multilayer SIW technology, with characterization studies of ridged SIW (RSIW) conducted in [11]–[13], [92], [93]. In Fig. 2.15(a), the general layout of a RSIW is shown, where a row of periodic blind vias is added along the center of the waveguide channel to form a ridge. Bandgap effects caused by the ridge's periodic metal posts limit the monomode bandwidth of this design. By inserting a metal strip along the bottom of the ridge posts, the structure in Fig. 2.15(b) has demonstrated an increase in monomode bandwidth by 168%, with a miniaturization of 40% compared to standard SIW, as shown in Fig. 2.16 [11].

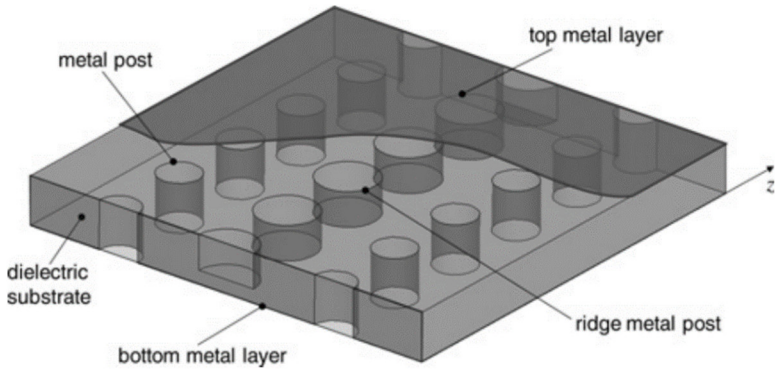

(a)

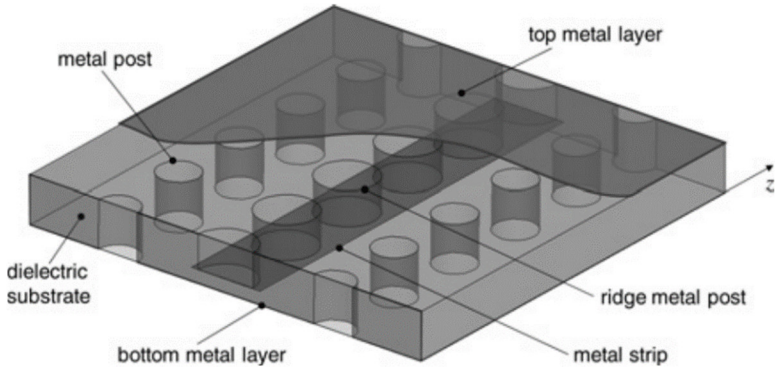

(b)

Fig. 2.15. General layout of an RSIW with (a) blind via ridge posts and (b) with additional ridge metal strip [11]. Reproduced by permission of the Institution of Engineering & Technology.

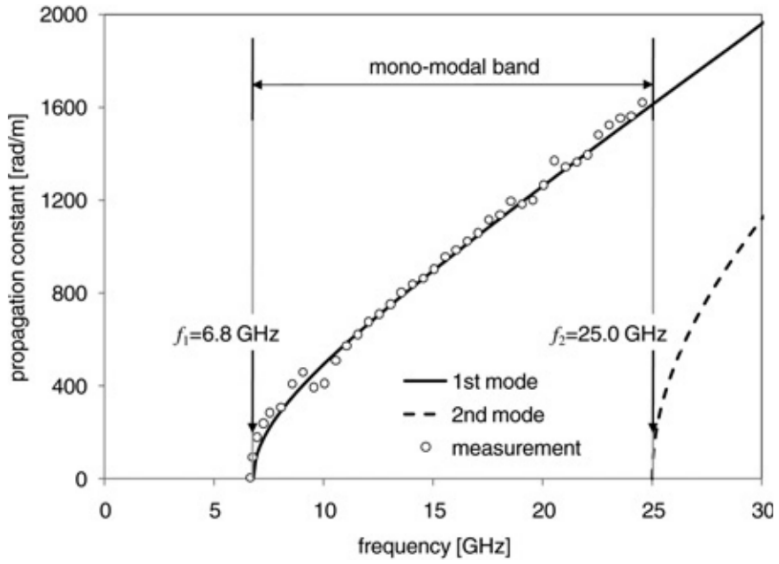

Fig. 2.16. Simulated and measured propagation constant showing increased monomode bandwidth of the RSIW (1:3.6) compared to standard SIW (~1:2) [11]. Reproduced by permission of the Institution of Engineering & Technology.

RSIW has been used in different applications, including a hybrid ring coupler in [94], and ultra-wideband (UWB) applications in [13]. Yet, for mm-wave design, its transverse size is still large, and further miniaturization to reduce the footprint is necessary.

2.3.4 Folded Substrate Integrated Waveguides

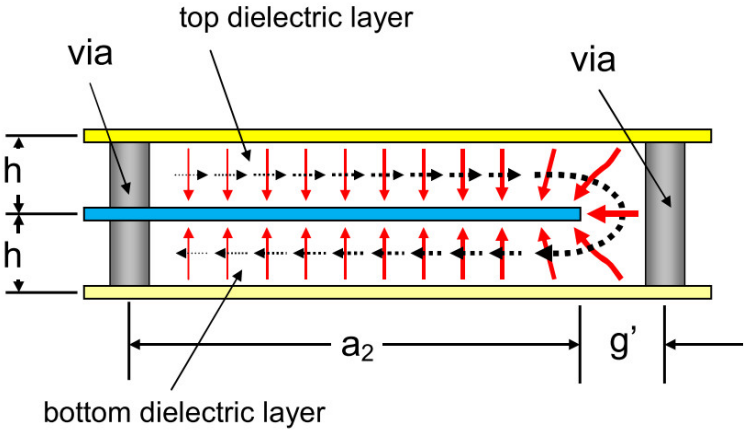

Fig. 2.17. Cross-section of a folded SIW [95] © 2010 Asia-Pacific Microwave Conference by IEEE. Reproduced with permission of IEEE in the format Republish in a thesis/dissertation via Copyright Clearance Center.

Folded substrate integrated waveguide (FSIW) is another miniaturized SIW topology that employs multilayer technology, which was originally introduced for conventional RWG in [96], [97]. By folding (or wrapping) the fundamental $TE_{1,0}$ mode of SIW between two or more substrates, broadside miniaturizations of 50% or more have been reported [14], [98]. In Fig. 2.17, the cross-section of a typical FSIW is shown, where the transverse electric (solid red arrows) and transverse magnetic (dashed black arrows) illustrate the folding of the fundamental $TE_{1,0}$ mode of SIW across two substrate layers [95]. Applications of the FSIW include filters [14], [15], couplers [16], power dividers [95], and phase shifters [99]. FSIW has also been combined with ridged (FRSIW) [15] and half-mode (FHMSIW) [16]

technologies to improve miniaturization potential. However, further improvements to reduce the broadside width of FSIW remain possible and beneficial.

Chapter 3

Ridged Half-Mode Substrate Integrated Waveguide

The primary goal of this thesis is to develop a new type of miniaturized integrated waveguide design platform. In this chapter, following the first objective stated in Section 1.2, the benefits of ridged and half-mode techniques are combined into a single waveguide structure to produce significant miniaturization of SIW. It is shown that the proposed ridged half-mode substrate integrated waveguide (RHMSIW) not only achieves a 75% reduction in broadside width compared to a standard SIW, but also reduces the radiation losses closer to cutoff frequency compared to HMSIW.

The organization of the chapter is as follows. Section 3.1 begins with a theoretical investigation of the proposed RHMSIW, including the analytical calculation of the fundamental mode cutoff frequency. A parametric study to examine the attenuation due to radiation and conductor loss with a capacitive ridge is performed in Section 3.2. The design, simulation, and measurement results of a RHMSIW and a HMSIW are provided in Section 3.3, along with a comparison of their performances. Furthermore, a study of the measured attenuation is performed in order to demonstrate the tradeoff between radiation and conductor losses. In Section 3.4, the design of a thru-reflect-line (TRL) calibration kit for the extraction of the de-embedded scattering parameters for both the measured HMSIW and RHMSIW is presented. Finally, Section 3.5 compares the measured unwanted

radiation fields of the HMSIW and RHMSIW at an operating frequency of 1.25 × f_c to illustrate the reduction in radiation loss of the RHMSIW. The important conclusions of the chapter are given in Section 3.6.

3.1 Principle of Operation

To examine the effect of a continuous capacitive loading along the open aperture of a half-mode waveguide, a simplified model using ANSYS High Frequency Structure Simulator (HFSS) was studied. As shown in Fig. 3.1, a lumped capacitance boundary condition was extended along the half-mode waveguide's open side, with perfect electric conductor PEC boundary conditions for the remaining three walls. The waveguide's simulated phase constant is plotted in Fig. 3.2, which clearly illustrates that by increasing the lumped capacitive loading, a reduction in the cutoff frequency is achieved. Therefore, it was concluded that by applying a capacitive loading along the open aperture of the half-mode waveguide, significant miniaturization of the structure could be obtained. To physically realize this continuous capacitive loading, a ridged structure extended along the entire open aperture of the half-mode waveguide was considered, leading to a ridged half-mode substrate integrated waveguide (RHMSIW).

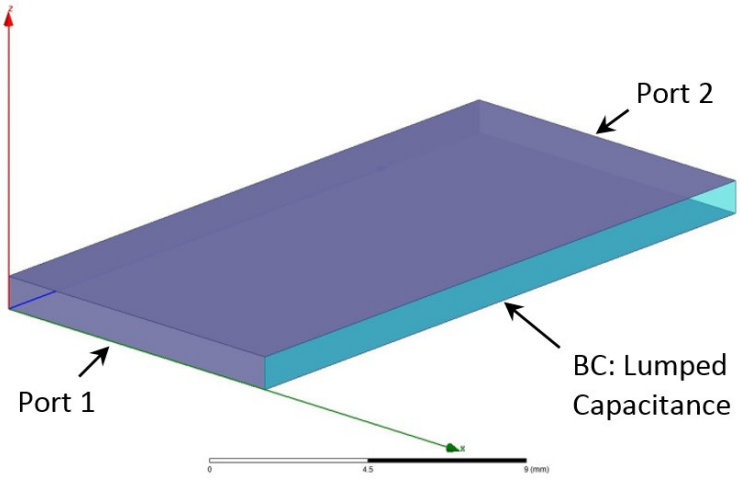

Fig. 3.1. Simple half-mode waveguide model simulated in HFSS with a lumped capacitance boundary condition extended along the open aperture of the waveguide.

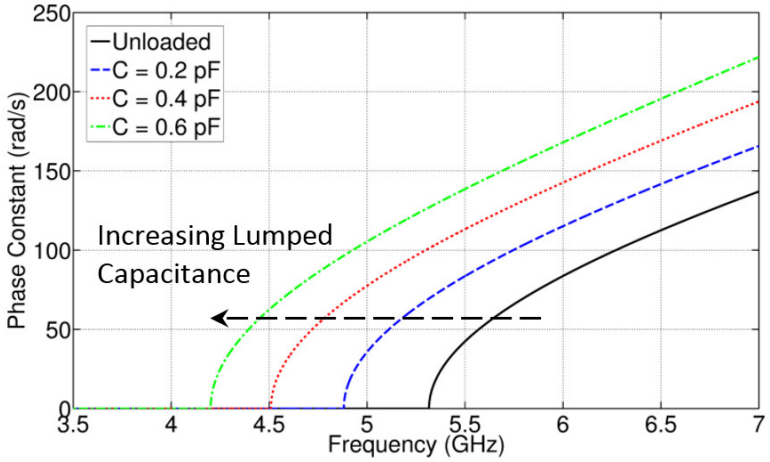

Fig. 3.2. Simulated phase constant of the half-mode waveguide model with an increasing lumped capacitance, decreasing the effective cutoff frequency of the waveguide.

As shown in Fig. 3.3, the cross-section of the RHMSIW is similar to the HMSIW, with a partially reduced height, or ridge, introduced at the open side of the waveguide. This partially reduced height loads the waveguide with a step capacitance, which allows for substantial miniaturization of the width, while still supporting the same fundamental quasi-$TE_{0.5,0}$ mode of the HMSIW. The principle behind the miniaturization can be explained using the transverse resonance technique, shown in Fig. 3.3, and is similar to the technique used for determining

the cutoff frequency of ridge waveguides [91], [12]. Due to the large width to height ratio of the HMSIW and RHMSIW, a magnetic wall is used to model the open side of the waveguide, and a resonance plane T is placed at the location of the capacitive ridge. When the resonance condition is obtained, the summation of the admittances at T in Fig. 3.3(a) will add to zero, and for the HMSIW, lead to the equation

$$Y_{in}^{(1)} + Y_{in}^{(2)} = 0. \tag{3.1}$$

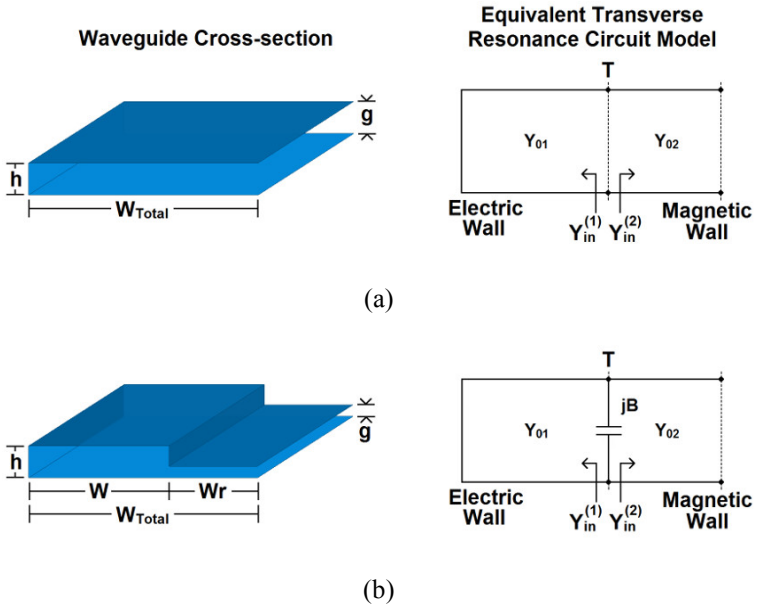

Fig. 3.3. Cross-section and transverse model of (a) the HMSIW, and (b) the RHMSIW.

Due to the reduction in height introduced by a step capacitance in the transverse plane, the characteristic admittance of Y_{02} for the RHMSIW increases compared to that for the HMSIW. Admittance jB is also introduced due to the step in height along the transverse direction, as shown in Fig. 3.3(b). The total increase in admittance leads to a reduction in the width W in order to maintain the resonance

condition from (3.1), resulting in the transverse resonance equation for the RHMSIW

$$Y_{in}^{(1)} + jB + Y_{in}^{(2)} = 0 \tag{3.2}$$

which is the main principle behind the RHMSIW miniaturization.

The first mode cutoff frequency for a given set of dimensions of the RHMSIW can be calculated by first expanding the input admittances from (3.2), yielding

$$-\cot\left(\frac{2\pi}{\lambda_c}W\right) + {}^{B}\!/_{Y_{01}} + {}^{Y_{02}}\!/_{Y_{01}} \tan\left(\frac{2\pi}{\lambda_c}Wr\right) = 0 \tag{3.3}$$

with λ_c the desired cutoff wavelength, Y_{01} and Y_{02} the characteristic admittances of the main waveguide channel and ridge section, respectively, W and Wr the widths of the main waveguide channel and ridge section, respectively, h the total waveguide height, and g the ridge height. The value for the step capacitance B/Y_{01} and characteristic admittance ratio Y_{02}/Y_{01} is found using the equations from [100]:

$${}^{Y_{02}}\!/_{Y_{01}} = {}^{h}\!/_{g} \tag{3.4}$$

$$\frac{B}{Y_{01}} = \frac{2h}{\lambda_g}\left[\ln\left(\frac{1-\alpha^2}{4\alpha}\right)\left(\frac{1+\alpha}{1-\alpha}\right)^{1/2\left(\alpha+\frac{1}{\alpha}\right)} + 2\frac{A+A'+2C}{AA'-C^2}\right.$$

$$\left. + \left(\frac{h}{4\lambda_g}\right)^2\left(\frac{1-\alpha}{1+\alpha}\right)^{4\alpha}\left(\frac{5\alpha^2-1}{1-\alpha^2} + \frac{4}{3}\frac{\alpha^2 C}{A}\right)^2\right] \tag{3.5}$$

where

$$\alpha = {}^{g}/_{h} \tag{3.6}$$

$$\lambda_g = \lambda / \sqrt{1 - \left({}^{\lambda}/_{\lambda_c}\right)^2} \tag{3.7}$$

and

$$A = \left(\frac{1+\alpha}{1-\alpha}\right)^{2\alpha} \frac{1+\sqrt{1-\left(\frac{h}{\lambda_g}\right)^2}}{1-\sqrt{1-\left(\frac{h}{\lambda_g}\right)^2}} - \frac{1+3\alpha^2}{1-\alpha^2} \tag{3.8}$$

$$A' = \left(\frac{1+\alpha}{1-\alpha}\right)^{2/\alpha} \frac{1+\sqrt{1-\left(\frac{g}{\lambda_g}\right)^2}}{1-\sqrt{1-\left(\frac{g}{\lambda_g}\right)^2}} + \frac{3+\alpha^2}{1-\alpha^2} \tag{3.9}$$

$$C = \left(\frac{4\alpha}{1-\alpha^2}\right)^2. \tag{3.10}$$

The above analysis was used to demonstrate the effect of the ridge on the cutoff frequency of the structure, with the results illustrated in Fig. 3.4. Using HFSS, the simulated cutoff wavelength for various width to height ratios W_{Total}/h, where $W_{\text{Total}} = W + Wr$, were also obtained and are shown in the same figure. It is clear that the analysis has good agreement with that of simulations.

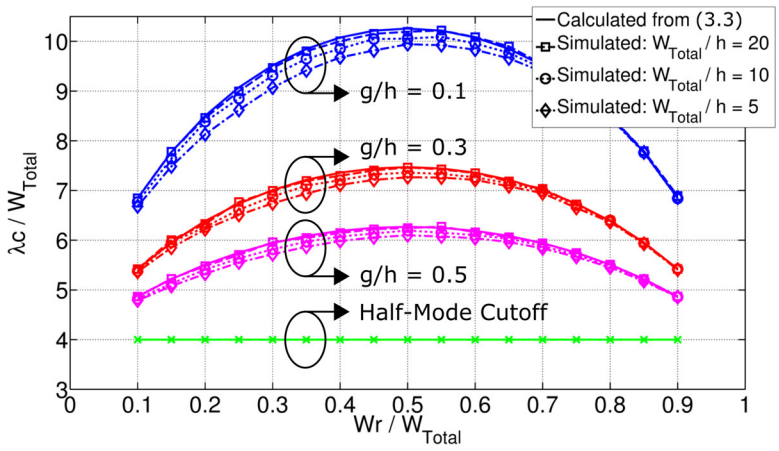

Fig. 3.4. Calculated (3.3) and simulated (HFSS) RHMSIW cutoff wavelength λ_c versus capacitive ridge width Wr for various width to height ratios normalized to the total waveguide width W_{Total}.

The calculated cutoff wavelength λ_c is shown for an increasing capacitive ridge width Wr, both normalized to the waveguide's total width W_{Total}, and also for various gap to height ratios g/h. The results demonstrate that as g/h reduces, λ_c increases, leading to significant miniaturization. It is also found that choosing a ridge width Wr of 0.45 to 0.55 of the total waveguide width produces the greatest miniaturizations.

3.1.1 Theoretical Limits of Miniaturization

To demonstrate the theoretical limits of miniaturization of the RHMSIW, the calculated (3.3) and simulated (HFSS) cutoff wavelength normalized to the waveguide total width (λ_c/W_{Total}) are plotted versus the gap to height ratio (g/h) in Fig. 3.5, with a ridge width normalized to the waveguide total height (Wr/W_{Total}) equal to 0.5, i.e., the point of maximum miniaturization. With good agreement between (3.3) and simulation, it is clear that by reducing the gap to height ratio, the cutoff frequency of the RHMSIW continues to decrease at an exponential rate. Thus, with greater capacitive loading, the resonance condition in (3.3) continues to

produce a larger cutoff wavelength λ_c, approaching a cutoff frequency equal to zero. However, when the ridge finally touches the ground plane, a switching action occurs, and the PMC boundary condition shown in Fig. 3.3(b) becomes a PEC boundary condition, and the fundamental quasi-$TE_{0.5,0}$ mode is shorted out.

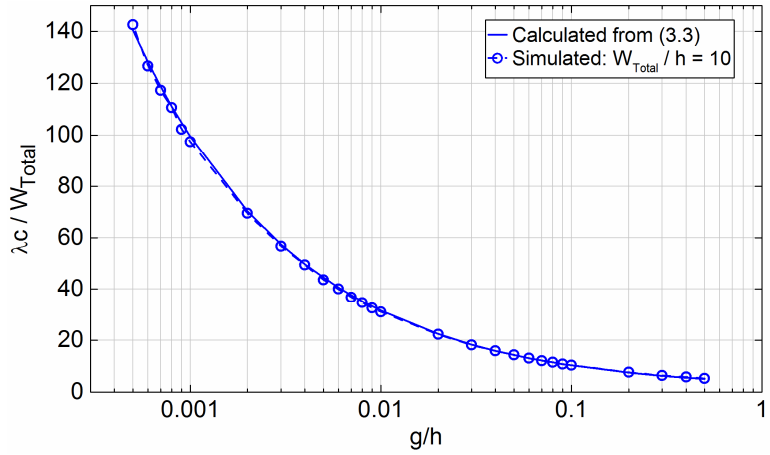

Fig. 3.5. Calculated (3.3) and simulated (HFSS) RHMSIW normalized cutoff wavelength λ_c/W_{Total} versus gap to height ratio g/h, with normalized capacitive ridge width Wr/W_{Total} equal to 0.5.

While decreasing the gap to height ratio produces greater miniaturization of the waveguide, the increased field concentration within the ridge region requires consideration in terms of the theoretical limits of miniaturization of the device. This is clearly shown in Fig. 3.6, which plots the simulated maximum electric field magnitude ($|E_{MAX}|$) versus gap to height ratio (g/h), where the incident RF power is set to 1 W. Similar to the cutoff wavelength shown in Fig. 3.5, as the gap to height ratio continues to decrease, the magnitude of the electric field increases exponentially. Thus, for greater miniaturizations with smaller gap to height ratios, power handling issues such as microwave gas breakdown become an important consideration in regards to the waveguides overall performance [101].

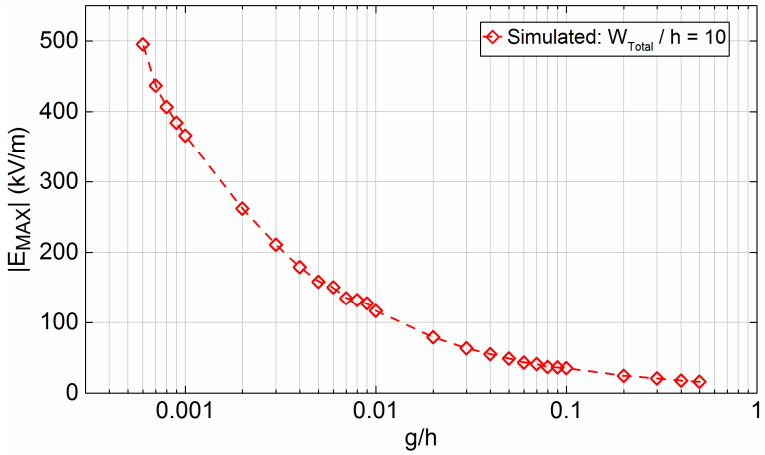

Fig. 3.6. Simulated maximum electric field magnitude ($|E_{MAX}|$) of the RHMSIW versus gap to height ratio g/h, with incident RF power equal to 1 W.

Furthermore, it is worth noting that generally for full-mode waveguides, there is a concern that by reducing the height and increasing the current density, the conductive loss increases and degrades the overall waveguide performance. However, it is not always the case for half-mode waveguides. This is because for the half-mode, by reducing the gap, the radiation loss can be mitigated. Therefore, the addition of a ridge not only could reduce the size, but by balancing between the conductive and radiation losses, the overall performance could potentially improve. This matter will be explained further in the following section.

3.2 Attenuation

To examine the change in radiation and conductor losses of the HMSIW due to the introduction of the capacitive ridge, a parametric study was performed with the complex propagation constant extracted utilizing a dual-line technique called the multiline method [102], [103] (see Appendix B for more details). As suggested by the results in Fig. 3.4, a Wr/W_{Total} equal to 0.5 was chosen for the greatest miniaturization, and then the gap to height ratio g/h of the ridge was decreased, as

shown in Fig. 3.7. For each parametric study, two lines of different length were simulated in HFSS to extract the attenuation constant.

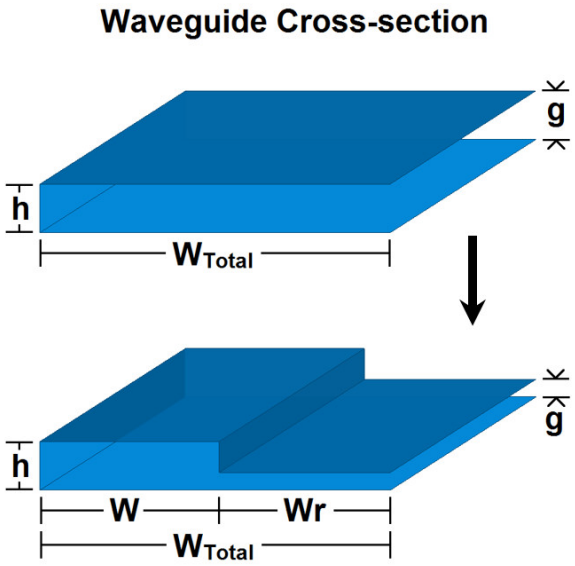

Fig. 3.7. Cross-section of the HMSIW waveguide for the attenuation study, introducing a ridge at the mid-point of the waveguide, and decreasing the gap to height ratio *g*/*h*.

As illustrated by the extracted phase constants in Fig. 3.8, by decreasing the *g*/*h* ratio, the cutoff frequency of the waveguide decreases, which agrees well with the results presented in Fig. 3.2.

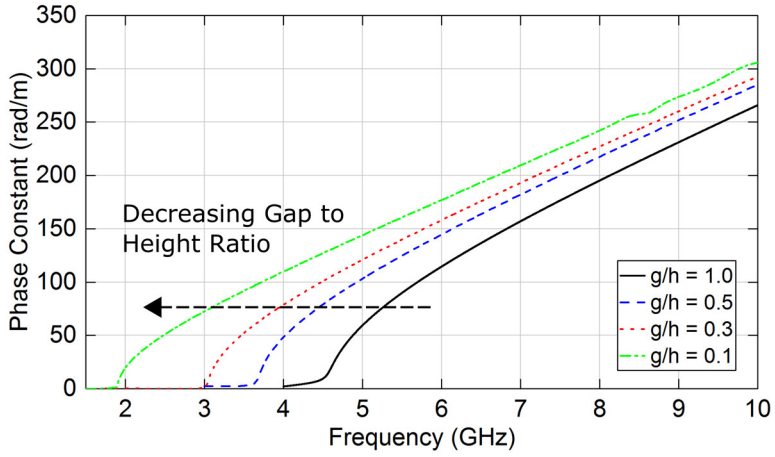

Fig. 3.8. Extracted phase constant showing a decrease in cutoff frequency due to the introduction of a continuous ridge along the open side of the HMSIW.

Fig. 3.9 shows the effect of the decreasing gap to height ratio on the extracted attenuation constant as a result of radiation losses only, i.e., simulated with perfect electrical conductors and no dielectric losses. The radiation loss with no ridge added is considerably higher close to the cutoff frequency, where the maximum miniaturization for half-mode structures occurs. It is evident that by applying the ridge and reducing the gap, the radiation loss reduces, decreasing the attenuation across the band. Fig. 3.9 also shows the extracted attenuation with both conductor and dielectric losses. By decreasing the ridge gap, the overall losses are noticeably reduced at a region close to cutoff frequency due to the reduction in radiation loss. Yet, due to this also increasing the field concentration within the ridge, the conductor losses increase, and there is a transition point of approximately $f/f_c \approx 1.45$ where the attenuation due to the conductor losses becomes slightly greater than the attenuation due to radiation losses. Below this critical point, the RHMSIW performs significantly better than the HMSIW, with lower attenuation.

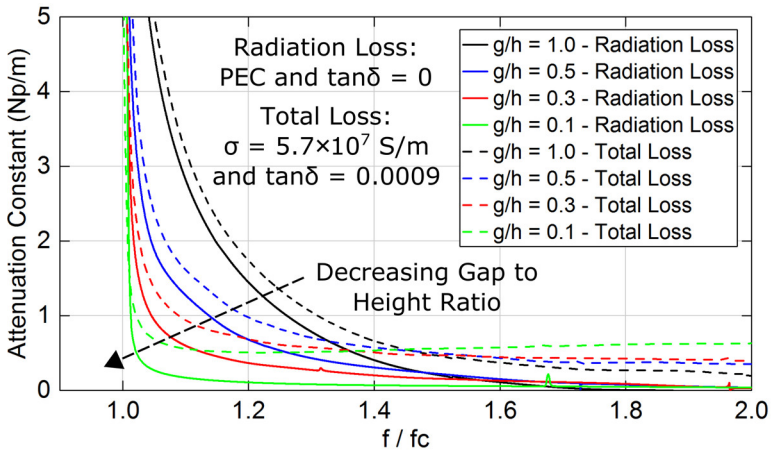

Fig. 3.9. Extracted attenuation constant with radiation loss only (solid lines) and then including total loss (dashed lines) for decreasing gap to height ratio.

3.3 Experimental Design

To verify the performance of the RHMSIW experimentally, designs of both a RHMSIW and HMSIW with equivalent cutoff frequencies for C-band operation were fabricated. A parametric study done in HFSS was carried out to optimize the dimensions of the RHMSIW, i.e., the main channel width and ridge width for a given cutoff frequency of f_c = 4.8 GHz. Fig. 3.10 shows the final design layouts for the two waveguide types. Due to the requirement of a middle conductor layer for the ridge metallization, a multilayer substrate configuration was required. Rogers RT/duroid 5880 was chosen for low dielectric loss, with thicknesses of 31 mil and 5 mil for the top and bottom substrates, respectively. A layer of Rogers 4450F Bondply with a thickness of 4 mil was used to bond the top and bottom substrates together, where the ridge metallization was realized on the bottom conductor layer of the top substrate. Therefore, the bonding layer contributed to the thickness of the capacitive gap, for a total thickness of 9 mil. This placement of the bonding layer was necessary to achieve the electroplating of the blind vias connecting the ridge metallization to the waveguide's top metallization. The size of the vias were chosen with a diameter of d = 0.508 mm and spacing s = 0.7112 mm.

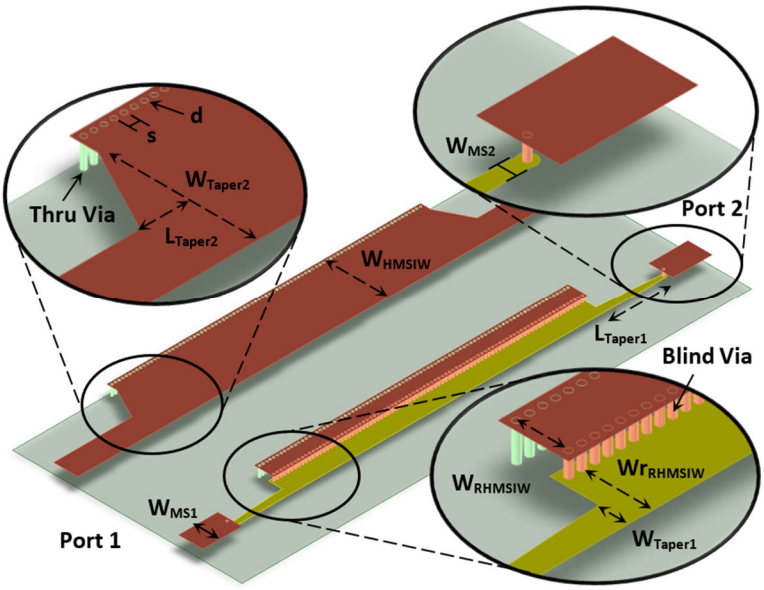

Fig. 3.10. Design layouts for simulation and fabrication of the HMSIW and the RHMSIW, with dimensions (units in mm) W_{HMSIW} = 9.5, W_{RHMSIW} = 2.2, Wr_{RHMSIW} = 3, W_{MS1} = 3.1, W_{MS2} = 0.58, W_{Taper1} = 1.3, W_{Taper2} = 7.5, L_{Taper1} = 7.8, L_{Taper2} = 2, with device lengths L_1 = 40 and L_2 = 80. The vias have a diameter d = 0.508 and spacing s = 0.7112.

To feed the RHMSIW, a tapered microstrip transition similar to the typical method used to feed HMSIWs was used [6], positioned on the ridge of the waveguide at the quasi-$TE_{0.5,0}$ mode peak, located in the middle conductor layer. A transition from the top conductor layer to the middle conductor layer was required, which was achieved by tapering the middle microstrip line to a 50-Ω impedance, and then using a metallized via with a diameter of 0.508 mm to connect it to a matched 50-Ω microstrip line above.

A picture of the fabricated devices is shown in Fig. 3.11, illustrating the significantly smaller footprint of the RHMSIW. In Fig. 3.12(a) and Fig. 3.13(a), the simulated and measured scattering parameters of the RHMSIW and the HMSIW with device lengths L_1 = 40 mm and L_2 = 80 mm are plotted, including transition and SMA connector losses. The measured return loss and insertion loss at an

operating frequency of $1.25 \times f_c = 6$ GHz for the 40 mm RHMSIW device are 18.45 dB and 0.897 dB, respectively, while for the HMSIW device they are 12.74 dB and 1.363 dB, respectively. For the 80 mm devices, the return loss and insertion loss for the RHMSIW are measured as 26.35 dB and 1.303 dB, respectively, and for the HMSIW device are 23.32 dB and 1.835 dB, respectively. Therefore, at this particular operating frequency, the RHMSIW outperforms the HMSIW with approximately a 0.5 dB reduction in insertion loss. Fig. 3.12(b) and Fig. 3.13(b) show a closer view of the simulated and measured insertion losses of the two devices, clearly illustrating the improved performance of the RHMSIW over the HMSIW closer to cutoff frequency up to approximately 6.9 GHz.

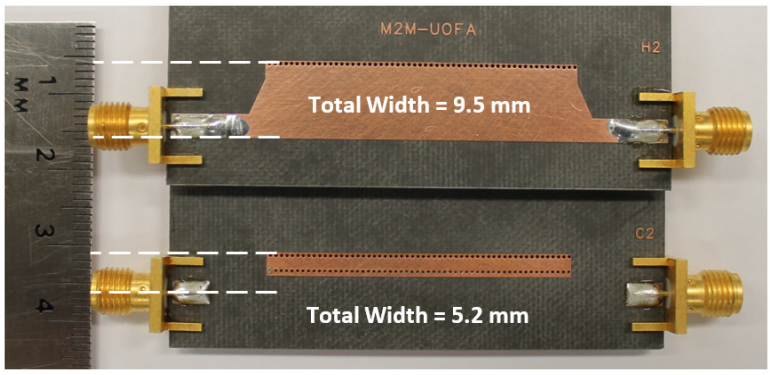

Fig. 3.11. PCB layout of the fabricated RHMSIW and HMSIW with device lengths $L_1 = 40$ mm.

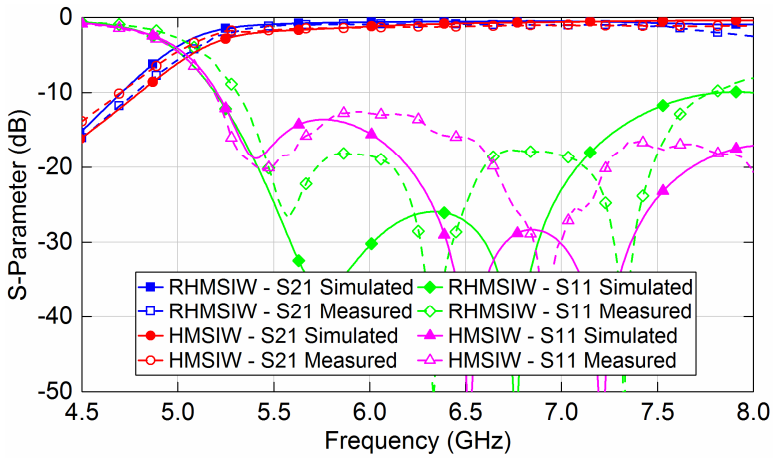

(a)

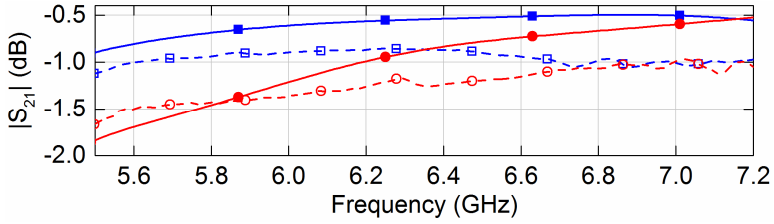

(b)

Fig. 3.12. (a) Simulated and measured scattering parameters of the RHMSIW and HMSIW with device length L_1 = 40 mm, and (b) closer view of the insertion loss.

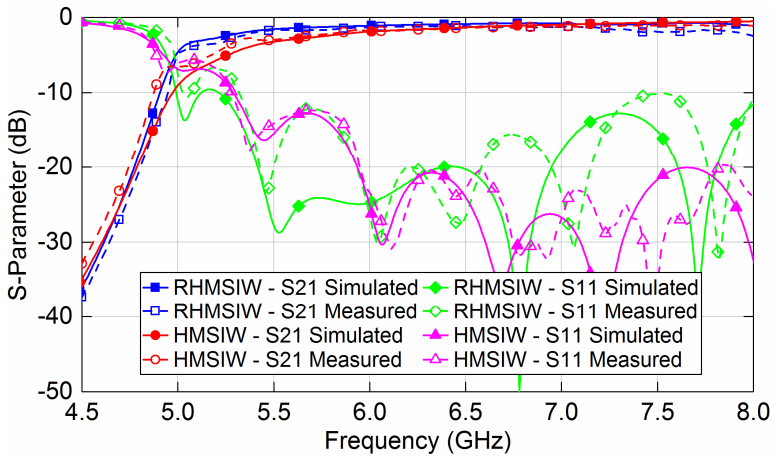

(a)

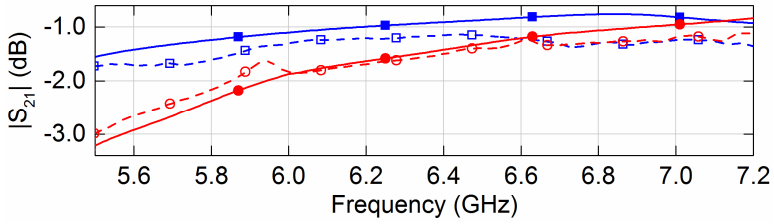

(b)

Fig. 3.13. (a) Simulated and measured scattering parameters of the RHMSIW and HMSIW with device length L_2 = 80 mm, and (b) closer view of the insertion loss.

The simulated and measured complex propagation constants of the RHMSIW and HMSIW were extracted using the multiline method [102], [103], and are shown in Fig. 3.14 and Fig. 3.15, with good agreement between the results. At the operating frequency of $1.25 \times f_c = 6$ GHz, the measured attenuation constant for the RHMSIW is 1.258 Np/m and for the HMSIW is 1.938 Np/m. The measured attenuation of the HMSIW becomes lower than the RHMSIW at approximately 6.9 GHz. This is close to the critical frequency point derived in Section 3.2 above, and therefore confirms that the performance of the RHMSIW exceeds or matches that of the HMSIW below the critical frequency point of $f/f_c \approx 1.45$.

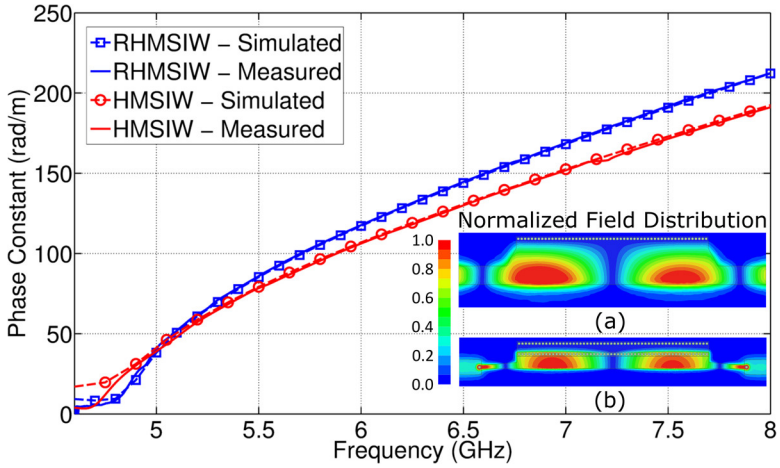

Fig. 3.14. Measured and simulated phase constants of the quasi-$TE_{0.5,0}$ mode, including the simulated normalized electric field distribution ($|E|/|E_{MAX}|$) of the (a) HMSIW with $|E_{MAX}|$ = 11.6×10^3 V/m, and (b) RHMSIW with $|E_{MAX}| = 45.4\times10^3$ V/m.

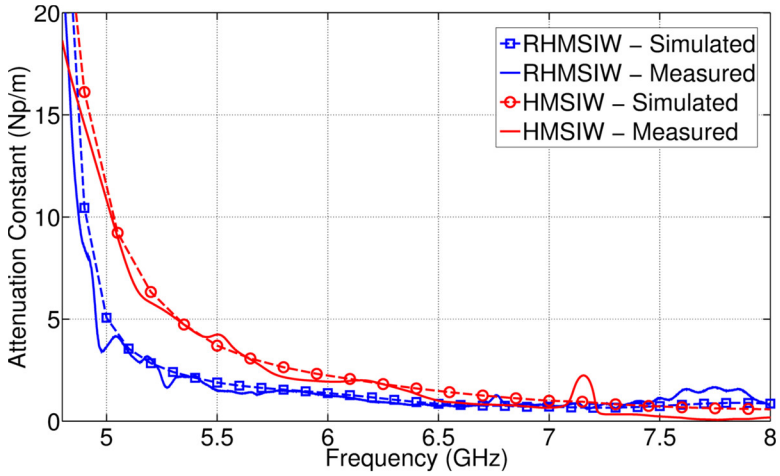

Fig. 3.15. Measured and simulated attenuation constant of the quasi-$TE_{0.5,0}$ mode of the RHMSIW and HMSIW.

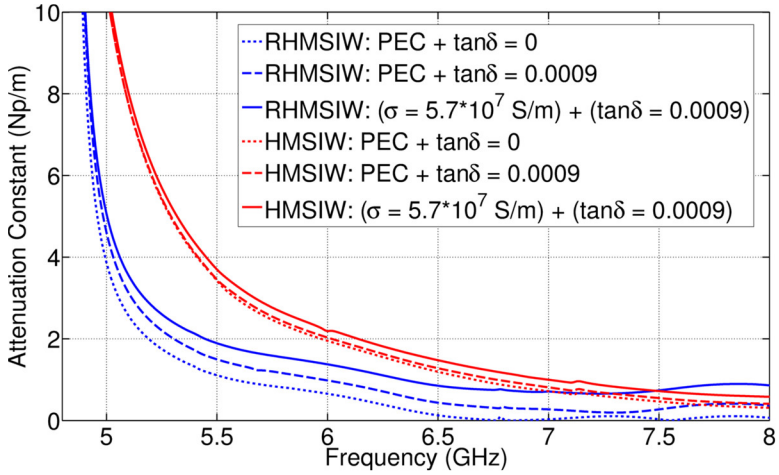

Fig. 3.16. Simulated attenuation constant of the quasi-$TE_{0.5,0}$ mode of the RHMSIW and HMSIW with radiation losses only, subsequently adding dielectric losses and then conductor losses to compare their cumulative effect on the device performance.

With good agreement between the simulated and measured results for the attenuation constant in Fig. 3.15, a comparison between the simulated attenuation constants of the RHMSIW and HMSIW is shown in Fig. 3.16 to individually examine the effect of radiation, dielectric, and conductor loss on the device performance. With a cumulative effect starting with only radiation losses (PEC and $tan\delta = 0$), then introducing dielectric losses (PEC and $tan\delta = 0.0009$), and finally including conductor losses ($\sigma = 5.7\times10^7$ S/m and $tan\delta = 0.0009$), it is clear that the radiation losses are the main contributor to loss in the HMSIW, while for the RHMSIW it is the conductor losses. This is due to the increased field concentration within the reduced ridge height of the RHMSIW, illustrated by the simulated field distributions in Fig. 3.14. The attenuation due to the dielectric loss is also larger for the RHMSIW due to the increased field confinement, but has a smaller impact on the total attenuation than the conductor loss. Both dielectric and conductor losses are minimal for the HMSIW. From the results of the above design realization, a total miniaturization of the RHMSIW compared to the HMSIW of approximately

45% is achieved. Also, the improved performance below the critical frequency point of $f/f_c \approx 1.45$ of the RHMSIW offers great design potential at operating frequencies closer to cutoff than the HMSIW. In the next section, a thru-reflect-line calibration kit for the RHMSIW is designed, fabricated, and analyzed.

3.4 Thru-Reflect-Line Calibration

To directly compare the measured insertion loss of the RHMSIW and HMSIW without transition and SMA connector losses, a thru-reflect-line (TRL) calibration kit was fabricated, using a method outlined in [104], and similarly carried out for SIW in [105].

Fig. 3.17 shows the measured TRL extracted insertion loss of the RHMSIW and HMSIW with 80 mm device lengths, along with pictures of the fabricated RHMSIW open circuit reflect device and thru device. The 40 mm fabricated devices were used for the line standard. The insertion loss for the RHMSIW at the operating frequency of 6 GHz is 0.905 dB, and for the HMSIW is 1.43 dB. Compared to the measured insertion loss with transitions and SMA connectors above, an approximate difference of 0.4 dB for both designs is noted. Therefore, each microstrip transition and SMA connector for the RHMSIW and HMSIW introduces about 0.2 dB of loss.

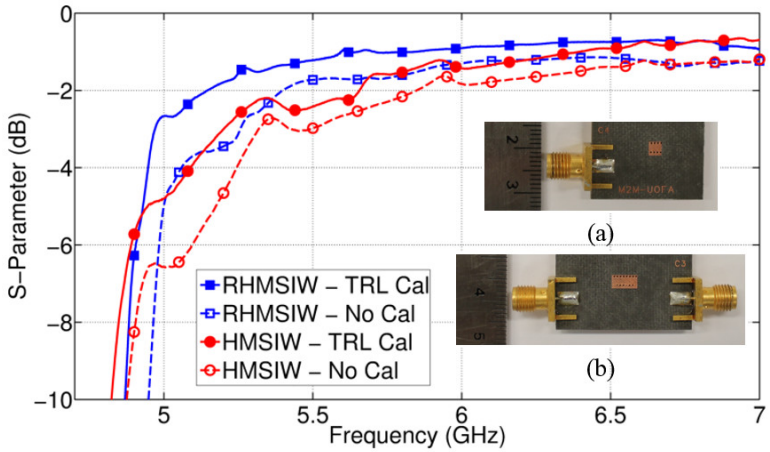

Fig. 3.17. Measured comparison of the TRL extracted insertion loss of the RHMSIW and HMSIW, each with device lengths of L_2 = 80 mm, including pictures of the fabricated RHMSIW TRL calibration kit (a) open circuit reflect device, and (b) thru device.

3.5 Near-Field Measurement

To compare and analyze the field loss, the near-field radiation patterns for the HMSIW and RHMSIW were measured using an EMSCAN RFxpert Scanner RFX2, which measures the radiated magnetic fields tangential to the surface of the scanner. Fig. 17 shows the measurement setup, with the L_2 = 80 mm length DUT placed face down on the scanner. The scanner measures the field strength 25 mm below the scanner's surface. A Rohde & Schwarz Signal Generator was used to supply a 6 GHz CW signal at a power level of 8 dBm into the device (bottom port in Fig. 19). A 50-Ω matched load terminates the other port.

Fig. 3.19 and Fig. 3.20 show the measured near-field radiation patterns for the RHMSIW and HMSIW, respectively. It is clear from these measurements that the radiation loss of the RHMSIW is reduced compared to the HMSIW at the chosen operating frequency of 6 GHz.

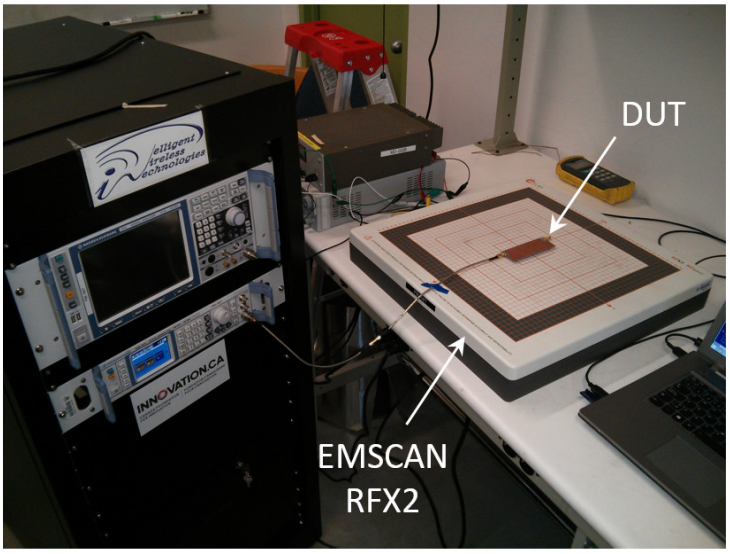

Fig. 3.18. Picture of the experimental setup for measurement of the near-field radiation pattern.

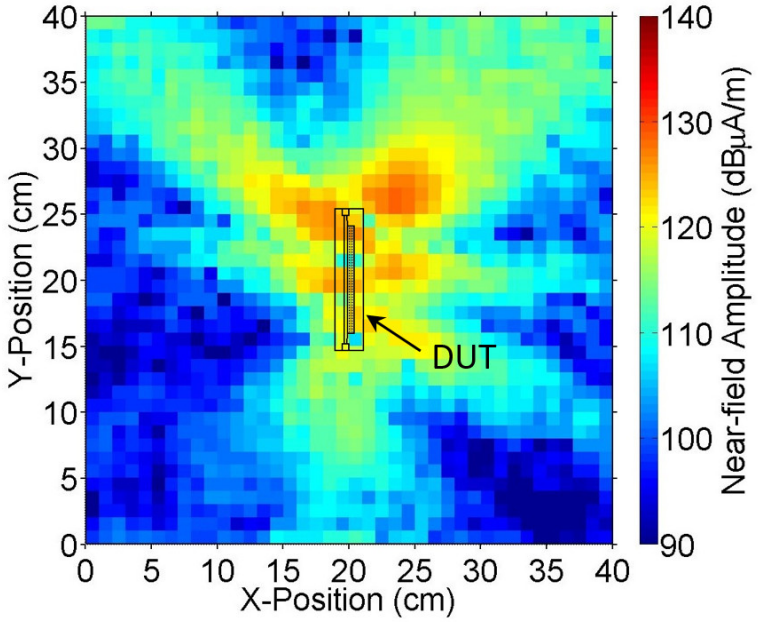

Fig. 3.19. Measured near-field radiation pattern for the RHMSIW with device length L_2 = 80 mm.

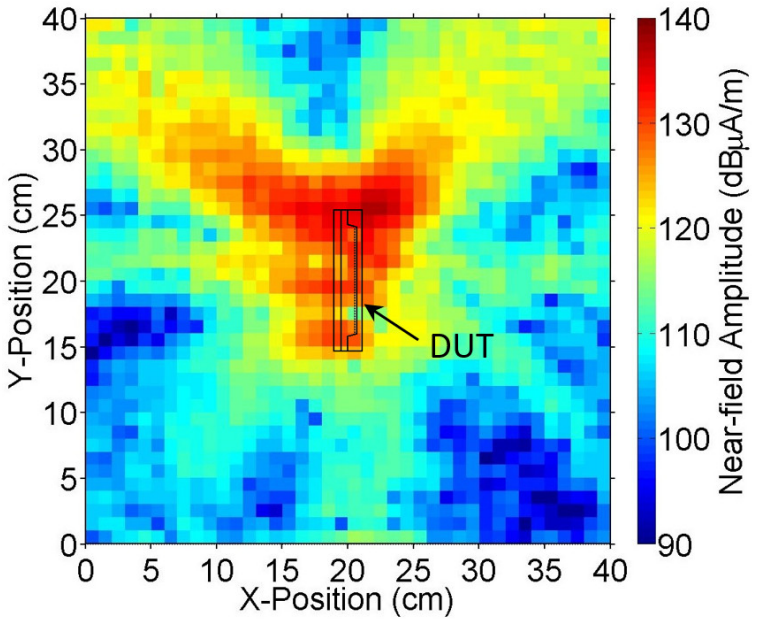

Fig. 3.20. Measured near-field radiation pattern for the HMSIW with device length L_2 = 80 mm.

3.6 Summary

This chapter has outlined the design, fabrication, and characterization of a ridged half-mode SIW, which allows for significant miniaturization of approximately 45% over half-mode SIW, as well as improved performance closer to cutoff frequency. The structure also presents substantial miniaturization of about 75% or more over standard SIW. An analytical calculation for the fundamental quasi-$TE_{0.5,0}$ mode cutoff frequency of the ridged half-mode SIW has been shown, and the measured extraction of the complex propagation constant using the multiline method has illustrated the improved region of performance of the ridged half-mode SIW over half-mode SIW. A critical frequency point of approximately 1.45 × f_c has been determined, where below this point the ridged half-mode SIW has reduced radiation loss, and thus lowered attenuation loss, compared to the half-mode SIW. A near-field measurement of the radiated field loss was also carried out

to confirm this assertion, which clearly illustrated the improvement in radiation loss of the ridged half-mode SIW over half-mode SIW at an operating frequency of 1.25 $\times f_c$. In conclusion, the ridged half-mode SIW is a promising alternative to half-mode SIW as a way to develop miniaturized systems.

Chapter 4

Applications of the Ridged Half-Mode Substrate Integrated Waveguide

The theory and characterization of a new type of miniaturized waveguide platform, namely a ridged half-mode SIW (RHMSIW) was presented in Chapter 3. Compared to a HMSIW, the RHMSIW achieved a measured broadside miniaturization of 45%, while simultaneously reducing the radiation losses suffered by HMSIW closer to cutoff frequency. In this chapter, the benefits of ridged half-mode technology are applied to a variety of microwave applications, including the design of a Riblet short-slot hybrid coupler, two and four-pole slotted bandpass filters, and quarter-mode humidity sensors. For each application, it is shown that RHMSIW technology not only improves the overall size, but also offers certain performance upgrades compared to its counterparts as presented in the literature.

The chapter is organized as follows. First, a study of the use of RHMSIW technology in high density signal routing and interconnects is investigated in Section 4.1. Next, an application of the RHMSIW in a quadrature-type short-slot hybrid coupler is presented in Section 4.2. In Section 4.3, the high-pass property of the RHMSIW is investigated for use in slotted bandpass filter design. For applications in passive microwave sensing, the combination of quarter-mode and ridged technology is investigated in Section 4.4, producing the first ridged quarter-mode SIW (RQMSIW) cavity. Finally, an overall conclusion is provided in Section 4.5.

4.1 High Density Routing and Interconnection

In applications such as filters, multiplexers, and antenna array feeding networks, there is a requirement for the close proximity of transmission line sections, each carrying different signals. It is, therefore, important to provide high isolation between neighboring channels in order to maintain acceptable signal-to-noise ratios and limit crosstalk. Studies comparing the crosstalk between parallel HMSIW with that of MS lines have been performed in [72], [73]. It was found that the isolation of the HMSIW is comparable, or in some configurations improved, to that of MS, but only for frequencies well above the fundamental mode cutoff.

As was shown in Chapter 3, the RHMSIW reduces the radiation losses of the HMSIW closer to cutoff frequency. Therefore, the RHMSIW is expected to improve the isolation between neighboring transmission lines compared to HMSIW. In this section, a study of the RHMSIW for high density signal routing is performed, where significant improvement in terms of crosstalk and signal isolation of the RHMSIW compared to HMSIW is achieved.

4.1.1 Theory and Experiment

The reduced radiation losses of the RHMSIW compared to the HMSIW is expected to improve the isolation between neighboring transmission lines, especially close to cutoff frequency. To study this effect, an experiment using two parallel RHMSIWs in different configurations was performed. As shown in Fig. 4.1, the setup consisted of (a) open-side to open-side, (b) open-side to closed-side, and (c) closed-side to closed-side configurations. The coupling gap g_c was varied

in discrete values between 0 to 20 mm, depending on the configuration and the constraint imposed by the SMA connectors. RHMSIW and HMSIW transmission line sections were diced with a distance of 5 mm from their open-side and 0 mm from their closed-side, and were then placed in parallel, with copper tape applied underneath. The whole setup was clamped to another copper-cladded substrate to limit the effect of the ground plane discontinuity. Small discrete pieces of substrate with the same parameters and thicknesses as those for the RHMSIW and HMSIW were placed in-between the transmission lines to vary the coupling gap.

(a)

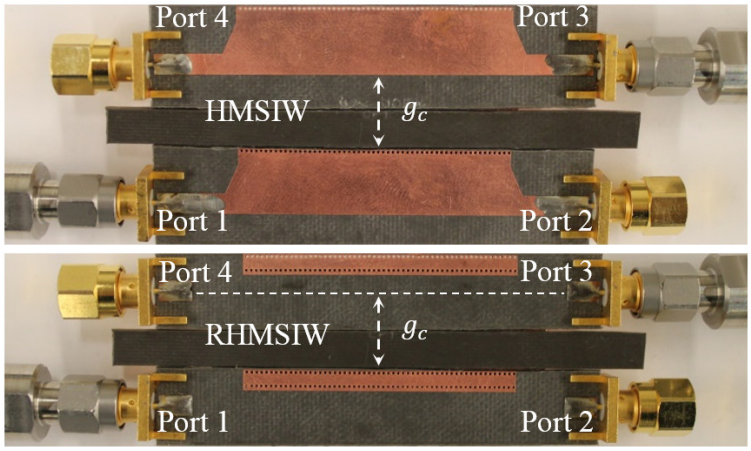

(b)

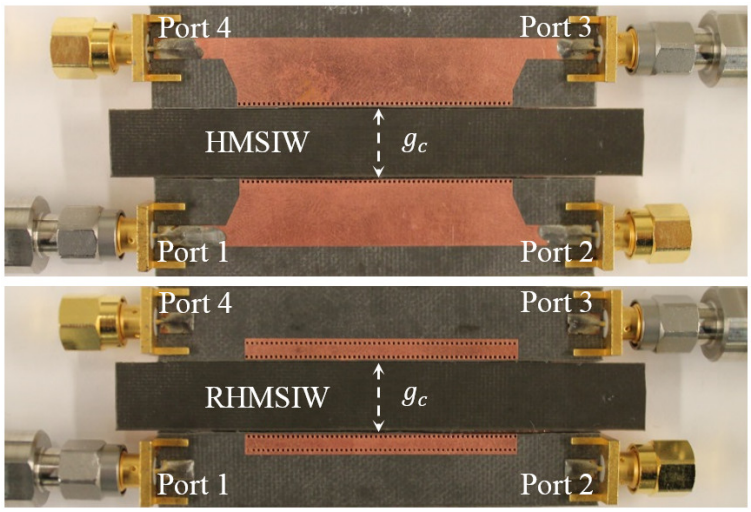

(c)

Fig. 4.1 Pictures of the crosstalk measurement setup for the HMSIW and RHMSIW parallel transmission lines in (a) open-side to open-side, (b) open-side to closed-side, and (c) closed-side to closed-side configurations.

For the open-side to open-side configuration shown in Fig. 4.1(a), the measured far-end coupling (S_{31}) and near-end coupling (S_{41}) of the RHMSIW and HMSIW are shown in Fig. 4.2 for coupling gaps g_c equal to 10 mm, 15 mm, and 20 mm. At an operating frequency of 6 GHz, the measured far-end couplings with increasing g_c for the RHMSIW are -29.6 dB, -32.8 dB, and -34.8 dB, respectively, while for the HMSIW are -22.1 dB, -23.5 dB, and -25.2 dB, respectively. The measured near-end couplings for both the RHMSIW and HMSIW at 6 GHz are below -30 dB. The results show that the RHMSIW provides close to 10 dB greater far-end isolation for each coupling gap than the HMSIW in this configuration, and is close to or below -30 dB across the entire measured band.

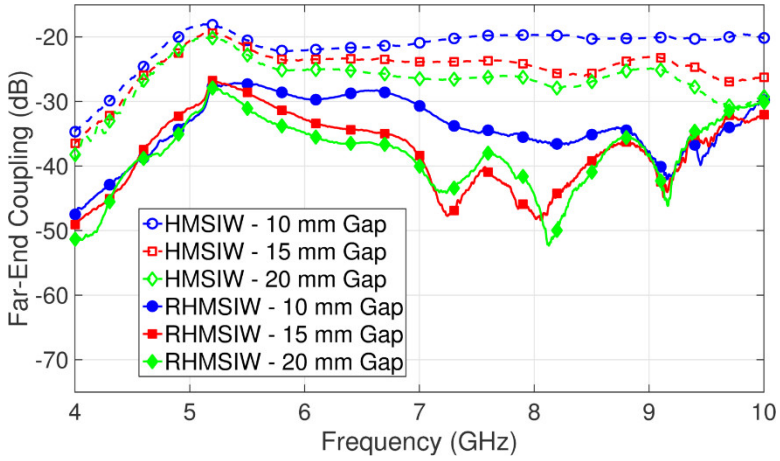

(a)

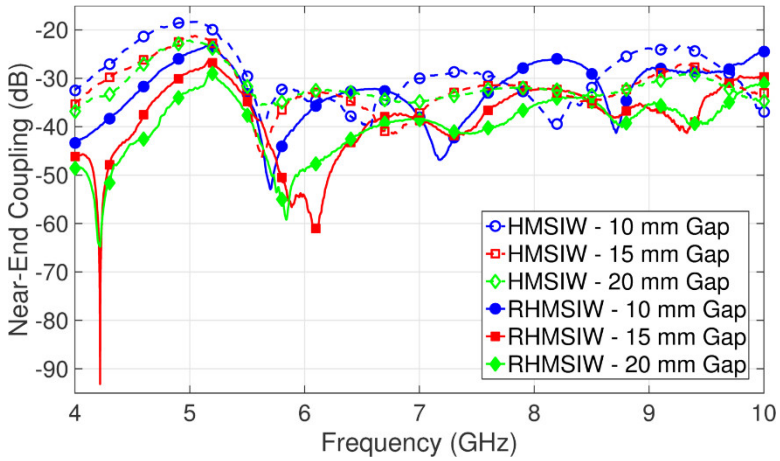

(b)

Fig. 4.2. Measured open-side to open-side coupling between two parallel RHMSIWs and two parallel HMSIWs with various gaps for (a) far-end coupling (S_{31}) and (b) near-end coupling (S_{41}).

Fig. 4.3 shows the crosstalk for the open-side to closed-side configuration in Fig. 4.1(b) with coupling gaps g_c equal to 5 mm, 10 mm, and 15 mm. At the operating frequency of 6 GHz, the measured far-end couplings with increasing g_c for the RHMSIW are -34.6 dB, -36.6 dB, and -37.9 dB, respectively, while for the HMSIW are -26.8 dB, -28.4 dB, and -29.7 dB, respectively. The measured near-end couplings for both the RHMSIW and HMSIW are below -30 dB for most of the measured band. The RHMSIW again provides improved far-end isolation over

the HMSIW by approximately 8 dB. At higher frequencies where $f/f_c \approx 1.45$, or approximately 7.2 GHz and above, the radiation losses of the HMSIW decrease and the far-end couplings for both transmission line types become comparable.

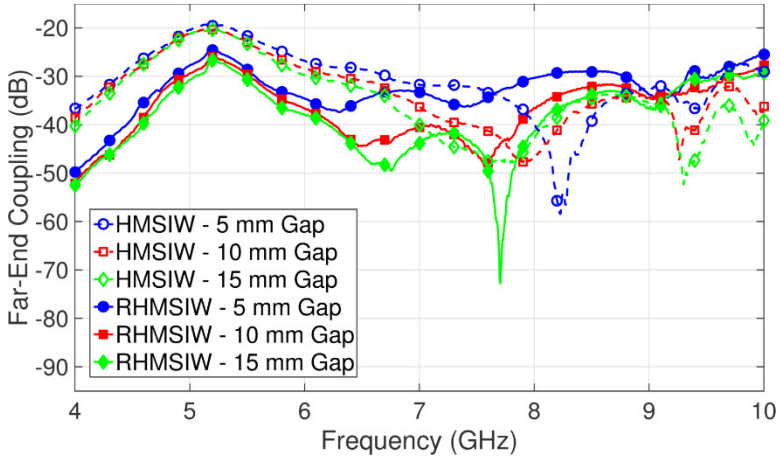

(a)

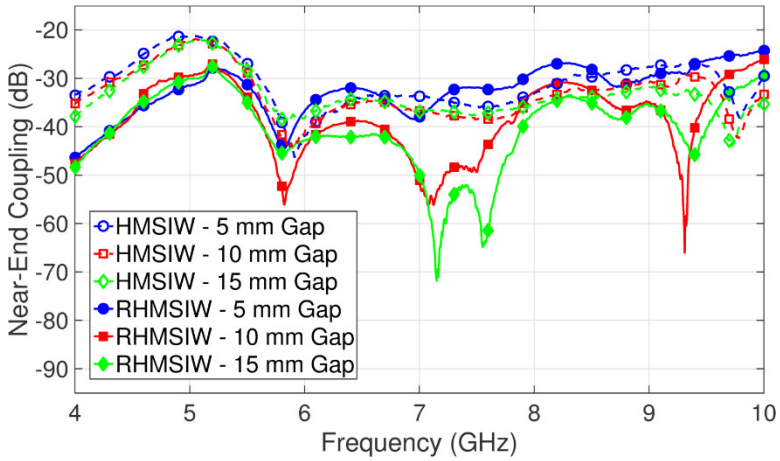

(b)

Fig. 4.3. Measured open-side to closed-side coupling between two parallel RHMSIWs and two parallel HMSIWs with various gaps for (a) far-end coupling (S_{31}) and (b) near-end coupling (S_{41}).

Finally, the measured crosstalk of the closed-side to closed-side configuration in Fig. 4.1(c) is shown in Fig. 4.4 for coupling gaps g_c equal to 0 mm, 5 mm, and 10 mm. At 6 GHz operating frequency the measured far-end crosstalk with

increasing g_c for the RHMSIW are -30.4 dB, -37.6 dB, and -38.1 dB, respectively, while for the HMSIW are -27.3 dB, -31.8 dB, and -33.6 dB, respectively. The measured near-end couplings are close to or below -30 dB for both types, except for the RHMSIW above 7.5 GHz with g_c equal to 0 mm, likely due to the coupling between the microstrip transitions. For this configuration, at the operating frequency of 6 GHz, the RHMSIW provided approximately 5 dB of reduced far-end crosstalk. At higher frequencies, 1.45 times cutoff and above, the HMSIW has reduced far-end crosstalk compared to the RHMSIW, again due to the decrease in radiation losses.

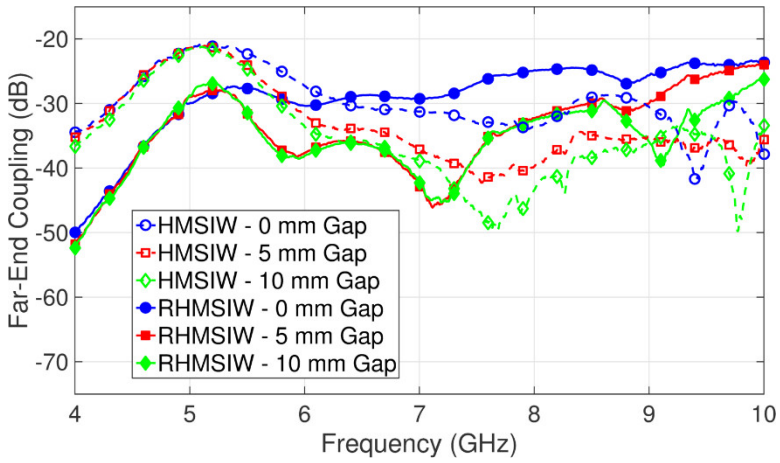

(a)

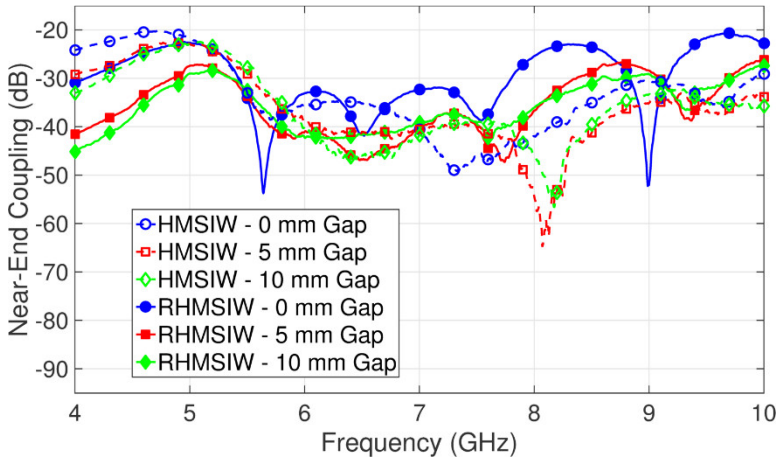

(b)

Fig. 4.4. Measured closed-side to closed-side coupling between two parallel RHMSIWs and two parallel HMSIWs with various gaps for (a) far-end coupling (S_{31}) and (b) near-end coupling (S_{41}).

4.1.2 Discussion

Overall, the RHMSIW clearly provides improved far-end coupling isolation over the HMSIW, especially closer to cutoff frequency, allowing for reduced crosstalk between neighboring transmission lines. For the worst-case scenario of open-side to open-side configuration, the largest improvement is made with 10 dB or greater isolation of the RHMSIW over the HMSIW. For the more common open-side to closed-side configuration, the RHMSIW provided approximately 8 dB of

increased isolation up to approximately 7.2 GHz. Furthermore, the reduced cross-sectional size of the RHMSIW over the HMSIW by approximately 45% also allows for a greater density of interconnects with an equivalent or even greater isolation. Therefore, the reduced footprint, along with the equal or greater isolation and improved attenuation up to approximately 1.45 × f_c makes the RHMSIW an enabling technology for the miniaturization of microwave components requiring high density signal routing, where standard SIW and HMSIW structures are too wide and therefore require more surface area within an RF system.

4.2 Riblet Short-Slot Hybrid Coupler

Hybrid couplers remain critical components of mobile communication systems, including 5G [106], [107]. In this section, the application of RHMSIW technology is applied to miniaturized Riblet short-slot hybrid coupler design, illustrating comparable performance to similar HMSIW and SIW couplers in the literature, but with significant size reduction.

4.2.1 Coupler Design

To explore the potential of the RHMSIW in waveguide coupler applications, a quadrature short-slot hybrid coupler was designed, fabricated, and measured. Following a similar design procedure outlined in [66] for a HMSIW coupler, the coupling is achieved using a slot inserted in the effective broadside wall achieved with electric vias between two side-by-side RHMSIW transmission lines. As shown in the general layout of Fig. 4.5, the final width of the coupling slot *Wcouple* was optimized using HFSS, where it can be tuned for different coupling ratios. Similar

substrates as the fabricated RHMSIW interconnects in Section 3.3 were chosen for the fabrication, along with an equivalent electric via diameter and spacing. The final optimized dimensions are shown in Table 4.1 for operation of the coupler in C-band. Fig. 4.6 shows a picture of the fabricated RHMSIW short-slot hybrid coupler.

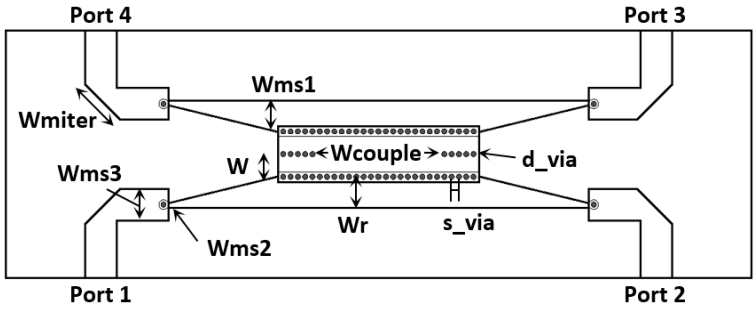

Fig. 4.5. General layout of the proposed RHMSIW short-slot hybrid coupler.

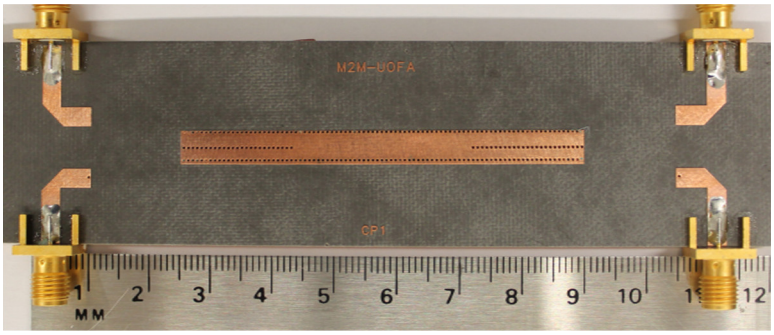

Fig. 4.6. Picture of the fabricated RHMSIW short-slot hybrid coupler.

W	*Wr*	*Wcouple*
2.2 mm	3 mm	29.8 mm
Wms1	*Wms2*	*Wms3*
3 mm	0.58 mm	3.1 mm
Wmiter	*d_via*	*s_via*
4.95 mm	0.508 mm	0.711 mm

Table 4.1. Design Parameters for the RHMSIW Short-Slot Hybrid Coupler

4.2.2 Experimental Results

The simulated and measured scattering parameters are shown in Fig. 4.7. The measured center frequency f_c is approximately 7.0 GHz, with a return loss ($|S_{11}|$) greater than 15 dB from approximately 6.1 GHz to 8.8 GHz. The measured power equality between the through port ($|S_{21}|$) and coupled port ($|S_{31}|$) is 4.98 dB ± 0.5 dB from 6.8 GHz to 7.3 GHz, for a 7% bandwidth. This includes transition and SMA connector loss. The isolation ($|S_{41}|$) is at or above 15 dB across the entire operating frequency range from 6.0 GHz to 7.3 GHz. The insertion loss of the RHMSIW coupler, removing the losses incurred from the SMA connectors, microstrip transitions, and mitered bends, i.e., approximately 0.7 dB total loss, is estimated to be 1.28 dB.

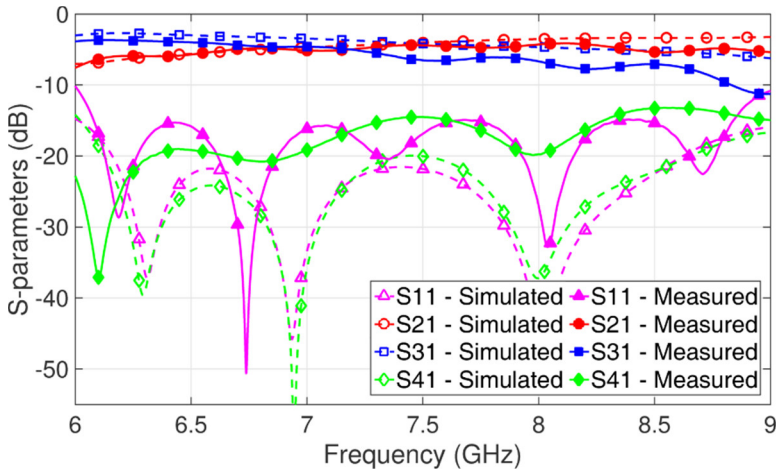

Fig. 4.7. Simulated and measured scattering parameters of the RHMSIW coupler design.

The simulated and measured phase balance between the through (S_{21}) and coupled (S_{31}) ports are shown in Fig. 4.8. Similar to what is expected for quadrature type Riblet short-slot hybrid coupler designs using rectangular waveguide sections [108], the simulated phase balance for the RHMSIW coupler is 90° ± 2.5° from 6.4

GHz to 8.8 GHz. The measured phase balance is 105.6° ± 2.5° over the same frequency range. The discrepancy between simulated and measured results is likely due to fabrication errors, more specifically a misalignment of via holes in the fabricated prototype. This misalignment yielded a slight difference between the two coupled waveguide channel and ridge widths. Due to the sensitivity of the cutoff frequency of the RHMSIW to the ridge width, the phase delay of each waveguide channel will be different at a particular frequency, causing a shift in the measured phase balance.

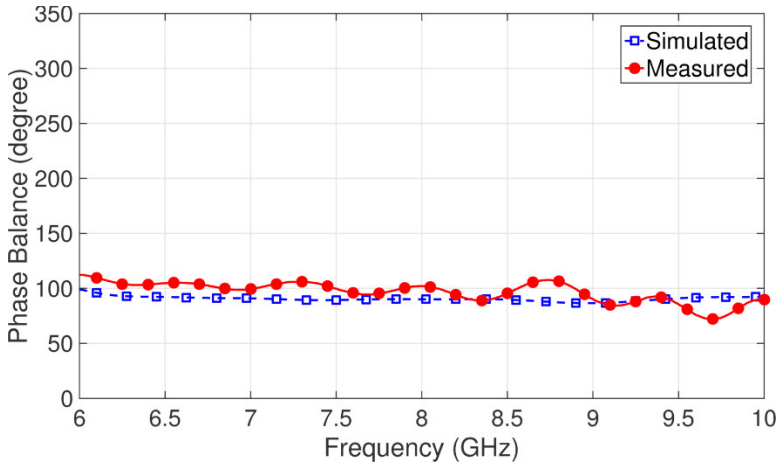

Fig. 4.8. Simulated and measured phase balance between the through (S_{21}) and coupled (S_{31}) ports of the RHMSIW coupler design.

Table 4.2 compares the RHMSIW coupler of this work with the HMSIW and SIW couplers designed in [66]. It can be seen that the RHMSIW and SIW have comparable performance, but the RHMSIW achieves a 60% miniaturization, with a much lower operating frequency range and waveguide cutoff frequency. If the RHMSIW was to be designed with a similar frequency range and cutoff frequency of the HMSIW and SIW designs in [66], even greater miniaturizations could be achieved.

Technology	RHMSIW	HMSIW [66]	SIW [66]
Return Loss ($\|S_{11}\|$)	> 15 dB 6.1 to 8.8 GHz	> 15 dB 10.3 to 15 GHz	> 13.1 dB 10.1 to 11.4 GHz
Power Equality ($\|S_{21}\|$ & $\|S_{31}\|$)	4.98 dB ± 0.5 dB 6.8 to 7.3 GHz	4.1 dB ± 0.5 dB 10.9 to 13.5 GHz	4.4 dB ± 0.4 dB 10.5 to 11.9 GHz
Isolation ($\|S_{41}\|$)	> 15 dB 6 to 7.3 GHz	> 20 dB 10.5 to 13.1 GHz	> 14.1 dB 10.4 to 11.6 GHz
Insertion Loss	1.28 dB	0.5 dB	0.9 dB
Total Width	10.4 mm	13 mm	25.4 mm

Table 4.2. Measured Coupler Performance Comparison

4.3 Slotted Bandpass Filter Design

SIW filters play an integral role in modern RF front-end integrated circuit (IC) design [109]. Yet, with an increasing demand for components delivering greater integration with smaller footprints, SIW technology is becoming less convenient to use. To this effect, bandpass filters utilizing the high-pass property of the HMSIW, along with the bandpass property of coupled slotted resonators, have not only reduced the overall design footprint, but have also improved performance compared to similar SIW filters [68].

In this section, further miniaturization of slotted HMSIW bandpass filters is demonstrated by the incorporation of a capacitive ridge. In addition, the lower insertion loss of the RHMSIW compared to HMSIW closer to cutoff frequency, as described in Chapter 3, also improves the bandpass filter performance utilizing the high pass property of RHMSIW. Compared to previously reported slotted HMSIW filters, the proposed structure has a smaller footprint, lower insertion loss, and a larger stopband all at once.

4.3.1 Filter Design

The design of a slotted RHMSIW bandpass filter (BPF) is based on the procedure for a slotted HMSIW BPF presented in [68]. The filter design combines the high-pass property of the RHMSIW with the bandpass property of quasi-TEM coupled slotted resonators. As shown in Fig. 4.9, a single quasi-TEM mode slotted resonator can be formed by inserting two transverse slots within a small section of either (a) HMSIW, or (b) RHMSIW. By incorporating a capacitive ridge, the RHMSIW resonator reduces the transverse width of the HMSIW resonator by approximately 50%. Furthermore, due to the reduced radiation losses and therefore lower attenuation closer to cutoff frequency of the RHMSIW compared to HMSIW (see Section 3.2), an improvement in performance of the slotted RHMSIW resonator is also achieved.

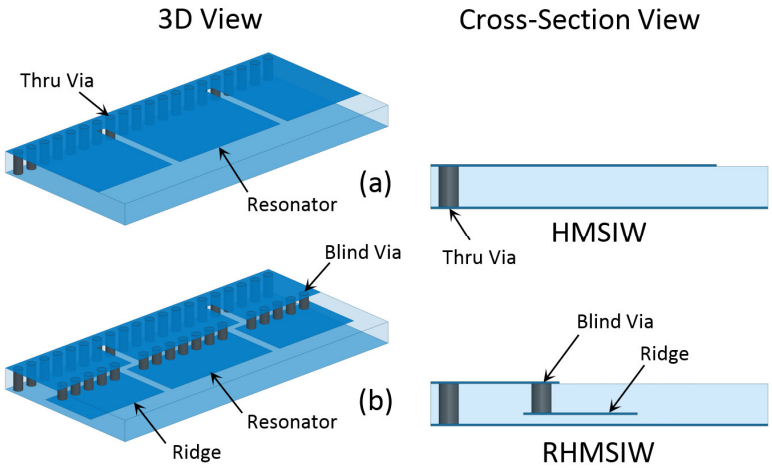

Fig. 4.9. General 3D configuration and cross-sectional view of the (a) half-mode substrate integrated waveguide, and (b) ridged half-mode substrate integrated waveguide for a single quasi-TEM slotted resonator.

Using the coupling synthesis method [22], [110], two-pole and four-pole slotted BPFs were designed using RHMSIW technology. Fig. 4.10 shows the general layouts of the two designs, with dimensions shown in Table 4.3 and Table 4.4.

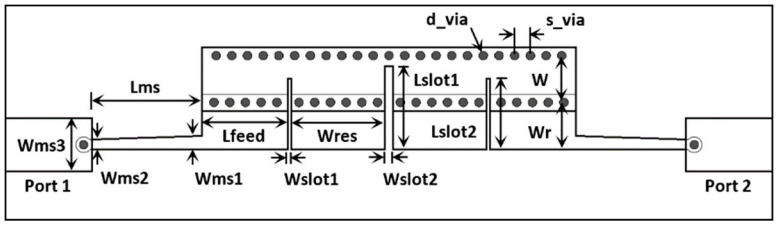

(a)

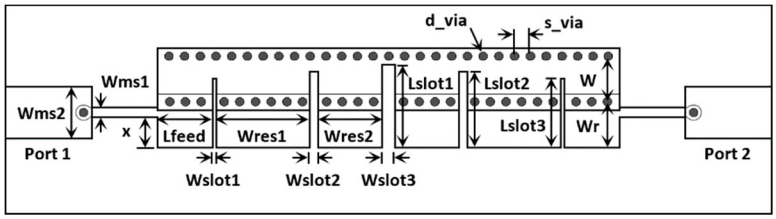

(b)

Fig. 4.10. Layout of the (a) two-pole, and (b) four-pole RHMSIW slotted BPFs.

Parameter	Quantity (mm)	Parameter	Quantity (mm)
W	2.2	*Wres*	5.5
Wr	3	*Wms1*	0.8
Lfeed	5	*Wms2*	0.58
Lslot1	4.8	*Wms3*	3.1
Lslot2	4.1	*Lms*	13
Wslot1	0.15	*d_via*	0.508
Wslot2	0.4	*s_via*	0.914

Table 4.3. Two-Pole Bandpass Filter Dimensions

Parameter	Quantity (mm)	Parameter	Quantity (mm)
W	2.2	*Wres1*	4.8
Wr	3	*Wres2*	3.4
Lslot1	4.55	*Lfeed*	3
Lslot2	4.15	*x*	2.3
Lslot3	3.65	*Wms1*	0.58
Wslot1	0.15	*Wms2*	3.1
Wslot2	0.6	*d_via*	0.508
Wslot3	0.6	*s_via*	0.864

Table 4.4. Four-Pole Bandpass Filter Dimensions

To design the filter, the ridge width for a desired RHMSIW cutoff frequency is first determined by solving the transverse resonance equation (3.3) as described in Section 3.1 with the channel and ridge widths *W* and *Wr* shown in Fig. 4.10. The design of the 50-Ω microstrip feed network follows the same procedure as previously discussed in Section 3.3.

Next, a single resonator is formed by a section of the RHMSIW transmission line located in between two transverse slots, as per Fig. 4.9. This creates a resonator transverse to the direction of propagation with 90° electrical length at center frequency f_0. Due to the input/output loading, the resonator's effective length is shortened, increasing f_0 above the cutoff frequency of the RHMSIW. This allows the high-pass property of the RHMSIW feed sections to improve the isolation and lower skirt of the passband. Increasing the slot width also decreases the resonant frequency (and vice versa), by increasing the amount of fringing capacitance of the resonator. Simulated in HFSS, f_0 and Q_u of a single resonator can be determined. For dimensions given in Table 4.3, the simulated Q_u was 236. Increasing the resonator width decreases f_0, and vice versa, by changing its characteristic

admittance. The maximum value chosen is so the undesired spurious passband generated by an axial $\lambda/2$ resonance is approximately three times higher than f_0. This allows for a wide stopband above the passband.

Finally, the inter-resonator and input/output coupling is determined. The coupling between two resonators splits f_0 into an even and odd mode resonance. Two resonators are simulated in HFSS, with their coupling coefficients determined from the scattering parameters. Increasing the width of the slot decreases the coupling between resonators, and vice versa. The input/output feed network coupling predominantly controls the insertion loss of the filter.

4.3.2 Experimental Results

Following the layouts in Fig. 4.10, two-pole and four-pole filters were fabricated using conventional printed circuit board (PCB) processes. Due to the ridge of the RHMSIW, a multilayer substrate was required. A Rogers RT/duroid 5880 substrate was chosen with 31 mil and 5 mil thicknesses for the top and bottom, respectively. Rogers 4 mil RO4450F Bondply was used to bond the two substrates together. A picture of the fabricated devices is shown in Fig. 4.11. Although the main filter region of the four-pole device is clearly longer than for the two-pole device, a direct 50-Ω microstrip feed was designed for the four-pole filter, removing the need for a taper. Therefore, the total overall width and length of the four-pole filter was reduced. Also, the bottom substrate required no patterned trace, thus decreasing the alignment complexity in fabrication compared to the RHMSIW filter in [111].

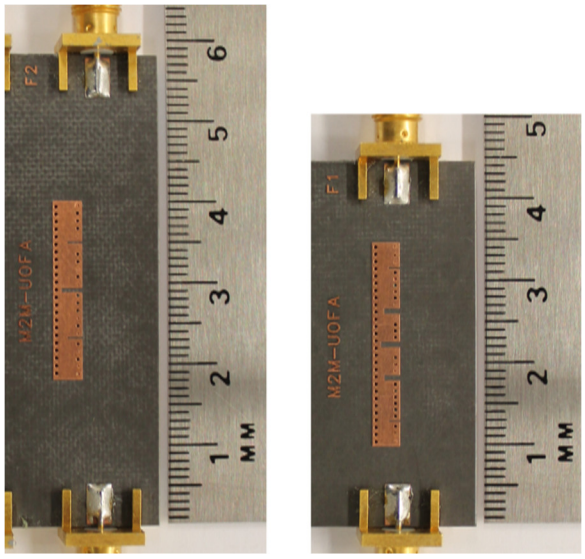

(a) (b)

Fig. 4.11. Photographs of the (a) two-pole, and (b) four-pole RHMSIW slotted BPFs.

The measured and simulated scattering parameters of the two-pole and four-pole filters are presented in Fig. 4.12, with their corresponding group delays given in Fig. 4.13, all showing good agreement. The two-pole filter's f_0 is at 5.13 GHz, with a fractional bandwidth (FBW) of 19%. The measured insertion loss at f_0 is 0.81 dB, with a return loss greater than 28 dB. The four-pole filter's f_0 is at 5.5 GHz, with a FBW of 21%. The measured insertion loss at f_0 is 0.86 dB, with a return loss greater than 17 dB. The measured insertion losses include both transition and SMA connector losses. The increased variation in group delay at the bandpass edges of the four-pole versus the two-pole filter is typical of higher order filters.

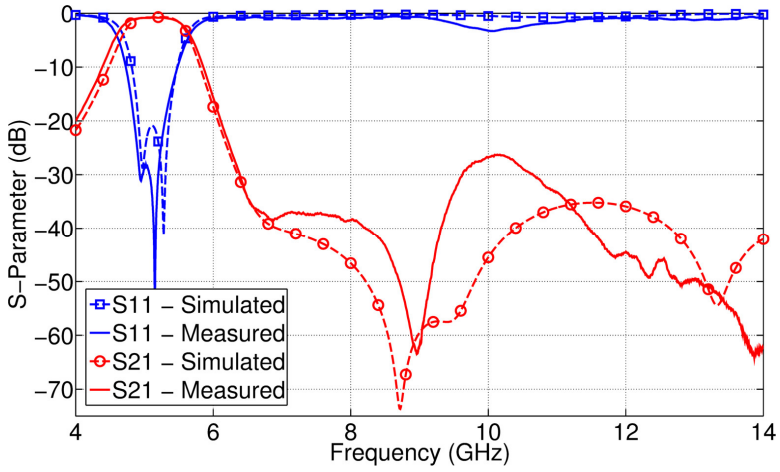

(a)

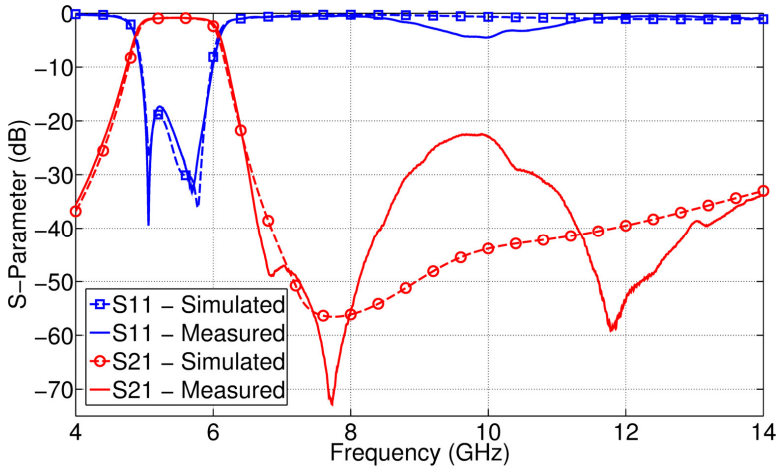

(b)

Fig. 4.12. Simulated and measured scattering parameters of the (a) two-pole, and (b) four-pole RHMSIW slotted BPFs.

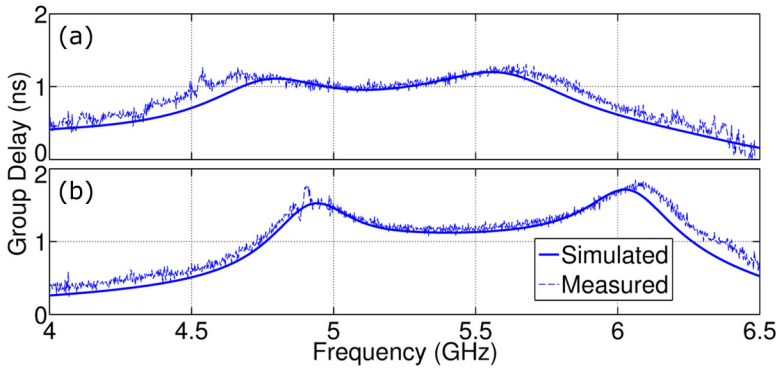

Fig. 4.13. Simulated and measured group delay of the (a) two-pole, and (b) four-pole RHMSIW slotted BPFs.

In Fig. 4.12, a discrepancy between simulation and measurement is noticed around 10 GHz for both the two-pole and four-pole filters. This is due to the choice of SMA connector (Johnson 142-0701-801), where in the upper stopband region the transition from coaxial-to-microstrip generates a coupling at approximately 10 GHz. In Fig. 4.14(a), the measured scattering parameters of the four-pole filter are compared to simulation including SMA connectors, where the coupling at 10 GHz is now seen in both the simulated and measured response. In Fig. 4.14(b), the loss of the measured four-pole filter is compared to simulation with and without SMA connectors, calculated using the standard equation $Loss = 1 - |S_{11}|^2 - |S_{21}|^2$. At 10 GHz, compared to the simulated results without SMA connectors, a large increase in loss (above 3 dB) is noticed for both the measured results and the simulated results with SMA connectors. Thus, a significant amount of energy is coupled out of the system at this frequency. As this coupling is not desired, a better choice of SMA connector or microstrip pad layout is recommended for use of this structure in an industrial setting. However, the simulated results highlight the large upper stopband greater than 8 GHz for both the two-pole and four-pole RHMSIW slotted BPFs.

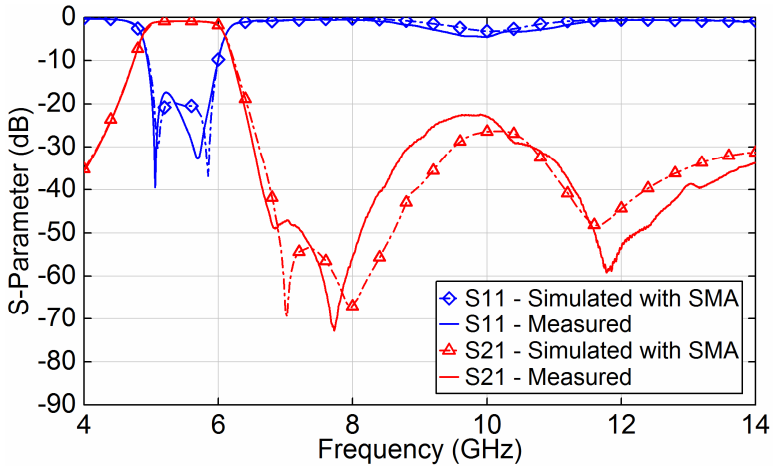

(a)

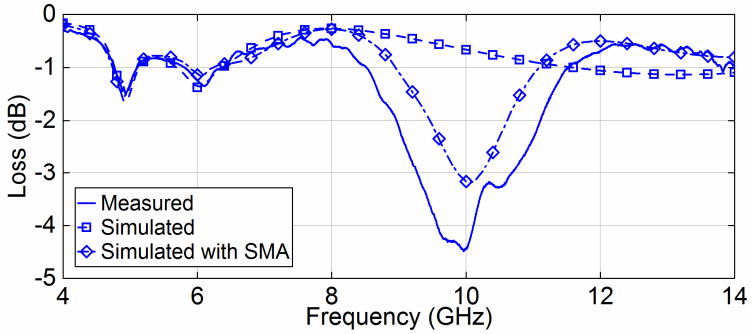

(b)

Fig. 4.14. (a) Simulated and measured scattering parameters of the four-pole RHMSIW slotted BPF, where the simulation now includes the SMA connectors and their effect in the upper stopband, and (b), calculated loss of the measured four-pole filter compared to simulation with and without SMA connectors.

In Table 4.5, a comparison is made between the proposed RHMSIW slotted BPF, along with a similar HMSIW slotted BPF [68], and a mixed magnetic and electric coupling RHMSIW BPF [111]. Dimensions are normalized to free-space wavelength (λ_0). It is clear that the proposed slotted RHMSIW filter technology provides excellent potential for miniaturization over conventional half-mode design, with both operating at lower center frequencies and reduced widths. The insertion losses of the recommended designs are also improved considerably. Comparing to the recently presented RHMSIW that incorporates mixed coupling

[111], the slotted coupling presented here demonstrates a much larger stopband, where the undesired spurious passband was attributed to a resonance due to the mixed coupling structure. The alignment of patterned traces on both the top and bottom substrates of the multilayer structure also increases fabrication complexity compared to the slotted RHMSIW presented here. The two-pole RHMSIW filter of this work also achieves a 0.1 dB reduction in insertion loss compared to the mixed coupling type filter. This is likely due to the simpler design architecture of the slotted RHMSIW filter.

Technology	RHMSIW	RHMSIW [111]	HMSIW [68]
Coupling / # of Poles	Slotted / 2P, 4P	Mixed / 4P	Slotted / 3P, 5P
Center Freq. (f_0)	2P: 5.1 GHz 4P: 5.5 GHz	6.43 GHz	3P: 7.8 GHz 5P: 8.8 GHz
Insertion Loss ($\|S_{21}\|$)	2P: 0.81 dB 4P: 0.86 dB	0.9 dB	3P: 1.5 dB 5P: 1.2 dB
Return Loss ($\|S_{11}\|$)	2P: > 28 dB 4P: > 17 dB	> 20 dB	3P: > 10 dB 5P: > 10 dB
FBW	2P: 19% 4P: 21%	38%	3P: 22% 5P: 40%
Stopband	2P: > 8 GHz 4P: > 8 GHz	4 GHz	3P: 10 GHz 5P: 9 GHz
Total Waveguide Width (W_{Total}/λ_0 at f_0)	2P: 0.089 4P: 0.095	0.13	3P: 0.18 5P: 0.21
Largest Resonator Area ($W_{Res}\times L_{Res}/\lambda_0$ at f_0)	2P: 0.0083 4P: 0.0084	0.017	3P: 0.024 5P: 0.026

Table 4.5. Bandpass Filter Design Comparison

4.4 Quarter-Mode Cavity Humidity Sensor

Passive microwave sensors are increasingly being explored for *in situ*, noninvasive remote sensing for a range of industrial and radio frequency ID (RFID) applications, offering simplified, low-cost, robust and mass-producible methods

and structures [112]. Planar structures have been heavily studied for sensing in various configurations [113]. They have small form factors and are amenable to different applications. Recently, such structures have been combined with active components to enhance their quality factor and as a result achieve high sensing resolution. However, for *in situ* measurements, such structures require DC power consumption and limits their long time use.

Substrate integrated waveguides (SIW) are becoming increasingly popular in part due to their unique combination of characteristics, including low loss and high Q with that of planar technology, such as integration and low cost [5]. Yet limited research has been conducted on their sensing applications. The first SIW cavity resonator capable of environmental sensing was recently introduced in [114], [115]. By drilling small air holes in the region of highest electric field concentration, relative humidity (RH) measurements over a wide range were possible without the use of humidity sensitive materials. Resonant frequency shifts of 9.35 kHz/RH and 101 kHz/RH were reported, depending upon the sensitive region size. In [116], SIW cavity resonators with graphene sheets grown on the top of resonating slots were used for gas detection. Significant resonant frequency shifts up to 159 MHz were achieved detecting ammonia gas concentrations, but require deposition of sensitive materials. 3D printed SIW sensors have also been shown [117]. Although these SIW cavity sensors show promising results, they still have a large footprint.

In this section, we investigate sensor development utilizing the advantageous miniaturization techniques of SIW such as quarter-mode design and capacitive ridge structures as shown in Fig. 4.15. It is demonstrated that application of quarter-

mode SIW (QMSIW) and ridged quarter-mode SIW (RQMSIW) not only can significantly reduce the size of the sensor in [114], [115], but also better sensing performance can be achieved.

4.4.1 Sensor Theory, Design, and Fabrication

Fig. 4.15 shows the general 3D layouts of the QMSIW and RQMSIW cavities. From [10], the QMSIW cavity is created by dicing a SIW square cavity into four quarters, with two electric walls formed by periodic via arrays, and two open sides. Due to the large width to height ratio of the cavity compared to substrate thickness, the QMSIW resonant frequency largely remains the same as the SIW fundamental $TE_{1,0,1}$ mode, with the two open sides behaving as effective magnetic walls. The cavity is fed with a 50-Ω microstrip, input matched by changing the gap between the closest via and the microstrip line. This adjusts the amount of capacitance or inductance seen by S_{11} at resonance, allowing the resonator to be tuned to critical coupling. QMSIW uses a quarter of the SIW footprint.

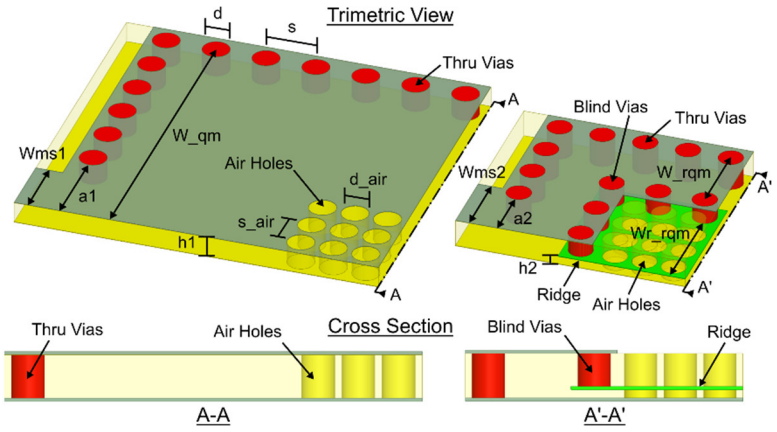

(a) (b)

Fig. 4.15. General 3D configuration of the (a) QMSIW resonator, and (b) RQMSIW resonator, with dimensions *W_qm* = 11.8 mm, *W_rqm* = 3.21 mm, *Wr_rqm* = 4.53 mm, *Wms1* = 2.4 mm, *Wms2* = 2.8 mm, *a1* = 3.17 mm, *a2* = 2.2 mm, *h1* = 0.787 mm, *h2* = 0.127 mm, *d* = 1 mm, *s* = 1.85 mm, *d_air* = 1 mm, *s_air* = 1.203 mm, ε_r = 2.2, *tanδ* = 0.0009, *tcopper* = 18 µm.

For further miniaturization, a capacitive ridge is placed in the area of maximum electric field of the QMSIW. This loading decreases the phase velocity, lowering the cutoff frequency, miniaturizing the cavity up to 50%. The design of the RQMSIW follows from Section 3.1, where the transverse resonance technique (3.3) is used to determine the cutoff wavelength λ_c. The resonant frequency is next found from λ_g, determined by the well-known relation $\lambda_g = \lambda \times (1 - (\lambda/\lambda_c)^2)^{-1/2}$, where λ is the wavelength of a plane wave in the dielectric medium filling the cavity. Input matching of the RQMSIW is similar to QMSIW, with a 50-Ω microstrip feed tuned to critical coupling. Two designs were fabricated using Rogers 5880 substrates. The sensitive region is created by drilling a 3×3 array of air holes into the region of maximum electric field for greatest sensitivity to humidity changes, in accordance to the SIW sensor in [114] for comparison. By adjusting relative humidity (RH), the change in permittivity inside the air holes shifts the cavity resonant frequency.

A picture of the fabricated devices is shown in Fig. 4.16, with the area of the RQMSIW approximately 48% less than the QMSIW. Due to the multilayer design and in-house fabrication of the RQMSIW, a slight air-gap existed between the two substrates, even with plastic screws used to tighten the layers together. This can be seen in Fig. 4.17, which shows the simulated and measured resonant frequencies of the two designs. While both were designed for 6 GHz, the measured RQMSIW frequency shifted up to 6.9 GHz due to the decreased capacitive loading. This air-gap was added to the simulation and determined to be 78 µm, matching the two results of the RQMSIW. The electric field distributions are displayed in Fig. 4.17, showing the fundamental mode resonance. The extracted unloaded quality factors for the measured QMSIW and RQMSIW resonators are 35 and 86, respectively. From the investigation in Chapter 3, the radiation loss of the RHMSIW was reduced compared to standard HMSIW, explaining the resulting higher quality factor measured here.

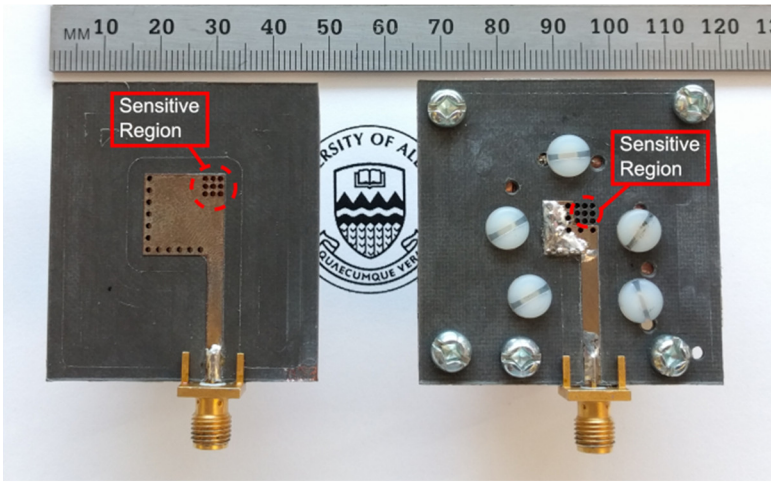

(a) (b)

Fig. 4.16. Picture of the fabricated devices used for humidity measurement; (a) QMSIW resonator, and (b) RQMSIW resonator.

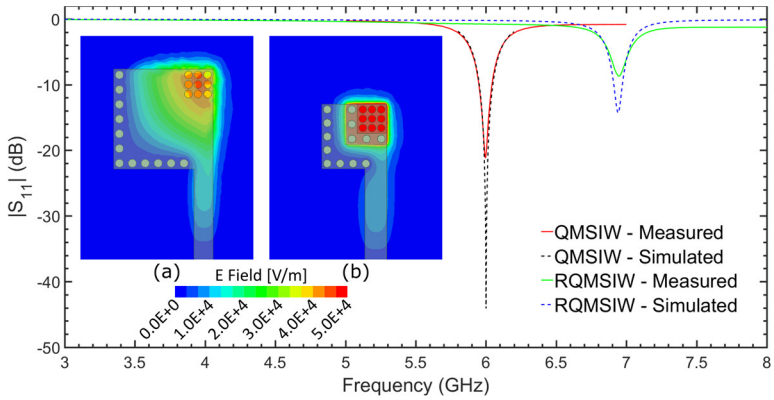

Fig. 4.17. Simulated and measured (RH = 20) resonant frequencies of the QMSIW and RQMSIW humidity sensors, with fundamental electric field distributions of (a) QMSIW, and (b) RQMSIW.

4.4.2 Experimental Setup

To measure the response to changes in humidity, the device under test (DUT) was place in a closed chamber, and different levels of humidity were pumped in. Fig. 4.18 shows a picture of the experimental setup, with a schematic diagram in Fig. 4.18(a). A glass bubbler was used to generate the humidity, and by varying the amount of flow through the two mass flow controllers (MFC), the desired humidity level within the chamber could be maintained. With a constant flow rate of 2 sccm into the chamber, mitigating condensation buildup inside the air holes, an adjustable RH level between 0% – 80% was achieved. At each discrete humidity level change, the chamber was given 10 minutes to settle. Four separate measurements were then taken by a vector network analyzer calibrated with 40 MHz bandwidth, 100 Hz IF, 0 dBm power, and 6401 number of points. RH measurement was recorded from a wireless humidity sensor placed in the chamber. Each individual experiment was repeated a minimum of three times and an error bar is included in the results.

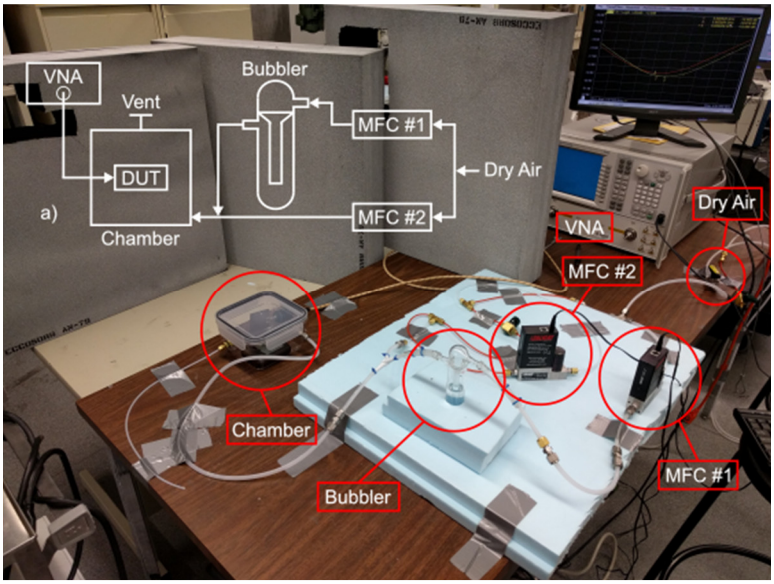

Fig. 4.18. Experimental setup used for humidity measurement including (a) schematic diagram, where an Agilent PNA E8361C is calibrated with BW of 40 MHz centered at 5.993 GHz with IF = 100 Hz and 6401 points.

4.4.3 Measured Results

The measured results of the QMSIW and RQMSIW humidity sensors are shown in Fig. 4.19 and Fig. 4.20, respectively. For the QMSIW sensor, measurements were taken at approximately 10% RH intervals. Due to the in-house fabrication challenges of the multilayer RQMSIW design, measurements at only the two humidity extremes were taken. The measured sensitivity of each sensor was extracted using $S = |\Delta f/\Delta\%RH|$ [114], [118]. For the QMSIW sensor, a sensitivity of 36.5 kHz/RH was measured, while the measured sensitivity of the RQMSIW sensor was 30.73 kHz/RH.

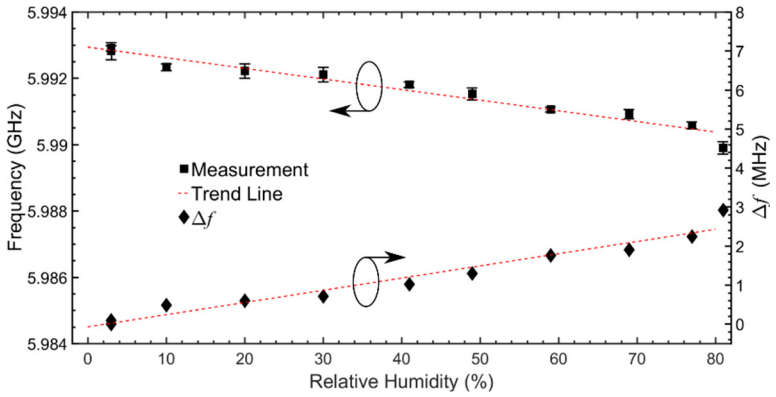

Fig. 4.19. Measured resonant frequency (left) and frequency shift Δf (right) as a function of relative humidity of the QMSIW sensor, including trend lines.

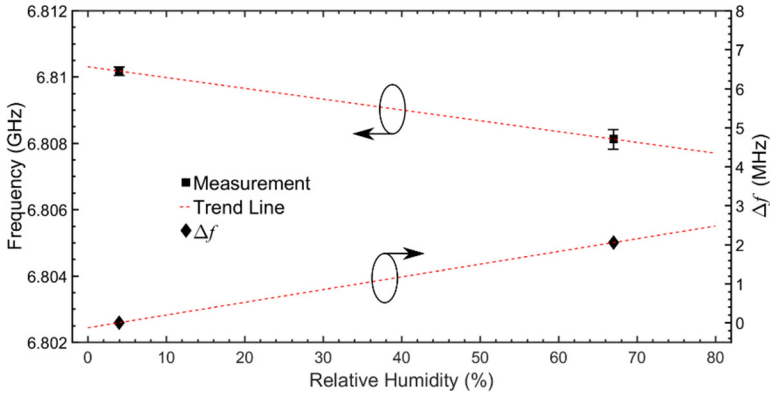

Fig. 4.20. Measured resonant frequency (left) and frequency shift Δf (right) as a function of relative humidity of the RQMSIW sensor, including trend lines.

Table 4.6 compares the measured performance with a standard SIW sensor in [114] with similar air hole placement. The QMSIW and RQMSIW sensors offer almost four times the sensitivity, with miniaturizations normalized to the respective wavelength in free-space (λ_0) of 73.3% and 86.2%, respectively. For the QMSIW, the higher sensitivity is likely due to fringing fields along the open side of the cavity, increasing interaction between the field and air region. Due to the ridge, the RQMSIW sensor fringing fields extend less out the open side, visible in the field profile shown in Fig. 4.17. Thus, the improved sensitivity of the RQMSIW over the SIW in [114] is likely due to the increased capacitance of the ridge region itself,

increasing its sensitivity to changes in permittivity. The slightly lower sensitivity of the RQMSIW versus QMSIW relates to a reduced field interaction with the environment, and thus lower sensitivity in comparison, but the higher quality factor allows smaller changes to be distinguished with greater resolution.

Technology (similar sensing region)	Sensing Method	Measured RH Range	Measured Sensitivity	Cavity Area	Miniat-urization	
SIW Cavity	Resonant Frequency Shift	0 – 80%	9.35 kHz/RH	$0.0116\times\lambda_0$	0% (Ref.)	[114]
QMSIW Cavity	Resonant Frequency Shift	0 – 80%	36.50 kHz/RH	$0.0031\times\lambda_0$	73.1%	This Work
RQMSIW Cavity	Resonant Frequency Shift	0 – 70%	30.73 kHz/RH	$0.0016\times\lambda_0$	86.1%	This Work

Table 4.6. Humidity Sensor Performance Comparison

4.5 Summary

This chapter has evaluated the use of RHMSIW technology in a variety of microwave applications, demonstrating its significant potential as a miniaturized integrated waveguide platform. First, a study of the RHMSIW for applications requiring high density routing or interconnections was conducted. Due to the lower radiation losses, the crosstalk between parallel RHMSIW transmission lines was reduced in all three configurations compared to the HMSIW, especially closer to the fundamental cutoff frequency. Next, a design application of a RHMSIW short-slot hybrid coupler was fabricated and measured, with good agreement between simulated and experimental results. A comparison was made between a related HMSIW and SIW coupler design in the literature, where it was shown the RHMSIW can achieve comparable performance, but with much greater

miniaturization, allowing for a substantially reduced circuit footprint. For applications in microwave filtering, the design and measurement of a two-pole and four-pole RHMSIW slotted BPF was presented. RHMSIW technology not only allows for substantial miniaturization over HMSIW, but the slotted BPF design shown also achieved much lower IL, while still maintaining a wide stopband. A comparison was also made between a mixed coupling RHMSIW BPF, where the filter of this work improved the insertion loss and achieved a much wider stopband. Finally, the design and measurement of QMSIW and RQMSIW cavities for passive humidity sensing was presented. Not only due these two technologies provide substantial miniaturization compared to SIW humidity sensors, but a dramatic increase in sensitivity has also been reported. Due to their smaller size and increased sensitivity, the results presented in this chapter illustrate the potential of these two technologies for the miniaturization of passive SIW sensors for *in situ*, noninvasive sensing applications.

Chapter 5

Folded Ridged Half-Mode Substrate Integrated Waveguide

In Chapter 3, a miniaturized integrated waveguide platform called a ridged half-mode SIW (RHMSIW) was introduced. By incorporating a capacitive ridge along the open side of a HMSIW, it was shown that the broadside width could be reduced by 45%, while simultaneously improving performance closer to cutoff frequency by decreasing the amount of radiation loss. Furthermore, compared to standard SIW, reductions in broadside width of 75% or more were shown to be possible. In Chapter 4, a range of applications using RHMSIW technology were investigated, including high density interconnects, couplers, filters, and sensors, each highlighting the significant potential of the proposed miniaturized integrated waveguide platform. However, through the application of folded SIW (FSIW) techniques, even greater miniaturizations of SIW are possible.

In this chapter, the combination of folded and ridged half-mode technology is investigated to achieve ultimate miniaturization of the broadside width of SIW. Using the FSIW technique, the ridge of a RHMSIW is transitioned to be within the waveguide channel, where the fundamental quasi-$TE_{0.5,0}$ mode then becomes folded around said ridge. With this new configuration, the proposed folded RHMSIW (FRHMSIW) technology achieves an additional miniaturization of approximately 50% over RHMSIW, yielding a total miniaturization compared to full-mode SIW of up to 87.5% or more. The objective of this chapter is to

thoroughly investigate the FRHMSIW structure and highlight the region of improvements compared to RHMSIW and HMSIW technology. As such, studies including the effect on the monomode bandwidth and comparison of the attenuation losses are detailed.

This chapter is organized as follows. First, Section 5.1 outlines the principle of operation of the FRHMSIW. A monomode bandwidth study is then presented in Section 5.2, comparing the proposed FRHMSIW structure to the monomode bandwidths of both RHMSIW and HMSIW technology. In Section 5.3, an attenuation analysis of the FRHMSIW is performed, investigating the sources of loss in the structure. Final conclusions are presented in Section 5.4.

5.1 Principle of Operation

FRHMSIW technology requires a small structural modification to previously reported RHMSIW technology. Quite simply, by moving the ridge structure from outside the waveguide channel to inside the waveguide channel, as per Fig. 5.1, the fundamental quasi-$TE_{0.5,0}$ mode of the electric field folds around said ridge structure. This folding of the fundamental mode is clearly seen by the electric field distributions, also shown in Fig. 5.1. Note that the blind via becomes the effective sidewall of the FRHMSIW. This new structure, while analogous to half-mode T-septum SIW [119], exhibits a key difference in the location of the ground plane in the open side region of the waveguide where the electric field is strongest. For the FRHMSIW, it is located along the bottom of the waveguide to reduce radiation and coupling by having the fringing fields contained within the substrate (see Fig.

5.1(c)). For the half-mode T-septum SIW in [119], the ground plane extended out from the ridge (middle metallization layer), leaving the fringing fields to extend greater into free-space. Furthermore, the ridge of the FRHMSIW is extended closer to the sidewall, achieving additional miniaturization due to the increased capacitive loading, described next.

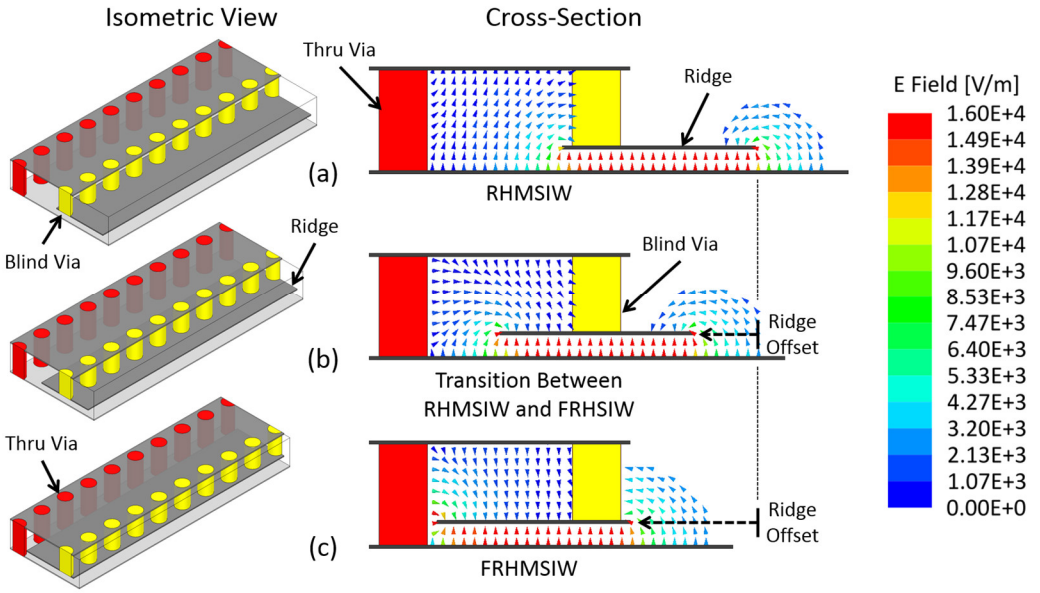

Fig. 5.1. Isometric and cross-section layouts of the (a) RHMSIW, (b) transition between RHMSIW and FRHMSIW, and (c) FRHMSIW along with their respective fundamental mode electric field distributions.

The calculation of the fundamental mode cutoff wavelength of the FRHMSIW follows the transverse resonance technique presented in Section 3.1 for RHMSIW structures, where an equivalent transverse circuit model is used for the FRHMSIW, as shown in Fig. 5.2. Due to the close proximity of the ridge edge to the sidewall, shown as dimension x in Fig. 5.2(a), an additional susceptance jB_C is added to the equivalent transverse circuit model in Fig. 5.2(b) to account for this additional capacitance. The original susceptance jB_S due to the change in height between the ridge and main channel regions remains the same as for RHMSIW.

By review of Fig. 5.1, another important difference between folded ridged half-mode and ridged half-mode structures is that the waveguide channel height is no longer the combined height of the two substrates, but is the height of the top substrate only. This reduces the ratio of the waveguide channel height to ridge height (shown in Fig. 5.2(a) as *subH1* and *subH2*, respectively), impacting the level of miniaturization, discussed more later.

With the above in mind, the FRHMSIW fundamental mode cutoff wavelength is determined by solving the following transcendental equation, where the input admittance looking to the left and right at the plane 'T' in Fig. 5.2(b) summate to zero

$$Y_{in}^{(1)} + j(B_S + B_C) + Y_{in}^{(2)} = 0 \tag{5.1}$$

which is expanded into

$$-\cot(\frac{2\pi}{\lambda_c}W) + \frac{B_S}{Y_{01}} + \frac{B_C}{Y_{01}} + \frac{Y_{02}}{Y_{01}}\tan(\frac{2\pi}{\lambda_c}(Wr + \Delta Wr)) = 0 \tag{5.2}$$

where W is the width of the waveguide channel, Wr the width of the capacitive ridge, ΔWr the additional effective length of the ridge due to fringing fields, λ_c the fundamental mode cutoff wavelength, and Y_{01} and Y_{02} the transverse characteristic admittance of the waveguide channel and ridge sections, respectively. The ratio of characteristic admittances Y_{02}/Y_{01}, and the transverse step capacitance B_S/Y_{01} due to the transition between the main waveguide channel and ridge section, can be calculated using the equations (3.4) and (3.5) found in Section 3.1.

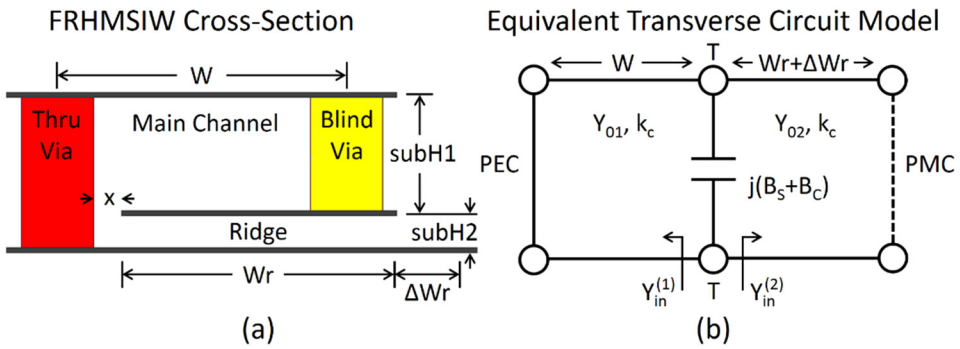

Fig. 5.2. (a) Cross-section including important dimensions, along with (b) equivalent transverse circuit model used to design the fundamental cutoff wavelength, of the FRHMSIW.

The capacitance B_C/Y_{01} between the edge of the ridge and sidewall, separated by dimension x with ridge metal thickness t, can be represented using the classic parallel-plate model

$$C_{pp} = {\epsilon_r \epsilon_0 t}/{x} \tag{5.3}$$

where C_{pp} is the parallel-plate capacitance per unit length and ε_r the dielectric constant of the substrate. A more accurate formula given in [120] can be used for the capacitance per unit length

$$C_f = \frac{\epsilon_r \epsilon_0 t}{x}\left[1 + \frac{x}{\pi t}\left(1 + \ln\left(\frac{2\pi t}{x}\right)\right)\right] \tag{5.4}$$

where C_f includes both the parallel-plate and fringing capacitance. Therefore, the term B_C/Y_{01} becomes either

$${B_C}/{Y_{01}} = \left(\frac{2\pi}{\lambda_c}\right)\left(\frac{subH1}{\epsilon_r \epsilon_0}\right) C_{pp} \tag{5.5}$$

$${B_C}/{Y_{01}} = \left(\frac{2\pi}{\lambda_c}\right)\left(\frac{subH1}{\epsilon_r \epsilon_0}\right) C_f \tag{5.6}$$

where $Y_{01} = (\eta \times subH1)^{-1}$ for which η is the intrinsic impedance of the substrate.

To study the accuracy of the above analytical model, Fig. 5.3 plots the cutoff frequency versus offset dimension *x*. First, a FRHMSIW is simulated in HFSS, with the offset dimension *x* parametrically swept from 0.02 mm to 1.0 mm (decreasing *Wr*, with all other dimensions constant). Next, the cutoff frequency is calculated using (5.2) for both the classic parallel-plate model (5.5) and fringing field model (5.6). For comparison, the transverse circuit model without the additional capacitance due to the ridge proximity ($B_C = 0$) is also included.

Each of the four cases are plotted in Fig. 5.3(a), while the error between the analytical models and simulation are plotted in Fig. 5.3(b). For larger *x* offset, model (5.2) with $B_C = 0$ is very accurate, with error under 5% above $x = 0.15$ mm. Yet as *x* decreases, the error increases exponentially. The error for (5.2) using the classic parallel-plate model (5.5) remains below 5% up to $x = 0.06$ mm, and using the fringing field model (5.6) remains below 5% for the entire range. Thus, incorporating the additional capacitance due to the proximity of the ridge edge to the sidewall significantly increases the accuracy of the analytical model, and with smaller *x*, allows a lower cutoff frequency and greater miniaturization to be achieved.

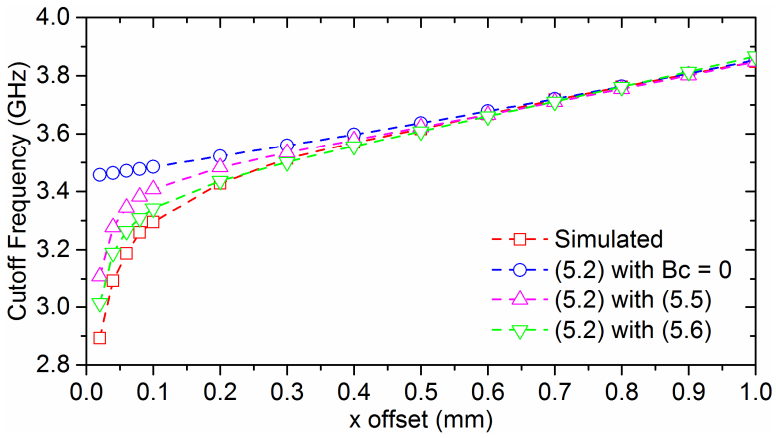

(a)

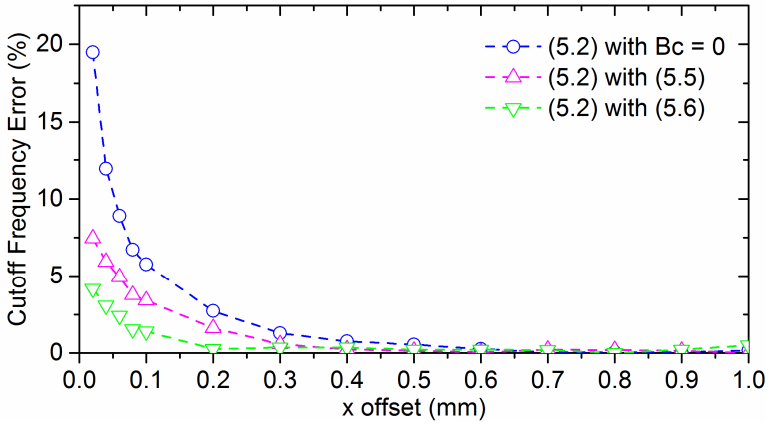

(b)

Fig. 5.3. (a) Comparison of simulated and analytical cutoff frequency versus decreasing offset dimension x (increasing Wr, all other dimensions constant) for the FRHMSIW, and (b) calculated error between model and simulation. For simulation in HFSS, the chosen dimensions are $W = 4$ mm, $subH1 = 62$ mil, $subH2 = 20$ mil, $\varepsilon_r = 2.2$, $tan\delta = 0.0009$, metal conductivity = 5.8×10^7 S/m, metal thickness = 70 μm. For simplicity, continuous vertical sidewalls are used instead of periodic vias.

However, the cost of smaller size is increased insertion losses. In Fig. 5.4, the effect of decreasing the dimenion x (normalized to cutoff λ_c) on the simulated FRHMSIW phase constant and attenuation constant are shown. While a substantially lower cutoff is achieved, the total attenuation begins to increase, which must be considered in the design of FRHMSIW (including fabrication limitations due to the requirement of tighter tolerances). Generally speaking, setting x to be approximately the height of the bottom substrate is recommended.

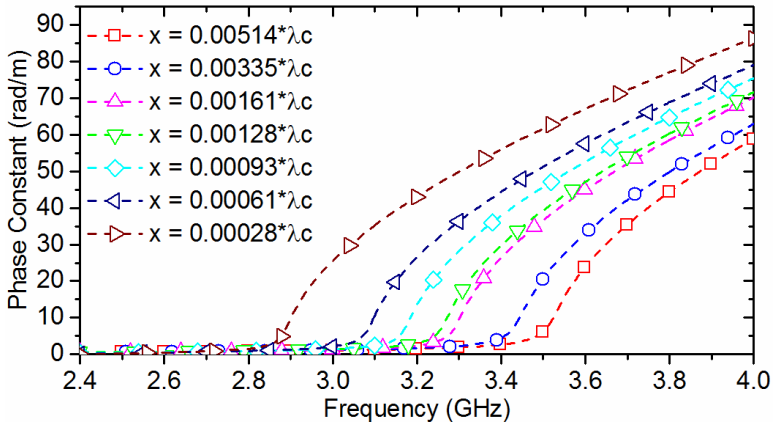

(a)

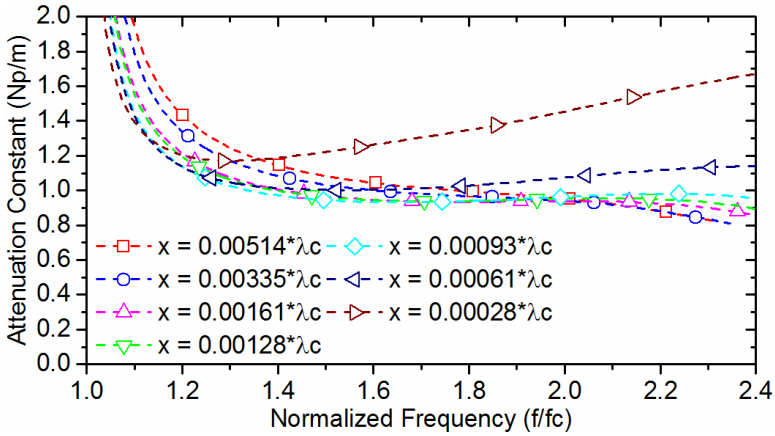

(b)

Fig. 5.4. Effect of decreasing the dimension x on the simulated (a) phase constant versus frequency, and (b) attenuation constant versus frequency normalized to cutoff frequency f_c. To improve clarity, x is normalized to its respective cutoff wavelength λ_c for each case.

5.2 Monomode Bandwidth Analysis

In this section, the monomode bandwidths of the FRHMSIW and RHMSIW are studied. Similar to half-mode [7], the open side boundary condition of the folded ridged half-mode and ridged half-mode prevents the rectangular waveguide equivalent $TE_{2,0}$ mode from propagating. Therefore, the next higher order mode is the equivalent $TE_{3,0}$ mode, or in the half-mode case, the quasi-$TE_{1.5,0}$ mode. Using (5.2), the 2nd order mode can be calculated, yet according to [121], is less accurate

for dissipative cases, especially for higher-order modes. Thus, a numerical approach is needed to study the monomode bandwidth more accurately.

Simulated in HFSS, the fundamental and 2nd order mode of the FRHMSIW and RHMSIW are plotted in Fig. 5.5(a), with field distributions plotted in Fig. 5.5(b) and Fig. 5.5(c), respectively. The first two modes of a standard HMSIW are also included in Fig. 5.5(a) for comparison. All three waveguides are designed with the same cutoff frequency of f_c = 4.8 GHz. It can be seen that the monomode bandwidths of the FRHMSIW and RHMSIW are increased compared to the HMSIW. The ridge structure lowers the cutoff frequency of their fundamental mode substantially, but the higher modes are less impacted by the ridge. In Fig. 5.5(b), the small additional capacitance due to the proximity of the ridge edge to sidewall can clearly be seen in both modes, explaining the slight decrease in monomode bandwidth of the FRHMSIW compared to the RHMSIW.

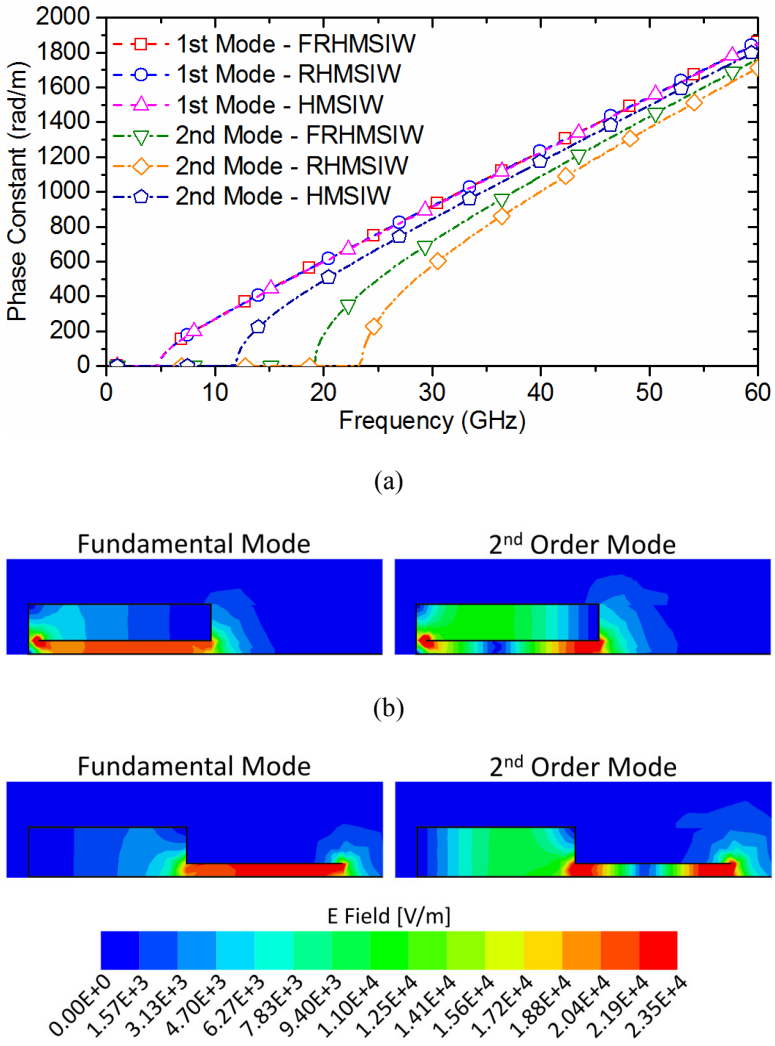

Fig. 5.5. (a) Simulated phase constant β of the fundamental and 2nd order mode for the FRHMSIW, RHMSIW, and HMSIW, with electric field distributions of the fundamental and 2nd order mode for the (b) FRHMSIW, and (c) RHMSIW (scale is for both FRHMSIW and RHMSIW field plots).

Table 5.1 shows the monomode bandwidth ratio of the three waveguides. RHMSIW achieves the largest monomode bandwidth ratio of 1:4.83, with FRHMSIW achieving a ratio of 1:3.97, and HMSIW a ratio of 1:2.47.

Waveguide Technology	Fundamental Mode (GHz)	2nd Order Mode (GHz)	Monomode Bandwidth (GHz)	Monomode Bandwidth Ratio
FRHMSIW	4.82	19.14	14.32	1:3.97
RHMSIW	4.87	23.49	18.63	1:4.83
HMSIW	4.82	11.93	7.1095	1:2.47

Table 5.1. Monomode Bandwidth Comparison

Further evaluating the monomode bandwidth, the transition from RHMSIW to FRHMSIW by moving the ridge section from outside to inside the waveguide channel is simulated in HFSS. Fig. 5.6 shows the electric field distribution of the fundamental mode and 2nd order mode during the transition from RHMSIW to FRHMSIW with increasing ridge offset. The folding of the fundamental mode around the ridge structure is again clear. The fundamental and 2nd order mode phase constants are plotted in Fig. 5.7. While there is small change in the fundamental mode frequency (<10%), the shift of the 2nd order mode frequency is more substantial (>20%).

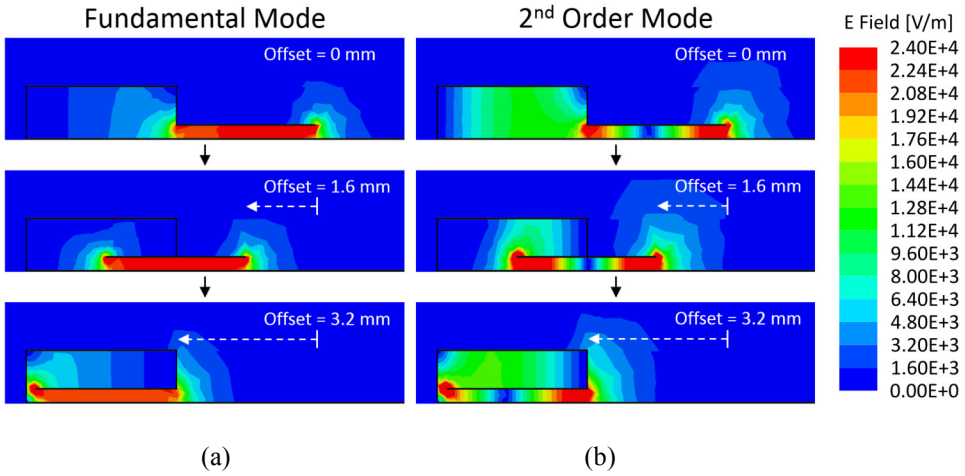

(a) (b)

Fig. 5.6. Transition from RHMSIW to FRHMSIW showing the electric field distribution for both the (a) fundamental mode, and (b) 2nd order mode.

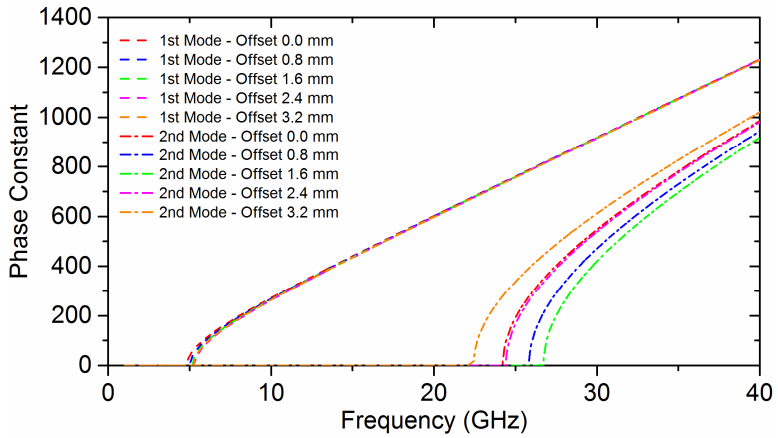

Fig. 5.7. Fundamental and 2nd order mode phase constants due to the transition from RHMSIW to FRHMSIW.

To better illustrate the effect on the monomode bandwidth versus ridge offset, Fig. 5.8 plots the change in fundamental mode, 2nd order mode, and total monomode bandwidth. It is interesting to note that the largest monomode bandwidth is achieved for a ridge offset of 1.6 mm, or when the ridge is half inside/half outside the main waveguide channel. Table 5.2 summarizes the results, where we see the largest monomode bandwidth ratio of 1:5.15 is achieved by the ridge halfway inside the waveguide channel. This is likely due to the step capacitance jB_S of the RHMSIW structure lowering the 2nd order mode cutoff, seen in Fig. 5.6(b). As the offset is increased, the 2nd order mode cutoff increases due to reduced capacitive loading, shown in Fig. 5.8(b). Above 1.6 mm offset, the ridge edge approaches the sidewall, again increasing capacitive loading due to jB_C, decreasing cutoff frequency. Furthermore, the monomode bandwidth ratio of the RHMSIW (1:5.01) is larger than for the FRHMSIW (1:4.28) not only due to the extra capacitive loading generated by the ridge edge to sidewall proximity, but also the smaller waveguide channel to ridge height ratio of the folded structure, which impacts the cutoff frequency according to (5.2).

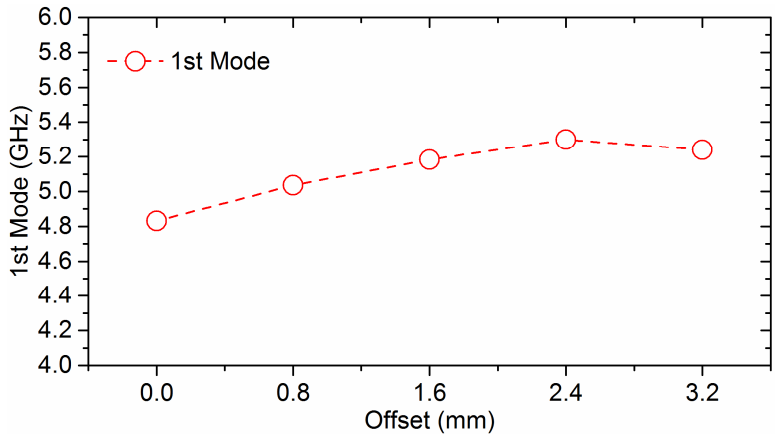

(a)

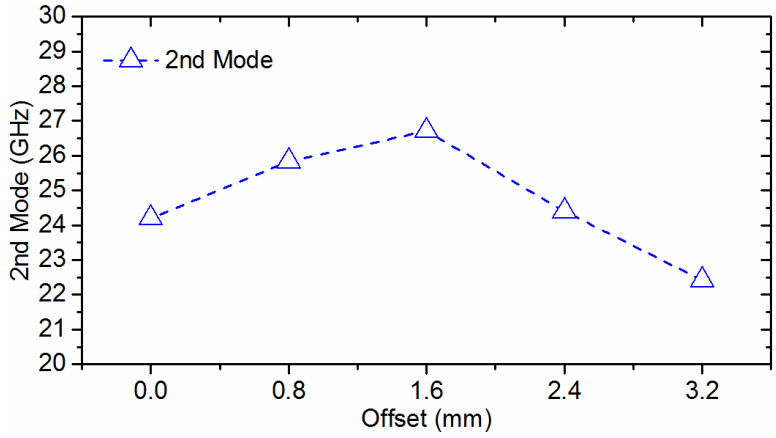

(b)

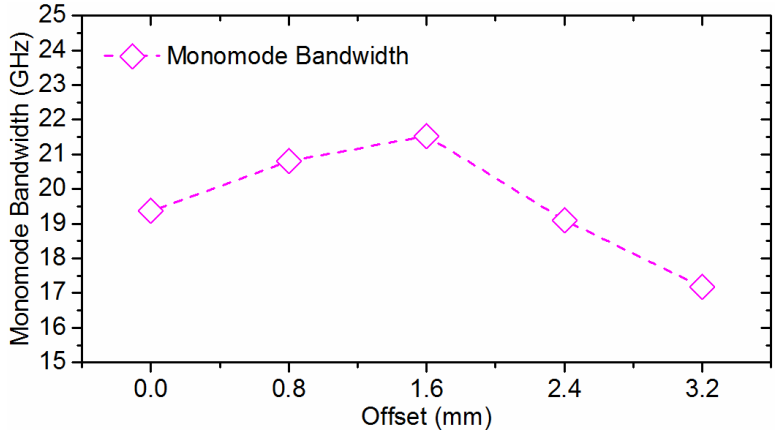

(c)

Fig. 5.8. The transition from RHMSIW to FRHMSIW versus ridge offset of the (a) fundamental mode, (b) 2nd order mode, and (c) total monomode bandwidth.

Offset	Fundamental Mode (GHz)	2nd Order Mode (GHz)	Monomode Bandwidth (GHz)	Monomode Bandwidth Ratio
0.0	4.83	24.20	19.36	1:5.01
0.8	5.04	25.83	20.80	1:5.13
1.6	5.18	26.71	21.53	1:5.15
2.4	5.30	24.40	19.10	1:4.60
3.2	5.24	22.41	17.17	1:4.28

Table 5.2. Transition from RHMSIW to FRHMSIW Monomode Bandwidth

Finally, the analytical calculation of the 2nd order mode cutoff frequency of the FRHMSIW using (5.2) yields a monomode bandwidth of 1:4.97, with an error of 13.9% between the numerically derived bandwidth given in Table 5.2. The error is likely due to the larger fringing field and step capacitance shown in Fig. 5.6(b) of the 2nd order mode compared to the fundamental mode in Fig. 5.6(a), shifting the cutoff frequency down and reducing the monomode bandwidth. Yet (5.2) can still be used for quick calculation, and numerical study applied when more accuracy is required.

5.3 Attenuation Analysis

To evaluate the performance of the FRHMSIW compared to the RHMSIW, two transmission lines of lengths L_1 = 11.4 mm ($\lambda_g/4$) and L_2 = 29.4 mm ($3\times\lambda_g/4$) are fabricated and measured for operation in C-band. Due to the embedded nature of the ridge, a multilayer PCB process was chosen, with 30 mil and 10 mil Rogers CuClad 217 for the top and bottom substrates, respectively. For the bonding layer, a 2.2 mil thick Adhesives Research, Inc. EL-7876 silicone transfer adhesive tape was used to attach the substrates together. Due to the electroplating requirement of the blind vias, the bonding tape contributes to the overall height of the ridge, for a

total thickness of 12.2 mil. Both the structures are fed by a 50-Ω microstrip line from the top metallization layer matched to a 50-Ω microstrip line on the middle metallization layer, connected using a blind via with diameter of 1.0 mm. The middle microstrip line is then tapered to match the lower impedance of the FRHMSIW and RHMSIW ridges.

In Fig. 5.9, the final design layouts are shown, where the cutoff frequency for both the FRHMSIW and RHMSIW is designed to be f_c = 4.8 GHz. Fig. 5.10 shows a picture of the fabricated and measured devices with length L_2 = 29.4 mm. The total broadside width of the FRHMSIW is 4.90 mm, while for the RHMSIW is 7.83 mm, thus an additional miniaturization of 37.4% is achieved using the folded ridged technique.

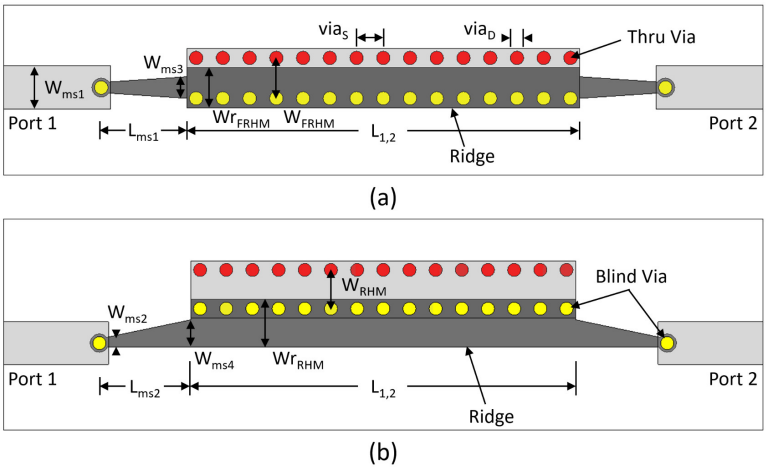

Fig. 5.9. Design layouts of the (a) FRHMSIW and (b) RHMSIW for complex propagation constant extraction, with light and dark grey areas the top and embedded ridge metallization layers, respectively. Final design dimensions (units in mm) are: W_{FRHM} = 3.0, Wr_{FRHM} = 3.0, W_{RHM} = 2.95, Wr_{RHM} = 3.65, W_{ms1} = 3.24, W_{ms2} = 0.65, W_{ms3} = 1.6, W_{ms4} = 2.1, L_1 = 11.4, L_2 = 29.4, L_{ms1} = 6.4, L_{ms2} = 7.0, via_D = 1.0, via_S = 2.0.

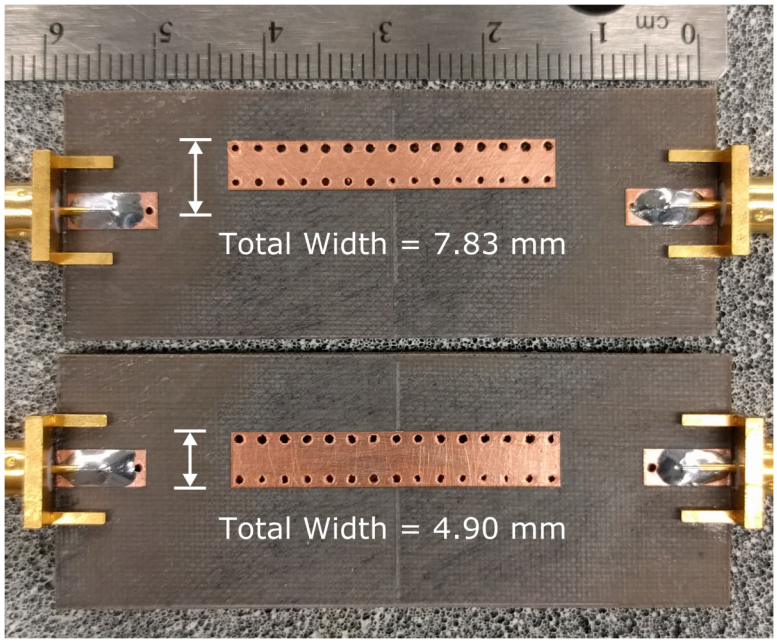

Fig. 5.10. Picture of fabricated devices, RHMSIW top and FRHMSIW bottom, with device length $L_2 = 29.4$ mm.

In Fig. 5.11 the simulated and measured scattering parameters are plotted with device length of $L_2 = 29.4$ mm. At an operating frequency of $1.45 \times f_c = 7$ GHz, the measured insertion loss for the FRHMSIW and RHMSIW are 1.52 dB and 1.37 dB, respectively. For the FRHMSIW, the measured return loss is above 20 dB from 6.4 GHz to 7.7 GHz, and for the RHMSIW is from 6.3 GHz to 7.5 GHz.

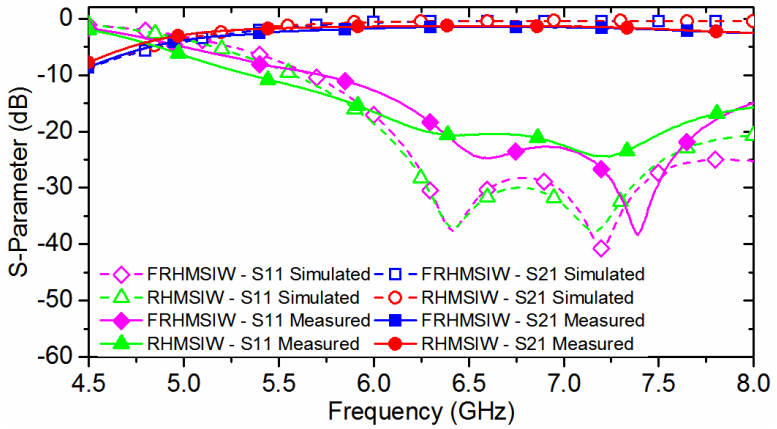

Fig. 5.11. Simulated and measured S-parameters of the FRHMSIW and RHMSIW with device length $L_2 = 29.4$ mm.

Using the multiline method [102], the complex propagation constants are extracted and plotted in Fig. 5.12 and Fig. 5.13, with reasonable agreement between simulation and measurement. The extracted phase constants in Fig. 5.12 show similar cutoff frequency and dispersion between the FRHMSIW and RHMSIW, with the simulated field distributions again illustrating the miniaturization achieved by the folded structure. At an operating frequency of $1.45 \times f_c = 7$ GHz, the attenuation constant of the FRHMSIW is 1.87 Np/m, and for the RHMSIW is 1.21 Np/m. This clearly shows minimal decrease in performance using the FRHMSIW over the RHMSIW, while achieving improved miniaturization of 37.4%. The slight discrepancy between simulated and measured attenuation constants for both the RHMSIW and FRHMSIW is due to the sensitivity of the bonding layer, described in more detail in Section 6.1.

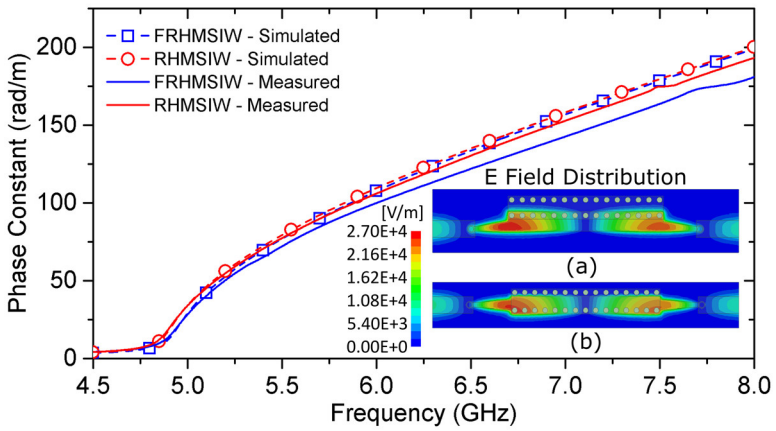

Fig. 5.12. Simulated and measured extracted phase constants of the quasi-$TE_{0.5,0}$ mode with simulated electric field distributions for the (a) FRHMSIW and (b) RHMSIW.

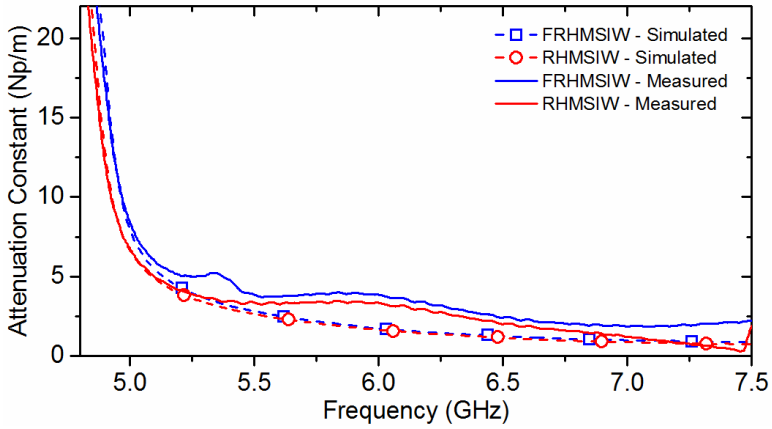

Fig. 5.13. Simulated and measured extracted attenuation constants of the quasi-$TE_{0.5,0}$ mode for the FRHMSIW and RHMSIW.

To examine the individual effects of radiation, dielectric, and conductor loss on the device performance, Fig. 5.14 plots the cumulative effect on the simulated attenuation constants of the FRHMSIW and RHMSIW. Starting with radiation losses only, and then adding dielectric losses, and finally conductor losses, we see that the FRHMSIW has only a minimal increase in both radiation and dielectric losses compared to RHMSIW. A slightly larger increase in conductor losses is noticed, likely due to the proximity of the ridge edge to the sidewall increasing ohmic losses within this region. However, the increase in total losses at 7 GHz is less than 0.13 Np/m, further confirming the overall performance of the FRHMSIW very closely matches the RHMSIW, yet with greater miniaturization.

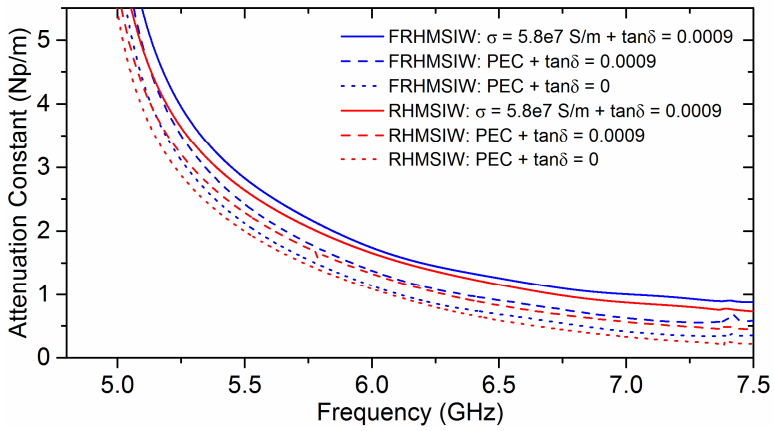

Fig. 5.14. Simulated attenuation constants of the quasi-$TE_{0.5,0}$ mode for the FRHMSIW and RHMSIW beginning with radiation losses only, then subsequently adding dielectric loss and conductor loss to compare the cumulative effect on the device performance.

5.4 Summary

In this chapter, the design, fabrication, and characterization of a FRHMSIW has been presented, allowing miniaturizations up to ~50% over RHMSIW, and greater than 87.5% of standard SIW. The effect of the transition from RHMSIW to FRHMSIW on the monomode bandwidth has been studied, where both technologies achieve 1:4.28 or greater bandwidth between their fundamental and 2nd order modes, more than twice compared to standard SIW. The measured complex propagation constant of the FRHMSIW has been extracted and compared to that of RHMSIW, which showed no loss in performance while achieving a miniaturization of 37.4%. As a promising alternative to RHMSIW, the FRHMSIW offers significant potential for the miniaturization of SIW-based systems, and is one of the smallest single conductor transmission lines in the present literature.

Chapter 6

Applications of the Folded Ridged Half-Mode and Quarter-Mode Substrate Integrated Waveguide in Filter Design

In this chapter, the significant miniaturization potential of folded ridged half-mode SIW (FRHMSIW) technology is explored in the design of both half-mode and quarter-mode SIW cavity resonators, for applications including tunable and reconfigurable bandpass and bandstop filters. As was demonstrated in Chapter 5, the combination of folded and ridged half-mode technology can produce substantial miniaturization of an integrated waveguide platform. From the measured results presented in Section 5.3, the proposed FRHMSIW achieved an additional miniaturization of 37.4% compared to ridged half-mode SIW (RHMSIW), while maintaining similar performance in terms of attenuation loss. Furthermore, the monomode region of operation for the FRHMSIW studied in Section 5.2 revealed a bandwidth approximately four times the cutoff frequency of the fundamental quasi-$TE_{0.5,0}$ mode, an increase of 200% compared to standard SIW with monomode bandwidth ratios typically around 1:2. By applying folded ridged technology to half-mode and quarter-mode SIW cavity design, this chapter will demonstrate that transverse dimensions of approximately $\lambda/16$ can be achieved, producing some of the smallest cavity-based resonators currently in the literature.

The chapter is organized as follows. First, in Section 6.1, a study of the folded ridged concept applied to half-mode and quarter-mode SIW cavities is presented,

yielding miniaturizations compared to standard SIW cavities equal to 96.6% and 98.0%, respectively. The design and measurement of a two-pole folded ridged quarter-mode SIW (FRQMSIW) bandpass filter prototype is then demonstrated, along with an investigation on the effect of substrate thickness versus filter performance. In Section 6.2, FRQMSIW cavity technology is applied to RF MEMS tunable filter design. An analytical model for the reactive loading of a FRQMSIW cavity is developed, and inductively- and capacitively-loaded two-pole FRQMSIW tunable BPF prototypes using packaged RF MEMS switches are designed, fabricated, and measured. Compared to RF MEMS tunable BPFs using HMSIW technology, a reduction in total design footprint by up to 78.8% is achieved, highlighting the significant amount miniaturization possible with the proposed FRQMSIW platform. Finally, in Section 6.3, folded ridged quarter-mode technology is applied to the design of multi-band bandstop filters (BSF). By utilizing nonresonating nodes (NRN), independent tuning of each stopband is achieved. A reconfigurable dual-band two-pole FRQMSIW BSF is designed, fabricated, and measured, where significant miniaturization is achieved compared to previously reported reconfigurable dual-band BSFs with similar filter topology, without any loss to performance.

6.1 Miniaturized Bandpass Filter Design

Bandpass filters are a critical component of any RF front end system, while SIW cavity filters allow for good integration and high performance. Yet, due to their large footprint, decreasing the size of the SIW cavity is critical. In this section, the miniaturization potential of the folded ridged technique is applied to both half-

mode and quarter-mode SIW cavity technology, and their performance is studied. Furthermore, a two-pole FRQMSIW bandpass filter is designed, fabricated, and measured, illustrating the miniaturization potential of the folded ridged technique applied to waveguide filter design.

6.1.1 Folded Ridged Half- and Quarter-Mode SIW Cavities

Both half-mode and quarter-mode SIW resonators can be formed using the folded ridged technique. To begin, a full-mode folded ridged SIW (FRSIW) cavity, as shown in Fig. 6.1, is formed from a standard ridged SIW (RSIW) cavity by folding the main waveguide channel around the ridge structure (see references [15], [122]). A single blind via in the center of the cavity becomes the effective sidewall, allowing for maximum miniaturization potential of the structure. Next, due to high width to height ratio, magnetic-walls can be inserted along lines of symmetry of the electric/magnetic field. First, the magnetic wall along A'-A' splits the FRSIW cavity in half, creating a folded ridged half-mode SIW (FRHMSIW) cavity. Next, the magnetic wall B'-B' splits the FRHMSIW cavity again in half to create the folded ridged quarter-mode SIW (FRQMSIW) cavity. In Fig. 6.2(a) and (b), the fundamental quasi-$TE_{0.5,0,1}$ resonant mode of the FRHMSIW and quasi-$TE_{0.5,0,0.5}$ mode of the FRQMSIW cavities are shown, where at the cutline T'-T', the symmetry of the magnetic field can be seen. Note that only a single blind via is used for the effective sidewall. While this was done in the FRSIW cavity to maximize miniaturization, it also keeps the final cross-section of the FRQMSIW cavity the same in both orthogonal directions as the FRHMSIW.

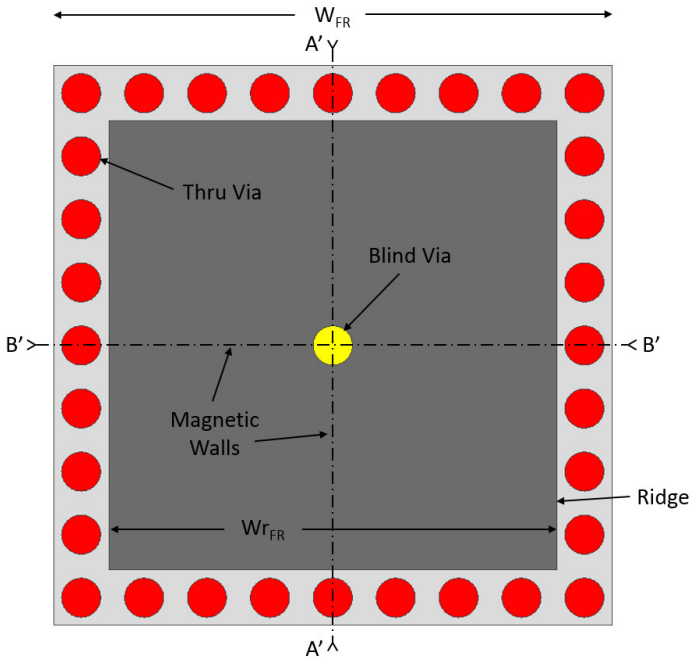

Fig. 6.1. Top view of a FRSIW cavity, showing magnetic walls at locations of electric/magnetic field symmetry. Light and dark grey areas are the top and embedded ridge metallization layers, respectively (ground plane not shown).

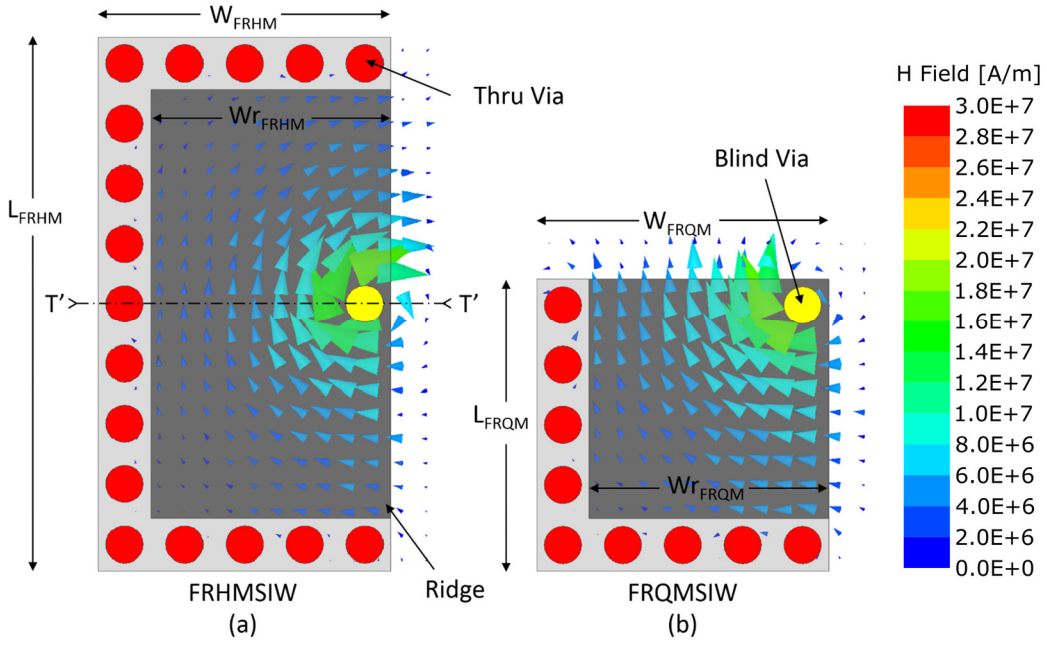

Fig. 6.2. Top view layouts of the (a) FRHMSIW and (b) FRQMSIW cavities, showing the magnetic field distribution within the top substrate (for clarity). The dimensions are $W_{FRHM} = W_{FRQM}$ = 7.8 mm, $Wr_{FRHM} = Wr_{FRQM}$ = 6.4 mm, L_{FRHM} = 14.2 mm, L_{FRQM} = 7.8 mm, with via diameter of 1.0 mm, via spacing of 1.6 mm, top and bottom substrate (Rogers RO3010) thicknesses of *subH1* = 25 mil and *subH2* = 10 mil, respectively.

Using the Eigenmode solver in HFSS, the simulated unloaded quality factor (Q_u) of the two structures is extracted. For the FRHM[1] cavity, $Q_u = 132$ at resonance frequency $f_0 = 1.131$ GHz, while for the FRQM cavity, $Q_u = 128$ at resonance frequency $f_0 = 1.211$ GHz, yielding approximately the same performance. With respect to $\lambda = c_0 / [(\varepsilon_r)^{1/2} \times f_0]$ at resonance for each structure, the FRQM cavity achieves an additional 41.2% miniaturization compared to the FRHM cavity.

To better highlight the extreme miniaturization potential of the folded ridged technique, a standard full-mode SIW cavity is also simulated, using the same substrate parameters as above. Compared to the area of a full-mode SIW with respect to λ at resonance, the FRHM and FRQM cavities achieve miniaturizations of 96.6% and 98.0%, respectively. Table 6.1 summarizes these results. Furthermore, compared to conventional miniaturized microstrip meander open-loop resonators presented in [123], with each resonator having an approximate area of $0.0197 \times \lambda^2$, the FRQM achieves a miniaturization of 48.7%. This highlights the extreme miniaturization potential of FRQM resonators for filter design.

Cavity Technology	f_0 (GHz)	Q_u at f_0	f_2 (GHz)	Q_u at f_2	f_2/f_0 Ratio	Cavity Area	Miniat-urization
SIW	1.21	174	2.41	197	2.00	$0.5001 \times \lambda^2$	Ref.
FRHMSIW	1.13	132	6.03	156	5.34	$0.0161 \times \lambda^2$	96.6%
FRQMSIW	1.21	128	5.81	152	4.82	$0.0101 \times \lambda^2$	98.0%

Table 6.1. Simulated FRHMSIW and FRQMSIW Cavity Performance

[1] To improve clarity, SIW will be assumed after FRHM and FRQM for the remainder of this section.

Another important characteristic of the FRHM and FRQM cavity is the large spurious mode separation between the fundamental resonance and 2nd order resonance. Similar to the discussion in Section 5.2, due to the half-mode and quarter-mode open-sided nature, even mode resonances are not supported, while the ridge structure decreases the resonance frequency of the fundamental mode without much impact to the 2nd mode resonance. The 2nd mode resonances f_2 are simulated with the Eigenmode solver in HFSS. For the FRHM cavity, f_2 = 6.03 GHz with Q_u = 156, while for the FRQM cavity, f_2 = 5.81 GHz with Q_u = 152. The spurious mode separation ratios of the two structures are 1:5.34 and 1:4.82, respectively. Compared to standard full-mode SIW, with ratio 1:2, the FRHM and FRQM achieve 2.4 and 2.67 times more spurious mode separation bandwidth. This is also true for standard microstrip resonators, which typically have 1:2 ratios.

To evaluate the sources of loss of the FRQM, the individual Q_u due to radiation (Q_r), dielectric (Q_d), and conductor (Q_c) losses are extracted from simulation, yielding 2350, 286, and 260, respectively. The conductor loss due to the small gap between the ridge and ground plane, where the electric field concentration is greatest, can be decreased by increasing *subH2*, discussed further in Section 6.1.2. The dielectric loss is close to the classic equation $Q_d = 1/tan\delta$, where for Rogers RO3010 substrate $tan\delta$ = 0.0035, and can be improved with lower loss substrates. Most significantly, the radiation loss is very low, allowing the structures use in high density areas.

6.1.2 Folded Ridged Quarter-Mode SIW Filter Design

Using the FRQM cavity, a two-pole bandpass filter (BPF) is designed. The top and bottom substrates of the multilayer structure are made with Rogers RO3010, 25 mil and 10 mil, respectively. Due to the folded nature of the electric field within the FRQM cavity, both horizontal and vertical vectors exist within the substrate. Therefore, the uniaxial anisotropic property of the Rogers RO3010 substrate is incorporated in HFSS simulation [124].

The coupling diagram for the bandpass filter is shown in Fig. 6.3. Based on the coupling matrix model for a two-pole Chebyshev bandpass filter, the required normalized coupling element M_{12} and normalized input impedances R_1, R_2 can be determined with

$$M_{12} = \frac{1}{\sqrt{g_1 g_2}}, R_1 = \frac{1}{g_0 g_1}, R_2 = \frac{1}{g_2 g_3} \tag{6.1}$$

where g_0, g_1, g_2, and g_3 are the Chebyshev lumped-element low-pass prototype elements [22]. For a two-pole bandpass filter with 20 dB return loss (or 0.0436 dB passband ripple), the N+2 normalized coupling matrix is determined to be

$$M = \begin{bmatrix} 0 & 1.500 & 0 & 0 \\ 1.500 & 0 & 1.659 & 0 \\ 0 & 1.659 & 0 & 1.500 \\ 0 & 0 & 1.500 & 0 \end{bmatrix} \tag{6.2}$$

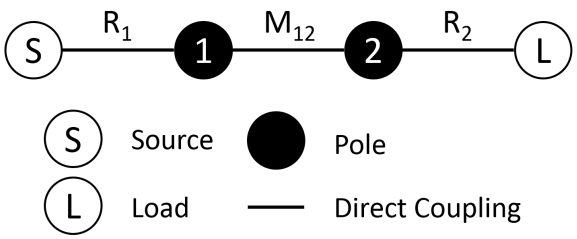

Fig. 6.3. Coupling diagram of the two-pole FRQMSIW bandpass filter with magnetic coupling between resonators using an inductive window.

A standard inductive window is used to couple two FRQM resonators, as shown in Fig. 6.4(a). The dimension w_{iris} controls the coupling element M_{12}, and is determined through simulation and extracted using

$$M = \frac{f_0}{BW}k;\ k = \frac{f_e^2 - f_m^2}{f_e^2 + f_m^2} \tag{6.3}$$

where f_0 is the center frequency and BW the filter bandwidth, k the coupling coefficient between two resonators, with f_e and f_m the odd- and even-mode resonance frequencies, respectively [110]. The 3D layout in Fig. 6.4(a) is used for extraction of k in HFSS Eigenmode solver. Due to the embedded ridge, the coupling between the two FRQM cavities is both electric and magnetic, or mixed type. This is illustrated in the magnetic (Fig. 6.4(b)) and electric field (Fig. 6.4(c)) plots of slice T'-T' through the center of the coupling structure. For both the even- and odd-mode magnetic field distributions, the maximum field strength is scaled to 1.0×10^7 A/m, while for the electric field even- and odd-modes, the maximum field strength is scaled to 1.8×10^8 V/m. Observing the field plots themselves, a large amount of electric coupling is present for both even- and odd-modes, to a greater degree than the magnetic field coupling for each mode.

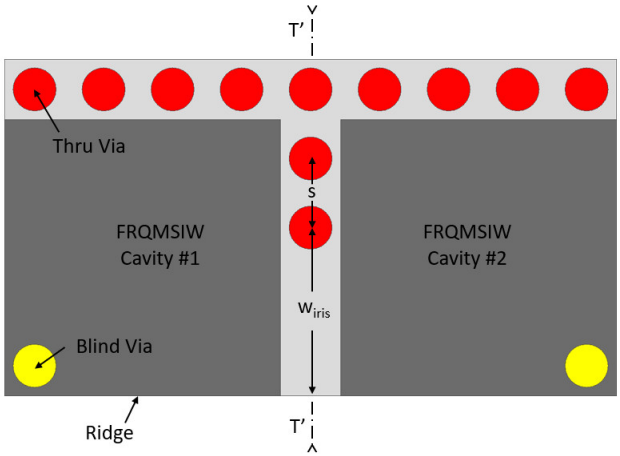

(a)

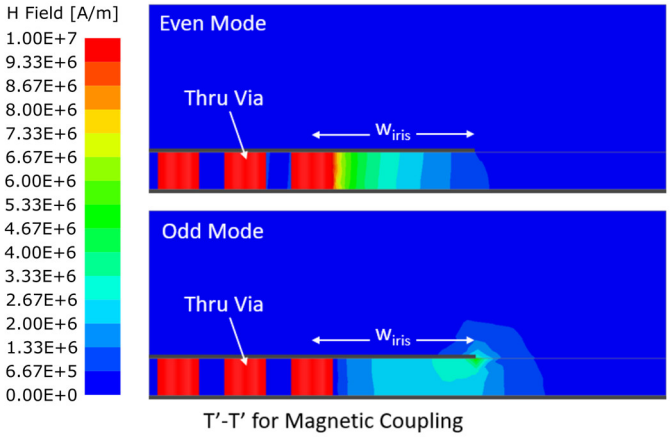

(b)

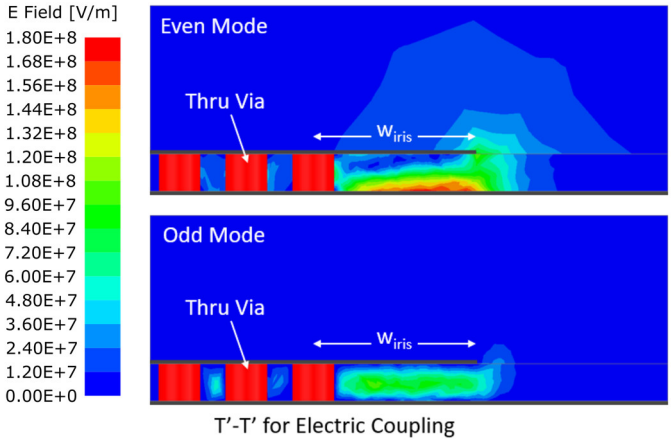

(c)

Fig. 6.4. In (a), the 3D layout for coupling coefficient k extraction using HFSS Eigenmode simulation is shown. For the T'-T' slice, the magnitude of the (b) magnetic and (c) electric field distributions are shown for the even mode (f_m) and odd mode (f_e) couplings.

To study this result further, Fig. 6.5 plots the maximum magnitude of the magnetic and electric fields versus iris width w_{iris} for both even- and odd-modes. While typically an inductive window coupling structure produces a magnetic coupling [22], for the FRQMSIW, the electric field coupling is an order or two stronger than the magnetic field coupling, depending upon w_{iris}. This is important if the structure is to be used in a filter requiring cross couplings or transmission zeros. Fig. 6.7(a) shows the simulated change in coupling coefficient k versus w_{iris}, where a good range of coupling is possible with this structure.

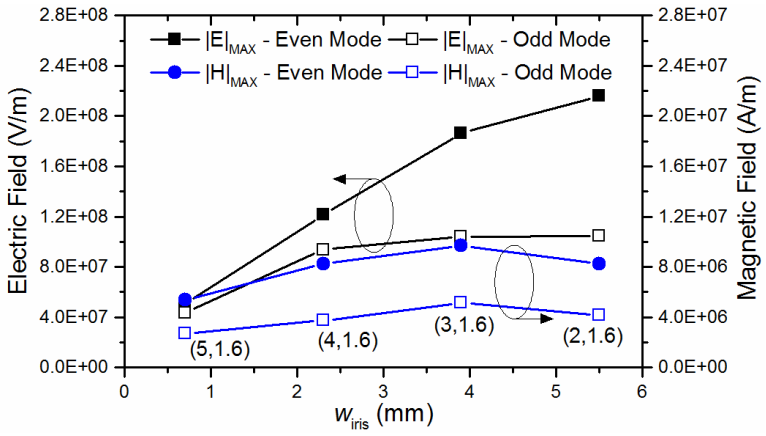

Fig. 6.5. Field plot versus iris width w_{iris} of the T'-T' slice for interresonator coupling, showing both maximum electric field magnitude and magnetic field magnitude (90° phase offset) for the even and odd mode resonances. Inset coordinates, i.e. (5, 1.6), represent the number of coupling vias and via spacing s (in mm), respectively, to achieve the specific iris width shown in the x-axis.

A 50-Ω microstrip line patterned on the top metallization layer is used to feed the filter. The input coupling is determined using the reflection coefficient group delay method [22], and is controlled by the dimension w_{offset}. The normalized input impedance R_1 and R_2 are extracted using

$$R_{1,2} = \frac{\omega_0}{(\omega_2 - \omega_1)} \frac{1}{Q_e};\ Q_e = \frac{\omega_0 \tau(\omega_0)}{4} \tag{6.4}$$

where $(\omega_2 - \omega_1)$ is the bandwidth in radians, Q_e the external quality factor, and $\tau(\omega_0)$ the reflection coefficient group delay at resonance [22]. In Fig. 6.6, the 3D layout for extraction of Q_e simulated in HFSS is shown. In Fig. 6.7(b) the external quality factor Q_e versus microstrip offset dimension w_{offset} is plotted, again illustrating a good range of possible input/output couplings for this structure.

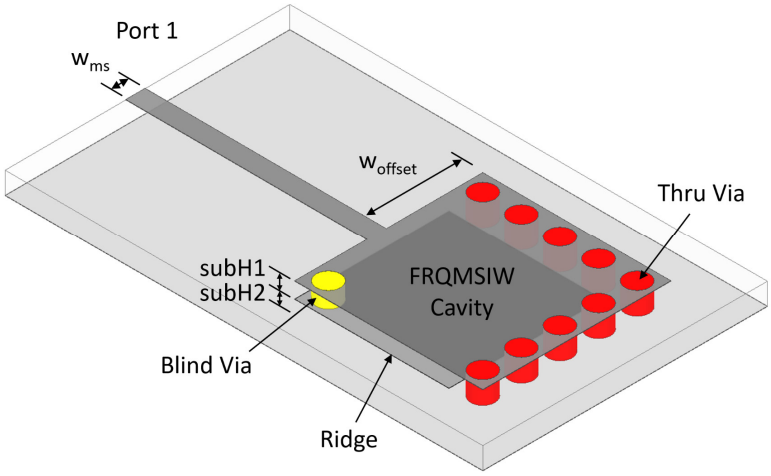

Fig. 6.6. 3D layout for external quality factor Q_e extraction simulated in HFSS, fed with a 50-Ω microstrip.

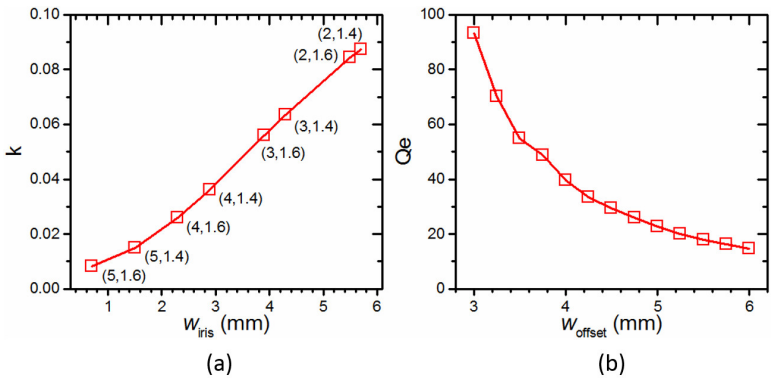

Fig. 6.7. Simulated extracted (a) coupling coefficient k versus iris window width w_{iris}, and (b) external quality factor Q_e versus microstrip feed offset w_{offset}. Inset coordinates, i.e. (5, 1.6), represent the number of coupling vias and via spacing s (in mm), respectively, to achieve the specific iris width shown in the x-axis.

In Fig. 6.8, the final design schematic for the FRQM two-pole BPF is shown including dimensions. An LPKF ProtoMat S62 is used to drill via holes, and an

LPKF ProtoLaser U3 is used to mill the top and middle metallization layers; both tools providing highly accurate fabrication tolerances. The via holes are activated using Think & Tinker, Ltd. Conductive Electroplating Ink and plated in an acid copper electroplating bath. The substrates are bonded together with 2 mil thick Adhesives Research, Inc. EL-7876 silicone transfer adhesive tape. An additional benefit of the proposed structure, which reduces fabrication complexity and therefore cost, is that the bottom substrate does not require accurate alignment during bonding. Since both the top and middle metallization layers are patterned on the same substrate, along with the blind via holes, the bottom substrate can be roughly aligned and bonded, and then the through vias aligned to the top metal with the LPKF fiducial system.

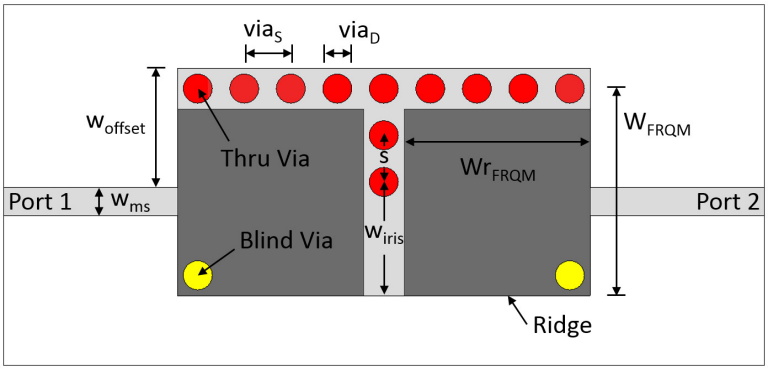

Fig. 6.8. Design schematic of the two-pole FRQMSIW cavity bandpass filter. Final design dimensions are (all units in mm): W_{FRQM} = 7.1, Wr_{FRQM} = 6.4, w_{iris} = 3.2, s = 1.3, w_{ms} = 0.95, w_{offset} = 4.1, via_D = 1.0, via_S = 1.6.

A picture of the fabricated two-pole FRQM BPF is shown in Fig. 6.9, with the simulated and measured scattering parameters plotted in Fig. 6.10. The measured center frequency is f_0 = 1.59 GHz, with an insertion loss of 2.72 dB and 3 dB bandwidth of 87.97 MHz, for a fractional bandwidth (FBW) of 5.53%. The second mode resonance appears at 5.81 GHz, showing the large spurious mode separation.

To extract the Q_u from the measured results, the method presented in [125] is used. From Fig. 6.10, the extracted measured $Q_u = 92$.

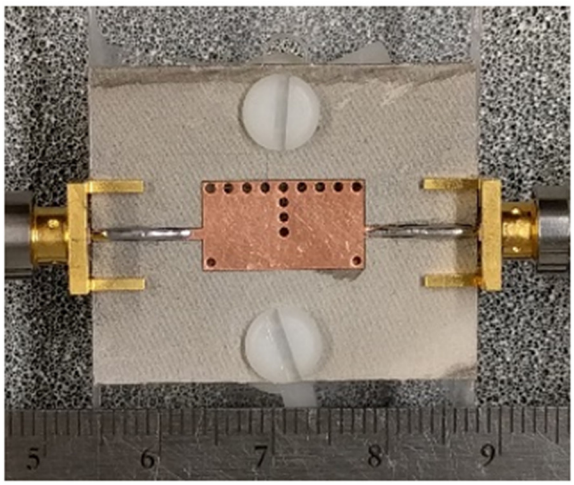

Fig. 6.9. Picture of the fabricated two-pole FRQMSIW bandpass filter with top and bottom substrate thickness of 25 mil and 10 mil, respectively.

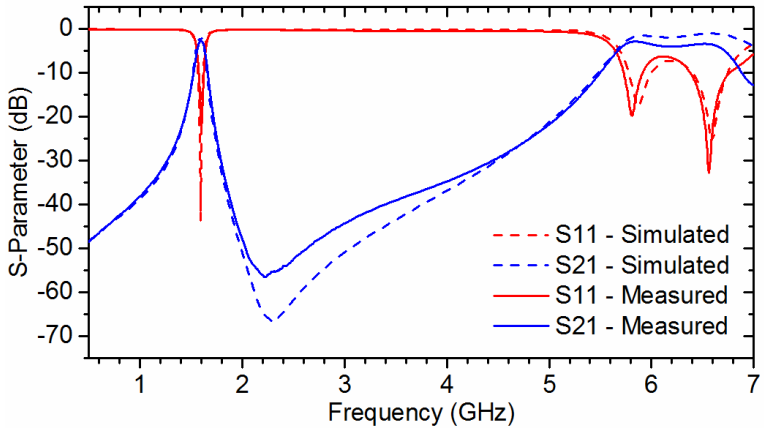

Fig. 6.10. Simulated and measured wideband scattering parameters for the two-pole FRQMSIW bandpass filter with 25 mil and 10 mil top and bottom substrate thickness, respectively.

The high insertion loss and lower quality factor (compared to simulated) of the FRQM BPF is likely due to the choice of adhesion layer and its location within the capacitive ridge section, the region with the highest electric field concentration. A sensitivity analysis on the FRQM BPF performance versus adhesive thickness, permittivity, and loss tangent is performed in HFSS. It is found that the greatest

sensitivity is with the adhesive thickness. This is an acceptable conclusion, as the ridge section can be approximated as a parallel plate capacitor, with capacitance $C = \varepsilon_r\varepsilon_0 A/g$, where A is the total area of the ridge, and g the adhesive plus the bottom substrate thickness. Due to the adhesive thickness being in the denominator, the final capacitance is more sensitive to this value. It is determined that the permittivity and loss tangent of the adhesive tape are $\varepsilon_r = 2.1643$ and $tan\delta = 0.01469$ at the designed frequency range based on a final tape thickness of 2 mil. Of course, due to the higher sensitivity of the FRQM cavity resonance and couplings on the final adhesive thickness, slight variation on these numbers is expected, and it is important to ensure the final thickness is consistent between fabrications.

6.1.3 Study on Quality Factor vs. Substrate Thickness

For the previous FRQM BPF design, the ratio of the waveguide channel to ridge height was 2.5:1, using *subH1* = 25 mil and *subH2* = 10 mil substrates, respectively (see Fig. 6.6). By evaluation of (5.2), the ratio between substrate heights is an important factor for determining overall miniaturization. Furthermore, in Chapter 3, it was shown that by increasing this ratio, greater miniaturizations could be achieved at the cost of greater conductor losses due to increased field concentration underneath the ridge. With this in mind, this section explores the effect of choosing thicker substrates on cavity quality factor while keeping the ratio of waveguide channel to ridge height relatively the same. First, an Eigenmode simulation in HFSS is performed for the FRHM and FRQM cavities, where the substrate thickness is increased while keeping the ratio between top and bottom substrates equal. Next, a comparison between the measured results of two similar FRQM BPF designs with

different substrate heights is performed, while maintaining similar channel to ridge height ratios. An improvement in quality factor and insertion loss with thicker substrates is discussed, highlighting the importance of substrate thickness choice and waveguide channel to ridge height ratio for performance and miniaturization.

To compare the change in performance versus substrate thickness, the top and bottom Rogers RO3010 substrates of the FRHM and FRQM cavities in Fig. 6.2 are increased, while maintaining the ratio between *subH1* and *subH2* equal to 2.5:1, with all other dimensions the same. In Fig. 6.11, the simulated unloaded quality factor extracted using HFSS Eigenmode solver is plotted versus *subH2* thickness (*subH1* thickness to maintain 2.5:1 ratio shown in figure inset). It can be seen that by increasing *subH1* and *subH2*, greater Q_u is achieved, up to approximately *subH2* = 30 mil, where the improvement in Q_u begins to taper off. At *subH1* = 75 mil and *subH2* = 30 mil, the FRHM cavity has $Q_u = 183$ at resonance frequency $f_0 = 1.053$ GHz, while the FRQM cavity has $Q_u = 188$ at resonance frequency $f_0 = 1.149$ GHz. Thus, compared to the cavities in Section 6.1.1 with *subH1* = 25 mil and *subH2* = 10 mil, an improvement in unloaded quality factor of 38.6% and 39.3% for the FRHM and FRQM cavities is shown, respectively. These results are summarized in Table 6.2, where an increase in performance using thicker substrates is clearly noticed.

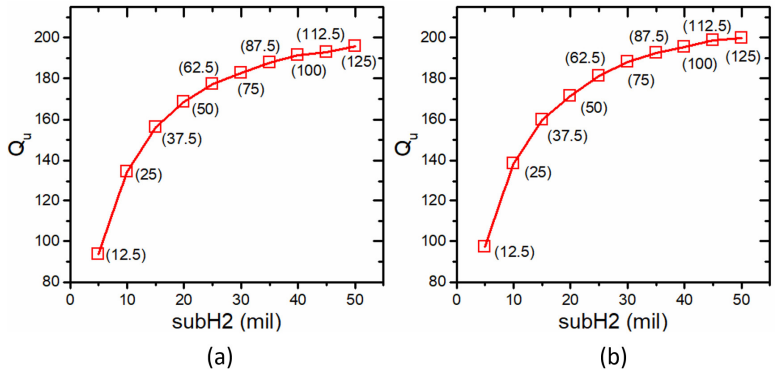

Fig. 6.11. Simulated Eigenmode extraction of unloaded quality factor Q_u for the (a) FRHMSIW cavity and (b) FRQMSIW cavity, versus substrate thickness with channel to ridge height ratio of 2.5:1. Inset values, i.e. (62.5), represent the thickness of the top substrate *subH1* (in mil) with respect to the bottom substrate *subH2* in the *x*-axis.

Top / Bottom Substrate (mil)	Height Ratio	FRHM Q_u / f_0 (GHZ)	FRHM Rise in Q_u	FRQM Q_u / f_0 (GHz)	FRQM Rise in Q_u
25 / 10	2.5:1	132 / 1.13	Ref.	135 / 1.21	Ref.
75 / 30	2.5:1	183 / 1.05	38.6%	188 / 1.15	39.3%

Table 6.2. Comparison of Simulated FRHMSIW and FRQMSIW Cavity Performance with Respect to Top / Bottom Substrate Choice

To verify the result experimentally, a FRQM two-pole BPF is designed using Rogers RO3010 substrates with *subH1* = 50 mil and *subH2* = 25 mil, giving a channel to ridge height ratio of 2:1, with all other dimensions the same as those in Fig. 6.8. While not exactly the same as the previous ratio of 2.5:1, due to the standard substrate sizes produced by Rogers, this was the closest available ratio for test. The substrates are again bonded together with 2 mil thick Adhesives Research, Inc. EL-7876 silicone transfer adhesive tape. Due to the thicker total height of 77 mil, Rosenberger 32K243-40ML5 SMA clamp connectors were used to feed the filter.

A picture of the fabricated two-pole FRQM BPF with thicker substrate is shown in Fig. 6.12, with the measured scattering parameters plotted in Fig. 6.13. The

measured center frequency is f_0 = 1.61 GHz, with an insertion loss of 1.93 dB and 3 dB bandwidth of 103.5 MHz, for a fractional bandwidth (FBW) of 6.43%. The measured extracted Q_u = 116. The inset of Fig. 6.13(a) shows a close-up of the insertion loss of both the thin and thick substrate filter performances for comparison. An improvement of 0.79 dB in insertion loss and a 26.1% increase in measured extracted Q_u is achieved by using thicker substrates over thinner substrates with a similar channel to ridge height ratio. The small shift in resonance frequency is due to the decreased channel to ridge ratio, but is insignificant compared to the improvement in performance, and is only a consequence of limited available substrate heights. In Table 6.3, a summary of the two measured FRQM filters is shown, illustrating the improved performance using thicker substrates.

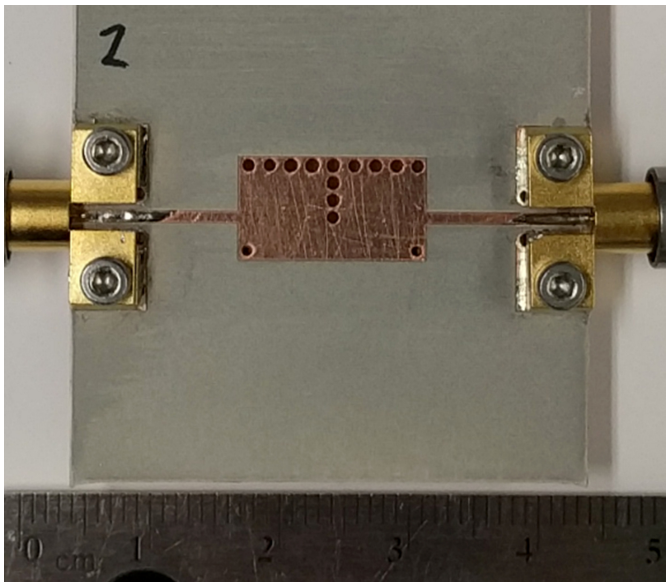

Fig. 6.12. Picture of the fabricated two-pole FRQMSIW bandpass filter with top and bottom substrate thickness of 50 mil and 25 mil, respectively.

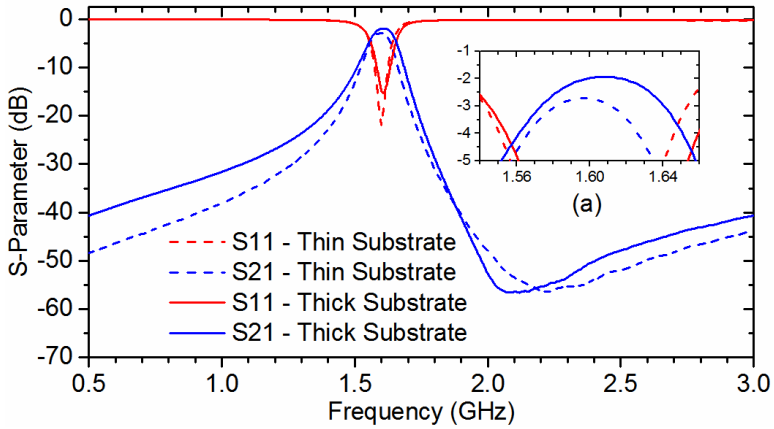

Fig. 6.13. Measured scattering parameters for the two-pole FRQMSIW bandpass filters with thin (25/10 mil top/bottom substrate thicknesses) and thick (50/25 mil top/bottom substrate thickness), with inset (a) highlighting the improvement in insertion loss with thicker substrates.

Top / Bottom Substrate (mil)	Height Ratio	f_0 (GHz)	FBW	Insertion Loss (dB)	Extracted Q_u	Rise in Q_u
25 / 10	2.5:1	1.59	5.53%	2.72	92	Ref.
50 / 25	2:1	1.61	6.43%	1.93	116	26.1%

Table 6.3. Measured FRQMSIW Filter Performance

Manufacturing tolerances are an important consideration regarding industrial-scale fabrication. As mentioned in Section 6.1.2, the most sensitive region of the FRQM cavity to variation in fabrication is the thickness of the bottom substrate underneath the capacitive ridge. Based on the tolerances reported for Rogers RO3010 substrates, the permittivity varies by $\varepsilon_r = 10.2 \pm 0.3$, while the substrate thicknesses of 10 mil and 25 mil vary by ± 0.7 mil and ± 1 mil, respectively [126]. In Fig. 6.14, a manufacturing tolerance study is simulated for FRQM bandpass filters using both thin (25/10 mil top/bottom) and thick (50/25 mil top/bottom) substrates. For both bandpass filters, the bottom substrate's permittivity and thickness are varied according to the above Rogers RO3010 substrate tolerances. The adhesive tape is removed for this study as it was primarily used for research-based prototyping, and is not a typical industrial scale approach.

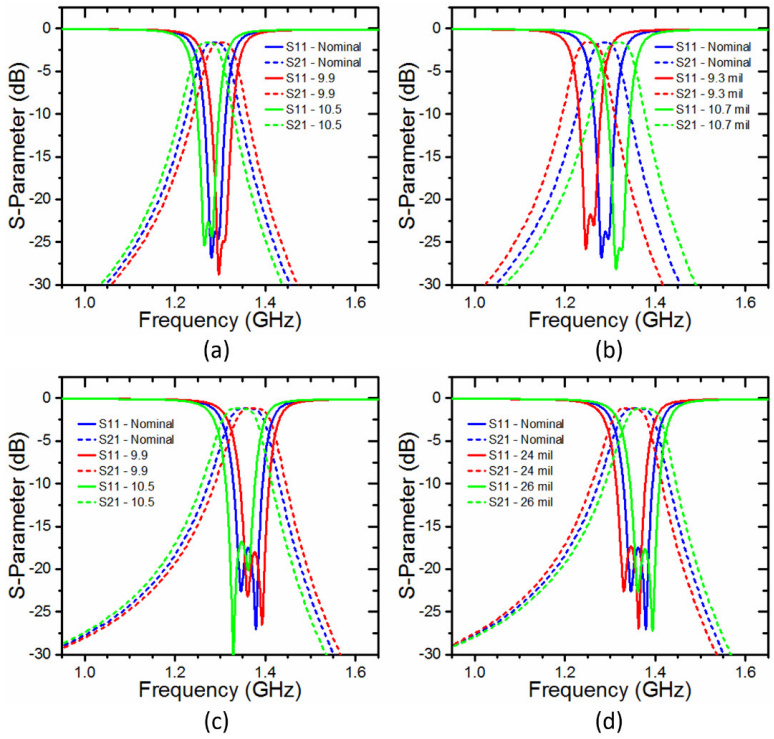

Fig. 6.14. Manufacturing tolerance study for the thin (25/10 mil top/bottom substrate) and thick (50/25 mil top/bottom substrate) FRQMSIW bandpass filters, by varying the bottom substrate permittivity and thickness based on Roger RO3010 substrate tolerance specifications. Simulated scattering parameters are plotted for (a) thin bandpass filter with bottom substrate $\varepsilon_r = 10.2 \pm 0.3$, (b) thin bandpass filter with bottom substrate thickness 10 mil ± 0.7 mil, (c) thick bandpass filter with bottom substrate $\varepsilon_r = 10.2 \pm 0.3$, and (d) thick bandpass filter with bottom substrate thickness 25 mil ± 1 mil.

In Fig. 6.14(a) and Fig. 6.14(c), the scattering parameters for the thin and thick bandpass filters with variation in the permittivity of their bottom substrates are plotted, respectively. For the thin bandpass filter, the resonance frequency shift is f_0 = 1.287 GHz ± 1.17%, while for the thick bandpass filter, the resonance frequency shift is f_0 =1.358 GHz ± 1.10%. In Fig. 6.14(b) and Fig. 6.14(d), the scattering parameters are plotted for variation in bottom substrate thickness for the thin and thick bandpass filters, respectively. The resonance frequency shifts for the thin and thick bandpass filters are f_0 = 1.287 GHz ± 2.50% and f_0 = 1.358 GHz ± 1.14%, respectively. The larger frequency shift in the thin bandpass filter with

variation in substrate thickness is expected due to the greater capacitance within this region, confirming the previous analysis in Section 6.1.2. Table 6.4 summarizes the results due to changes in permittivity and thickness of the bottom substrate versus the nominal resonance frequency f_0. It is clear that by using thicker substrates, the sensitivity to fabrication tolerances is reduced. Overall, these results show good performance of FRQM filters across the most significant manufacturing discrepancies within the resonator's region of greatest sensitivity.

Top / Bottom Substrate (mil)	Nominal f_0 (GHz)	Shift in f_0 with Bottom Substrate Δ in Permittivity	Shift in f_0 with Bottom Substrate Δ in Thickness
25 / 10	1.287	± 1.17%	± 2.50%
50 / 25	1.358	± 1.10%	± 1.14%

Table 6.4. Manufacturing Tolerance Study of FRQMSIW Filters

6.2 RF MEMS Tunable Bandpass Filter

Reconfigurable filters will play a critical role in future mobile communication systems, in which RF microelectromechanical systems (MEMS) based tunable elements offer superior performance in terms of insertion loss, power handling, and linearity [127], [128]. As the building blocks of filters, substrate integrated waveguide (SIW) cavities also have improved performance compared to standard planar technologies in terms of power handling and quality factor [5]. The benefits of SIW cavities and RF MEMS have previously been combined in [129], where a two-pole SIW bandpass filter achieved a 28% tuning range from 1.2-1.6 GHz with a Q_u from 93-132, and insertion losses from 2.2-4.1 dB. However, the overall footprint of the filter was large (80 mm × 114 mm) due to the use of a standard SIW cavity. In [130], a miniaturized two-pole HMSIW bandpass filter was designed

using packaged RF MEMS to switch between different inductive loadings along the open side of the waveguide. Comparable performance was achieved with a tuning ratio of 28% from 1.2-1.6 GHz, with a Q_u from 75-140 and insertion losses of 1.2-3.4 dB, and a 60% reduction in size (50 mm × 74 mm) compared to standard SIW.

In this section, the potential of the folded ridged quarter-mode SIW (FRQMSIW) is applied to RF MEMS tunable filter design to reduce the size even further, where miniaturized prototypes utilizing FRQMSIW cavity resonators with transverse widths as small as $\lambda/16$ are demonstrated. First, an equivalent circuit model is presented for the design of reactively-loaded FRQMSIW tunable cavity resonators. The derived analytical model is then compared to the simulation of both inductively- and capacitively-loaded FRQMSIW cavities, where a packaged RF MEMS SP4T switch is used to reconfigure the reactive loading, shifting the resonance frequency. Two different tunable BPFs are designed and measured, using both inductively- and capacitively-loaded FRQMSIW cavities tuned using RF MEMS switches. Compared to a HMSIW RF MEMS tunable bandpass filter reported in [130], the inductively- and capacitively-tuned filters achieve miniaturizations of 70.3% and 78.8%, respectively, highlighting the extreme amount miniaturization possible with the proposed designs.

6.2.1 Principle of Operation

In this section, the combination of FRQMSIW technology with reactive loadings is investigated for tunable waveguide cavity design. Following the design procedure in Section 6.1.1, a FRQMSIW can be formed from a FRSIW cavity by

cutting the waveguide into quarters along planes of symmetry of the fundamental $TE_{1,0,1}$ resonance, where due to a large aspect ratio, the open sides can be approximated as perfect magnetic conductor (PMC) walls [10].

In Fig. 6.15, the 3D layout and cross-section of a FRQMSIW cavity along with the electric field distribution of the fundamental quasi-$TE_{0.5,0,0.5}$ resonant mode is shown. For additional insight, a ridged quarter-mode SIW (RQMSIW) cavity as introduced in Section 4.4 is also included in Fig. 6.15. With regard to the RQMSIW cavity, a capacitive ridge was inserted into a QMSIW cavity miniaturizing the cavity area by 48% or more while also decreasing radiation loss. In the case of FRQMSIW, the cavity area of the RQMSIW is further decreased by moving the ridge within the waveguide channel, effectively folding the fundamental quasi-$TE_{0.5,0,0.5}$ resonant mode around the ridge structure. Compared to the RQMSIW (transverse width ~λ/8) and QMSIW (transverse width ~λ/4), the FRQMSIW (transverse width ~λ/16) miniaturizes the cavity area by approximately 75% and 93.75%, respectively.

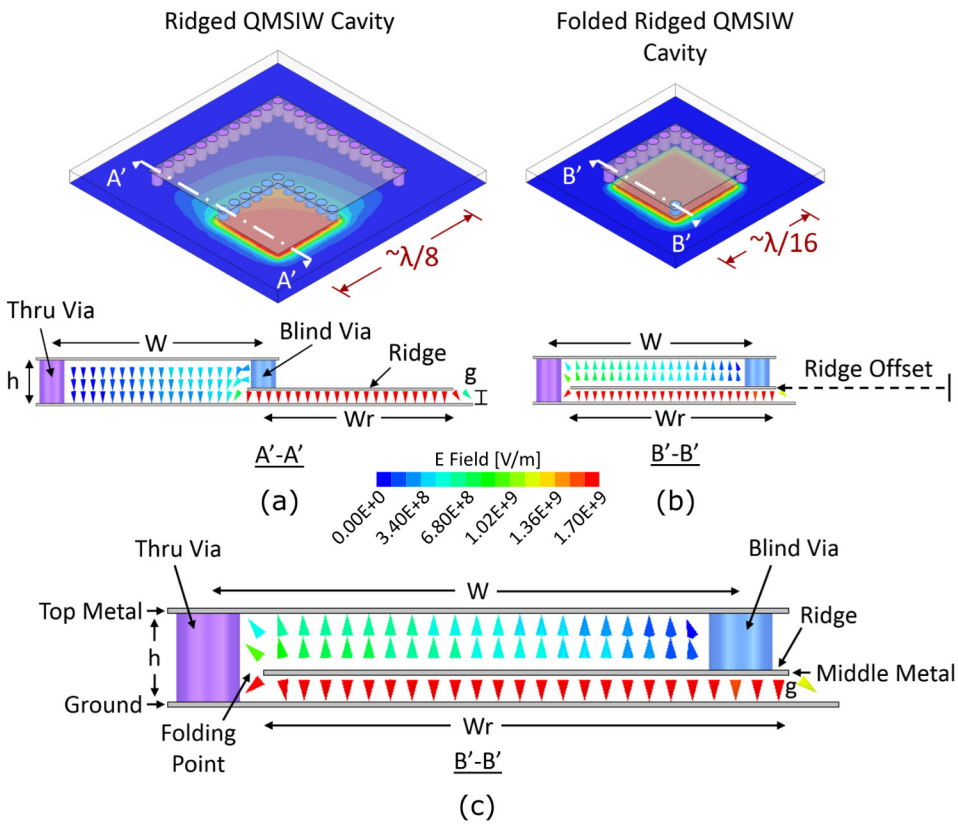

Fig. 6.15. 3D layout and cross-section showing the transition from (a) RQMSIW cavity, to (b) FRQMSIW cavity, along with the electric field distribution of the fundamental resonant mode for each cavity. In (c), a close-up of the FRQMSIW cross-section highlighting the three metallizations layers (ground, middle, and top metals), along with the folding point and wrapping of the field distribution between two substrates.

To calculate the resonance frequency of the FRQMSIW cavity, the transverse resonance technique developed in Section 5.1 for FRHMSIW is applied to the equivalent circuit model in Fig. 6.16(a), where a PMC wall represents the open side of the cavity. The resonance frequency is determined by solving the transcendental equation (5.2), where W and Wr are the widths of the waveguide channel and capacitive ridge, respectively, Y_{01} and Y_{02} the transverse characteristic admittance of the waveguide channel and ridge sections, respectively, and B the transverse step capacitance due to the transition between the channel and ridge at the folding point shown in Fig. 6.15. The additional capacitance due to the proximity between the

ridge edge and sidewall in the folding point region (see Section 5.1) is disregarded for this analysis, but can be included for greater design accuracy if needed.

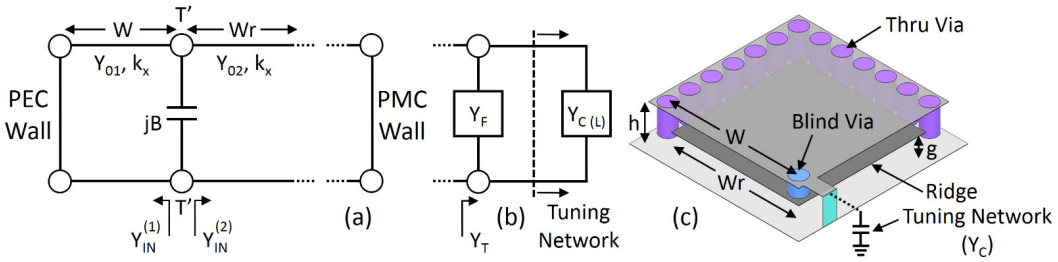

Fig. 6.16. Equivalent circuit model of the FRQMSIW cavity with (a) PMC wall for unloaded FRQMSIW, (b) PMC wall replaced with a tuning network, and (c) location of tuning network on the FRQMSIW cavity.

To model a reactive loading on the FRQMSIW resonance frequency, according to the circuit diagram of Fig. 6.16(b), an admittance of $Y_T = Y_F + Y_{C\,(L)}$ replaces the PMC boundary condition used in (5.2), where $Y_{C\,(L)}$ represents either a capacitive or inductive loading, and Y_F represents the fringing fields associated with the open structure. The modified transverse resonance equation becomes

$$-\cot\left(\frac{2\pi}{\lambda_c}W\right) + {B}/{Y_{01}} - j\,{Y_{02}}/{Y_{01}}\left(\frac{Y_T + jY_{02}\tan\left(\frac{2\pi}{\lambda_c}Wr\right)}{Y_{02} + jY_T\tan\left(\frac{2\pi}{\lambda_c}Wr\right)}\right) = 0. \tag{6.5}$$

Considering that the tuning element satisfies the condition, equation (6.5) can be simplified with the approximation $Y_{02} \gg jY_T \times tan(2\pi Wr/\lambda_c)$ to the following

$$-\cot\left(\frac{2\pi}{\lambda_c}W\right) + {B}/{Y_{01}} + {Y_{02}}/{Y_{01}}\tan\left(\frac{2\pi}{\lambda_c}Wr\right) - j\,{Y_T}/{Y_{01}} = 0 \tag{6.6}$$

which is the original (5.2), with the added loading term representing the reactive (capacitive or inductive) loading and fringing fields. This additional loading can be expressed as

$$-j\,{Y_T}/{Y_{01}} = -j\,{Y_F}/{Y_{01}} + {\omega C}/{Y_{01}} \tag{6.7}$$

$$-j\,{Y_T}/{Y_{01}} = -j\,{Y_F}/{Y_{01}} - {1}/{(Y_{01}\omega L)} \tag{6.8}$$

for either capacitive (6.7) or inductive (6.8) loading.

According to (6.7) and (6.8), the loading admittance Y_T is proportional to capacitance C, while inversely proportional to inductance L. Therefore, larger tuning ratios can more easily be achieved in practice using capacitive loading compared to inductive loading, due to the inherent inductance of conductive through vias. Furthermore, increased capacitive loading also decreases the resonance frequency, further miniaturizing the filter. With these considerations, the next section compares the derived analytical model with simulated FRQMSIW cavity resonators using both capacitive and inductive RF MEMS tunable loadings.

6.2.2 RF MEMS Tunable Cavity Design

6.2.2.1 Inductively-Loaded FRQMSIW Cavity

In Fig. 6.17, the design layout of a single FRQMSIW cavity with inductive loading is shown for simulation in Keysight Advanced Design System (ADS). Rogers RO3010 is used for the top and bottom substrates, 25 mil and 10 mil, respectively. Adhesives Research EL-7876 2.2 mil thick silicone transfer adhesive tape is used as the bonding layer between the two substrates. A 50-Ω microstrip feed is weakly coupled to the resonator to extract the unloaded resonance frequency f_0 and unloaded quality factor Q_u.

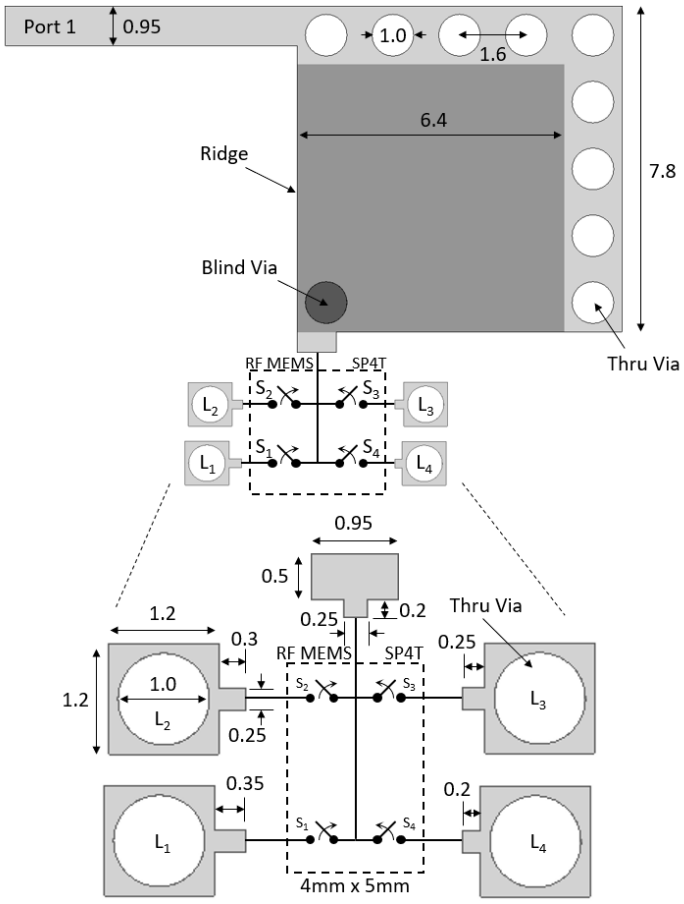

Fig. 6.17. General schematic with dimensions of the FRQMSIW cavity resonator with packaged RF MEMS SP4T (Analog Devices, Inc. ADGM1304) to switch inductive loading (units in mm). Light and dark grey areas are the top and embedded ridge metallizations, respectively.

Analog Devices, Inc. ADGM1304 single-pole, four-throw (SP4T) RF MEMS switch, with low insertion loss, high linearity, and independent switch control, is used to reconfigure the inductive loading. Due to the fabrication limitations, the RF MEMS chips are placed on the top substrate and connected to the top metallization layer in a location above the peak electric field location to maximize the inductive loading potential, as shown in Fig. 6.16(c) and Fig. 6.17. Conductive through vias shorted to ground are chosen to provide inductive loading at the output of each switch. From (6.8), since the admittance of the inductive loading is proportional to L^{-1}, it can be seen that lower inductive loadings yield larger resonance frequency

shifts. Therefore, with more inductor loadings in parallel, greater tunability can be achieved. The dimensions of the inductive loadings are given in Fig. 6.17. Due to the relatively large inductance inherent in conductive through via [131], the total length of each loading is very short, in order to achieve an inductance less than 5 nH for each loading.

In Table 6.5, the total simulated inductive loading and quality factor (Q) for each switch state of the tuning element is shown. While 16 different states are achieved, since the RF MEMS switch is capacitive in tuning mode 0A, i.e., when all switches are in the OFF state, this mode is not used for this design. Therefore, 15 unique states are used to tune the resonator. Furthermore, as additional switches are turned on, the Q of the tuning element increases, due to the series resistance in each switch adding in parallel. It is generally understood that the Q of a tuning element has a large impact on the overall Q_u of a tunable resonator [132]. As such, Table 6.5 also shows the simulated f_0 and Q_u of the inductively-loaded FRQMSIW cavity for each switch state. For tuning mode 0A, which approximates an unloaded case, the FRQMSIW cavity has a Q_u of 135. However, when a single switch is turned on for tuning mode 1A, the Q_u drops to 69. Thus, the Q of the RF MEMS tuning element has a significant impact on the overall Q_u of the FRQMSIW cavity. Nevertheless, the advantages of the RF MEMS chip make it a good choice as a tuning element for applications requiring high linearity and high power handling.

Tuning Mode	S1,S2,S3,S4	Total Inductive Loading (nH)	Tuning Element Q	FRQMSIW Cavity f_0 (GHz)	FRQMSIW Cavity Q_u
0A	0000	(0.51 pF)	N/A	1.609	135
1A	1000	3.42	15	1.731	69
1B	0001	3.30	15	1.734	71
1C	0100	3.11	23	1.739	82
1D	0010	2.99	19	1.742	78
2A	1100	2.21	22	1.769	76
2B	0011	2.15	21	1.772	73
2C	1001	2.02	20	1.778	70
2D	0101	1.90	23	1.784	73
2E	1010	1.89	21	1.785	70
2F	0110	1.79	24	1.791	76
3A	1101	1.65	24	1.799	74
3B	1011	1.64	23	1.799	71
3C	1110	1.57	25	1.804	71
3D	0111	1.57	25	1.805	74
4A	1111	1.43	26	1.814	71

Table 6.5. RF MEMS Switch Tuning Modes, Total Inductive Loading, and Tuning Element Q along with the Resonance Frequency f_0 and Unloaded Quality Factor Q_u of the Inductively-Loaded FRQMSIW Cavity.

In Fig. 6.18, the change in resonance frequency with variation of the normalized total inductive loading admittance Y_T/Y_{01} from (6.6) is plotted for the different tuning modes, along with the simulated case of the loaded FRQMSIW cavity in Fig. 6.17. From the circuit model, the total shift in resonance frequency is 83.2 MHz at center frequency f_0 = 1.774 GHz, for a tuning ratio of 4.7%, while for the simulated FRQMSIW cavity, the shift is 83 MHz at f_0 = 1.773 GHz, with tuning ratio of 4.7%.

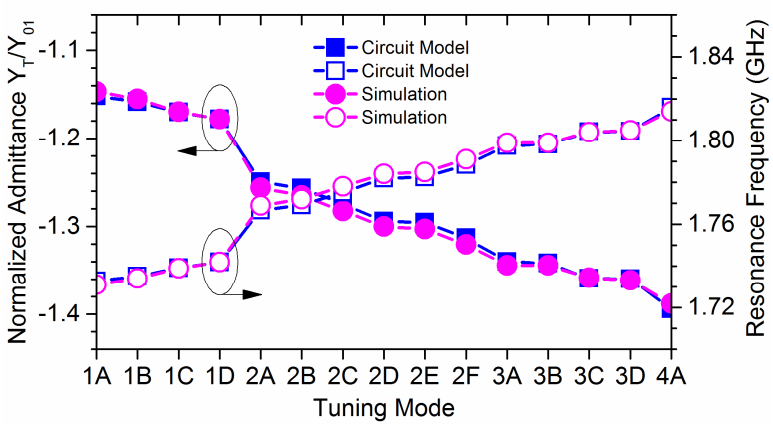

Fig. 6.18. Change in resonance frequency of an inductively-loaded FRQMSIW cavity resonator with variation in the normalized admittance for each tuning mode using the circuit model (6.6) and ADS simulation.

It is noted that four main tuning states are achieved, i.e. when one switch is on, or two switches are on, etc., and within each of these main tuning states, the impact of the specific switch used yields only a small change in resonance frequency. While the inductive loadings for each switch were designed to have successively larger values by having longer lengths, as seen in Fig. 6.17, it was found that the internal inductance (ON state) and internal capacitance (OFF state) of the RF MEMS chip itself was different for each path. Regardless, good agreement between the circuit model and simulated model is shown, validating the analytical theory developed in Section 6.2.1. Furthermore, the small shift in resonance frequency within the four main tuning states can be used for fine-tuning due to fabrication tolerances.

For the inductively-loaded FRQMSIW cavity above, the small tuning ratio of 4.7% is due to the inverse relationship between loading admittance and inductance shown in (6.8), and the difficulty in realizing small inductance values in practice. While other benefits exist for using inductive loading, such as a wider spurious-

free region above the passband (discussed in more detail in Section 6.2.3), the capacitive loading of a simulated FRQMSIW cavity is now explored.

6.2.2.2 Capacitively-Loaded FRQMSIW Cavity

In Fig. 6.19, the design layout of a single FRQMSIW cavity with capacitive loading is shown for simulation in ADS. Rogers RO3010 is again chosen, however, thicker substrates 50 mil and 25 mil are used for the top and bottom, respectively, to improve the resonator's quality factor, while keeping the ratio (and therefore cavity miniaturization) between the top and bottom relatively the same (see Section 6.1.3). Rogers RO4450F Bondply with 4 mil thickness is used for the bonding layer between substrates. A 50-Ω microstrip feed is again used to weakly couple to the resonator to extract the unloaded resonance frequency f_0 and Q_u.

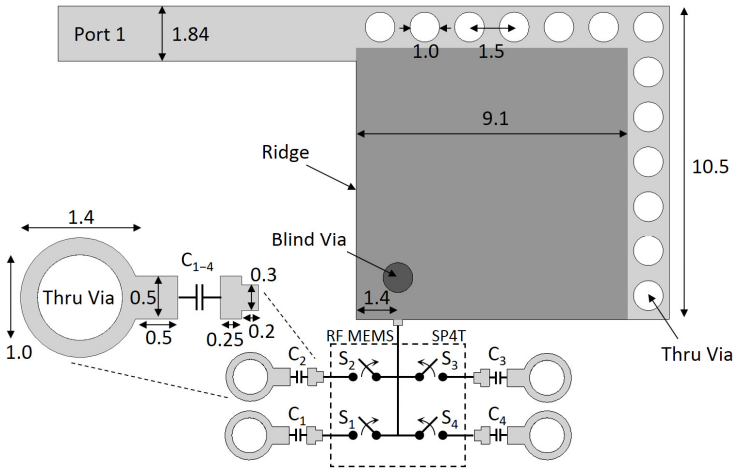

Fig. 6.19. General schematic with dimensions of the FRQMSIW cavity resonator with packaged RF MEMS SP4T (Analog Devices, Inc. ADG1304) to switch capacitive loading (units in mm). For capacitances $C_{1\text{-}4}$, surface mount 0402 ceramic capacitors (Taiyo Yuden UVK Series) are used with values $C_1 = C_2 = C_3 = 2.4$ pF, $C_4 = 1.2$ pF. Light and dark grey areas are the top and embedded ridge metallizations, respectively.

An Analog Devices, Inc. ADGM1304 SP4T RF MEMS switch is again used to tune the capacitive loading, and similarly placed on the top metallization of the top

substrate, in a location above the peak electric field location. The capacitive loadings are achieved with 0402 surface mount ceramic capacitors (Taiyo Yuden UVK series), which are terminated with through vias shorted to ground. From (6.7), it can be seen that larger capacitive loadings generate larger resonance frequency shifts. Thus, increased capacitive loading is achieved when more switches are placed in the ON state, where their admittance adds in parallel.

In Table 6.6, the total simulated capacitive loading and Q for each switch state of the tuning element is shown, along with the simulated f_0 and Q_u of the capacitively-loaded FRQMSIW cavity. While 16 unique states are possible with the chosen SP4T switch, for this design, 8 unique states are used to allow for a relatively linear change in capacitive loading between tuning modes. This is achieved by having capacitor C_4 equal to half the value of each of the other three capacitive loadings. Thus, four broad tuning states are achieved using switches S1, S2, and S3, i.e., 000, 001, 011, and 111, while switch S4 toggles a capacitive loading that is approximately halfway between each state. It is noticed that the tuning element Q decreases with more switches in the ON state, opposite to the effect for the inductive loading in Section 6.2.2.1. This is due to the parallel resistance of the capacitive loading for each switch adding in parallel when more switches are turned on, decreasing the overall parallel resistance of the total capacitive loading. For tuning mode 1A, with all switches in the OFF state, the FRQMSIW cavity has a Q_u of 204. However, for tuning mode 1B, when switch S4 is turned on, the Q_u of the FRQMSIW cavity drops to 147, and with each additional switch turned on, the Q_u continues to decrease. This again confirms the significant

impact of the tuning element Q on the FRQMSIW cavity performance. Still, as mentioned in Section 6.2.2.1 for the inductively-loaded FRQMSIW cavity, the advantages of RF MEMS make them a good choice for design applications requiring high linearity and high power handling.

Tuning Mode	S1,S2,S3,S4	Total Capacitive Loading (pF)	Tuning Element Q	FRQMSIW Cavity f_0 (GHz)	FRQMSIW Cavity Q_u
1A	0000	0.48	125	1.080	204
1B	0001	2.51	39	1.041	147
2A	0010	4.78	25	0.995	90
2B	0011	7.32	23	0.942	62
3A	0110	9.32	22	0.901	52
3B	0111	11.83	22	0.854	46
4A	1110	14.30	18	0.811	34
4B	1111	16.72	18	0.773	33

Table 6.6. RF MEMS Switch Tuning Modes, Total Capacitive Loading, and Tuning Element Q along with the Resonance Frequency f_0 and Unloaded Quality Factor Q_u of the Capacitively-Loaded FRQMSIW Cavity.

In Fig. 6.20, the change in resonance frequency with variation of the normalized total capacitive loading admittance Y_T/Y_{01} from (6.6) is plotted for the different tuning modes, along with the simulated case of the loaded FRMQSIW cavity in Fig. 6.19. From the circuit model, the total shift in resonance frequency is 292 MHz at f_0 = 934 MHz, for a tuning ratio of 31.3%, while for the simulated FRQMSIW cavity, the shift is 307 MHz at f_0 = 927 MHz, for a tuning ratio of 33.1%. Compared to the inductively-loaded case in Fig. 6.18, we note a larger tuning ratio and a more linear change in resonance frequency between each state. In addition, good agreement between the circuit model and simulated model is shown, further validating the theory developed in Section 6.2.1.

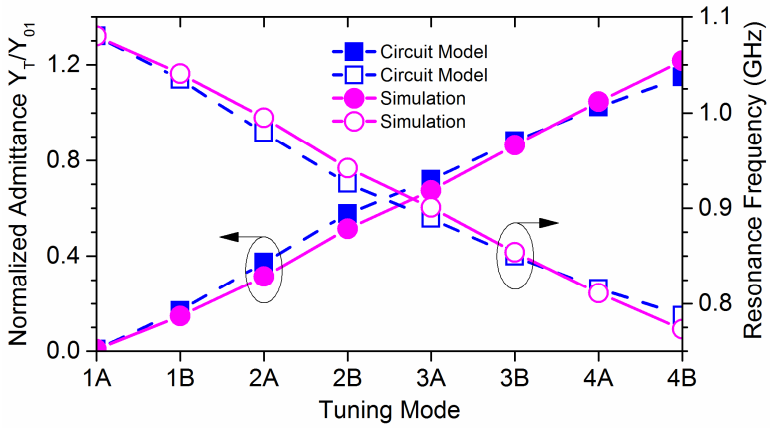

Fig. 6.20. Change in resonance frequency of a capacitively-loaded FRQMSIW cavity resonator with variation in the normalized admittance for each tuning mode using the circuit model (6.6) and ADS simulation.

6.2.3 Experimental Results

In this section, both the inductively- and capacitively-loaded FRQMSIW cavities detailed above are used to design RF MEMS tunable bandpass filters (BPF). The fabrication and experimental results of two-pole BPF prototypes using inductive or capacitive loading are presented, while the benefits of each technology are discussed and compared. As a general note, the centre frequency of each BPF was chosen due to in-house fabrication limitations, thus the operating range of the measured prototypes are presented as a proof-of-concept. However, as previously shown in Section 6.1.1, the FRQMSIW cavity is slightly smaller than even conventional miniaturized microstrip resonators operating at the same resonance frequency, while also having a larger spurious-free region above the passband.

6.2.3.1 Inductively-Loaded FRQMSIW RF MEMS Tunable Bandpass Filter

In Fig. 6.21, the coupling routing diagram of an inductively-loaded two-pole FRQMSIW tunable bandpass filter is shown, where resonators #1 and #2 are loaded with RF MEMS SP4T switches to reconfigure their resonance frequency using

inductive loadings L_1, L_2, L_3, and L_4. As presented in Section 6.1.2 for the coupling synthesis of a two-pole FRQMSIW BPF with 20 dB return loss, the required normalized coupling coefficient M_{12} and normalized input resistances R_1, R_2 are determined from (6.1), with the respective N+2 normalized coupling matrix shown in (6.2).

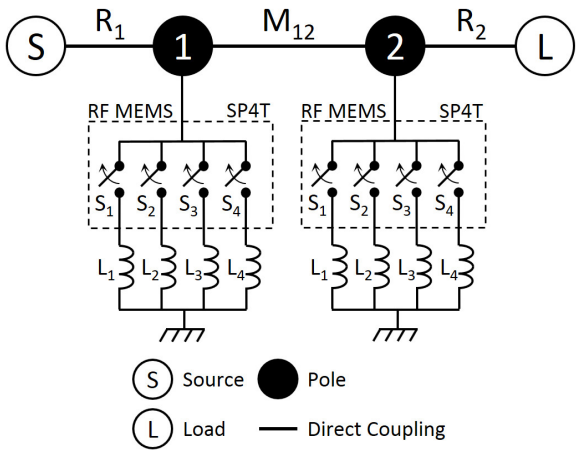

Fig. 6.21. Coupling routing diagram of a two-pole Chebyshev bandpass filter with RF MEMS switchable inductive loading.

In Fig. 6.22, the layout of the final design is shown. Rogers RO3010 is used for the top and bottom substrates, with thicknesses of 25 mil and 10 mil, respectively. Adhesives Research EL-7876 2.2 mil thick silicone transfer adhesive tape is used to bond the substrates together.

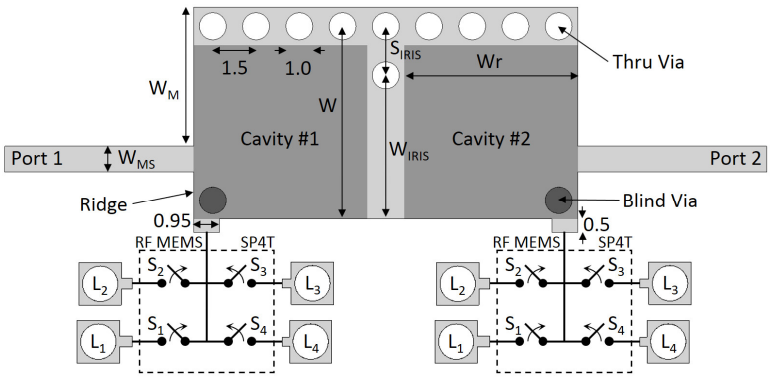

Fig. 6.22. General schematic of the inductively-loaded two-pole FRQMSIW tunable BPF with W = 7.1, Wr = 6.4, W_{IRIS} = 5.3, S_{IRIS} = 1.8, W_M = 5.1, and W_{MS} = 0.95 (units in mm). Light and dark grey areas are the top and embedded ridge metallizations, respectively.

A standard iris inductive coupling window is used to couple the two resonators, where the dimension W_{IRIS} is mapped to the coupling element M_{12} by simulating two weakly coupled resonators and extracting the coupling coefficient k using (6.3) [110]. In Fig. 6.23(a), the simulated extracted coupling coefficient k is plotted versus iris dimension W_{IRIS}. While the filter is initially designed with a small amount of inductive loading (in this case tuning mode 1B was used), greater inductive loadings perturbate the field distribution within the cavity, and thus impact the amount of coupling between cavities. In Fig. 6.23(a), when the RF MEMS switch is moved into higher inductively-loaded states, a drop in the amount of coupling is noticed. The effect of decreased coupling is a reduction in bandwidth and increase in passband insertion loss.

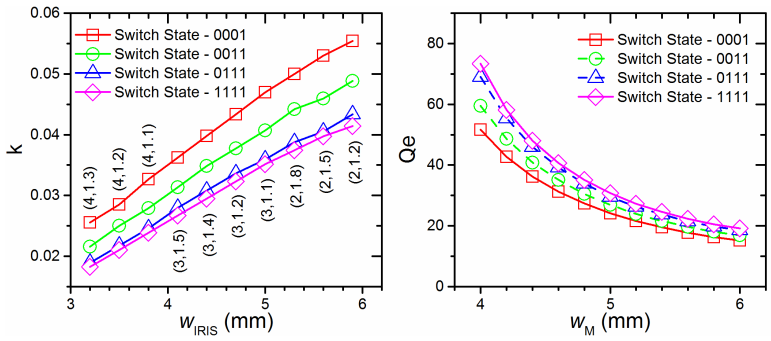

(a) (b)

Fig. 6.23. Simulated extracted (a) coupling coefficient k versus iris window width W_{IRIS}, and (b) external quality factor Q_e versus microstrip feed offset W_M, for the inductively-loaded FRQMSIW tunable BPF. Within each graph, four different switch states with increasing inductive loading are plotted. The inset coordinates in (a), i.e. (4,1.3), represent the number of coupling vias and via spacing S_{IRIS} (in mm), respectively, to achieve the specific dimension W_{IRIS} shown in the x-axis.

Each cavity is fed by a 50-Ω microstrip line connected to the top metallization of the top substrate, and the input/output coupling, controlled by the dimension W_M, is determined using the reflection coefficient group delay method [22]. A single microstrip fed cavity is simulated, and the normalized input impedances R_1 and R_2, along with external quality factor Q_e are extracted using (6.4). In Fig. 6.23(b), the simulated extracted Q_e versus dimension W_M is plotted. Similar to the coupling coefficient, a change in the extracted Q_e at a fixed dimension W_M is noted as the inductive loading is increased. Due to the change in field distribution, the amount of energy coupled into the cavity is decreased with greater loading, decreasing the return loss.

After a last optimization in ADS, the final dimensions of the filter are shown in Fig. 6.22, where each RF MEMS chip has similar inductive loading dimensions and values as for the single resonator in Section 6.2.2.1. In Fig. 6.24, a picture of the fabricated filter is shown, including a close-up of the RF MEMS SP4T switch and inductive loadings. The total area of the filter is 23.5 mm by 38.2 mm.

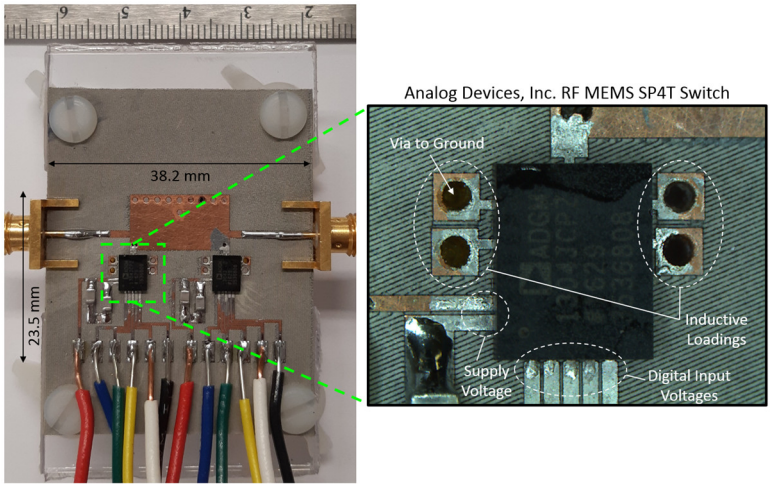

Fig. 6.24. Picture of the fabricated inductively-loaded two-pole FRQMSIW tunable BPF with packaged RF MEMS SP4T switches (Analog Devices, Inc. ADG1304).

The measured and simulated scattering parameters for tuning mode 1B are plotted in Fig. 6.25. For the simulated filter (ADS), the insertion loss is 2.55 dB at resonance frequency f_0 = 1.670 GHz, with 1-dB and 3-dB bandwidths of 77 MHz and 124 MHz ($FBW_{1\text{-}dB}$ = 4.6% and $FBW_{3\text{-}dB}$ = 7.4%), respectively. For the measured filter, the insertion loss is 3.10 dB at resonance f_0 = 1.675 GHz, with 1-dB and 3-dB bandwidths of 75 MHz and 123 MHz ($FBW_{1\text{-}dB}$ = 4.5% and $FBW_{3\text{-}dB}$ = 7.4%), respectively. The return loss for both measured and simulated is greater than 20 dB. The shift in simulated versus measured resonance frequency is only 0.3%, showing good modelling accuracy of the RF MEMS chips and inductive loadings.

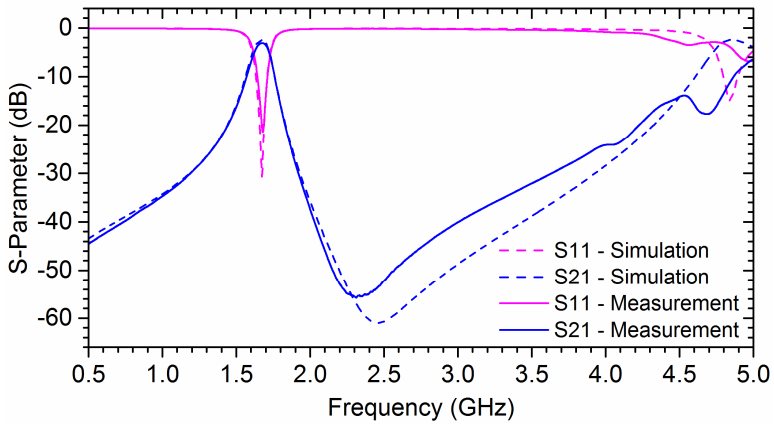

Fig. 6.25. Measured and simulated scattering parameters of switch tuning mode 1B (see Table 6.5) for the inductively-loaded two-pole FRQMSIW tunable BPF, showing a wideband spurious-free response.

A wide spurious-free region is also noted in Fig. 6.25. As developed in Section 6.1.1, it was shown for FRQMSIW cavities that the ratio between the fundamental and 2nd order resonances is approximately 1:5. Due to the loading being entirely inductive, no additional resonances are introduced. Thus, for the inductively-loaded FRQMSIW RF MEMS tunable BPF, the large spurious-free region above the filter passband of the FRQMSIW cavity is maintained.

In Fig. 6.26, the measured filter performance for three of the main tuning modes 1B, 2B, and 3D are shown, with the inset plotting the finer tuning modes 3A to 3D. The total frequency tuning range is from 1.675 GHz to 1.750 GHz, for a tuning bandwidth of 75 MHz, or 4.4%, with respect to a center frequency of 1.713 GHz, again noting that tuning mode 0A is not used due to the significant jump from capacitive (all switches in OFF state) to inductive loading. The low tuning range is due to the difficulty of achieving small inductive loading values in practice, which are necessary for high tuning ratios as determined in (6.6). The conductive through vias themselves are inductive [131], thus a very short microstrip line was used for

each loading. Furthermore, some fabrication errors led to a poor connection between the RF MEMS chip and one of the inductive loadings, thus the full tuning range was not possible in measurement. The insertion loss varies between 3.10 dB to 3.92 dB. The high insertion loss with small loading is likely due to the fabrication bonding layer. The increase in insertion loss with greater loading is likely due to the conductive through vias used for inductive loading. A small amount of additional loss is incurred when more switches are in the ON state, however the reported insertion loss of the Analog Devices, Inc. RF MEMS SP4T switch ADGM1304 is less than 0.26 dB below 2.5 GHz [133]. The return loss for all measured states is above 15 dB.

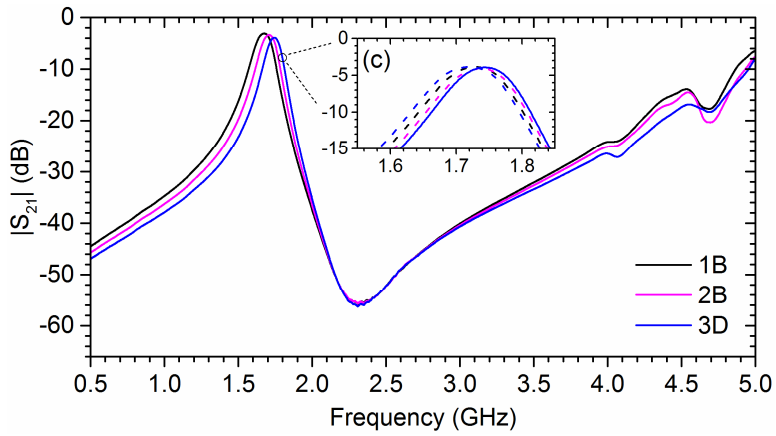

(a)

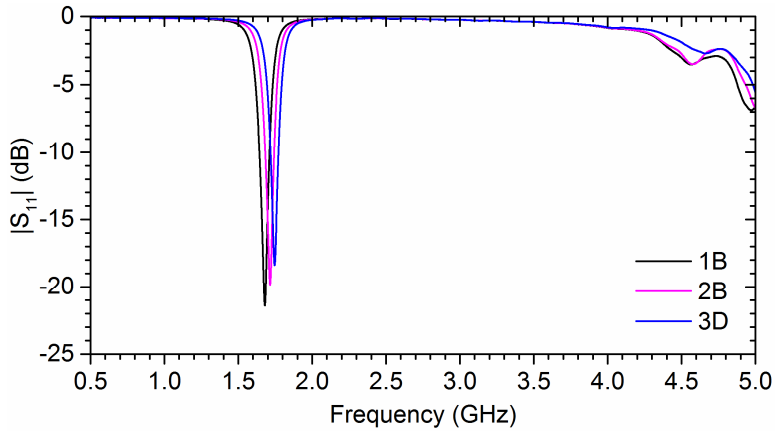

(b)

Fig. 6.26. Measured (a) power transmission ($|S_{21}|$) and (b) power reflection ($|S_{11}|$) responses of switch tuning modes 1B, 2B, and 3D (see Table 6.5) for the inductively-loaded two-pole FRQMSIW tunable BPF, where inset (c) shows finer tuning within broad switch tuning mode group 3A-3D (left to right).

In Fig. 6.27, both the 1-dB and 3-dB bandwidths and fractional bandwidths (FBW) are plotted for the main tuning modes 1B, 2B, and 3D. The 1-dB and 3-dB bandwidths range from 67.3 MHz ±7.2 MHz and 112.7 MHz ±10.2 MHz, respectively, where the fractional bandwidths are $FBW_{1\text{-dB}}$ = 3.96% ±0.51% and $FBW_{3\text{-dB}}$ = 6.62% ±0.73%. While a small shift in bandwidth is noted across the tuning range, the shift in FBW is slightly greater since the resonance frequency increases with greater inductive loading (FBW = $\Delta f/f_0$). To improve the design for

constant bandwidth across the tuning range, the thickness of the coupling through vias can be optimized by choosing a smaller drill diameter. For this work, the available in-house fabrication tools limited the choice to 1 mm via diameters, but diameters as low as 0.25 mm or less are possible in industrial PCB fabrication facilities.

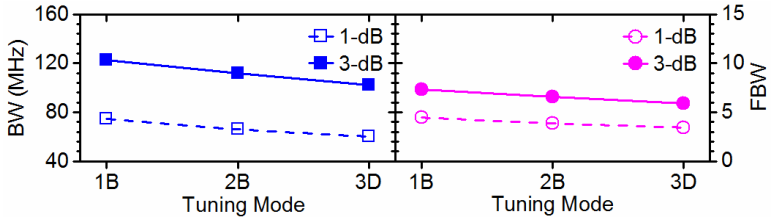

Fig. 6.27. Measured 1-dB and 3-dB bandwidth (BW) and fractional bandwidth (FBW) of the inductively-loaded two-pole FRQMSIW tunable BPF for main switching states 1B, 2B, and 3D.

The measured average unloaded quality factor Q_u can be extracted using the formula

$$Q_u = \frac{27.3 \times f_0 \times \tau(f_0)}{|S_{21}(f_0)|} \tag{10}$$

where f_0 is the resonance frequency (in GHz), $\tau(f_0)$ is the group delay of S_{21} at f_0 (in ns), and $|S_{21}(f_0)|$ is the insertion loss at f_0 (in dB) [134]. For the measured filter, the average Q_u ranges from 90 to 54, with the largest value when all switches are in the OFF state.

6.2.3.2 Capacitively-Loaded FRQMSIW RF MEMS Tunable Bandpass Filter

In Fig. 6.28, the coupling routing diagram of a capacitively-loaded two-pole FRQMSIW tunable bandpass filter is shown. Similar to the inductively-loaded case, the resonance frequency of resonators #1 and #2 are each tuned by an RF

MEMS SP4T switch, which reconfigures the total capacitive loading of C_1, C_2, C_3, and C_4. The required normalized coupling coefficient M_{12} and normalized input resistances R_1 and R_2 are again determined using (6.1), where the N+2 normalized coupling matrix for 20 dB return loss is shown in (6.2).

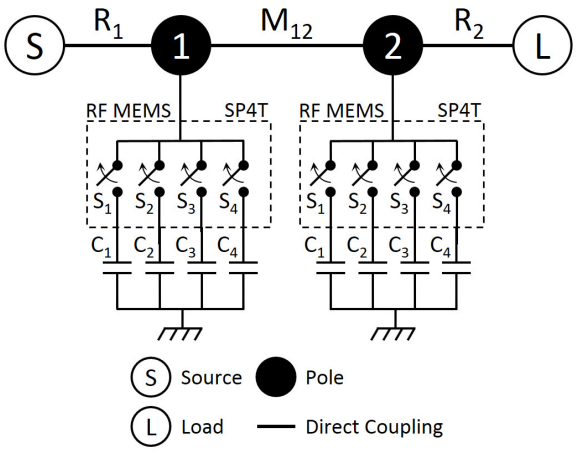

Fig. 6.28. Coupling routing diagram of a two-pole Chebyshev bandpass filter with RF MEMS switchable capacitive-loading.

Fig. 6.29 shows the final design layout, where each RF MEMS chip has similar capacitive loading dimensions and values as for the single cavity in Fig. 6.19. Rogers RO3010 is used for the top and bottom substrates, with thicknesses of 50 mil and 25 mil, respectively. As for the single capacitively-loaded cavity design in Section 6.2.2.2, thicker substrates are chosen while maintaining a similar ratio between the top and bottom substrate thicknesses to improve insertion loss (see Section 6.1.3). Rogers RO4450F Bondply with 4 mil thickness is used to bond the substrates together.

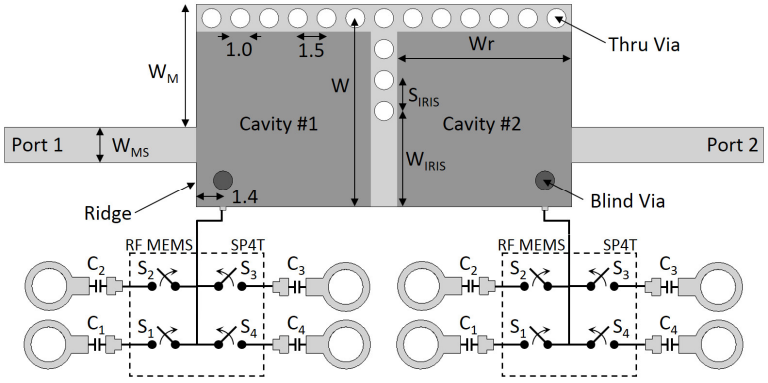

Fig. 6.29. General schematic of the capacitively-loaded two-pole FRQMSIW tunable BPF, with W = 9.8, Wr = 9.1, W_{IRIS} = 5, S_{IRIS} = 1.6, W_M = 6.34, and W_{MS} = 1.84 (units in mm). Light and dark grey areas are the top and embedded ridge metallizations, respectively.

A standard iris inductive coupling window is used to couple the two resonators, where the dimension W_{IRIS} can be mapped to the required M_{12} by (6.3). In Fig. 6.30(a), the extracted coupling coefficient k versus coupling dimension W_{IRIS} is plotted. It is noticed that the change in the coupling coefficient between switch state 0001 and 1111 remains relatively constant across the entire range of W_{IRIS}. Furthermore, opposite to the inductively-loaded case, greater coupling is achieved with greater capacitive loading. This is likely due to increased field concentration within the capacitive ridge region, increasing the amount of coupling between the two resonators.

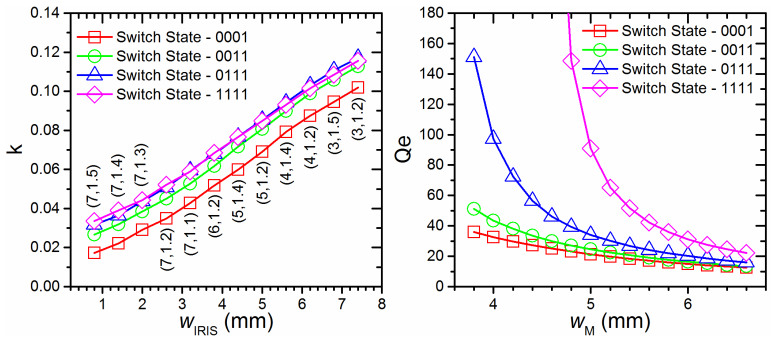

(a) (b)

Fig. 6.30. Simulated extracted (a) coupling coefficient k versus iris window width W_{IRIS}, and (b) external quality factor Q_e versus microstrip feed offset W_M, for the capacitively-loaded FRQMSIW tunable BPF. For each plot, four different switch states with increasing inductive loading are included. The inset coordinates in (a), i.e. (4,1.3), represent the number of coupling vias and via spacing S_{IRIS} (in mm), respectively, to achieve the specific dimension W_{IRIS} shown in the x-axis.

A 50-Ω microstrip line is used to feed the two cavities, connected to the top metallization layer of the top substrate. The required input/output coupling is determined by mapping the normalized input impedances R_1 and R_2 to the dimension W_M using (6.4). In Fig. 6.30(b), the extracted Q_e versus W_M is plotted. Similar to the inductively-loaded case, a change in Q_e is noticed for greater loading states, where the amount of energy coupled into the cavity decreases. This is again likely due to a perturbation in field distribution with increased loading. As the dimension W_M increases, this effect becomes less noticeable.

A last design optimization is performed in ADS, and the final dimensions are shown in Fig. 6.29. A picture of the fabricated filter is shown in Fig. 6.31. Due to the increased thickness of the substrates, Rosenberger 32K243-40ML5 SMA clamp connectors were used to connect to the filter. The total area of the filter is 25.7 mm by 49.4 mm.

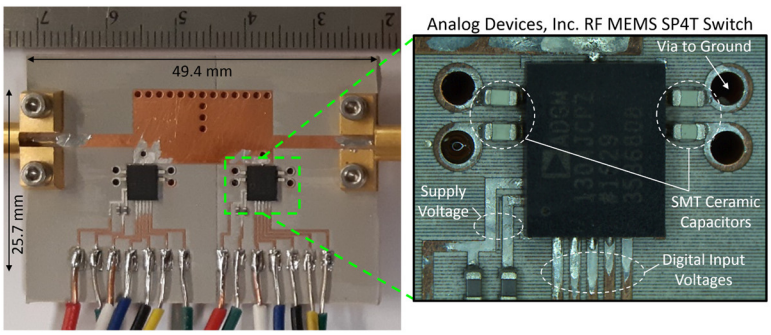

Fig. 6.31. Picture of the fabricated capacitively-loaded two-pole FRQMSIW tunable BPF with packaged RF MEMS SP4T switches (Analog Devices, Inc. ADG1304).

In Fig. 6.32, the measured and simulated scattering parameters for tuning mode 1B are plotted, showing good agreement. For the simulated filter, the insertion loss is 0.96 dB at resonance frequency f_0 = 990 MHz, with 1-dB and 3-dB bandwidths of 62 MHz and 96 MHz ($FBW_{1\text{-dB}}$ = 6.3% and $FBW_{3\text{-dB}}$ = 9.7%), respectively. For the measured filter, the insertion loss is 1.80 dB at resonance frequency f_0 = 974 MHz, with 1-dB and 3-dB bandwidths of 65 MHz and 99 MHz ($FBW_{1\text{-dB}}$ = 6.7% and $FBW_{3\text{-dB}}$ = 10.2%), respectively. Both measured and simulated return loss is greater than 17 dB. The shift between simulated and measured resonance frequency is 1.6%, again showing good modelling accuracy of the RF MEMS chip with capacitive loading. While slightly larger than the inductively-loaded filter, this is likely caused by parasitic effects due to soldering of the surface mount capacitors, altering the loading on the filter. Furthermore, a 1.3 dB decrease in measured insertion loss compared to the inductively-loaded filter with the same tuning mode (1B) is achieved. This improved performance is attributed to the thicker substrates and choice of bonding layer with lower dielectric loss.

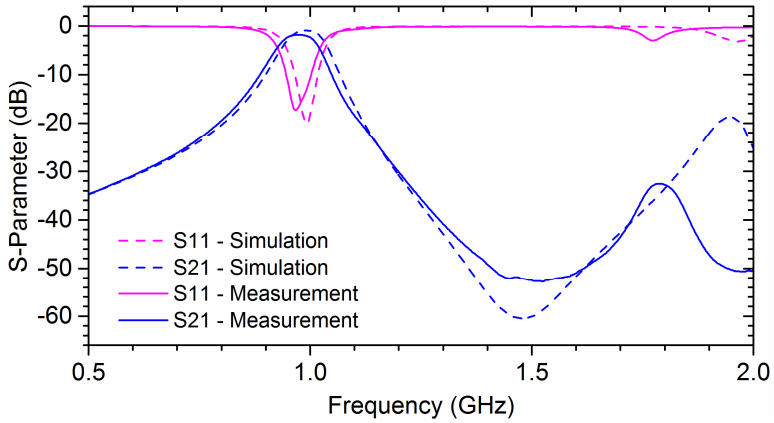

Fig. 6.32. Measured and simulated scattering parameters of switch tuning mode 1B (see Table 6.6) for the capacitively-loaded two-pole FRQMSIW tunable BPF.

In Fig. 6.33, the measured filter performance is plotted for each of the 8 tuning states. The frequency tuning range is from 713 MHz to 1.017 GHz, for a tuning bandwidth of 305 MHz, or 35.2%, with respect to a center frequency of 865 MHz. The insertion loss varies between 1.59 dB to 4.29 dB, while the return loss is above 10 dB for each tuning state. The higher insertion loss at greater capacitive loadings is likely due to the losses incurred in the surface mount capacitors and conductive through vias, i.e., when more switches are in the ON state. A decrease in the spurious-free region above the passband is also noticed with greater capacitive loading. Since each load has effectively a capacitor in series with an inductor (conductive through via), an additional resonance occurs above the passband, decreasing the spurious-free region compared to the inductively-loaded BPF.

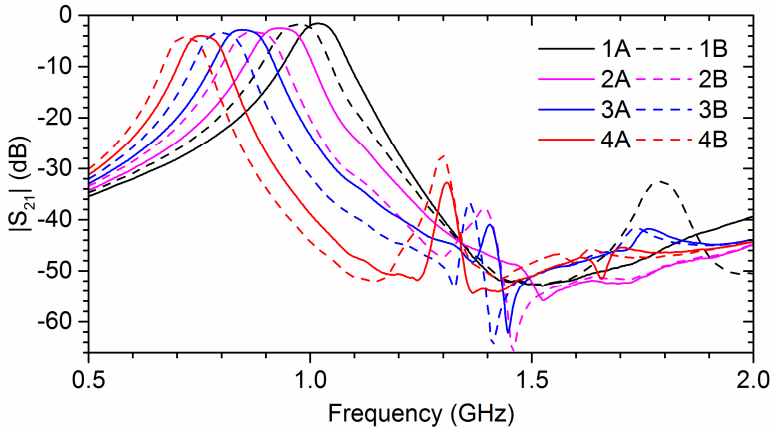

(a)

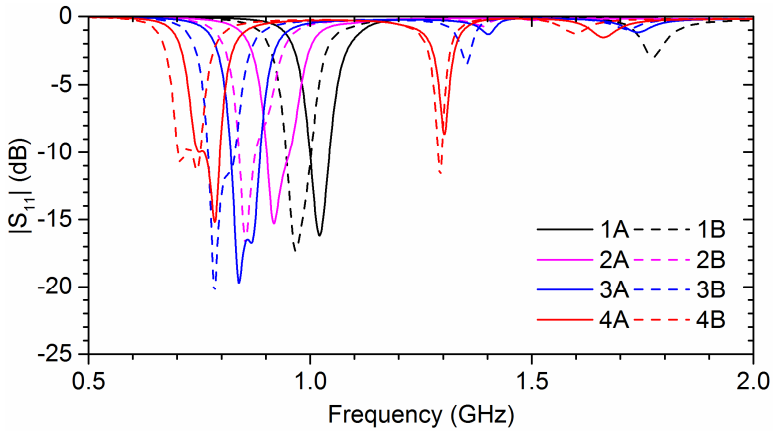

(b)

Fig. 6.33. Measured (a) power transmission ($|S_{21}|$) and (b) power reflection ($|S_{11}|$) responses of the capacitively-loaded two-pole FRQMSIW tunable BPF for all switch tuning states.

In Fig. 6.34, the 1-dB and 3-dB bandwidths and FBWs are plotted for all tuning modes. The 1-dB and 3-dB bandwidths range from 61.8 MHz ±8.7 MHz and 91.8 MHz ±11.9 MHz, respectively, where the fractional bandwidths are $FBW_{1\text{-dB}}$ = 7.72% ±0.34% and $FBW_{3\text{-dB}}$ = 11.47% ±0.39%. While the relative change in bandwidth is greater compared to the inductively-loaded BPF, the change in FBW is decreased. This is due to the resonance frequency decreasing with increased capacitive loading, while for the inductively-loaded case, the resonance frequency

increased with greater loading. Thus, the FBW remains relatively stable across the entire tuning range for the capacitively-loaded BPF.

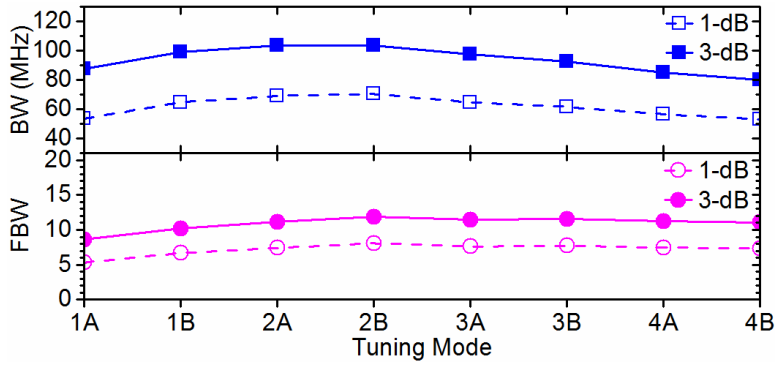

Fig. 6.34. Measured 1-dB and 3-dB bandwidth (BW) and fractional bandwidth (FBW) of the capacitively-loaded two-pole FRQMSIW tunable BPF for all switch tuning states.

The measured extracted Q_u for the capacitively-loaded BPF ranges from 92 to 27, with the largest value when all switches are in the OFF state, and the lowest value when all switches are in the ON state. A greater swing in Q_u is noticed compared to the inductively-loaded BPF, as expected from the discussion in Section 6.2.2 where the tuning element Q decreases with more switches turned on. Furthermore, greater field concentration within the ridge region as the capacitive loading is increased is also expected to decrease Q_u.

6.2.4 Final Discussion

In Table 6.7, the performance of the measured inductively-loaded and capacitively-loaded FRQMSIW filters are shown, along with the RF MEMS tunable HMSIW filter in [130] and RF MEMS tunable SIW filter in [129]. While a small tuning range of 4.4% is achieved for the inductively-loaded case of the FRQMSIW, the tuning range of 35.2% for the capacitively-loaded case is greater than both the HMSIW and SIW tunable filters. With respect to free-space lambda

at each filters center frequency, the inductively-loaded FRQMSIW filter of this work achieves a miniaturization of 70.3% compared to the HMSIW, and 88.0% compared to the SIW, while the capacitively-loaded FRQMSIW achieves a miniaturization of 78.8% compared to HMSIW, and 91.4% compared to the SIW. This is a substantial amount of miniaturization, considering the fact that the RF MEMS tunable HMSIW filter in [130] is reported to be ~2.5 times smaller than the tunable standard SIW filter in [129]. Furthermore, the significant miniaturization of the capacitively-loaded tunable FRQMSIW filter compared to the standard tunable SIW filter is achieved while also improving the filters measured insertion loss.

SIW Technology	Loading Type	Frequency Shift (GHz)	Tuning Range	Total Area	Miniat-urization	
FRQMSIW	Capacitive	0.713–1.017	35.2%	$0.004\times\lambda_0$	91.4%	This Work
FRQMSIW	Inductive	1.675–1.750	4.4%	$0.005\times\lambda_0$	88.0%	This Work
HMSIW	Inductive	1.2–1.6	28%	$0.017\times\lambda_0$	59.4%	[130]
SIW	Tuning Post	1.2–1.6	28%	$0.043\times\lambda_0$	Ref.	[129]

Table 6.7. RF MEMS Tunable Filter Performance Comparison

6.3 Reconfigurable Dual-Band Bandstop Filter

Modern software defined radios (SDR) continue to require higher levels of adaptability and reconfigurability to meet the demand of both military and consumer microwave systems in increasingly dynamic spectral environments and scenarios [135]. Within the filtering stage of such systems, tunable bandstop filters (BSF) play a critical role in dynamic suppression of interference signals within operating bandwidths, offering improved transmission band insertion losses than narrowband bandpass filters. Recently, a new type of highly reconfigurable

multiband filter technology has been developed, incorporating quasi-bandpass sections and nonresonating nodes (NRN) to allow independent tuning and coupling of resonators, for extreme adaptability of the filter transfer function [136]. In [137], a design approach for fully reconfigurable multiband bandstop filters was presented using planar microstrip resonators, with independent control of each stopband's centre frequency and bandwidth.

The benefits of substrate integrated waveguide (SIW) cavity resonators over traditional planar technology, including high Q and high power handling, have been investigated in the design of bandstop filters [138], [139]. However, due to the large size of SIW cavity, their use in systems requiring high density routing becomes impractical. Miniaturization techniques have explored the reduction of the SIW $\sim\lambda/2$ broadside width condition for use in bandstop filter design. These techniques include ridged SIW (RSIW) [140], [141], half-mode SIW (HMSIW) [142], [143], and evanescent-mode SIW cavities [144]–[146]. While these miniaturization techniques have been successfully applied to many filter applications, research into quarter-mode SIW (QMSIW) cavity technology for bandstop filter design remains limited.

In this section, the potential of tunable folded ridged quarter-mode SIW (FRQMSIW) cavity as developed in Section 6.2 is applied to reconfigurable bandstop filter design. Application of such a structure in the design of multi-band bandstop filters utilizing NRNs provides the opportunity of independent tuning of each stopband. A reconfigurable dual-band bandstop filter is then designed using miniaturized FRQMSIW cavity, and the measured results are presented. It is shown

that a significant miniaturization has been achieved compared to previously reported reconfigurable dual-band bandstop filters with similar filter topology, without any loss to performance. Furthermore, this section presents the first dual-band bandstop filter using QMSIW cavity technology in the present literature.

6.3.1 Principle of Operation

In Fig. 6.35, a simplified coupling-matrix diagram of a reconfigurable dual-band bandstop filter is shown, along with the synthesized power transmission ($|S_{21}|$) and reflection ($|S_{11}|$) response. The coupling matrix coefficients are shown in the figure caption. Following the design procedure in [137], two frequency tunable resonators are individually coupled to the same nonresonating node (NRN) [147], forming a frequency agile filtering section, which allows for independent tuning of each resonator's centre frequency without any impact to the other resonator. This filtering section is then coupled to another NRN with a pair of resonators by an impedance inverter, forming a reconfigurable dual-band two-pole bandstop filter. By tuning the resonance frequency of each resonator, different filtering states can be achieved.

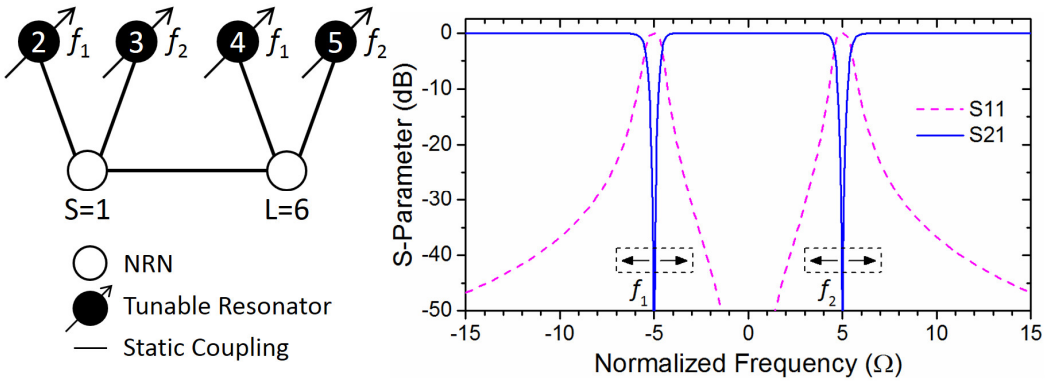

(a) (b)

Fig. 6.35. (a) Coupling-matrix diagram of a dual-band two-pole reconfigurable bandstop filter, and (b) synthesized power transmission ($|S_{21}|$) and reflection ($|S_{11}|$) responses with coupling-matrix element values $M_{22} = M_{44} = -5$, $M_{33} = M_{55} = 5$, $M_{12} = M_{46} = 0.8$, $M_{13} = M_{56} = 0.8$, and $M_{16} = 1$.

To realize the above filter implementation, the miniaturized frequency tunable FRQMSIW cavities developed in Section 6.2 are used for each resonator node. Following the design procedure presented in Section 6.2.1, the transverse resonance technique is applied to design a tunable FRQMSIW cavity, where a variable capacitor is placed in the tuning network region of the FRQMSIW cavity shown in Fig. 6.16(c). As previously mentioned, while the capacitor is best positioned in an area where the electric field is maximum, i.e., the open side of the ridge, due to fabrication limitations it is placed on the top metallization layer above this region. The blind via located next to the capacitor and above the ridge adds a small parasitic inductance to the load, lowering the self-resonance, but is negligible compared to the parasitic inductance of the variable capacitor itself, as discussed later. A 50-Ω microstrip provides the through line impedance inverter and NRNs. In Fig. 6.36, the final design layout of the dual-band reconfigurable BSF is shown, along with dimensions. For this design, the FRQMSIW cavities are capacitively coupled to the

NRN by an embedded parallel plate located underneath the microstrip line, yielding static coupling.

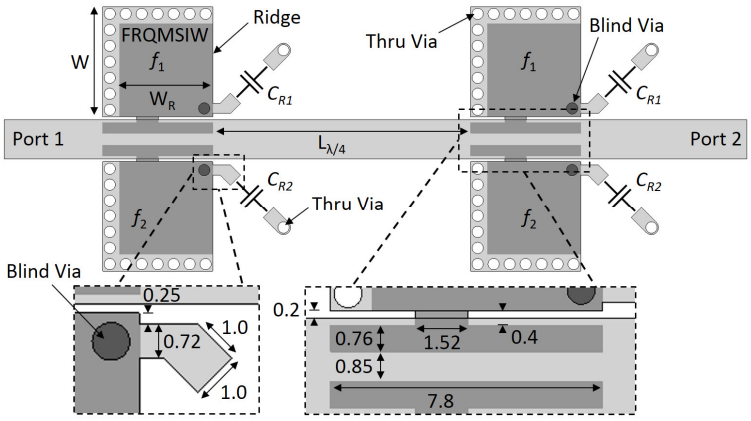

Fig. 6.36. Design layout of the reconfigurable dual-band FRQMSIW BSF simulated in ADS, with dimensions W = 7.8, W_R = 6.6, $L_{\lambda/4}$ = 18.3, via diameter = 0.8, and via spacing = 1.13 (all units in mm). Light and dark grey areas are the top and embedded ridge metallization layers, respectively.

The design was fabricated using Rogers RO3003 substrates (top/bottom thickness = 30/10 mil) and an LPKF ProtoLaser U3 and ProtoMat S62. Through and blind vias were plated using Think & Tinker, Ltd. Conductive Electroplating Ink and an acid copper electroplating bath. The substrates were bonded using 4 mil Rogers RO4450F Bondply. The tunable capacitors are realized with thin-trim capacitors from Johanson Manufacturing Corporation, specifically model 9702-0SL-1 with quality factor above 3000 at 100 MHz and a tuning range of 0.5 pF to 2.5 pF. The structure is simulated using Keysight Advanced Design System (ADS).

6.3.2 Measured Results and Discussion

In Fig. 6.37, a picture of the fabricated device is shown. The total area of the filter is 9.91 cm^2, while the total area of a single resonator is only 0.61 cm^2. Compared to a standard QMSIW cavity with the same parameters and resonance

frequency, a miniaturization of 92.0% is achieved. Considering a QMSIW is already 75% smaller than a standard SIW cavity, this is a significant amount of miniaturization. To further illustrate the reduced size of filters using FRQMSIW cavity, a comparison to the analogous dual-band bandstop filter using microstrip resonators in [148] yields a miniaturization of 58%, without any loss to performance (where the total filter area is normalized to the substrate wavelength at each filters lowest stopband frequency).

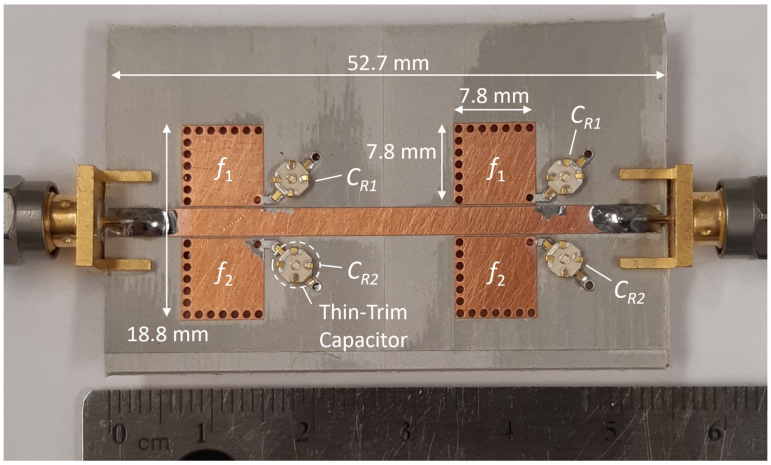

Fig. 6.37. Picture of the fabricated and measured FRQMSIW reconfigurable dual-band BSF.

In Fig. 6.38, the measured scattering parameters of a particular tuning mode are compared to simulation, showing good agreement. The lower stopband has an attenuation of 24.8 dB at f_1 = 1.53 GHz, while the upper stopband has 19.2 dB attenuation at f_2 = 1.71 GHz. The inter-band insertion loss is 0.39 dB while the return loss is 18.8 dB. While the FRQMSIW cavity itself has a large spurious-free region above the fundamental resonance (see Section 6.1.1), due to the parasitic inductance of the tunable capacitor (calculated to be ~2.8 nH including solder

connections), the passband above the upper stopband is limited to 0.564 GHz by the capacitor's self-resonance.

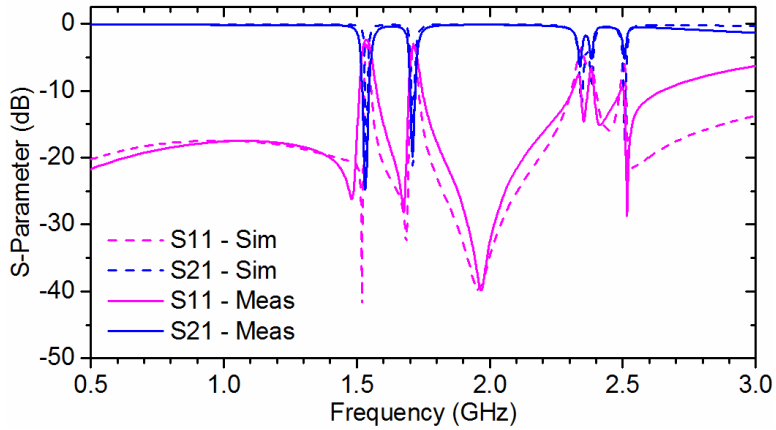

Fig. 6.38. Simulated and measured scattering parameters of the FRQMSIW reconfigurable dual-band BSF, with C_{R1} = 2.05 pF and C_{R2} = 1.53 pF.

As discussed earlier, the combination of NRNs with FRQMSIW cavity provides the opportunity not only for miniaturized filter design, but also independent tuning of each stopband. The reconfigurability of the BSF is illustrated in Fig. 6.39(a) and Fig. 6.39(b), presenting the independent tuning of each band. For example, decreasing the loading capacitance C_{R1} increases the lower stopband frequency f_1, while increasing the loading capacitance C_{R2} decreases the upper stopband frequency f_2. In Fig. 6.39(c), the two bands are combined to form a single stopband with increased attenuation and likewise tuned by increasing both C_{R1} and C_{R2}.

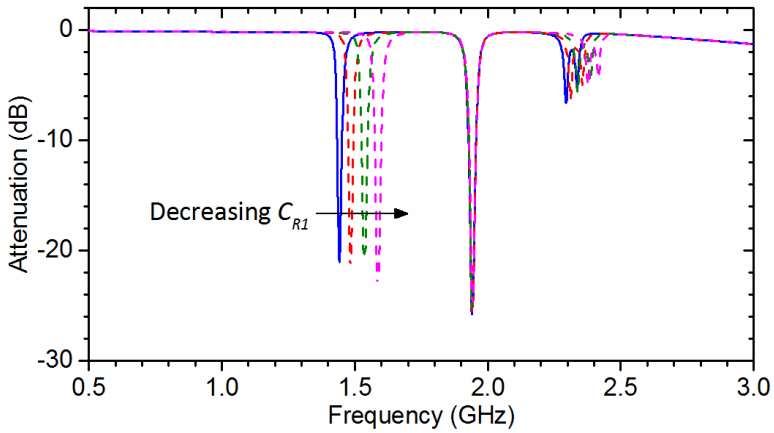

(a)

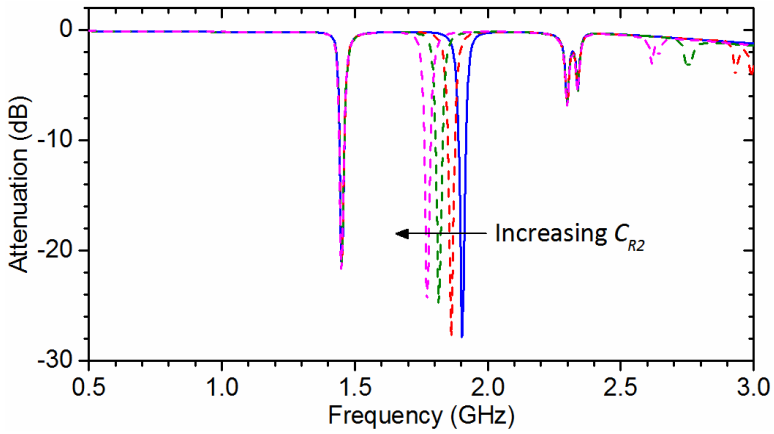

(b)

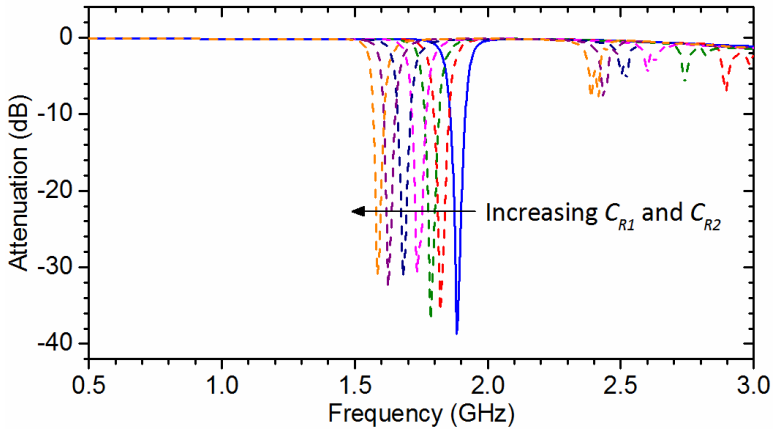

(c)

Fig. 6.39. Measured attenuation ($|S_{21}|$) of the FRQMSIW reconfigurable dual-band BSF for demonstration states (a) independent tuning of the lower stopband, (c) independent tuning of the upper stopband, and (c) combination of the lower and upper stopband into one main stopband, along with its tuning.

6.4 Summary

For applications in microwave filter design, this chapter has explored the performance and miniaturization potential of folded ridged half-mode and quarter-mode SIW cavities. While maintaining good Q_u, the FRHMSIW and FRQMSIW cavities achieved miniaturizations compared to standard SIW cavity of 96.6% and 98.0%, respectively, with improved spurious-free ratios of 1:5.34 and 1:4.82, respectively. Furthermore, the study of substrate thickness on Q_u was presented, where using thicker substrates while maintaining the ratio between waveguide channel to ridge height increased Q_u up to 38.6% or greater, without any significant change to the cavity's resonance frequency. The design of a two-pole FRQMSIW bandpass filter was outlined, and two prototypes with different substrate thicknesses were fabricated, showing good agreement between simulation and measurement.

The proposed FRQMSIW was then applied in tunable and reconfigurable bandpass and bandstop filter design. First, the design of both inductively- and capacitively-loaded RF MEMS tunable FRQMSIW bandpass filters was presented. Significant miniaturization was achieved for both inductively- and capacitively-loaded cases, with 70.3% and 78.8% reductions in filter area, respectively, compared to a similar RF MEMS tunable filter using HMSIW technology. An analytic theory was developed to calculate the shift in resonance frequency of a reactively loaded FRQMSIW cavity. Two filter prototypes were measured, with the inductively-loaded bandpass filter achieving 4.4% tuning ratio with respect to GHz center frequency, and the capacitively-loaded bandpass filter achieving 35.2%

tuning ratio with respect to MHz center frequency, highlighting the potential for FRQMSIW cavities in miniaturized tunable bandpass filter design, especially using capacitive tuning elements.

Finally, a reconfigurable dual-band bandstop filter using miniaturized tunable FRQMSIW cavity was presented. Employing the benefits of NRN design, dynamic filter functionality was combined with the small size of FRQMSIW cavity technology to realize ultra-compact filtering components. A prototype was designed and fabricated, showing good agreement between simulation and measurement. Independent tuning of each stopband was achieved, along with 58% miniaturization with no performance loss compared to an analogous dual-band bandstop filter with microstrip resonators, thus demonstrating the promising potential of miniaturized FRQMSIW cavity technology in the design of highly-adaptable bandstop filter design.

Chapter 7

Microfabrication of Integrated Monolithic Wafer-Level Air-Filled Waveguides for Millimeter-Wave Applications

As the world prepares for the revolution of 5G, with its vision to provide wireless data rates on the order of gigabits per second with extremely low latencies, the current sub-6 GHz bands currently in use will not be enough to meet the increased requirements on spectral efficiency and bandwidth [1]–[3]. Therefore, engineers are looking towards utilizing higher frequency bands called millimeter-waves (mm-waves), where a large portion of the spectrum remains relatively unused. This need has generated an exciting new challenge to provide low loss, integrated, planar, and tunable devices at mm-wave frequencies, with the goal of complete system-on-chip (SoC) integration. Unfortunately, traditional planar circuit technology becomes very lossy at such high frequencies, where demonstrations have shown CMOS integrated microstrip (MS) and coplanar waveguide (CPW) with attenuations greater than 0.5 dB/mm above 30 GHz [149], while high performance technology such as rectangular waveguides (RWG) are significantly large in size compared to planar technology and suffer poor integration. Consequently, as the example of a typical transceiver block diagram in Fig. 7.1 illustrates, there is a missing link to provide the interconnection between the antenna and chip with high performance.

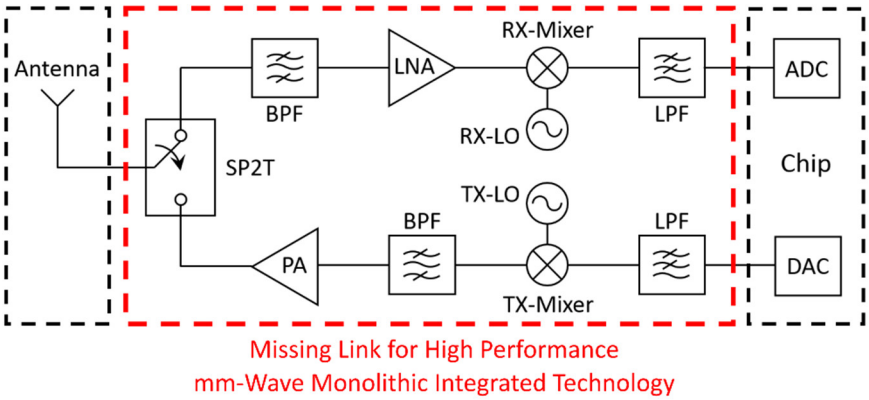

Fig. 7.1. Typical transceiver block diagram, with the box in red representing the missing link between antenna and chip for high performance mm-wave monolithic integrated technology.

In order to address this challenge, as discussed in Section 2.2, research into integrated waveguides have shown promising results, combining the benefits of RWGs such as low loss and high power handling with those of planar technology including improved integration and low cost. However, conventional PCB or machine-milling techniques no longer offer the miniaturized dimensions and cost-effective fabrication at mm-wave frequencies.

Fortunately, the use of microfabrication technology offers a variety of state-of-the-art fabrication processes for compete integration of high performance waveguides with IC directly at the wafer-level. Thus, a number of innovative techniques have been shown in the literature for the microfabrication of wafer-level integrated waveguides, including the incorporation of both bulk micromachining and hybrid techniques [41]–[45], and fabrication techniques including LIGA and EFAB [37]–[40]. In addition, methods employing low-cost photolithography for complete CMOS integration have created fully monolithic wafer-level structures with considerable performance. In [50], [60], dielectric-filled RWGs have produced attenuations of 0.2 dB/mm up to W-band using photoimageable pastes or thick

negative photoresists. Furthermore, by removing the sacrificial material used to build the structure, air-filled RWGs have shown attenuations as low as 0.1 dB/mm, while also allowing integration of MEMS tunable elements inside the channel for switching functionality [63], [64]. However, due to broadside widths of $\lambda/2$, these structures remain large for realistic IC integration.

The primary objective of this chapter is to reduce the footprint of monolithic wafer-level integrated microfabricated waveguides, while still providing high performance. To achieve this, the miniaturized integrated waveguide platforms developed in the previous chapters, including the ridged half-mode SIW (Chapter 3) and folded ridged half-mode SIW (Chapter 5) are applied to on-wafer monolithic waveguide structures. Using conventional CMOS microfabrication technology, along with sacrificial materials to build air-filled 3D structures, the first realization of a fully monolithic wafer-level air-filled miniaturized waveguide platform is presented. It is shown that by using such techniques, the footprint is reduced by up to 73%, paving the way for cost effective utilization of waveguides and their superior performance in mm-waves.

The chapter is organized as follows. First, in Section 7.1, half-mode waveguide (HMWG) technology is employed to reduce the footprint and maintain the performance of monolithic wafer-level RWGs. Next, the ridged half-mode waveguide (RHMWG) technology developed in Chapter 3 is investigated in Section 7.2 to miniaturize the footprint even further, while also improving the performance compared to HMWG due to lower radiation losses. In Section 7.3, the folded waveguide technique as developed in Chapter 5 is applied to RHMWG,

exploring the significant miniaturization potential of folded ridged half-mode waveguide (FRHMWG) technology on wafer. In each case, the first successful realization of a monolithic wafer-level air-filled miniaturized waveguide using either half-mode, ridged half-mode, or folded ridged half-mode waveguide technologies is presented. Final conclusions are summarized in Section 7.4.

7.1 Monolithic Half-Mode Waveguide

In this section, we propose to employ half-mode technology to reduce the footprint and maintain the performance of monolithic wafer-level RWGs, producing the first realization of a monolithic wafer-level air-filled half-mode waveguide. Utilizing a CMOS compatible fabrication process developed by the authors in [150], a half-mode waveguide prototype is designed and experimental results discussed. Compared to conventional waveguide, a 56% reduction in footprint is achieved, with only a small increase in attenuation loss. A study on the effect of sacrificial height with respect to miniaturization and performance is also discussed.

7.1.1 Principle of Operation

In Fig. 7.2, the cross-section and fundamental quasi-$TE_{0.5,0}$ mode electric field distribution of a monolithic wafer-level air-filled half-mode waveguide (HMWG) is compared to the $TE_{1,0}$ mode of a full-mode waveguide (FMWG). Due to a large width to height ratio, the field profile of the HMWG is equivalent to half the field of the FMWG ($W_{HM} = W_{FM}/2$), with an additional width Δw due to fringing fields at the open side [7]. The impact of Δw slightly increases the effective width of the

HMWG, decreasing cutoff frequency f_c. In Fig. 7.3, the HMWG phase constant is plotted with W_{HM} = 1.25 mm and heights h = 50, 75, and 100 µm, simulated in HFSS and extracted using the multiline method [102]. The phase constant of a FMWG with exactly twice the width of the HMWG is also plotted for comparison. It is noted that increased height yields an increase in miniaturization of the HMWG due to greater fringing fields, where f_c equals 56 GHz and 53 GHz at 50 µm and 100 µm, respectively, compared to a cutoff frequency of 60 GHz for the FMWG.

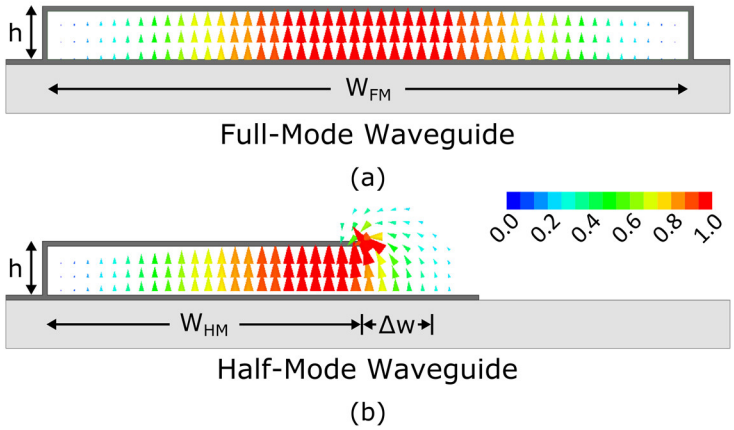

Fig. 7.2. Cross-sectional layouts and their respective fundamental mode normalized electric field distributions ($|E|/|E_{MAX}|$) of a monolithic (a) full-mode waveguide with $|E_{MAX}| = 6.2\times10^4$ V/m, and (b) half-mode waveguide with $|E_{MAX}| = 1.03\times10^5$ V/m.

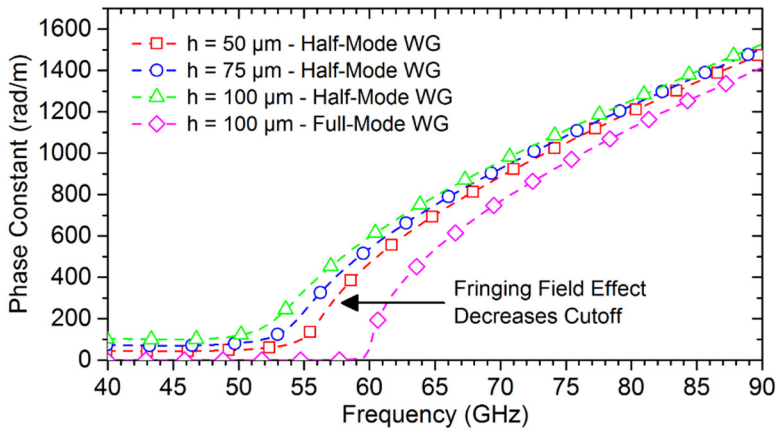

Fig. 7.3. Simulated extracted phase constant β of a monolithic HMWG with increasing channel height h. The phase constant of a FMWG with twice the width of the HMWG is also plotted for comparison.

While greater channel heights improve miniaturization, the drawback is increased radiation losses. In Fig. 7.4, the attenuation constant of the HMWG is plotted versus normalized frequency f/f_c for both radiation losses (σ = PEC) and total losses ($\sigma = 5.8\times10^7$) with increasing height. At $1.4 \times f_c$, the radiation and total losses for h = 50 µm equal 0.16 dB/mm and 0.20 dB/mm, respectively, while for h = 100 µm they equal 0.31 dB/mm and 0.33 dB/mm, respectively. Thus, as h increases, not only does radiation loss increase, but it also becomes a larger percentage of the total loss, from 80% to 94%, while conductor loss decreases from 20% to 6% of total loss. Therefore, the choice of channel height becomes a balance between radiation loss, conductor loss, and miniaturization. Regardless, at $1.45 \times f_c$ or greater, the total attenuation with height 100 µm is less than 0.29 dB/mm. Below $1.45 \times f_c$, the HMWG can be used for leaky-wave antenna applications [9].

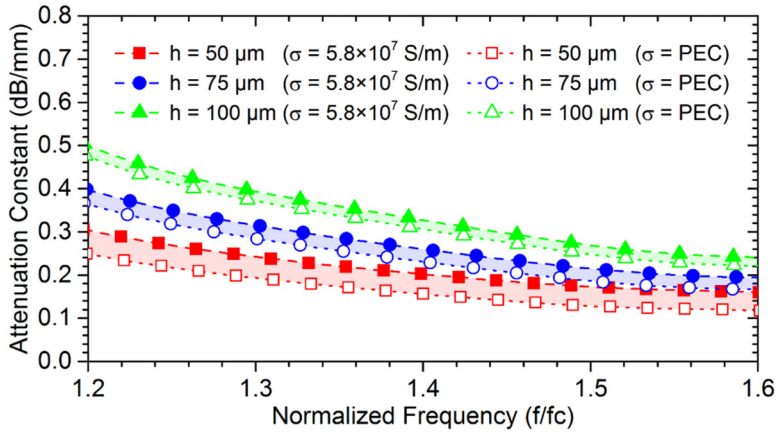

Fig. 7.4. Simulated extracted attenuation constant of the monolithic HMWG, showing both radiation losses (σ = PEC) and total losses ($\sigma = 5.8\times10^7$ S/m) with increasing channel height h.

In Fig. 7.5, the final design layout of a monolithic wafer-level air-filled HMWG is shown. A 50-Ω CPW-to-HMWG transition feeds the waveguide, following the design details provided in [64]. Thick positive photoresist AZ 40XT-11D is used

as a sacrificial material to build the structure, then removed to allow an air-filled channel, opening the possibility for integration of MEMS tunable elements [64].

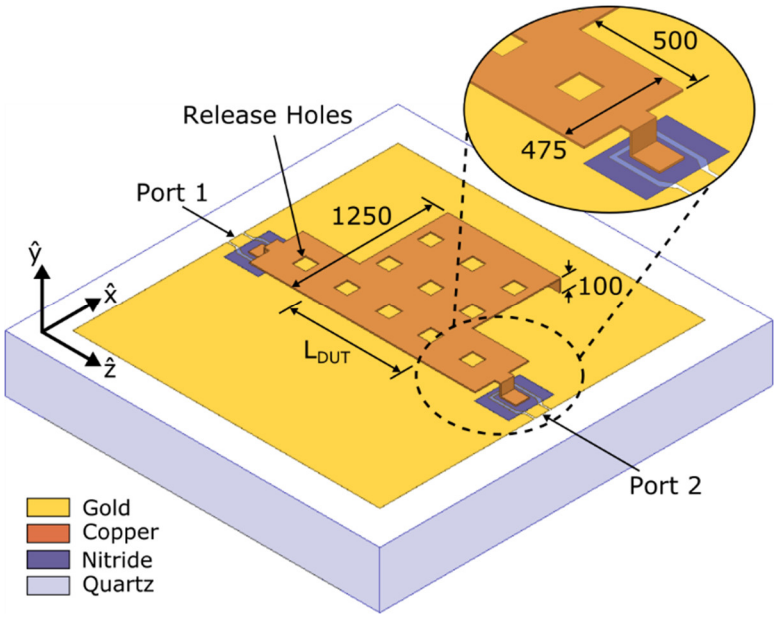

Fig. 7.5. Design layout of a monolithic wafer-level air-filled HMWG along with CPW-to-HMWG transition for probe characterization (dimensions in μm).

7.1.2 Microfabrication Process Flow

The process flow to fabricate the proposed monolithic wafer-level air-filled HMWG structure is shown in Fig. 7.6(a)-(j), based on the process flow for FMWG developed by the authors in [150] using standard CMOS fabrication technologies [151]. The fabrication begins with (a) deposition and patterning of metallization layer M1, 40/500 nm of Cr/Au sputtered on a Schott BOROFLOAT borosilicate wafer 1.1 mm thick [152], chosen due to its low coefficient of thermal expansion. However, the additive nature of the fabrication process means the design is independent of carrier substrate choice. Next, to protect small CPW features on M1, a 500 nm nitride film is deposited and patterned (b) using PECVD and RIE, respectively.

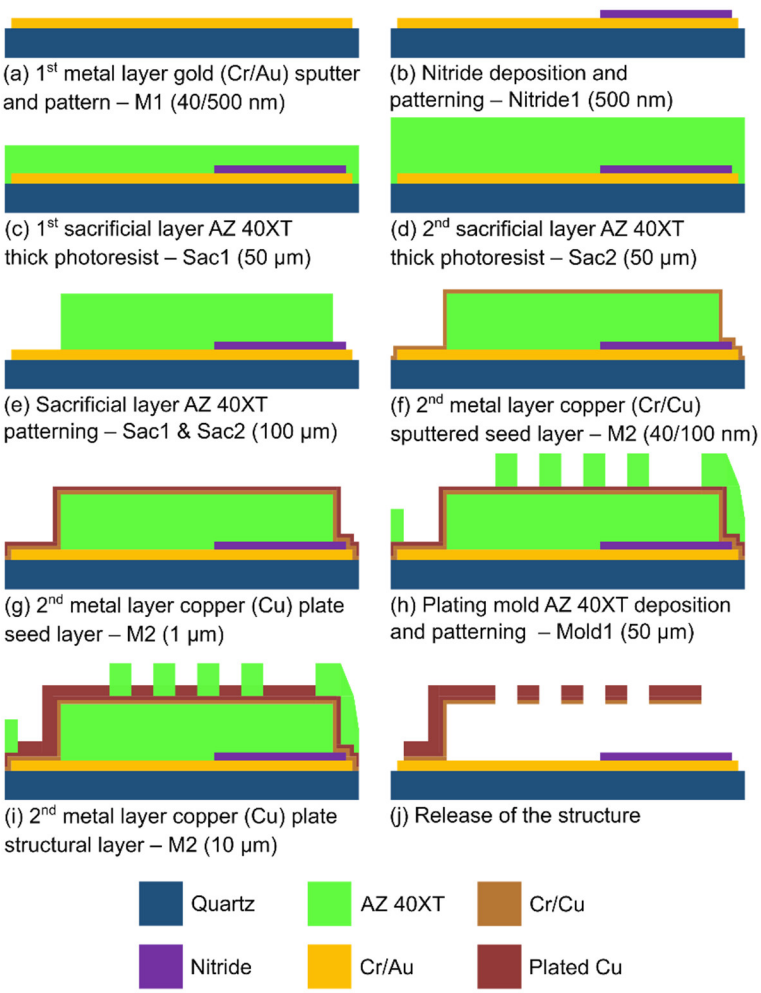

Fig. 7.6. Process flow for the microfabrication of a monolithic wafer-level air-filled HMWG.

The first and second sacrificial layers are then deposited (c)-(d), for a total channel height of 100 µm. Both layers are then patterned with the same exposure (e). MicroChemicals chemically amplified thick positive resist AZ 40XT-11D is chosen due to benefits including single dispenses from 20 to 60 µm thick, and simplified removal using standard wet chemical strippers [65]. While Fig. 7.4 shows improved attenuation with 50-µm total HMWG height, the AZ 40XT-11D is double coated to illustrate the flexibility of the microfabrication process to achieve various channel heights.

A 40/100 nm Cr/Cu film is then sputtered (f) as a copper electroplating seed layer for the top metallization layer M2. Copper is chosen due to its higher conductivity than gold, as well as lower cost. Copper is also used for backside CMOS interconnect layers [153]. To improve planarity during the subsequent plating mold bake, an additional 1 μm of low stress electroplated copper is deposited (g). A 50 μm thick electroplating mold using AZ 40XT-11D is then deposited, patterned, and hard-baked (h). Next, 10 μm of electroplated copper is deposited (i), thick enough to not require critical point drying upon release. Finally, the mold is stripped, the copper seed layer is etched, and the sacrificial layer is removed using a standard wet chemical stripper (j). Oxygen plasma ashing is used at the end to clean up any residual resist.

7.1.3 Measured Results and Discussion

In Fig. 7.7, the measurement setup for the fabricated monolithic wafer-level air-filled HMWG is shown. The device was characterized using an Agilent E83A61C PNA with N5260A Millimeter Head Controller, N5260-60003/60004 Test Head Modules, and Cascade Microtech Summit 11000 Probe Station. In Fig. 7.8 and Fig. 7.9, the measured scattering parameters are compared with simulation for the monolithic HMWG with device lengths L_{DUT} = 1.0 mm and 1.5 mm, respectively, with good agreement. For the 1.0 mm length HMWG, the insertion loss at 75 GHz is 1.08 dB. The poor return loss above 65 GHz is caused by Cascade |Z| Probes used in measurement. Furthermore, some underplating occurred in the region of the CPW-to-HMWG post transition. For the HMWG with length 1.5 mm, measured with Cascade Infinity Probes, the insertion loss at 90 GHz is 1.41 dB. The return

loss is greater than 10 dB above 75 GHz, with discrepancy between measured and simulated due to fabrication tolerances of the final AZ 40XT-11D thickness causing an issue with impedance matching. To de-embed transition losses, a back-to-back CPW-to-HMWG transition is simulated in HFSS, with 0.79 dB and 0.96 dB of insertion loss at 75 GHz and 90 GHz, respectively. Therefore, the measured HMWG is estimated to have an attenuation loss of 0.3 dB/mm.

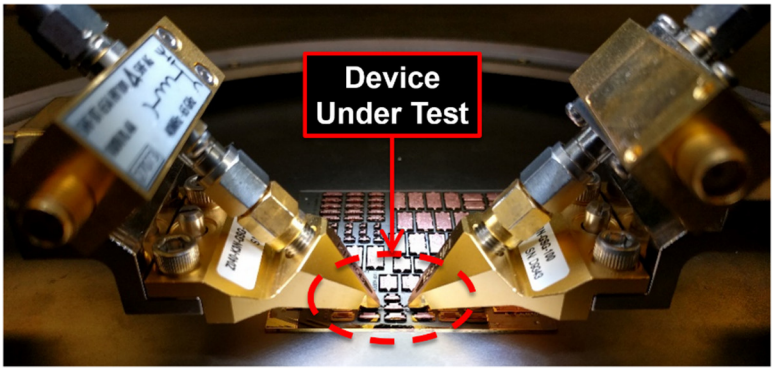

Fig. 7.7. Picture of the measurement setup with device under test (DUT).

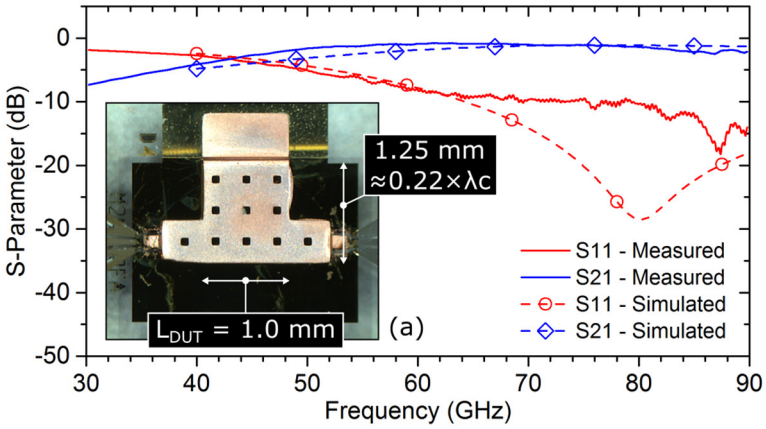

Fig. 7.8. Measured and simulated scattering parameters ($|S_{11}|$ and $|S_{21}|$), and inset (a) an optical microscope picture, of the fabricated monolithic HMWG with device length L_{DUT} = 1.0 mm and total width approximately 0.22 × λ_c.

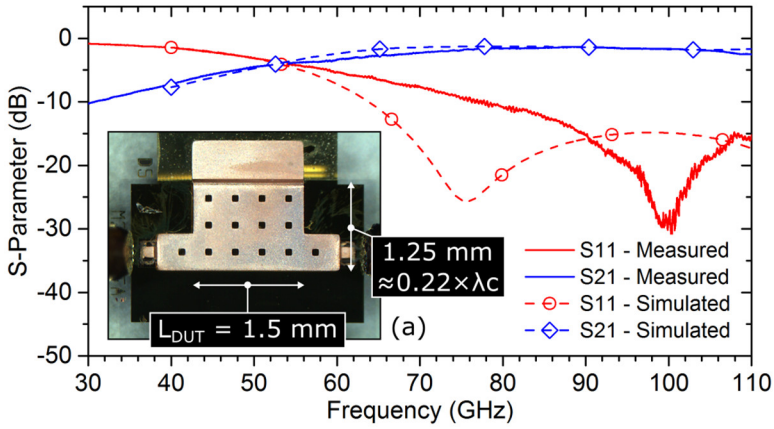

Fig. 7.9. Measured and simulated scattering parameters ($|S_{11}|$ and $|S_{21}|$), and inset (a) an optical microscope picture, of the HMWG with L_{DUT} = 1.5 mm.

Optical microscope pictures of the HMWG are shown in Fig. 7.8(a) and Fig. 7.9(a) for the two device lengths. The total width of the HMWG is 0.22 × λ_c, yielding a miniaturization of 56% compared to a full-mode waveguide with width 0.5 × λ_c. To highlight the open side of the HMWG, an angled view is presented in Fig. 7.10, where the freestanding structure is cleared of sacrificial AZ 40XT-11D photoresist.

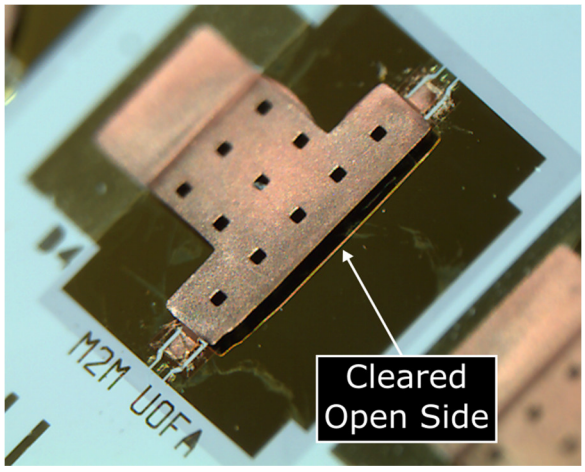

Fig. 7.10. Optical microscope picture with angled view of the fabricated monolithic HMWG with device length L_{DUT} = 1.0 mm, showing the open side.

In Table 7.1, the monolithic HMWG performance is compared with the literature. Only a small increase in attenuation compared to full-mode waveguides is noted, while achieving 56% reduction is size with respect to λ_c.

Waveguide Technology	f_c (GHz)	Permittivity ε_r	Width (mm)	Atten. in W-Band (dB/mm)	Ref.
Full-Mode	60	8	0.90 ($0.5\times\lambda_c$)	0.2	[50]
Full-Mode	57	Air-Filled	2.64 ($0.5\times\lambda_c$)	0.1-0.2	[64]
Half-Mode	52	Air-Filled	1.25 ($0.22\times\lambda_c$)	0.3	This Work

Table 7.1. Comparison of Monolithic Wafer-Level Waveguide Performance

7.2 Monolithic Ridged Half-Mode Waveguide

To further miniaturize the broadside width of monolithic wafer-level air-filled RWG, this section will investigate the use of ridged half-mode waveguide (RHMWG) technology at the wafer-level, previously developed for SIW-based structures in Chapter 3. An additional metallization layer will be incorporated within the microfabrication process flow developed for HMWG in Section 7.1, allowing for the creation of an embedded ridge structure located between two sacrificial layers. The measured results of a fabricated prototype will be presented, demonstrating the first realization of a monolithic wafer-level air-filled RHMWG.

7.2.1 Principle of Operation

In Fig. 7.11, the general layouts of a monolithic wafer-level air-filled (a) HMWG and (b) RHMWG are shown. By loading the open side of the HMWG with a capacitive ridge structure, the phase velocity of the fundamental quasi-$TE_{0.5,0}$

mode is reduced, further miniaturizing the broadside width of the RHMWG by approximately 50%. Using the transverse resonance technique presented in Section 3.1, the cutoff wavelength λ_c of the RHMWG structure is determined from (3.3), where W and Wr are the waveguide channel and ridge widths, respectively, h the total waveguide channel height, and g the ridge height.

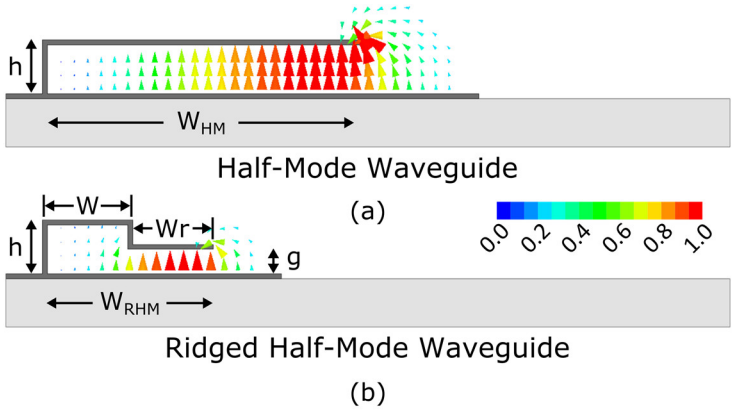

Fig. 7.11. General layout illustrating the size comparison and normalized electric field configuration ($|E|/|E_{MAX}|$) for the fundamental quasi-$TE_{0.5,0}$ mode of a monolithic wafer-level air-filled (a) HMWG with $|E_{MAX}| = 1.03\times10^5$ V/m, and (b) RHMWG with $|E_{MAX}| = 1.94\times10^5$ V/m.

Similar to the monolithic wafer-level air-filled HMWG presented in Section 7.1, two layers of thick positive photoresist AZ 40XT-11D are used as the sacrificial material to build the monolithic wafer-level air-filled RHMWG structure, with thicknesses ranging from 20 µm to 60 µm. Furthermore, as was discussed in Section 3.2, by decreasing the ridge height g while keeping $(h - g)$ constant, greater miniaturizations can be achieved. In Fig. 7.12, the phase constant β of the RHMWG is plotted with W = 505 µm and Wr = 475 µm while the ridge height g is varied from 20 µm to 50 µm, keeping $(h - g)$ = 50 µm constant. The phase constant of a HMWG with W_{HM} = 1.25 mm with g = 50 µm is also plotted for comparison. It can be seen that for the RHMWG, decreasing the ridge gap height (thickness of the first

AZ 40XT-11D sacrificial layer) lowers the cutoff frequency, providing greater miniaturization, where f_c equals 51.9 GHz and 43.1 GHz for g equal to 50 µm and 20 µm, respectively. This is opposite to the HMWG, where lower heights increase cutoff (see Section 7.1.1). Thus, with respect to λ_c, the RHMWG achieves 23.3% to 38.0% miniaturization compared to HMWG with g equal to 50 µm or 20 µm, respectively.

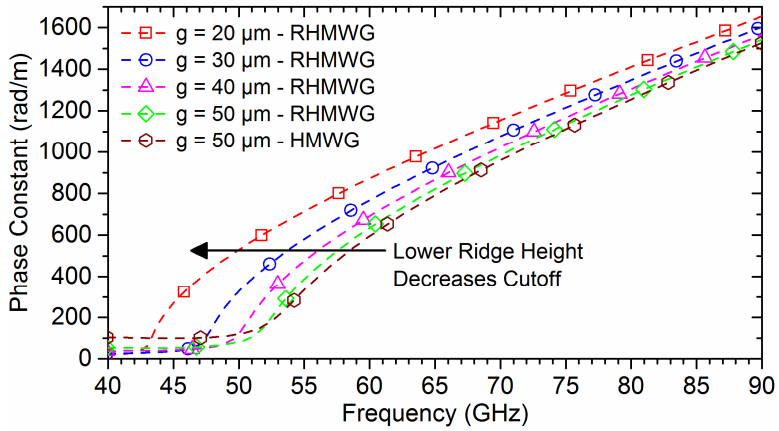

Fig. 7.12. Phase constant β of the monolithic RHMWG for various ridge heights g, simulated in HFSS and extracted using the multiline method [102]. The phase constant of an equivalent monolithic HMWG is also shown for comparison.

In Fig. 7.13, the simulated extracted attenuation constant α versus normalized cutoff frequency f/f_c of the monolithic wafer-level air-filled RHMWG is plotted for ridge heights g from 20 µm to 50 µm, separating radiation losses (all metals PEC) and total losses ($\sigma = 5.8\times10^7$). The results are summarized in Table 7.2. At a ridge height of 20 µm, the total loss is approximately half compared to a ridge height of 50 µm. Furthermore, as the ridge height is increased from 20 µm to 50 µm, the percentage of radiation loss compared to total loss increases from 62.5% to 96.8%, while for conductor loss it decreases from 37.5% to 3.23%. These results agree well with the attenuation analysis presented in Section 3.2 for RHMSIW structures.

However, it should be noted that due to the increased effect of surface roughness and lower overall conductivity of metals at mm-wave frequencies, the discrepancy between simulation and measurement will increase as the ridge height of the RHMWG is decreased [154], [155]. Thus, for the cases where more rigorous design and analysis is required, these effects must be incorporated during the simulation.

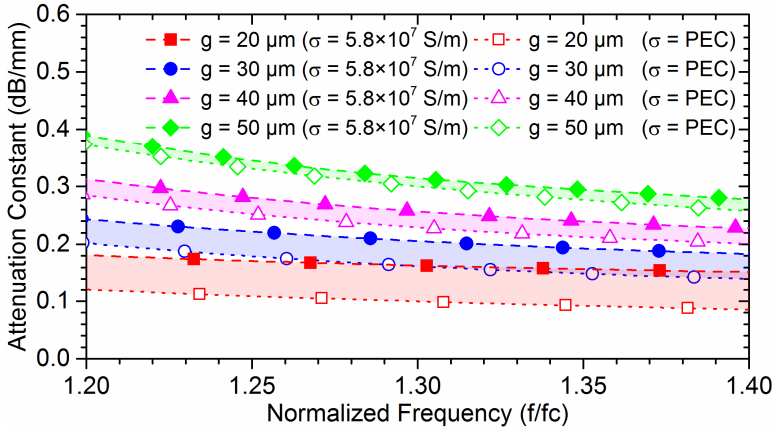

Fig. 7.13. Simulated extracted attenuation constant α of the monolithic RHMWG for various ridge heights g, comparing radiation losses (all metals PEC) and total losses ($\sigma = 5.8\times10^7$).

Ridge Gap Height g (μm)	f_c (GHz)	Total Losses @ 1.3×f_c (dB/mm)	Rad. Losses @ 1.3×f_c (dB/mm)	Cond. Losses @ 1.3×f_c (dB/mm)
20	43.1	0.16	0.10	0.06
30	47.5	0.21	0.16	0.05
40	50.1	0.26	0.23	0.03
50	51.9	0.31	0.30	0.01

Table 7.2. Monolithic RHMWG Performance for Various Ridge Gap Heights

In Fig. 7.14, the final design layout of the monolithic wafer-level air-filled RHMWG is shown. The RHMWG is designed for a cutoff frequency f_c = 52 GHz, with channel width of 505 μm and ridge width of 475 μm. A 50-Ω CPW-to-RHMWG transition feeds the waveguide similar to the HMWG in Section 7.1. Sacrificial material AZ 40XT-11D is used as a mechanical layer and then finally

removed, allowing for an air-filled waveguide channel. To reduce microfabrication complexity, the total height h is equal to twice the ridge height g, discussed further in the next section.

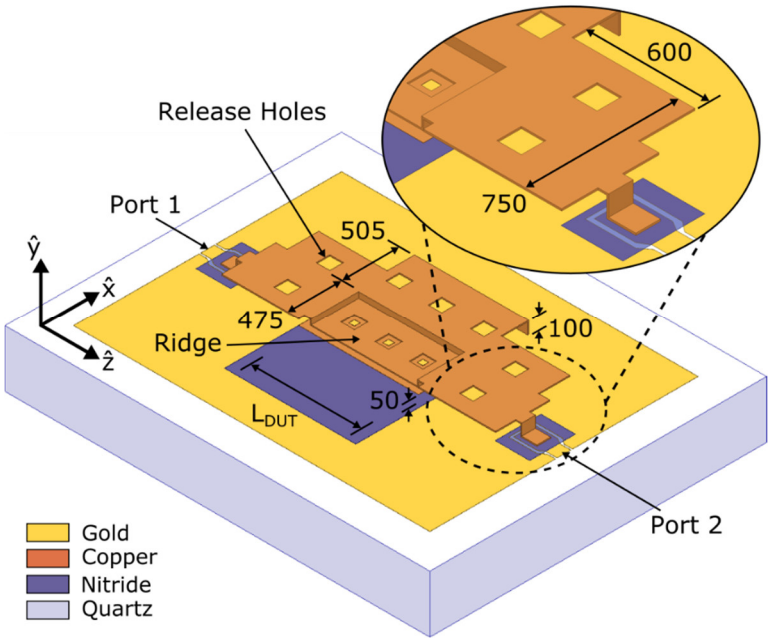

Fig. 7.14. Design layout of the monolithic wafer-level air-filled RHMWG along with CPW-to-RHMWG transition for probe characterization (dimensions in µm).

7.2.2 Microfabrication Process Flow

The microfabrication process flow for a monolithic wafer-level air-filled RHMWG is shown in Fig. 7.15, with fabrication steps (a) to (k). Details regarding steps (a) through (c), and (f) through (k), are provided in Section 7.1.2 and follow the same procedure for monolithic wafer-level air-filled HMWG. For the RHMWG design layout in Fig. 7.14, in order to create the capacitive ridge structure, an additional metallization layer is deposited between two sacrificial layers. Following the deposition of the first sacrificial layer of AZ 40XT-11D with a thickness of 50 µm (c), the embedded middle conductor M2 is deposited, plated, and patterned in

(d) and (e). First, a 25/30 nm Cr/Cu film is sputtered as an electroplating seed layer. Then, the wafer is placed in an acid copper plating bath for 20 minutes at a current density of 4 mA/cm^2 to deposit approximately 1.5 μm of copper. Due to its lower residual stress, plated copper allows for a more rigid and stable structure during the subsequent thermal processes. The embedded metallization layer M2 is then patterned using standard lithography processes [151]. Another sacrificial layer of AZ 40XT-11D is then deposited to a thickness of 50 μm and patterned (f). Both sacrificial layers are patterned at the same time to help reduce alignment errors, for a total height of 100 μm in the main waveguide channel, and 50-μm height underneath the ridge, where the embedded metallization layer M2 acts as a mask for the first sacrificial layer located below during UV exposure. While in Section 7.2.1 it was shown that improved miniaturization and lower attenuation loss of the RHMWG is achieved with a smaller ridge height, i.e. depositing a thinner sacrificial layer in step (c), to reduce fabrication complexity, the two sacrificial layers were deposited with the same thickness. This helped speed up prototyping by keeping the same process parameters of the AZ 40XT-11D for each deposition, including the plating mold in (i).

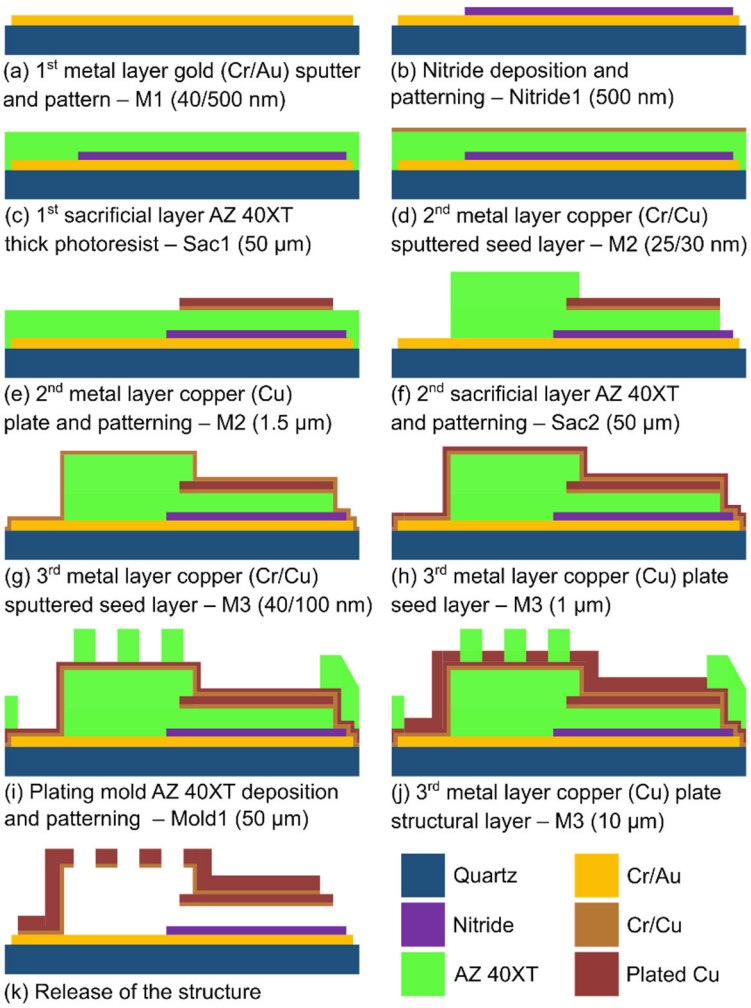

Fig. 7.15. Process flow for the microfabrication of a monolithic wafer-level air-filled RHMWG.

Finally, the electroplating mold is stripped away, the Cr/Cu seed layer is etched, and the structure is released using standard wet photoresist strippers (k). Due to the 10-µm thickness of the electroplated copper, the effects of stiction were eliminated; therefore, no critical point drying was required.

7.2.3 Measured Results and Discussion

In Fig. 7.16 a microscope picture of the fabricated monolithic wafer-level air-filled RHMWG is shown, where Cascade Infinity Probes and a CPW-to-RHMWG

transition feeding the waveguide from the top 100-µm height are used for on-wafer characterization. With a total width of 980 µm (0.17 × λ_c), the RHMWG achieves a broadside miniaturization (with respect to cutoff wavelength λ_c) of 23% compared to the measured HMWG presented in Section 7.1.3. Furthermore, compared to a standard RWG with a width equal to 0.5 × λ_c, the RHMWG achieves a broadside miniaturization of 66%.

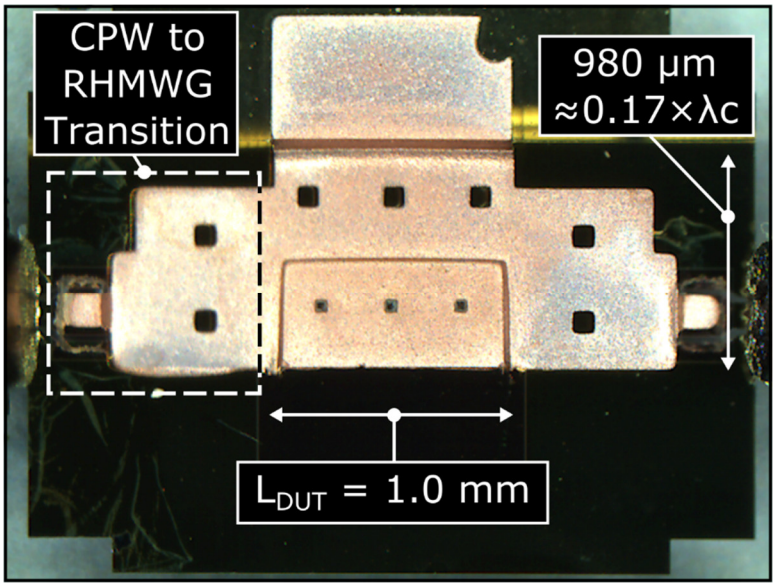

Fig. 7.16. Optical microscope picture of the fabricated monolithic wafer-level air-filled RHMWG, with probe fed CPW-to-RHMWG transition.

The measured scattering parameters are compared with simulation in Fig. 7.17, with good agreement. The measured return loss is greater than 15 dB from 54 GHz to 85 GHz. The discrepancy between simulated and measured return loss is likely due to geometrical differences between the simulated model and the final fabricated structure; for example, minor copper underplating in the leftmost CPW-to-RHMWG transition is noticed in Fig. 7.16. At a frequency of 75 GHz, the measured insertion loss is 0.77 dB, including transitions. Compared to the measured insertion

loss of the HMWG in Section 7.1.3, a 0.33 dB improvement in insertion loss is achieved.

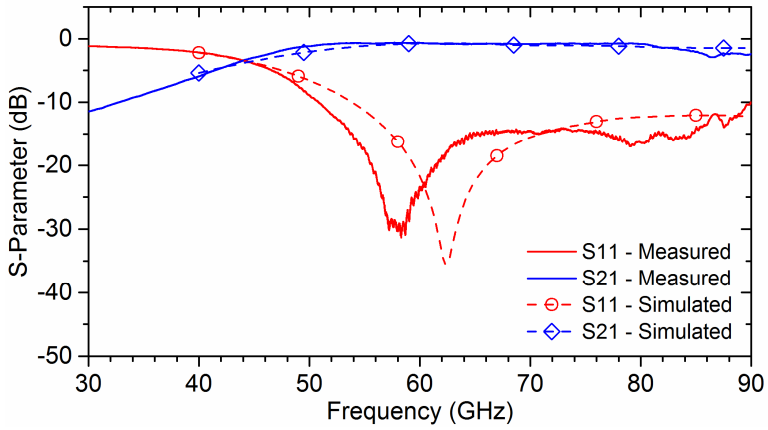

Fig. 7.17. Measured and simulated scattering parameters of the monolithic RHMWG.

In Fig. 7.18(a), an optical microscope picture showing an angled view of the fabricated monolithic RHMWG is shown, along with a close-up of the capacitive ridge structure in Fig. 7.18(b). The removal of the sacrificial AZ 40XT-11D photoresist beneath the ridge is clearly illustrated. With such a drastic decrease in footprint, the RHMWG offeres the possibilities of increased signal routing for high density interconnects.

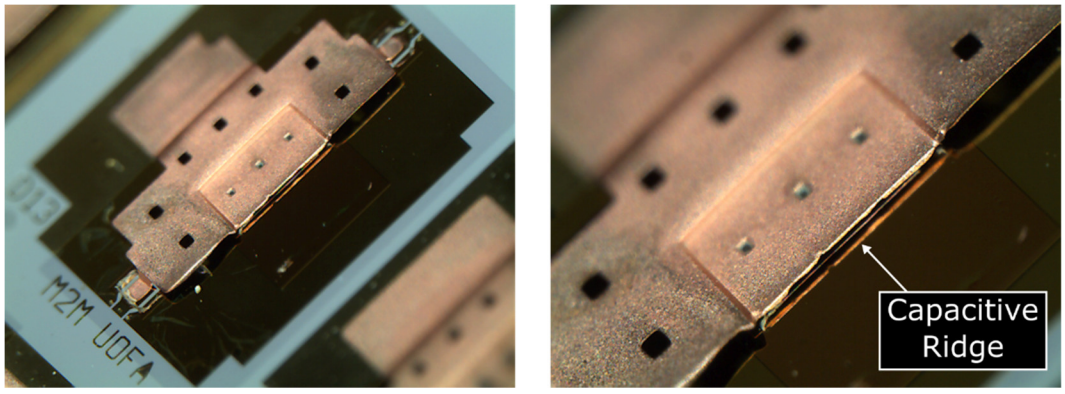

(a) (b)

Fig. 7.18. (a) Optical microscope picture with angled view of the fabricated monolithic RHMWG with device length L_{DUT} = 1.0 mm, with (b) close-up of the capacitive ridge clear of photoresist.

7.3 Monolithic Folded Ridged Half-Mode Waveguide

This section will now investigate the use of folded waveguide techniques combined with ridged half-mode technology, as described in Chapter 5, for even greater miniaturization of the transverse width of monolithic wafer-level air-filled waveguides. The measured results of two fabricated prototypes are presented, demonstrating the first realization of a monolithic wafer-level air-filled folded ridged half-mode waveguide (FRHMWG), while achieving miniaturizations of 72.8% compared to standard RWG.

7.3.1 Principle of Operation

In Fig. 7.19, the general layout and electric field distribution of the fundamental quasi-$TE_{0.5,0}$ mode for a monolithic wafer-level air-filled (a) RHMWG and (b) FRHMWG are shown. As described in Section 5.1 for SIW-based structures, the FRHMWG is created by essentially moving the ridge of the RHMWG inside the waveguide channel. The fundamental quasi-$TE_{0.5,0}$ mode then becomes folded around the ridge structure, realizing an additional miniaturization up to

approximately 50%, depending on chosen design parameters. The transverse resonance technique developed in Section 5.1 is used to calculate the fundamental mode cutoff frequency λ_c by applying (5.2), where W_{FRHM} is the waveguide channel width, Wr the ridge width, x the distance between the edge of the ridge and the sidewall, and h and g the total waveguide height and ridge height, respectively.

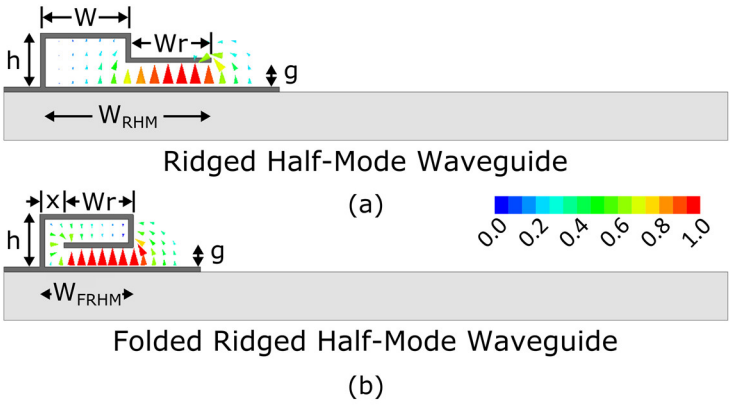

Fig. 7.19. Cross-sectional layouts and their respective fundamental quasi-$TE_{0.5,0}$ mode normalized electric field distributions ($|E|/|E_{MAX}|$) of a monolithic (a) ridged half-mode waveguide with $|E_{MAX}| = 1.94\times10^5$ V/m, and (b) folded ridged half-mode waveguide with $|E_{MAX}| = 2.30\times10^5$ V/m.

In Fig. 7.20, the corresponding phase constant of a FRHMWG with cutoff frequency f_c = 60 GHz is shown, with dimensions W_{FRHM} = 590 µm, Wr = 520 µm, h = 100 µm, and g = 50 µm, simulated in HFSS and extracted using the multiline method [102]. The phase constant of a RHMWG with similar cutoff frequency is also plotted for comparison, with a similar dispersion relation between the two structures, as expected from the analysis performed in Section 5.3. However, the FRHMWG achieves an additional 34% miniaturization.

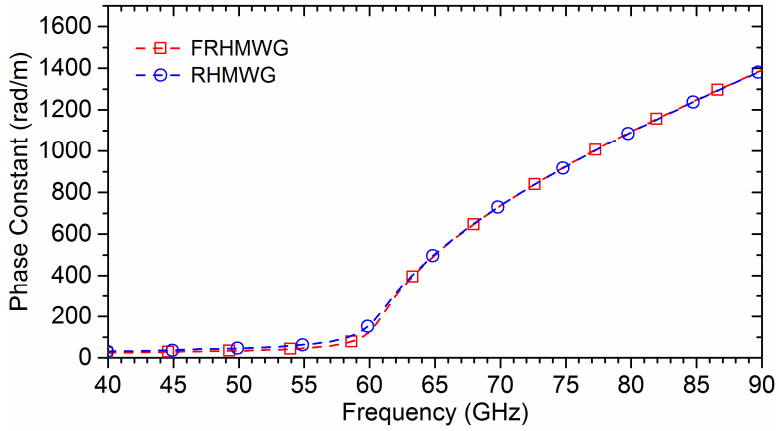

Fig. 7.20. Simulated extracted phase constant β of a monolithic FHMWG compared to a monolithic RHMWG with equivalent cutoff frequency.

In Fig. 7.21, the final design layout of a monolithic wafer-level air-filled FRHMWG is shown, where an exploded view of the main channel is used to illustrate the embedded ridge inside. Similar to the RHMWG in Section 7.2, two 50-µm thick sacrificial layers of AZ 40XT-11D are used to build the waveguide, and then removed to allow a freestanding air-filled structure. The FRHMWG is designed for a cutoff frequency f_c of 60 GHz, where the ridge-to-sidewall gap x and ridge width Wr are equal to 70 µm and 610 µm, respectively, for a total width of 680 µm. Instead of feeding the top metallization layer, similar to the RHMWG in Section 7.2, the CPW-to-FRHMWG transition feeds directly to the ridge in the middle metallization layer.

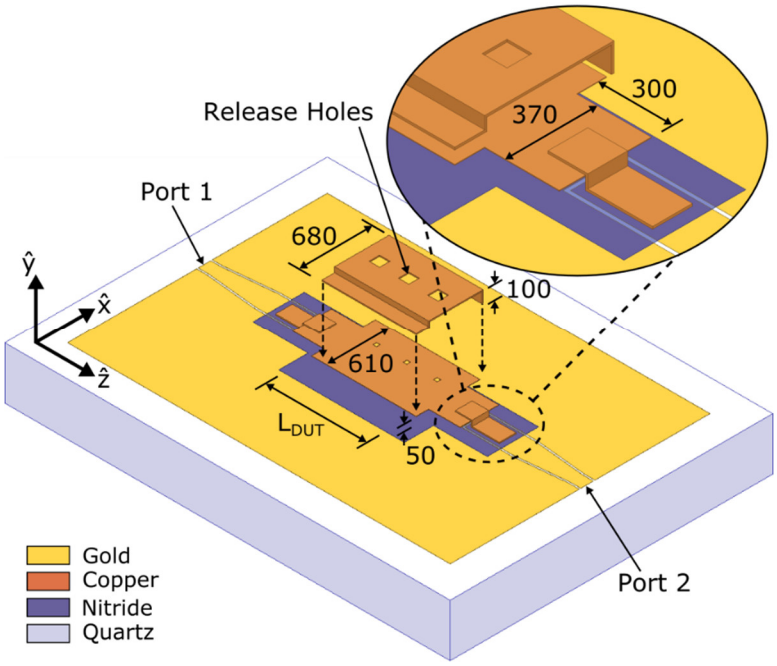

Fig. 7.21. Exploded design layout of a monolithic wafer-level air-filled FRHMWG along with CPW-to-FRHMWG transition for probe characterization (dimensions in μm).

7.3.2 Microfabrication Process Flow

The microfabrication process flow for a monolithic wafer-level air-filled FRHMWG is shown in Fig. 7.22, with fabrication steps (a) to (m). Based on the process flow for RHMWG presented in Section 7.2.2, the location of the ridge is now moved underneath the waveguide channel. Furthermore, two additional steps (i) and (k) are added to improve device yield, discussed in the paragraph to follow. Details for steps (a) through (c) are provided in Section 7.1.2, while details for steps (d) through (h) and (j), (l), and (m) are provided in Section 7.2.2. In addition, a comprehensive description of the final microfabrication process flow for the fabrication of miniaturized monolithic wafer-level air-filled waveguide structures is provided in Appendix A.

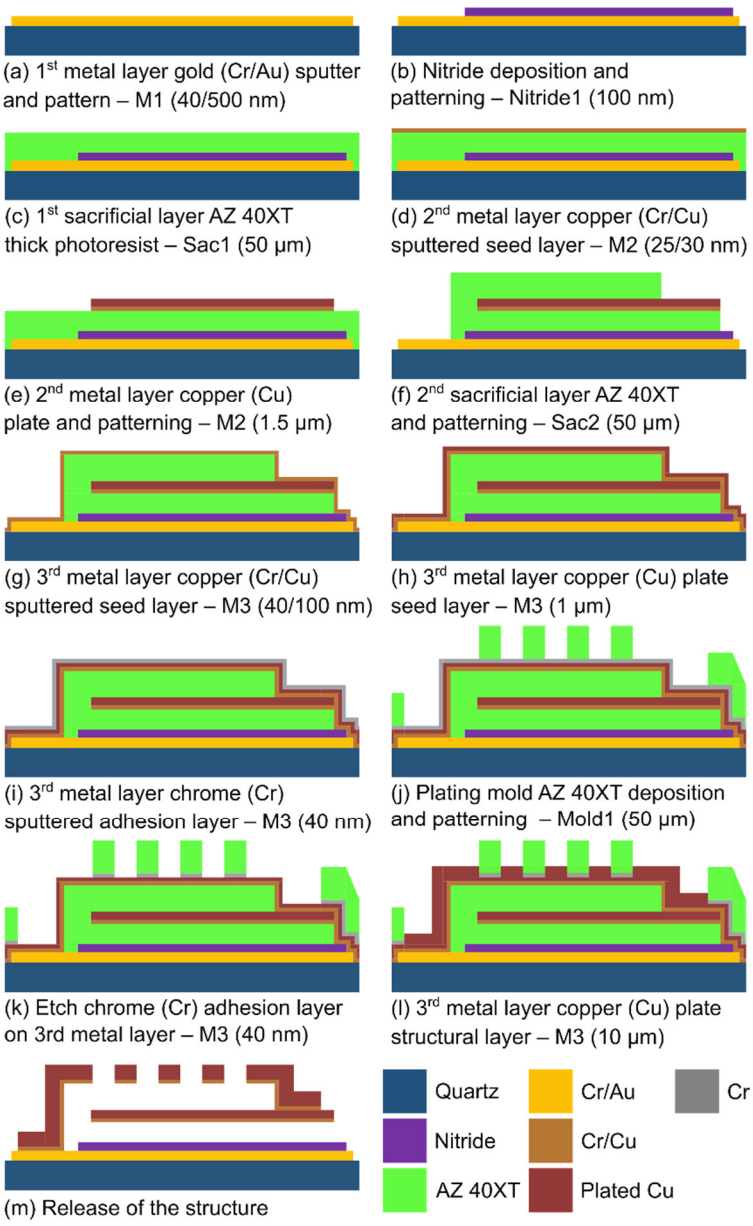

Fig. 7.22. Process flow for the microfabrication of a monolithic wafer-level air-filled FRHMWG.

A recurring fabrication problem significantly reducing device yield for both the previous HMWG and RHMWG processes was underplating during step (j) of Fig. 7.15; electroplating of the top metallization layer M3. As illustrated in Fig. 7.23 for a fabricated RHMWG sample using the process flow described in Section 7.2.2, underplating occurs when metal deposits underneath the photoresist used as the

electroplating mold. Due to poor adhesion between the resist and seed layer, the affected feature is essentially washed out, causing the electromagnetic behaviour of the fabricated sample to no longer perform as designed. To address this problem, in step (i) an additional chrome adhesion layer 40-nm thick is sputtered on top of the electroplated copper seed layer of step (h) [156]. The chrome is then etched in step (k) after patterning the electroplating mold. This allows the copper seed layer to be exposed for subsequent electroplating, while improving adhesion of the mold photoresist to the structure. A significant reduction in the amount of underplating was achieved, as evident in the measured device pictures of FRHMWG structures in the following section.

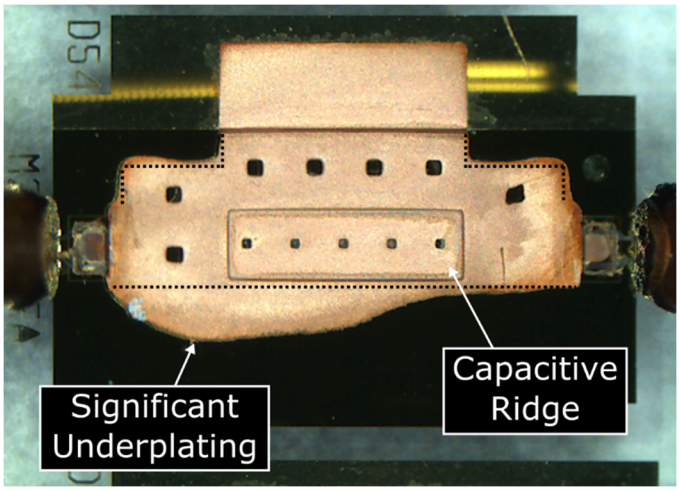

Fig. 7.23. Optical microscope picture of a monolithic RHMWG with significant underplating. The dotted lines represent the desired feature dimensions as patterned in the electroplating mold.

7.3.3 Measured Results and Discussion

In Fig. 7.24, optical microscope pictures of two fabricated monolithic wafer-level air-filled FRHMWG prototypes with device lengths L_{DUT} = 1.0 mm and L_{DUT} = 1.5 mm are shown. Cascade Infinity Probes were used to measure the samples.

The total width of both prototypes is 680 μm, or 0.14 × λ_c with respect to cutoff wavelength λ_c. Compared to the measured RHMWG in Section 7.2.3, the measured FRHMWG achieves an additional broadside miniaturization of 19.9%, while compared to standard RWG with width equal to 0.5 × λ_c, the FRHMWG achieves 72.8% miniaturization.

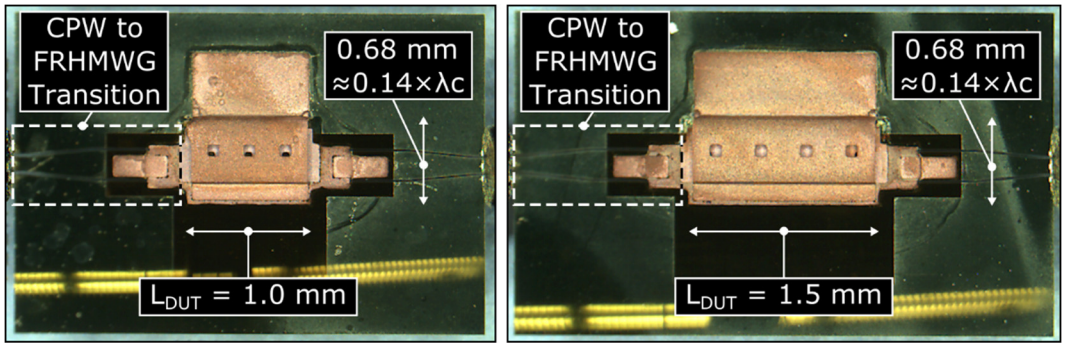

(a) (b)

Fig. 7.24. Optical microscope pictures of a fabricated monolithic wafer-level air-filled FRHMWG including CPW-to-FRHMWG transition, with device lengths (a) L_{DUT} = 1.0 mm and (b) L_{DUT} = 1.5 mm, and total width approximately 0.14 × λ_c.

The measured scattering parameters, including CPW-to-FRHMWG transitions, for the FRHMWG prototypes with L_{DUT} = 1.0 mm and L_{DUT} = 1.5 mm are compared to simulation in Fig. 7.25 and Fig. 7.26, respectively, both showing good agreement. For the first prototype with L_{DUT} = 1.0, the measured return loss is above 10 dB from 67.5 GHz up to 110 GHz. At a frequency of 75 GHz, the measured insertion loss is 2.44 dB, while at 90 GHz, the measured insertion loss is 2.01 dB. For the second prototype with L_{DUT} = 1.5 mm, the measured return loss is above 10 dB from 70 GHz to 110 GHz, and above 15 dB from 79 GHz to 110 GHz. The measured insertion loss at a frequency of 75 GHz is 2.68 dB, while at a frequency of 90 GHz the measured insertion loss is 2.21 dB.

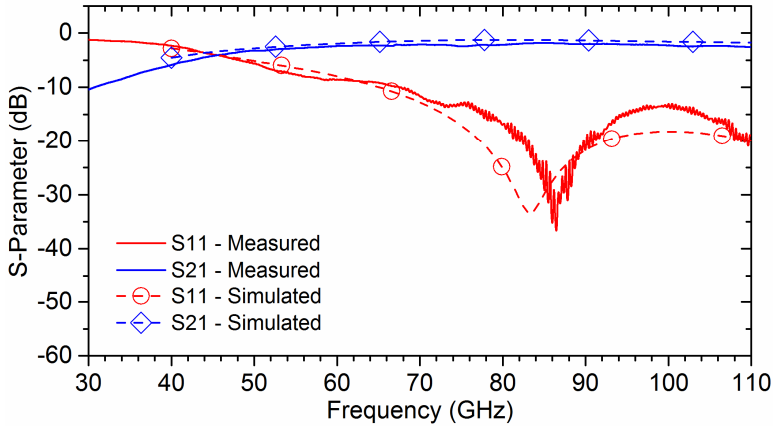

Fig. 7.25. Measured and simulated scattering parameters ($|S_{11}|$ and $|S_{21}|$) of the fabricated monolithic FRHMWG with device length L_{DUT} = 1.0 mm.

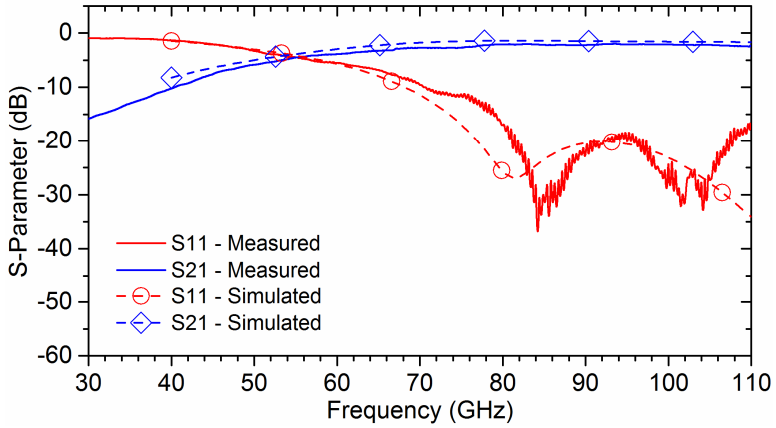

Fig. 7.26. Measured and simulated scattering parameters ($|S_{11}|$ and $|S_{21}|$) of the fabricated monolithic FRHMWG with device length L_{DUT} = 1.5 mm.

The high insertion loss of the measured prototypes is likely due to the CPW-to-FRHMWG feed structure. The longer length (approximately 1.0 mm) of CPW transmission line used to feed the FRHMWG structure increases loss. In Fig. 7.27, the measured scattering parameters and microscope picture of a 1.0 mm long 50-Ω CPW line fabricated on the same wafer and with the same cross-sectional dimensions used to feed the FRHMWG are shown. At a frequency of 75 GHz, the insertion loss of the CPW trace is 0.69 dB, while at 90 GHz, the insertion loss is

1.04 dB. Thus, a significant amount of attenuation in the measured FRHMWG prototypes likely occurs in the CPW line of their feed networks.

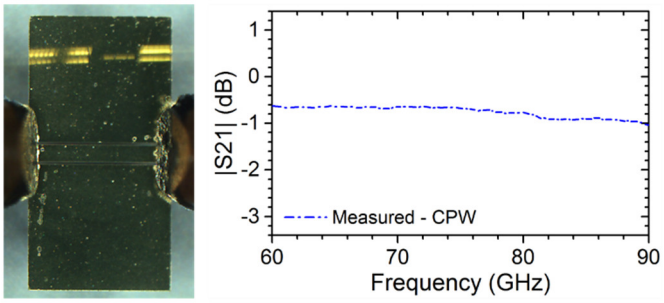

(a) (b)

Fig. 7.27. (a) Optical microscope image and (b) measured $|S_{21}|$ of a CPW line with length 1.0 mm.

In Fig. 7.28(a), an angled optical microscope picture of the fabricated FRHMWG with device length L_{DUT} = 1.5 mm is shown. A close-up in Fig. 7.28(b) of the ridge structure now inside the main waveguide channel shows the open side cleared of sacrificial photoresist and no sections of the ridge shorting to ground. Furthermore, the amount of underplating is reduced, with sharp features along the edges of the fabricated sample, an improvement over the structures presented in Sections 7.1.3 and 7.2.3. In Fig. 7.29(a), a field-emission scanning electron microscope (FESEM) image of the fabricated FRHMWG with device length L_{DUT} = 1.5 mm is shown. A close-up of the CPW-to-FRHMWG transition from the bottom metallization M1 to the middle metallization M2 is shown in Fig. 7.29(b), feeding the ridge structure directly. Finally, in Fig. 7.29(c), a close-up of the embedded ridge inside the main waveguide channel is shown, along with the 100 μm main sidewall.

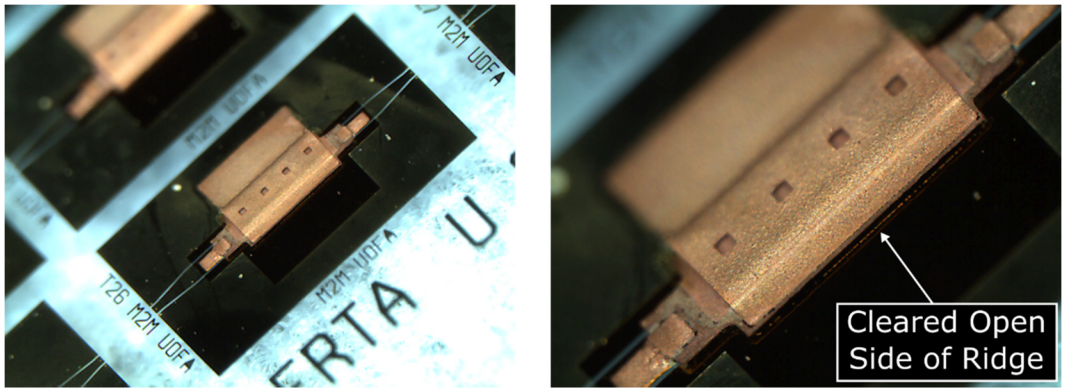

(a) (b)

Fig. 7.28. (a) Optical microscope picture with angled view of the fabricated monolithic FRHMWG with device length L_{DUT} = 1.5 mm, with (b) close-up of the open side of the ridge clear of photoresist.

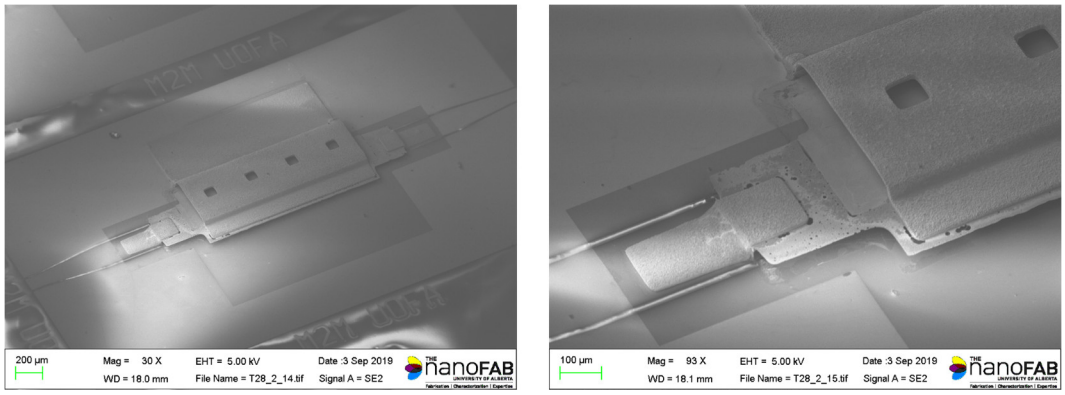

(a) (b)

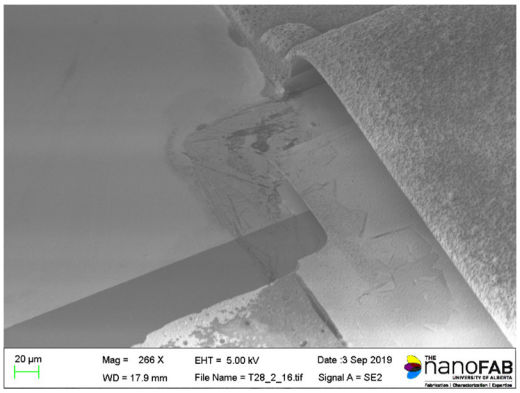

(c)

Fig. 7.29. Field-emission scanning electron microscope images of (a) the fabricated monolithic FRHMWG, (b) a close-up of the CPW-to-FRHMWG transition from the bottom metallization M1 to the middle metallization M2 (feeding the ridge directly), and (c) a close-up of the embedded ridge and 100 µm sidewall.

7.4 Summary

In this chapter, the first realizations of miniaturized monolithic wafer-level air-filled waveguides for operation at mm-wave frequencies in W-band have been presented. Utilizing half-mode, ridged half-mode, and folded ridged half-mode waveguide techniques, broadside miniaturizations of 56%, 66%, and 73% compared to standard rectangular waveguide have been demonstrated, respectively. A low-cost, flexible, and CMOS compatible fabrication process was developed, allowing for a variety of waveguide channel heights and device configurations for a wide range of performance and miniaturization levels. Furthermore, the proposed fabrication process is independent of carrier substrate choice, and therefore can be applied in many types of semiconductor technologies including silicon, gallium arsenide, and gallium nitride. The results presented in this chapter highlight the significant potential of monolithic wafer-level air-filled waveguides for low-loss mm-wave interconnects, bridging the gap between chip and antenna of RF front ends for future 5G mobile communication systems.

Chapter 8

Conclusions and Future Considerations

8.1 Summary

The main goal of this thesis was to introduce a new design platform for the miniaturization of integrated waveguides for 5G wireless communication and sensing. To accomplish this goal, two new types of miniaturized integrated waveguides were introduced, and their uses in a variety of 5G technologies including high density interconnects, hybrid couplers, reconfigurable bandpass and bandstop filters, and passive non-contact sensors were explored.

First, in Chapters 3 and 4, the development of a miniaturized integrated waveguide structure by combining ridged and half-mode SIW technology was presented, reducing the $\lambda/2$ transverse width of standard SIW by 75%. Applications of the proposed ridged half-mode SIW (RHMSIW) technology were then investigated, including couplers, filters, and microwave sensors, each exhibiting significant miniaturization compared to their counter parts in the literature.

By applying folded waveguide techniques to the proposed RHMSIW, even greater miniaturization of the transverse width of SIW (up to 88%) was presented in Chapters 5 and 6. The proposed folded ridged half-mode SIW (FRHMSIW) was then applied to quarter-mode SIW (QMSIW) cavity resonator design, achieving transverse widths of approximately $\lambda/16$, and miniaturizations of 98% compared to standard SIW cavity area. Applications of the folded ridged quarter-mode SIW

(FRQMSIW) in both tunable and reconfigurable bandpass and bandstop filters were then presented.

Finally, in Chapter 7, the potential of ridged half-mode and folded ridged half-mode technologies were applied to the realization of the first miniaturized fully monolithic wafer-level air-filled integrated waveguide platform.

8.2 Thesis Contributions

The list of original accomplishments described in this thesis can be summarized as the following:

- The design, fabrication, and characterization of a miniaturized ridged half-mode SIW is presented. The full analytical calculation of the fundamental mode cutoff frequency is described, where compared to standard SIW, the proposed ridged half-mode SIW allows for miniaturizations up to 75% or greater. Fabricated prototypes of the ridged half-mode SIW are compared to half-mode SIW, with their respective complex propagation constants extracted for analysis of the tradeoff between radiation and conductor loss. A reduction in insertion loss of the ridged half-mode SIW up to 1.45 times the cutoff frequency is shown, with a total width approximately 0.45 times the width of half-mode SIW. The near-field radiation patterns of ridged half-mode SIW and half-mode SIW are measured, clearly illustrating a reduction in radiation loss of the ridged half-mode SIW.
- High density interconnection using ridged half-mode SIW is demonstrated. The measured isolation between two parallel ridged half-mode SIWs in

three different orientations are compared to half-mode SIW. From the experimental results, the capacitive ridge of the ridged half-mode SIW is shown to reduce the cross-talk between neighboring waveguides by up to 10 dB, depending upon the configuration. With an already reduced footprint, the greater isolation of ridged half-mode SIW make it an enabling technology for miniaturized microwave components requiring high density signal routing.

- A miniaturized Riblet short-slot hybrid coupler using ridged half-mode SIW technology is designed, fabricated, and measured. A miniaturization of 60% is achieved compared to a similar hybrid coupler using standard SIW, while maintaining equivalent performance.
- The significant miniaturization potential of ridged half-mode SIW in slotted bandpass filter design is demonstrated. Two and four-pole slotted ridged half-mode SIW bandpass filters are designed and fabricated. The filter prototypes operate at 5.1 and 5.5 GHz, with total widths as small as 5.2 mm, measured insertion losses of 0.8 dB, and stopbands larger than 8 GHz. Compared to previously published slotted bandpass filters in the literature, the presented ridged half-mode SIW structures simultaneously achieve smaller footprints, lower insertion losses, and larger stopbands.
- The first realization of a ridged quarter-mode SIW humidity sensor is developed. The use of the ridged half-mode technique combined with quarter-mode SIW cavity for the miniaturization of passive non-contact SIW-based sensors to detect changes in relative humidity from 0% to 80%

is demonstrated. Miniaturizations up to 86.2% are reported, while also achieving up to four times more humidity sensitivity than previously reported, opening new possibilities and applications for sensor design. Furthermore, the first ridged quarter-mode SIW cavity resonator is presented, improving both quality factor and reducing the footprint of previously reported quarter-mode SIW structures in the literature.

- The design, fabrication, and characterization of a miniaturized folded ridged half-mode SIW is presented. Utilizing folded waveguide techniques, further reduction in the transverse width of the ridged half-mode SIW platform is achieved by moving the ridge inside the main waveguide channel, effectively folding the fundamental mode around the ridge structure. The proposed folded ridged half-mode SIW demonstrates an additional 50% reduction in transverse width compared to ridged half-mode SIW, and a total miniaturization of 88% compared to standard SIW. A full analytical calculation of the fundamental mode cutoff frequency is developed, including additional capacitance due to ridge edge to sidewall proximity. The monomode bandwidths of folded ridged half-mode SIW and ridged half-mode SIW are studied, showing fundamental to second-order mode ratios of 1:4.28 or greater for all cases, and approximately twice the monomode bandwidth compared with half-mode SIW. Fabricated prototypes of the folded ridged half-mode SIW are compared with ridged half-mode SIW, and their respective phase and attenuation constants are extracted to confirm equivalent propagation characteristics, while the

folded ridged half-mode SIW provides an additional 37.4% in broadside miniaturization.

- The first realization of a folded ridged quarter-mode SIW bandpass filter is demonstrated. The characterization of folded ridged half-mode SIW and folded ridged quarter-mode SIW cavity resonators are presented, resulting in miniaturizations compared to standard SIW cavity area equal to 96.6% and 98.0%, respectively. Two different folded ridge quarter-mode SIW bandpass filter prototypes are measured, and a study of quality factor versus substrate thickness is performed, where an improvement in quality factor of 26.1% without any significant change to the cavity's resonance frequency is shown.
- Tunable bandpass filters using packaged RF MEMS SP4T switches and folded ridged quarter-mode SIW cavity are designed, fabricated, and measured. An analytic expression for the calculation of a reactively-loaded folded ridged quarter-mode SIW cavity's resonance frequency is developed. Two fabricated prototypes with inductive and capacitive loadings are measured, with 70.3% and 78.8% reductions in total filter area, respectively, compared to similar SIW-based structures in the literature.
- A reconfigurable dual-band bandstop filter using folded ridged quarter-mode SIW cavity is developed. Nonresonating nodes are employed for independent tuning of individual stopbands. With equivalent performance, the fabricated prototype provides 58% miniaturization in total filter area

compared to an analogous dual-band microstrip bandstop filter as presented in the literature.

- The first realization of a miniaturized monolithic wafer-level air-filled integrated waveguide platform for 5G communication systems operating at mm-wave frequencies up to W-band is presented. Using half-mode, ridged half-mode, and folded ridged half-mode waveguides technologies, fabricated and measured broadside miniaturizations compared to standard rectangular waveguide of 56%, 66%, and 73% are achieved. A flexible and low-cost CMOS compatible microfabrication process is developed, where a variety of integrated waveguide technologies can be manufactured with an array of performance and miniaturization potentials.

In conclusion, the work of this thesis has pushed the envelope of possibility for the miniaturization of integrated waveguides in both substrate integrated form and on wafer. The introduction and characterization of a new type of miniaturized design platform has been presented, and its applications ranging from microwave to mm-wave frequencies have been explored, achieving some of the largest miniaturizations of integrated waveguide systems as presently reported in the literature.

A high degree of potential still remains for future expansion of this work into miniaturized monolithic wafer-level waveguide switches and switch matrices, along with tunable and reconfigurable filters, diplexers, and multiplexers. The outcome of this thesis has provided a foundation for the development of

miniaturized systems that will help launch an entirely new generation of integrated waveguide technology.

8.3 Future Considerations

The results presented in this thesis have demonstrated the significant potential of the proposed miniaturized integrated waveguide platform. However, a number of key design elements and challenges remain for its successful implementation into larger integrated systems including reconfigurable diplexers and multiplexers for 5G mm-wave communication systems. Therefore, a list of potential future considerations is provided below.

- Research into monolithic wafer-level waveguide cavity resonators at mm-wave frequencies utilizing the proposed miniaturized folded ridge half-mode waveguide and folded ridged quarter-mode waveguide techniques should be investigated. As the building blocks of filters, the development of monolithic cavity resonators integrated on the chip is a critical step for the building of more complex filtering components including diplexers, multiplexers, and filter banks.
- The air-filled channel of the proposed miniaturized monolithic waveguide allows for the integration of MEMS tunable elements within the structure itself. Furthermore, the reduced height of the ridge, along with the open side of the half-mode or quarter-mode waveguide, offers the opportunity to develop unique tuning capabilities of the structure. Research into the design and fabrication of RF MEMS tuning elements or phase change materials

(PCM) inside the proposed miniaturized monolithic wafer-level air-filled waveguide to introduce switch functionality or tunable cavities should be explored. Once completed, larger systems including switch matrixes and tunable or reconfigurable filter networks can be developed.

- A power handling study should be completed in order to characterize the performance of the proposed miniaturized monolithic wafer-level air-filled waveguides for applications in high power mm-wave transmitters.
- A high density interconnect study comparing the performance of a pair of parallel folded ridged half-mode SIWs and ridged half-mode SIWs to a pair of parallel standard SIWs in terms of their near- and far-end cross-talk would further highlight the significant miniaturization potential of the proposed integrated waveguide platforms for applications requiring tightly packed signal routing.
- Electroplating the miniaturized monolithic waveguide structures 10 μm in thickness or more, making them rigid enough to survive wet chemical release without critical point drying, would have mass production advantages. In additional, packaging of such structures needs to be investigated in order to move into commercialization scenarios with the proposed technology. Physical stresses, contamination, and humidity are some examples of real-use environmental conditions that need to be mitigated.
- A couple microfabrication challenges remain in the presented process flow for monolithic wafer-level air-filled miniaturized waveguides, and an

exploration into their solution could help to improve device yield. First, resist reflow during subsequent baking steps (for example baking the electroplating mold) causes sidewall rounding, effecting the waveguides EM performance. Methods to cure the resist after it is developed, such as RIE or UV exposure, should be researched. Furthermore, improving mask alignment accuracy before exposure could help reduce alignment issues with thick photoresists. The use of backside alignment tools such as the SUSS MicroTec mask aligner can be explored.

Thesis Publication List (as of Sept. 9, 2019)

This section lists the refereed journals and conference papers published during the course of this thesis work.

Journal Papers

[J1] T. R. Jones and M. Daneshmand, "Microfabrication of a monolithic wafer-level air-filled half-mode waveguide for millimeter-wave applications," (submitted to *IEEE Microw. Wirel. Compon. Lett.*; revision requested on August 28, 2019).

[J2] T. R. Jones and M. Daneshmand, "Miniaturized folded ridged quarter-mode substrate integrated waveguide RF MEMS tunable bandpass filters," (submitted to *IEEE Access*; revision requested on July 7, 2019).

[J3] T. R. Jones and M. Daneshmand, "Miniaturized folded ridged half-mode and quarter-mode substrate integrated waveguides for filter design," *IEEE Trans. Microw. Theory Tech.*, vol. 67, no. 8, pp. 3414–3426, Aug. 2019.

[J4] T. R. Jones, N. Vahabisani, E. T. Der, and M. Daneshmand, "Monolithic millimeter-wave air-filled waveguide resonator for filter applications," *IEEE Microw. Wirel. Compon. Lett.*, vol. 29, no. 6, pp. 379–381, June 2019.

[J5] T. R. Jones, J. P. Grey, and M. Daneshmand, "Solar panel integrated circular polarized aperture-coupled patch antenna for CubeSat applications," *IEEE Antennas Wirel. Propag. Lett.*, vol. 17, no. 10, pp. 1895–1899, Oct. 2018.

[J6] S. Khan, T. R. Jones, S. Deif, and M. Daneshmand, "Developing microfluidically controlled SPDT waveguide switch using 3D printing," *Electron. Lett.*, vol. 53, no. 7, pp. 480–482, Mar. 2017.

[J7] T. R. Jones, M. H. Zarifi, and M. Daneshmand, "Miniaturized quarter-mode substrate integrated cavity resonators for humidity sensing," *IEEE Microw. Wirel. Compon. Lett.*, vol. 27, no. 7, pp. 612–614, July 2017.

[J8] T. R. Jones and M. Daneshmand, "The characterization of a ridged half-mode substrate-integrated waveguide and its application in coupler design," *IEEE Trans. Microw. Theory Tech.*, vol. 64, no. 11, pp. 3580–3591, Nov. 2016.

[J9] T. R. Jones and M. Daneshmand, "Miniaturized slotted bandpass filter design using a ridged half-mode substrate integrated waveguide," *IEEE Microw. Wirel. Compon. Lett.*, vol. 26, no. 5, pp. 334–336, May 2016.

Conference Papers

[C1] T. R. Jones and M. Daneshmand, "Miniaturized reconfigurable dual-band bandstop filter with independent stopband control using folded ridged quarter-mode substrate integrated waveguide," in *IEEE MTT-S Int. Microw. Symp. Dig.*, Boston, MA, June 2019, pp. 102–105.

[C2] E. T. Der, T. R. Jones, and M. Daneshmand, "Miniaturized tunable phase shifter using a periodically loaded ridged half-mode substrate integrated waveguide," in *IEEE MTT-S Int. Microw. Symp. Dig.*, Boston, MA, June 2019, pp. 180–183.

[C3] T. R. Jones and M. Daneshmand, "The microfabrication of monolithic miniaturized ridged half-mode waveguides for 5G millimeter-wave communication systems," in *IEEE MTT-S Int. Microw. Symp. Dig.*, Philadelphia, PA, June 2018, pp. 323–326.

[C4] T. R. Jones and M. Daneshmand, "Miniaturized folded ridged half-mode substrate integrated waveguide," in *Proc. 47th Eur. Microw. Conf.*, Nuremberg, Germany, Oct. 2017, pp. 528–531.

[C5] T. R. Jones, N. Vahabisani, M. Ye, and M. Daneshmand, "Advanced microfabrication techniques for the development of millimeter-wave wafer-level waveguide devices," in *International Applied Computational Electromagnetics Society Symposium (ACES)*, Suzhou, China, Aug. 2017, pp. 1–2.

[C6] T. R. Jones and M. Daneshmand, "A new type of capacitively-loaded half-mode substrate integrated waveguide for miniaturized guided wave applications," in *IEEE MTT-S Int. Microw. Symp. Dig.*, Phoenix, AZ, May 2015, pp. 1–4.

Bibliography

[1] J. G. Andrews *et al.*, "What will 5G be?," *IEEE J. Sel. Areas Commun.*, vol. 32, no. 6, pp. 1065–1082, June 2014.

[2] W. H. Chin, Z. Fan, and R. Haines, "Emerging technologies and research challenges for 5G wireless networks," *IEEE Wirel. Commun.*, vol. 21, no. 2, pp. 106–112, Apr. 2014.

[3] M. Agiwal, A. Roy, and N. Saxena, "Next generation 5G wireless networks: a comprehensive survey," *IEEE Commun. Surv. Tutorials*, vol. 18, no. 3, pp. 1617–1655, Feb. 2016.

[4] D. Deslandes and K. Wu, "Integrated microstrip and rectangular waveguide in planar form," *IEEE Microw. Wirel. Components Lett.*, vol. 11, no. 2, pp. 68–70, Feb. 2001.

[5] X.-P. Chen and K. Wu, "Substrate integrated waveguide filter: basic design rules and fundamental structure features," *IEEE Microw. Mag.*, vol. 15, no. 5, pp. 108–116, July 2014.

[6] W. Hong *et al.*, "Half mode substrate integrated waveguide: a new guided wave structure for microwave and millimeter wave application," in *Proc. Joint 31st Int. Infrared Millimeter Wave Conf./14th Int. Terahertz Electron. Conf.*, Shanghai, China, Sept. 2006, p. 219.

[7] Q. Lai, C. Fumeaux, W. Hong, and R. Vahldieck, "Characterization of the propagation properties of the half-mode substrate integrated waveguide," *IEEE Trans. Microw. Theory Tech.*, vol. 57, no. 8, pp. 1996–2004, Aug. 2009.

[8] S. Sam and S. Lim, "Electrically small eighth-mode substrate-integrated waveguide (EMSIW) antenna with different resonant frequencies depending on rotation of complementary split ring resonator," *IEEE Trans. Antennas Propag.*, vol. 61, no. 10, pp. 4933–4939, Oct. 2013.

[9] N. Nguyen-Trong and C. Fumeaux, "Half-mode substrate-integrated waveguides and their applications for antenna technology: a review of the possibilities for antenna design," *IEEE Antennas Propag. Mag.*, vol. 60, no. 6, pp. 20–31, Dec. 2018.

[10] S. Moscato, C. Tomassoni, M. Bozzi, and L. Perregrini, "Quarter-mode cavity filters in substrate integrated waveguide technology," *IEEE Trans. Microw. Theory Tech.*, vol. 64, no. 8, pp. 2538–2547, Aug. 2016.

[11] M. Bozzi, S. A. Winkler, and K. Wu, “Broadband and compact ridge substrate-integrated waveguides,” *IET Microwaves, Antennas Propag.*, vol. 4, no. 11, pp. 1965–1973, Nov. 2010.

[12] W. Che, C. Li, D. Zhang, and Y. L. Chow, “Investigations on propagation and the band broadening effect of ridged rectangular waveguide integrated in a multilayer dielectric substrate,” *IET Microwaves, Antennas Propag.*, vol. 4, no. 6, pp. 674–684, June 2010.

[13] S. Moscato, R. Moro, M. Pasian, M. Bozzi, and L. Perregrini, “Two-material ridge substrate integrated waveguide for ultra–wideband applications,” *IEEE Trans. Microw. Theory Tech.*, vol. 63, no. 10, pp. 3175–3182, Oct. 2015.

[14] N. Grigoropoulos, B. Sanz-izquierdo, and P. R. Young, “Substrate integrated folded waveguides (SIFW) and filters,” *IEEE Microw. Wirel. Components Lett.*, vol. 15, no. 12, pp. 829–831, Dec. 2005.

[15] L.-S. Wu, J. Mao, and W.-Y. Yin, “Compact quasi-elliptic bandpass filter based on folded ridge substrate integrated waveguide (FRSIW),” in *Asia-Pacific Microwave Conference Proceedings (APMC)*, Kaohsiung, Taiwan, Dec. 2012, pp. 385–387.

[16] G. H. Zhai *et al.*, “Folded half mode substrate integrated waveguide 3 dB coupler,” *IEEE Microw. Wirel. Components Lett.*, vol. 18, no. 8, pp. 512–514, Aug. 2008.

[17] D. M. Pozar, *Microwave Engineering*, 4th ed. Hoboken, NJ: John Wiley & Sons, 2012.

[18] P. A. Rizzi, *Microwave Engineering: Passive Circuits*. Englewood Cliffs, NJ: Prentice Hall, 1998.

[19] C. A. Balanis, *Advanced Engineering Electromagnetics*, 2nd ed. Hoboken, NJ: John Wiley & Sons, Inc., 2012.

[20] K. Wu, “Integration and interconnect techniques of planar and non-planar structures for microwave and millimeter-wave circuits - current status and future trend,” in *Asia Pacific Microwave Conference (APMC)*, Taipei, Taiwan, Dec. 2001, pp. 411–416.

[21] N. Marcuvitz, *Waveguide Handbook*. New York: McGraw-Hill, 1951.

[22] R. J. Cameron, R. Mansour, and C. M. Kudsia, *Microwave Filters for Communication Systems: Fundamentals, Design and Applications*. Hoboken, NJ: John Wiley & Sons, 2018.

[23] J. Hirokawa and M. Ando, "Single-layer feed waveguide consisting of posts for plane TEM wave excitation in parallel plates," *IEEE Trans. Antennas Propag.*, vol. 46, no. 5, pp. 625–630, May 1998.

[24] D. Deslandes and K. Wu, "Design consideration and performance analysis of substrate integrated waveguide components," in *32nd European Microwave Conference*, Milan, Italy, Sept. 2002, pp. 1–4.

[25] K. Wu, D. Deslandes, and Y. Cassivi, "The substrate integrated circuits - a new concept for high-frequency electronics and optoelectronics," in *6th International Conference on Telecommunications in Modern Satellite, Cable and Broadcasting Service (TELSIKS)*, Nis, Yugoslavia, Oct. 2003, pp. 3–10.

[26] D. Deslandes and K. Wu, "Accurate modeling, wave mechanisms, and design considerations of a substrate integrated waveguide," *IEEE Trans. Microw. Theory Tech.*, vol. 54, no. 6, pp. 2516–2526, June 2006.

[27] F. Xu and K. Wu, "Guided-wave and leakage characteristics of substrate integrated waveguide," *IEEE Trans. Microw. Theory Tech.*, vol. 53, no. 1, pp. 66–73, Jan. 2005.

[28] L. Brillouin, *Wave Propagation and Group Velocity*. New York and London: Academic Press, 1960.

[29] Y. Cassivi, L. Perregrini, P. Arcioni, M. Bressan, K. Wu, and G. Conciauro, "Dispersion characteristics of substrate integrated rectangular waveguide," *IEEE Microw. Wirel. Components Lett.*, vol. 12, no. 9, pp. 333–335, Sept. 2002.

[30] J.-X. Chen, W. Hong, Z.-C. Hao, H. Li, and K. Wu, "Development of a low cost microwave mixer using a broad-band substrate integrated waveguide (SIW) coupler," *IEEE Microw. Wirel. Components Lett.*, vol. 16, no. 2, pp. 84–86, Feb. 2006.

[31] D. Deslandes and K. Wu, "Substrate integrated waveguide leaky-wave antenna: concept and design considerations," in *Asia Pacific Microwave Conference Proceedings (APMC)*, Suzhou, China, Dec. 2005, pp. 346–349.

[32] L. Yan, W. Hong, G. Hua, J. Chen, K. Wu, and T. J. Cui, "Simulation and experiment on SIW slot array antennas," *IEEE Microw. Wirel. Components Lett.*, vol. 14, no. 9, pp. 446–448, Sept. 2004.

[33] D.-D. Zhang, L. Zhou, L.-S. Wu, L.-F. Qiu, W.-Y. Yin, and J.-F. Mao, "Novel bandpass filters by using cavity-loaded dielectric resonators in a substrate integrated waveguide," *IEEE Trans. Microw. Theory Tech.*, vol. 62, no. 5, pp. 1173–1182, May 2014.

[34] K.-S. Chin, C.-C. Chang, C.-H. Chen, Z. Guo, D. Wang, and W. Che, "LTCC multilayered substrate-integrated waveguide filter with enhanced frequency selectivity for system-in-package applications," *IEEE Trans. Components, Packag. Manuf. Technol.*, vol. 4, no. 4, pp. 664–672, Apr. 2014.

[35] X. Chen and K. Wu, "Substrate integrated waveguide filters: design techniques and structure innovations," *IEEE Microw. Mag.*, vol. 15, no. 6, pp. 121–133, Sept. 2014.

[36] X. Chen and K. Wu, "Substrate integrated waveguide filters: practical aspects and design considerations," *IEEE Microw. Mag.*, vol. 15, no. 7, pp. 75–83, Nov. 2014.

[37] X. Zhang, X. N. Jiang, and C. Sun, "Micro-stereolithography of polymeric and ceramic microstructures," *Sensors Actuators, A Phys.*, vol. 77, no. 2, pp. 149–156, Oct. 1999.

[38] G. H, T. R. Christenson, K. J. Skrobis, J. Klein, and M. Karnowsky, "Design and testing of planar magnetic micromotors fabricated by deep X-ray lithography and electroplating," in *International Conference on Solid State Sensors and Actuators*, United States, May 1993, pp. 1–5.

[39] A. Cohen, G. Zhang, F.-G. Tseng, U. Frodis, F. Mansfeld, and P. Will, "EFAB: rapid, low-cost desktop micromachining of high aspect ratio true 3-D MEMS," in *IEEE Int. Microelectromech. Syst. Conf.*, Orlando, FL, Jan. 1999, pp. 244–251.

[40] W. D. Yan and R. R. Mansour, "Micromachined millimeter-wave ridge waveguide filter with embedded MEMS tuning elements," in *IEEE MTT-S International Microwave Symposium Digest*, San Francisco, CA, June 2006, pp. 1290–1293.

[41] C. E. Collins *et al.*, "Technique for micro-machining millimetre-wave rectangular waveguide," *Electron. Lett.*, vol. 34, no. 10, p. 996, May 1998.

[42] W. R. McGrath, C. Walker, M. Yap, and Y. C. Tai, "Silicon micromachined waveguides for millimeter-wave and submillimeter-wave frequencies," *IEEE Microw. Guid. Wave Lett.*, vol. 3, no. 3, pp. 61–63, Jan. 1993.

[43] C. E. Collins *et al.*, "A new micro-machined millimeter-wave and terahertz snap-together rectangular waveguide technology," *IEEE Microw. Guid. Wave Lett.*, vol. 9, no. 2, pp. 63–65, Feb. 1999.

[44] E. J. Naglich, M. Sinani, S. Moon, and D. Peroulis, "High-Q MEMS-tunable W-band bandstop resonators," in *IEEE MTT-S International Microwave Symposium (IMS)*, Tampa, FL, June 2014, pp. 1–3.

[45] M. S. Arif and D. Peroulis, "All-silicon technology for high-Q evanescent mode cavity tunable resonators and filters," *J. Microelectromechanical Syst.*, vol. 23, no. 3, pp. 727–739, June 2014.

[46] Y. Wang, M. Ke, M. J. Lancaster, and F. Huang, "Micromachined millimeter-wave rectangular-coaxial branch-line coupler with enhanced bandwidth," *IEEE Trans. Microw. Theory Tech.*, vol. 57, no. 7, pp. 1655–1660, May 2009.

[47] M. J. De Boer *et al.*, "Guidelines for etching silicon MEMS structures using fluorine high-density plasmas at cryogenic temperatures," *J. Microelectromechanical Syst.*, vol. 11, no. 4, pp. 385–401, Aug. 2002.

[48] S. Lucyszyn, Q. H. Wang, and I. D. Robertson, "0.1 THz rectangular waveguide on GaAs semi-insulating substrate," *Electron. Lett.*, vol. 31, no. 9, p. 721, Apr. 1995.

[49] M. S. Aftanasar, P. R. Young, I. D. Robertson, and S. Lucyszyn, "Fabrication of dielectric-filled rectangular waveguide using thick-film processing," in *6th IEEE High Frequency Postgraduate Colloquium (Cat. No.01TH8574)*, Cardiff, Wales, UK, Sept. 2001, pp. 82–87.

[50] D. Stephens, P. R. Young, and I. D. Robertson, "Millimeter-wave substrate integrated waveguides and filters in photoimageable thick-film technology," *IEEE Trans. Microw. Theory Tech.*, vol. 53, no. 12, pp. 3832–3837, Dec. 2005.

[51] M. Henry, C. E. Free, B. S. Izqueirdo, J. Batchelor, and P. Young, "Millimeter wave substrate integrated waveguide antennas: design and fabrication analysis," *IEEE Trans. Adv. Packag.*, vol. 32, no. 1, pp. 93–100, Feb. 2009.

[52] J. Zhang, K. L. Tan, and H. Q. Gong, "Characterization of the polymerization of SU-8 photoresist and its applications in micro-electro-mechanical systems (MEMS)," *Polym. Test.*, vol. 20, no. 6, pp. 693–701, Dec. 2001.

[53] B. Pan, Y. Li, M. M. Tentzeris, and J. Papapolymerou, "Surface micromachining polymer-core-conductor approach for high-performance millimeter-wave air-cavity filters integration," *IEEE Trans. Microw. Theory Tech.*, vol. 56, no. 4, pp. 959–970, Apr. 2008.

[54] A. Ghannam, C. Viallon, D. Bourrier, and T. Parra, "Dielectric microwave characterization of the SU-8 thick resin used in an above IC process," in *39th European Microwave Conference*, Rome, Italy, Sept. 2009, pp. 1041–1044.

[55] P. M. Dentinger, W. M. Clift, and S. H. Goods, "Removal of SU-8 photoresist for thick film applications," *Microelectron. Eng.*, vol. 61–62, pp. 993–1000, July 2002.

[56] N. Vahabisani, "3D micro-fabricated millimeter-wave devices: waveguides and waveguide switches," Ph.D. Dissertation, Department of Electrical and Computer Engineering, University of Alberta, 2014.

[57] M. Safari, C. Shafai, and L. Shafai, "X-band tunable frequency selective surface using MEMS capacitive loads," *IEEE Trans. Antennas Propag.*, vol. 63, no. 3, pp. 1014–1021, Mar. 2015.

[58] I. Llamas-garro, Y. Kim, C. Baek, and Y. Kim, "A planar high-Q micromachined monolithic half-coaxial transmission-line filter," *IEEE Trans. Microw. Theory Tech.*, vol. 54, no. 12, pp. 4161–4168, Dec. 2006.

[59] N. Vahabisani and M. Daneshmand, "Thick THB sacrificial layer and metal encapsulation process," in *2nd Microsystems and Nanoelectronics Research Conference*, Ottawa, ON, Canada, Oct. 2009, pp. 144–147.

[60] N. Vahabisani and M. Daneshmand, "THB-filled monolithic rectangular waveguides for millimeter wave applications," *IET Microwaves, Antennas Propag.*, vol. 8, no. 6, pp. 377–385, Apr. 2014.

[61] Z. Zhou, Q. A. Huang, W. Li, W. Lu, Z. Zhu, and M. Feng, "The swelling effects during the development processes of deep UV lithography of SU-8 photoresists: theoretical study, simulation and verification," in *Proceedings of IEEE Sensors*, Atlanta, GA, Oct. 2007, pp. 325–328.

[62] Y. Kim, I. Llamas-Garro, C.-W. Baek, J.-M. Kim, and Y.-K. Kim, "New release technique of a thick sacrificial layer and residue effects on novel half-coaxial transmission line filters," *J. Micromechanics Microengineering*, vol. 19, no. 5, p. 055018, May 2009.

[63] N. Vahabisani and M. Daneshmand, "Monolithic wafer-level rectangular waveguide and its transition to coplanar waveguide line using a simplified 3-D fabrication process," *IEEE Trans. Components, Packag. Manuf. Technol.*, vol. 4, no. 1, pp. 168–176, Jan. 2014.

[64] N. Vahabisani and M. Daneshmand, "Monolithic millimeter-wave MEMS waveguide switch," *IEEE Trans. Microw. Theory Tech.*, vol. 63, no. 2, pp. 340–351, Feb. 2015.

[65] *MicroChemicals AZ® 40XT-11D Photoresist*. [Online]. Available: https://microchemicals.com/micro/tds_az_40xt_photoresist.pdf. Accessed on: July 21, 2019.

[66] B. Liu, W. Hong, Y. Wang, Q. Lai, and K. Wu, "Half mode substrate integrated waveguide (HMSIW) 3-dB coupler," *IEEE Microw. Wirel. Components Lett.*, vol. 17, no. 1, pp. 22–24, Jan. 2007.

[67] Q. Lai, C. Fumeaux, and W. Hong, "On the transition from radiating to guiding behavior of the half-mode substrate integrated waveguide," in *Proceedings of Asia-Pacific Microwave Conference (APMC)*, Yokohama, Japan, Dec. 2010, pp. 1601–1604.

[68] Y. Wang *et al.*, "Half mode substrate integrated waveguide (HMSIW) bandpass filter," *IEEE Microw. Wirel. Components Lett.*, vol. 17, no. 4, pp. 265–267, Apr. 2007.

[69] B. Liu, W. Hong, Y. Zhang, H. J. Tang, X. Yin, and K. Wu, "Half mode substrate integrated waveguide 180° 3-dB directional couplers," *IEEE Trans. Microw. Theory Tech.*, vol. 55, no. 12, pp. 2586–2592, Dec. 2007.

[70] J. Xu, W. Hong, H. Tang, Z. Kuai, and K. Wu, "Half-mode substrate integrated waveguide (HMSIW) leaky-wave antenna for millimeter-wave applications," *IEEE Antennas Wirel. Propag. Lett.*, vol. 7, pp. 85–88, Apr. 2008.

[71] S. A. Shakib, V. Sekar, and K. Entesari, "A compact triple-band bandpass filter based on half-mode substrate integrated waveguides," in *42nd European Microwave Conference*, Amsterdam, Netherlands, Oct. 2012, pp. 116–119.

[72] M. Wei, W. Ke, H. Wei, and C. Yu-Jian, "Investigations on half-mode substrate integrated waveguide for high-speed interconnect application," in *Proc. IEEE MTT-S Int. Microw. Workshop Series on Art of Miniaturizing RF and Microw. Passi. Comp.*, Chengdu, China, Dec. 2008, pp. 120–123.

[73] Q. H. Lai, C. Fumeaux, and W. Hong, "Mutual coupling between parallel half-mode substrate integrated waveguides," in *International Conference on Microwave and Millimeter Wave Technology (ICMMT)*, Shenzhen, China, May 2012, pp. 1–4.

[74] X. Yuan, X. Li, N. Wang, X. Ma, Y. Shao, and J. Mao, "High-speed data transmission system using half mode substrate integrated waveguide," in *IEEE Electrical Design of Advanced Packaging & Systems Symposium (EDAPS)*, Bangalore, India, Dec. 2014, pp. 105–108.

[75] Y. Shao, X. C. Li, N. Wang, L. S. Wu, M. Tang, and J. F. Mao, "Theoretical and experimental investigation of HMSIW-based high-speed data transmission system using QPSK scheme," *IEEE Trans. Components, Packag. Manuf. Technol.*, vol. 8, no. 11, pp. 1938–1947, Nov. 2018.

[76] L.-S. Wu *et al.*, "A new type of periodically loaded half-mode substrate integrated waveguide and its applications," *IEEE Trans. Microw. Theory Tech.*, vol. 58, no. 4, pp. 882–893, Apr. 2010.

[77] T. Jang and S. Lim, "Novel capacitor-loaded substrate-integrated-waveguide structure and its electronically controlled leaky-wave antenna application," *Electromagnetics*, vol. 34, no. 8, pp. 585–592, Oct. 2014.

[78] K. W. Eccleston, "Half-mode buried corrugated substrate integrated waveguide," *IEEE Microw. Wirel. Components Lett.*, vol. 24, no. 4, pp. 215–217, Apr. 2014.

[79] Z. Zhang, N. Yang, and K. Wu, "5-GHz bandpass filter demonstration using quarter-mode substrate integrated waveguide cavity for wireless systems," in *IEEE Radio Wirel. Symp. Proc.*, San Diego, CA, Jan. 2009, pp. 95–98.

[80] C. Jin and Z. Shen, "Compact triple-mode filter based on quarter-mode substrate integrated waveguide," *IEEE Trans. Microw. Theory Tech.*, vol. 62, no. 1, pp. 37–45, Jan. 2014.

[81] A. P. Saghati, A. P. Saghati, and K. Entesari, "Ultra-miniature SIW cavity resonators and filters," *IEEE Trans. Microw. Theory Tech.*, vol. 63, no. 12, pp. 4329–4340, Dec. 2015.

[82] A. P. Saghati, S. B. Kordmahale, J. Kameoka, and K. Entesari, "Reconfigurable quarter-mode substrate integrated waveguide cavity filter employing liquid-metal capacitive loading," in *IEEE MTT-S International Microwave Symposium (IMS)*, Phoenix, AZ, May 2015, pp. 1–3.

[83] P. Li, H. Chu, and R. Chen, "Design of compact bandpass filters using quarter-mode and eighth-mode SIW cavities," *IEEE Trans. Components, Packag. Manuf. Technol.*, vol. 1, no. 6, pp. 1–8, June 2017.

[84] N. Delmonte, C. Tomassoni, M. Bozzi, and L. Perregrini, "Compact resonators in substrate integrated waveguide technology," in *Proceedings of the IEEE MTT-S International Wireless Symposium (IWS)*, Chengdu, China, May 2018, pp. 1–3.

[85] Y. Seo, M. U. Memon, and S. Lim, "Microfluidic eighth-mode substrate-integrated-waveguide antenna for compact ethanol chemical sensor application," *IEEE Trans. Antennas Propag.*, vol. 64, no. 7, pp. 3218–3222, July 2016.

[86] T. R. Jones, M. H. Zarifi, and M. Daneshmand, "Miniaturized quarter-mode substrate integrated cavity resonators for humidity sensing," *IEEE Microw. Wirel. Components Lett.*, vol. 27, no. 7, pp. 612–614, July 2017.

[87] X. Wang, X.-W. Zhu, L. Tian, P. Liu, W. Hong, and A. Zhu, "Design and experiment of filtering power divider based on shielded HMSIW/QMSIW technology for 5G wireless applications," *IEEE Access*, vol. 7, pp. 72411–72419, June 2019.

[88] H. Kang and S. Lim, "Electrically-small eighth-mode SIW antenna with fixed frequency and independently tunable frequency," in *IEEE Antennas and Propagation Society International Symposium (APSURSI)*, Orlando, FL, July 2013, pp. 668–669.

[89] C. Jin, R. Li, A. Alphones, and X. Bao, "Quarter-mode substrate integrated waveguide and its application to antennas design," *IEEE Trans. Antennas Propag.*, vol. 61, no. 6, pp. 2921–2928, June 2013.

[90] S. B. Cohn, "Properties of ridge wave guide," *Proc. I.R.E.*, vol. 35, no. 8, pp. 783–788, Aug. 1947.

[91] S. Hopfer, "The design of ridged waveguides," *IRE Trans. Microw. Theory Tech.*, vol. 3, no. 5, pp. 20–29, Oct. 1955.

[92] W. Che, C. Li, P. Russer, and Y. L. Chow, "Propagation and band broadening effect of planar integrated ridged waveguide in multilayer dielectric substrates," in *IEEE MTT-S International Microwave Symposium Digest*, Atlanta, GA, June 2008, pp. 217–220.

[93] M. Bozzi, S. A. Winkler, and K. Wu, "Novel compact and broadband interconnects based on ridge substrate integrated waveguide," in *IEEE MTT-S International Microwave Symposium Digest*, Boston, MA, June 2009, pp. 121–124.

[94] A. A. M. Ali, H. B. El-shaarawy, and H. Aubert, "Miniaturized hybrid ring coupler using electromagnetic bandgap loaded ridge substrate integrated waveguide," *IEEE Microw. Wirel. Components Lett.*, vol. 21, no. 9, pp. 471–473, Aug. 2011.

[95] K. W. Eccleston, "Folded substrate-integrated waveguide out-of-phase power divider," in *Proceedings of Asia-Pacific Microwave Conference*, Yokohama, Japan, Mar. 2010, pp. 1260–1263.

[96] T. L. Owens, "A folded waveguide coupler for plasma heating in the ion cyclotron range of frequencies," *IEEE Trans. Plasma Sci.*, vol. 14, no. 6, pp. 934–946, Dec. 1986.

[97] G. L. Chen, T. L. Owens, and J. H. Whealton, "Theoretical study of the folded waveguide," *IEEE Trans. Plasma Sci.*, vol. 16, no. 2, pp. 305–311, Apr. 1988.

[98] W. Che, L. Geng, K. Deng, and Y. L. Chow, "Analysis and experiments of compact folded substrate-integrated waveguide," *IEEE Trans. Microw. Theory Tech.*, vol. 56, no. 1, pp. 88–93, Jan. 2008.

[99] W. Wang, Y. Jiang, W. J. Zou, R. J. Luo, and X. Q. Lin, "A varactor-loaded tunable phase shifter based on folded half mode substrate integrated

waveguide," in *International Symposium on Antennas, Propagation and EM Theory (ISAPE)*, Xian, China, Oct. 2012, pp. 558–561.

[100] N. Marcuvitz, "Section 5-26 change in height of rectangular guide," in *Waveguide Handbook*, New York: McGraw-Hill, 1951, pp. 307–310.

[101] A. Semnani, K. Chen, and D. Peroulis, "Microwave gas breakdown in tunable evanescent-mode cavity resonators," *IEEE Microw. Wirel. Components Lett.*, vol. 24, no. 5, pp. 351–353, May 2014.

[102] R. B. Marks, "A multiline method of network analyzer calibration," *IEEE Trans. Microw. Theory Tech.*, vol. 39, no. 7, pp. 1205–1215, July 1991.

[103] F. Xu and K. Wu, "Numerical multimode calibration technique for extraction of complex propagation constants of substrate integrated waveguide," in *IEEE MTT-S Int. Microw. Symp. Dig.*, Fort Worth, TX, June 2004, pp. 1229–1232.

[104] W. Shuai, L. Ke, J. Yibo, C. Mifang, D. Huan, and H. Zhengsheng, "A thru-reflect-line calibration for measuring the characteristics of high power LDMOS transistors," *J. Semicond.*, vol. 34, no. 3, pp. 1–5, Mar. 2013.

[105] E. D. Caballero, A. Belenguer, H. Esteban, and V. E. Boria, "Thru-reflect-line calibration for substrate integrated waveguide devices with tapered microstrip transitions," *Electron. Lett.*, vol. 49, no. 2, pp. 132–133, Jan. 2013.

[106] Chih-Jung Chen and Tah-Hsiung Chu, "Design of a 60-GHz substrate integrated waveguide butler matrix— a systematic approach," *IEEE Trans. Microw. Theory Tech.*, vol. 58, no. 7, pp. 1724–1733, July 2010.

[107] Q. L. Yang, Y. L. Ban, K. Kang, C. Y. D. Sim, and G. Wu, "SIW multibeam array for 5G mobile devices," *IEEE Access*, vol. 4, pp. 2788–2796, June 2016.

[108] H. J. Riblett, "The short-slot hybrid junction," *Proc. I.R.E.*, vol. 40, no. 2, pp. 180–184, Feb. 1952.

[109] M. Bozzi, A. Georgiadis, and K. Wu, "Review of substrate-integrated waveguide circuits and antennas," *IET Microwaves, Antennas Propag.*, vol. 5, no. 8, pp. 909–920, June 2011.

[110] J.-S. Hong, *Microstrip Filters for RF/Microwave Applications*, 2nd ed. Hoboken, NJ: John Wiley & Sons, Inc., 2011.

[111] L. Huang and H. Cha, "Compact ridged half-mode substrate integrated waveguide bandpass filter," *IEEE Microw. Wirel. Components Lett.*, vol. 25, no. 4, pp. 223–225, Apr. 2015.

[112] E. M. Amin, M. S. Bhuiyan, N. C. Karmakar, and B. Winther-Jensen, "Development of a low cost printable chipless RFID humidity sensor," *IEEE Sens. J.*, vol. 14, no. 1, pp. 140–149, Jan. 2014.

[113] M. H. Zarifi, P. Shariaty, Z. Hashisho, and M. Daneshmand, "A non-contact microwave sensor for monitoring the interaction of zeolite 13X with CO2 and CH4 in gaseous streams," *Sensors Actuators B Chem.*, vol. 238, pp. 1240–1247, Jan. 2017.

[114] H. El Matbouly, N. Boubekeur, and F. Domingue, "Passive microwave substrate integrated cavity resonator for humidity sensing," *IEEE Trans. Microw. Theory Tech.*, vol. 63, no. 12, pp. 4150–4156, Dec. 2015.

[115] M. Ndoye, H. El Matbouly, Y. N. Sama, D. Deslandes, and F. Domingue, "Sensitivity evaluation of dielectric perturbed substrate integrated resonators for hydrogen detection," *Sensors Actuators A Phys.*, vol. 251, pp. 198–206, Nov. 2016.

[116] M. A. Ali, M. M. Cheng, J. C. Chen, and C. M. Wu, "Microwave gas sensor based on graphene-loaded substrate integrated waveguide cavity resonator," in *IEEE MTT-S International Microwave Symposium (IMS)*, San Francisco, CA, May 2016, pp. 4–7.

[117] S. Moscato *et al.*, "Exploiting 3D printed substrate for microfluidic SIW sensor," in *Proceedings of the 45th European Microwave Conference*, Paris, France, Sept. 2015, pp. 28–31.

[118] K. Chang, Y. H. Kim, Y. J. Kim, and Y. J. Yoon, "Functional antenna integrated with relative humidity sensor using synthesised polyimide for passive RFID sensing," *Electron. Lett.*, vol. 43, no. 5, pp. 7–8, Mar. 2007.

[119] L.-S. Wu, X.-L. Zhou, and W.-Y. Yin, "Ultra-wideband bandpass filter using half-mode t-septum substrate integrated waveguide with electromagnetic bandgap structures," *Microw. Opt. Technol. Lett.*, vol. 51, no. 7, pp. 1751–1755, July 2009.

[120] H. B. Palmer, "The capacitance of a parallel-plate capacitor by the Schwartz-Christoffel transformation," *Electr. Eng.*, vol. 56, no. 3, pp. 363–368, Mar. 1937.

[121] N. Marcuvitz, "Section 8-6 rectangular guides with ridges," in *Waveguide Handbook*, New York: McGraw-Hill, 1951, pp. 399–402.

[122] W. Shen and T. Zhao, "Compact t-septum substrate integrated waveguide (TSSIW) filter with wide stopband," *J. Electromagn. Waves Appl.*, vol. 29, no. 6, pp. 798–806, Apr. 2015.

[123] J. S. Hong and M. J. Lancaster, "Compact microwave elliptic function filter using novel microstrip meander open-loop resonators," *Electron. Lett.*, vol. 32, no. 6, pp. 563–564, Mar. 1996.

[124] J. C. Rautio, "Measurement of uniaxial anisotropy in Rogers RO3010 substrate material," in *IEEE International Conference on Microwaves, Communications, Antennas and Electronics Systems (COMCAS)*, Tel Aviv, Israel, Nov. 2009, pp. 1–4.

[125] G. MacChiarella, "Extraction of unloaded Q and coupling matrix from measurements on filters with large losses," *IEEE Microw. Wirel. Components Lett.*, vol. 20, no. 6, pp. 307–309, June 2010.

[126] *Rogers Corporation RO3000® Series Circuit Materials*. [Online]. Available: https://www.rogerscorp.com/documents/722/acs/RO3000-Laminate-Data-Sheet-RO3003-RO3006-RO3010.pdf. Accessed on: April 5, 2019.

[127] G. M. Rebeiz *et al.*, "Tuning in to RF MEMS," *IEEE Microw. Mag.*, vol. 10, no. 6, pp. 55–72, Oct. 2009.

[128] K. Entesari and G. M. Rebeiz, "RF MEMS, BST, and GaAs varactor system-level response in complex modulation systems," *Int. J. RF Microw. Comput. Eng.*, vol. 18, no. 1, pp. 86–98, Jan. 2008.

[129] V. Sekar, M. Armendariz, and K. Entesari, "A 1.2–1.6-GHz substrate-integrated-waveguide RF MEMS tunable filter," *IEEE Trans. Microw. Theory Tech.*, vol. 59, no. 4, pp. 866–876, Apr. 2011.

[130] V. Sekar and K. Entesari, "A half-mode substrate-integrated-waveguide tunable filter using packaged RF MEMS switches," *IEEE Microw. Wirel. Components Lett.*, vol. 22, no. 7, pp. 336–338, July 2012.

[131] M. E. Goldfarb and R. A. Pucel, "Modeling via hole grounds in microstrip," *IEEE Microw. Guid. Wave Lett.*, vol. 1, no. 6, pp. 135–137, June 1991.

[132] G. M. Rebeiz, *RF MEMS Theory, Design, and Technology*. Hoboken, NJ: John Wiley & Sons, 2003.

[133] *Analog Devices, Inc. Data Sheet ADGM1304*. [Online]. Available: https://www.analog.com/media/en/technical-documentation/data-sheets/adgm1304.pdf. Accessed on: July 21, 2019.

[134] G. L. Matthaei, L. Young, and E. M. T. Jones, "Sec. 6.15, Group Delay," in *Design of Microwave Filters, Impedance-Matching Networks, and Coupling Structures*, New York: McGraw-Hill, 1964, pp. 339–348.

[135] W. J. Chappell, E. J. Naglich, C. Maxey, and A. C. Guyette, "Putting the radio in 'software-defined radio': hardware developments for adaptable RF systems," *Proc. IEEE*, vol. 102, no. 3, pp. 307–320, Mar. 2014.

[136] R. Gomez-Garcia and A. C. Guyette, "Reconfigurable multi-band microwave filters," *IEEE Trans. Microw. Theory Tech.*, vol. 63, no. 4, pp. 1294–1307, Apr. 2015.

[137] D. Psychogiou, R. Gomez-Garcia, and D. Peroulis, "Fully adaptive multiband bandstop filtering sections and their application to multifunctional components," *IEEE Trans. Microw. Theory Tech.*, vol. 64, no. 12, pp. 4405–4418, Dec. 2016.

[138] B. H. Ahmad and I. C. Hunter, "Design and fabrication of a substrate integrated waveguide bandstop filter," in *Proceedings of the 38th European Microwave Conference*, Amsterdam, Netherlands, Oct. 2008, pp. 40–42.

[139] M. Esmaeili and J. Bornemann, "Substrate integrated waveguide triple-passband dual-stopband filter using six cascaded singlets," *IEEE Microw. Wirel. Components Lett.*, vol. 24, no. 7, pp. 439–441, July 2014.

[140] J. Bornemann, P. Krauss, and M. Esmaeili, "Substrate integrated waveguide bandstop filter using partial-height via-hole resonators in thick substrate," *IET Microwaves, Antennas Propag.*, vol. 9, no. 12, pp. 1307–1312, Apr. 2015.

[141] M. Esmaeili and J. Bornemann, "Novel tunable bandstop resonators in SIW technology and their application to a dual-bandstop filter with one tunable stopband," *IEEE Microw. Wirel. Components Lett.*, vol. 27, no. 1, pp. 40–42, Jan. 2017.

[142] Y. Cai, Z. Qian, W. Cao, Y. Zhang, and L. Yang, "HMSIW bandstop filter loaded with half complementary split-ring resonator," *Electron. Lett.*, vol. 51, no. 8, pp. 632–633, Apr. 2015.

[143] J. Hinojosa, M. Rossi, A. Saura-Rodenas, A. Alvarez-Melcon, and F. L. Martinez-Viviente, "Compact bandstop half-mode substrate integrated waveguide filter based on a broadside-coupled open split-ring resonator," *IEEE Trans. Microw. Theory Tech.*, vol. 66, no. 6, pp. 3001–3010, June 2018.

[144] J. Lee, E. J. Naglich, and W. J. Chappell, "Frequency response control in frequency-tunable bandstop filters," *IEEE Microw. Wirel. Components Lett.*, vol. 20, no. 12, pp. 669–671, Dec. 2010.

[145] J. Lee, E. J. Naglich, H. H. Sigmarsson, D. Peroulis, and W. J. Chappell, "New bandstop filter circuit topology and its application to design of a bandstop-to-bandpass switchable filter," *IEEE Trans. Microw. Theory Tech.*, vol. 61, no. 3, pp. 1114–1123, Mar. 2013.

[146] D. Peroulis, E. Naglich, M. Sinani, and M. Hickle, "Tuned to resonance," *IEEE Microw. Mag.*, vol. 15, no. 5, pp. 55–69, Aug. 2014.

[147] S. Amari, U. Rosenberg, and J. Bornemann, "Singlets, cascaded singlets, and the nonresonating node model for advanced modular design of elliptic filters," *IEEE Microw. Wirel. Components Lett.*, vol. 14, no. 5, pp. 237–239, May 2004.

[148] Z.-H. Chen, S.-X. Zhang, and Q.-X. Chu, "Dual-band reconfigurable bandstop filter with independently controlled stopbands and constant absolute bandwidths," in *IEEE MTT-S International Microwave Symposium Digest*, Honolulu, HI, June 2017, pp. 926–928.

[149] S.-Y. Lin, L.-W. Yang, and X.-W. Sun, "Millimeter-wave low-loss transmission lines and resonators in standard CMOS technology," *Microw. Opt. Technol. Lett.*, vol. 50, no. 6, pp. 1579–1582, June 2008.

[150] T. R. Jones, N. Vahabisani, E. T. Der, and M. Daneshmand, "Monolithic millimeter-wave air-filled waveguide resonator for filter applications," *IEEE Microw. Wirel. Com*, vol. 29, no. 6, pp. 379–381, June 2019.

[151] S. A. Campbell, *Fabrication Engineering at the Micro- and Nanoscale*, 3rd ed. New York: Oxford Universiyt Press, Inc., 2008.

[152] *Schott AG BOROFLOAT®*. [Online]. Available: https://www.schott.com/d/borofloat/b8e85c79-374f-460b-a0e2-1cd2f4a41974/1.0/borofloat_wafer_db_row.pdf. Accessed on: July 21, 2019.

[153] M. S. Mahani and G. W. Roberts, "A mmWave folded substrate integrated waveguide in a 130-nm CMOS process," *IEEE Trans. Microw. Theory Tech.*, vol. 65, no. 8, pp. 2775–2788, Feb. 2017.

[154] F. J. Tischer, "Effect of surface roughness on surface resistance of plane copper surfaces at millimetre waves," *Proc. Inst. Electr. Eng.*, vol. 121, no. 5, p. 333, May 1974.

[155] L. Proekt and A. C. Cangellaris, "Investigation of the impact of conductor surface roughness on interconnect frequency-dependent ohmic loss," in *53rd Electronic Components and Technology Conference*, New Orleans, LA, May 2003, pp. 1004–1010.

[156] R. W. McElhanon and W. K. Burns, "Adhesion enhancement for underplating problem," United States Patent 5755947, May 26, 1998.

[157] D. L. Huston, V. S. Kardashian, and A. H. Mones, "Selective process for etching chromium," United States Patent 4498954, Feb. 12, 1985.

[158] R. E. Collin, *Foundations for Microwave Engineering*, 2nd ed. New York: McGraw-Hill, 2001.

Appendix A: Miniaturized Monolithic Wafer-Level Air-Filled Waveguide Process Flow

In this appendix, a detailed description of the microfabrication process flow for the development of miniaturized monolithic wafer-level air-filled waveguides is presented.

1st mask – Pattern first metallization layer M1 (40nm/500nm Cr/Au)

1. Floated borosilicate glass (1.1mm thick) wafers are piranha cleaned and properly dried.
    a. Schott AG BOROFLOAT floated borosilicate glass wafers are used due to the low coefficient of expansion which is close to that of silicon, allowing for stable performance during high temperature processes (specifically PECVD) [152].
    b. Sputter within 24 hours after piranha etch.
    c. BOROFLOAT wafers are tinned on one side. Make sure to record which side is the tinned side before piranha etching.
        i. Use the tool in nanoFAB to determine which side is tinned. Gold will be sputtered on the non-tinned side.
        ii. nanoFAB will sometimes mark the tinned side with a letter 'T'.
    d. Alternatively, wafers are cleaned in acetone ultrasonic bath for approximately 10 minutes, rinsed in IPA and DI then dried with nitrogen N_2 gun (wait at least 1 day after dry due to leftover moisture in the quartz wafer).
        i. This method is not as good as piranha cleaning and leaves residue on the wafer which can cause bubbling in AZ 40XT layers above.
2. A 40/500 nm chrome/gold layer is sputtered.
    a. Chrome (Cr) is used as an adhesion layer.
    b. Chrome Deposition Parameters:
        i. Deposition Rate: 14.1 nm/min.
        ii. Power: 300 W.
        iii. Pressure = 7 mTorr.
        iv. For 40 nm film, deposition time is 2.83 min ≈ 3 min + 3 min burn-in.
        v. Voltage ≈ 360 V.

c. Gold Deposition Parameters:
    i. Deposition Rate: 7.6 nm/min.
    ii. Power = 75 W.
    iii. Pressure = 7 mTorr.
    iv. For 500 nm film, deposition time is 65.8 min ≈ 66 min + 1 min burn-in.
    v. Voltage ≈ 410 V.
d. Pump down to base pressure of approximately 1.5×10^{-6} Torr or less (time is approximately 70 minutes).

3. HPR-504 photoresist is spun on wafers for 1.4 μm of resist thickness.
    a. Clear wafers with nitrogen air gun next to HMDS station.
    b. Spread/spin for 10/40 seconds at 500/3000 rpm.
4. The wafer is transferred to the hotplate for softbake, vacuum on, for 2.5 minutes at 115°C.
5. Rest the wafers for 15 minutes to allow rehydration.
6. Exposure to both *h-line* (405 nm) and *i-line* (365 nm) for 169 mJ/cm^2 in lithography contact mask aligner.
    a. Determine required time in seconds from measured mW/cm2 value posted next to mask aligner.
    b. Time = (mJ/cm^2)/(mW/cm^2) (seconds).
7. Develop in 354 developer solution for approximately 35 seconds.
8. The Cr/Au layer is then etched in Cr/Au etchants, respectively. Watch colour change to determine when etch is complete.
    a. Au etchant: potassium iodine (etch time approximately 2 minutes).
    b. Cr etchant: ceric ammonium nitrate (etch time approximately 10 seconds).
9. The photoresist is removed using a 10 minute sonicate in acetone then rinsed in IPA and dried with the N_2 gun.

<u>2nd *mask* – Pattern nitride layer Nitride1 (100nm Si_3N_4)</u>

10. A 100 nm silicon nitride layer is deposited using PECVD with deposition time 1850 seconds.
    a. Clean chuck before deposition due to large thickness.
    b. Test deposition time with sample piece.
11. HPR-504 is spun and patterned using the same steps in 3-7.
12. The nitride layer is then etched by the Trion RIE.

a. 60 seconds of nitride recipe.

b. Watch the colour change to determine when etch is complete.

13. The photoresist is removed using a 10 minute sonicate in acetone then rinsed in IPA and dried with the N_2 gun.

    a. It is critical to remove photoresist using sonication due to burning of the photoresist in the RIE, otherwise scumming occurs.

3rd mask – Pattern second metallization layer M2 (40nm/1500nm Cr/Cu)

14. MicroChemicals Chemically amplified ultra-thick positive photoresist AZ 40XT-11D [65] is spun for 25/35 seconds at 300/1400 rpm to achieve a thickness of 50 µm .

    a. If the AZ 40XT-11D has been closed for a long period of time, open the bottle approximately 12 hours before processing to release any stored nitrogen gas within the resist. Do not leave the bottle open for longer than 12 hours due to evaporation of the solvent causing cracks in the resist after baking.

    b. Bubbles form easily in the resist. To mitigate bubble formation during dispensing, slowly pour the AZ 40XT-11D in a small spiral pattern at the center of the wafer about the size of a toonie, as close to the wafer as possible. Quickly move the resist bottle to the side and off the wafer once finished pouring.

15. Leave wafer to rest on chuck 5 minutes after dispensing and spinning.

16. Softbake AZ 40XT-11D for 11.5 minutes at 125°C using a proximity hotplate.

    a. Put on the hotplate with N_2 proximity ON vacuum OFF for the first 6 minutes, then N_2 proximity OFF vacuum ON for the remaining time.

17. A 25/30 nm Cr/Cu layer is then sputtered as a seed layer for electroplating.

    a. Cr is used as an adhesion layer.

    b. Place Kapton tape over a minimum of one pair of alignment marks.

    c. Chrome Deposition Parameters:

        i. See step 2(b) for deposition rate, power, pressure, and voltage.

        ii. For 25 nm film, deposition time is 1.77 min ≈ 1 min 46 sec + 3 min burn-in.

    d. Copper Deposition Parameters:

        i. Deposition Rate: 15.6 nm/min.

        ii. Power = 300 W.

        iii. Pressure = 7 mTorr.

iv. For 30 nm film, deposition time is 1.92 min ≈ 1 min 55 sec + 3 min burn-in.

v. Voltage ≈ 510 V.

18. The wafer is placed in an acid copper plating bath for 20 minutes to deposit approximately 1.5 μm of copper.
    a. Current density ≈ 4 mA/cm^2 (ramped).
19. HPR-504 is spun and patterned with the same steps as 3-7.
20. The Cr/Cu layer is then etched in Cr/Cu etchants, respectively.
    a. Copper etchant:
        i. Ferric chloride diluted 1:2 with DI water to slow etch rate to improve undercut control.
        ii. Etch time approximately 2 minutes.
    b. Chrome etchant [157]:
        i. Potassium permanganate (KMnO4 - 90 g/L), hydrochloric acid (HCl 36% - 1 mL/L), and DI solution for 60 seconds at room temperature.
        ii. Rinse in DI water.
        iii. Oxalic acid (C2H2O4 - 25 g/L) and DI solution for 10 seconds at room temperature.
        iv. Rinse in DI water.
        v. Repeat until all chrome is etched (typically 5 repetitions).
    c. The pH of the $KMnO_4$ + HCl solution should be approximately 2.3. Be careful to not add too much HCl, as the reaction produces chlorine gas. Furthermore, due to the release of chlorine gas, the etch should be carried out in a fume hood for safety. Generally, HCl needs to be added to the KMnO4 solution every few weeks, but a test with a pH meter before etching is recommended to confirm.
21. The photoresist is left on, to be removed later in step 29.

<u>*4th mask* – Pattern sacrificial layers Sac1 & Sac2 (100μm AZ 40XT-11D)</u>

22. A second layer of AZ 40XT-11D is spun for 25/35 seconds at 300/1400 rpm to achieve a thickness of 50 μm.
    a. Combined sacrificial layer thickness of 100 μm.
23. Leave wafer to rest on chuck 5 minutes after dispensing and spinning.
24. Softbake AZ 40XT-11D for 8 minutes at 125°C using proximity hotplate.
    a. Put on the hotplate with N_2 proximity ON vacuum OFF for the first 4 minutes, then N_2 proximity OFF vacuum ON for the remaining time.
25. Rest for 30 minutes (rehydration step to prevent photoresist cracking).

26. Exposure to *i-line* (365 nm) for 1000 mJ/cm^2 in lithography contact mask aligner.
27. Rest for 35 minutes (prevents cracks from forming in resist).
28. Post exposure bake (PEB) for 130 seconds at 105°C using proximity hotplate.
    a. Put on the hotplate with N_2 proximity ON vacuum OFF for the first 20 seconds, then N_2 proximity OFF vacuum ON for the remaining time.
29. Develop AZ 40XT-11D in MF CD-26 developer for approximately 4 minutes.
    a. If some exposed photoresist still not developing, PEB for an additional 30 seconds and redevelop.
30. Hardbake for 120 seconds at 100°C using proximity hotplate.
    a. Put on the hotplate with N2 proximity ON vacuum OFF for the first 10 seconds, then N2 proximity OFF vacuum ON for the remaining time.
    b. Always hardbake less than 4 hours before sputtering in the next step to retain effect, otherwise photoresist rehydrates.

5th mask – Inverse pattern copper plating mold Mold1 (50µm AZ 40XT-11D)

31. A 40/100 nm Cr/Cu layer is sputtered as a seed layer for electroplating.
    a. Cr is used as an adhesion layer.
    b. Chrome Deposition Parameters:
        i. See step 2(b) for deposition rate, power, and voltage.
        ii. Pressure = 10 mTorr (to improve sidewall coverage).
        iii. For 40 nm film, deposition time is 2.83 min ≈ 2 min 50 sec + 3 min burn-in.
    c. Copper Deposition Parameters:
        i. See step 17(d) for deposition rate, power, and voltage.
        ii. Pressure = 10 mTorr (to improve sidewall coverage).
        iii. For 100 nm film, deposition time is 6.41 min ≈ 6 min 25 sec + 3 min burn-in.
32. The wafer is placed in an acid copper plating bath for 12 minutes to deposit approximately 1 µm of copper.
    a. Current density ≈ 4 mA/cm^2 (ramped).
33. A 40 nm Cr layer is sputtered as an adhesion layer for the plating mold.
    a. Chrome Deposition Parameters:
        i. See step 31(b) for deposition rate, power, pressure, voltage, and time.
34. A layer of AZ 40XT-11D is spun for 25/35 seconds at 300/1400 rpm to achieve a thickness of 50 µm.

a. Used for copper electroplating mold.

35. Softbake AZ 40XT-11D for 22 minutes at 115°C using gravity oven.
36. Rest for 30 minutes (rehydration step to prevent photoresist cracking).
37. Exposure to *i-line* (365 nm) for 1000 mJ/cm^2 in lithography contact mask aligner.
38. Rest for 35 minutes (prevents cracks from forming in resist).
39. PEB for 15 minutes at 105°C using gravity oven.
40. Develop AZ 40XT-11D in MF CD-26 developer for approximately 4 minutes.
41. Wafer is diced into 2"×2" quarters to allow release in Critical Point Dryer and SEM characterization if needed.
42. The 40 nm Cr adhesion layer is then etched in Cr etchant.
    a. Chrome etchant:
        i. See step 20(b) for etch procedure.
43. The wafer is placed in an acid copper plating bath for 3 hours to deposit approximately 15 μm of copper.
    a. Current density ≈ 4 mA/cm^2 (ramped).

<u>Final Sacrificial Layer Etch and Structure Release</u>

44. The plating mold is removed in an acetone bath.
    a. Acetone bath for 2 minutes, quickly transferred to IPA bath for 1 minute, and then rinsed in DI water and dried with N_2 gun.
45. The Cr/Cu seed layer is then etched in Cr/Cu etchants, respectively.
    a. Copper etchant:
        i. See step 20(a) for etch procedure.
        ii. Etch time approximately 1 minute.
    b. Chrome etchant:
        i. See step 20(b) for etch procedure.
46. The sacrificial layer is etched using a Remover PG two-bath system.
    a. Stripping bath: Immerse wafer in Remover PG for 24 hours at room temperature. Dispose of the Remover PG when finished.
    b. Drag-out bath: Immerse wafer in Remover PG for 1 hour at room temperature. Save drag-out Remover PG bath to use for next stripping bath.
    c. 1st rinse bath: Immerse wafer in IPA 1st rinse bath for 10 minutes.
    d. 2nd rinse bath: Immerse wafer in IPA 2nd rinse bath for 10 minutes.

e. Remove wafer from 2nd IPA rinse bath and place on top of clean wipe on wet deck to air dry.
    i. Another option is to use the Critical Point Dryer if stiction becomes a problem. Due to the 15 μm thickness of the plated copper on M3, generally this was not a problem.
f. When removing the wafer from each bath, slowly take the wafer out at as much of a vertical angle as possible. Once out, quickly move the wafer to the next bath, and then slowly place the wafer in the bath again at as much of a vertical angle as possible. This helps reduce the amount of waveguide channel collapse during the transitions.

47. Finally, the wafers are taken for oxygen plasma ashing to remove any residual photoresist.
    a. Power = 200 W.
    b. Pressure = 1.4 Torr.
    c. Time = 5 minutes.

Appendix B: Multiline Method for Complex Propagation Constant Extraction

In this appendix, the multiline method is explained in greater detail, which appears a number of times throughout this thesis to characterize and evaluate the proposed miniaturized integrated waveguides. As a powerful yet simple calibration technique, the multiline method is used to extract the complex propagation constant γ of microwave transmission lines (TL) [102], [103]. By measuring two TLs of different length, with all other design parameters the same, the effect of connectors and feeding structures on the measured results can be removed, following the extraction of the propagation properties of the TL. The multiline method has been especially useful for the characterization of periodic and radiative non-TEM TL structures such as SIW and HMSIW, where even simulation software such as HFSS cannot accurately extract the propagation characteristics of the TL only [7], [9], [27], [67]. Furthermore, the individual effect of radiation, dielectric, and conductor losses on the attenuation constant can be evaluated in simulation, allowing for greater insight into the characteristics of the TL component [7].

In Fig. B.1, the block diagram of a general two-port device is shown. Due to the cascading property of a transmission matrix [158], the overall transmission matrix **T** can be decomposed into a cascade of error box A, the device under test (DUT), and error box B. Thus, **T** can be represented as

$$\mathbf{T} = \mathbf{T_A}\mathbf{T_{DUT}}\mathbf{T_B} \tag{B.1}$$

where $\mathbf{T_A}$ and $\mathbf{T_B}$ represent the error box A and B, respectively, which contain the effect of connectors and/or feeding structures on ports 1 and 2, respectively. Generally, it is assumed $\mathbf{T_A}$ is equal to $\mathbf{T_B}$. The DUT matrix $\mathbf{T_{DUT}}$ is a diagonal matrix with elements

$$\mathbf{T_{DUT}} = diag[e^{-\gamma L}, e^{\gamma L}] \tag{B.2}$$

where $\gamma = \alpha + j\beta$ is the complex propagation constant of the DUT, α and β are the attenuation and phase constants of the DUT, respectively, and L is the length of the DUT component to be extracted.

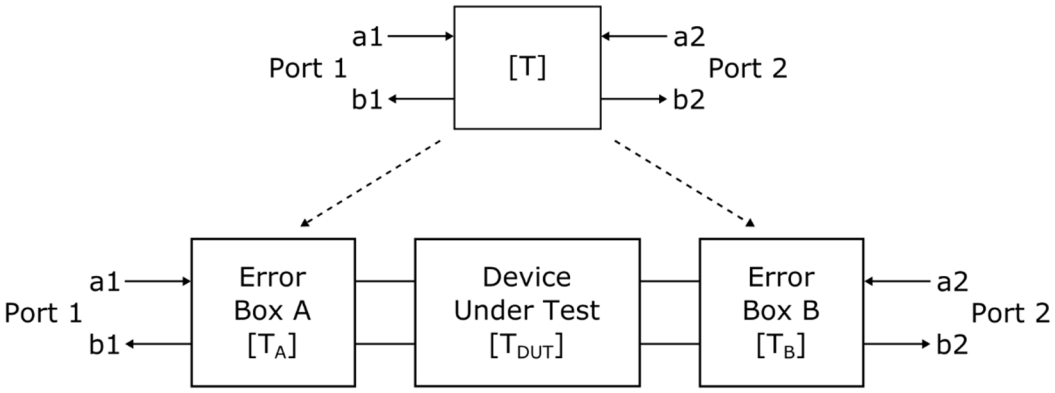

Fig. B.1. Block diagram of a general two-port device with transmission matrix **T**.

To apply the multiline method, following the procedure in [103], the transmission matrixes of two TLs with lengths L_1 and L_2 are combined into an eigenvalue equation of the form

$$\mathbf{T^{1,2}T_A} = \mathbf{T_A T_{DUT}^{1,2}} \tag{B.3}$$

where the matrix $\mathbf{T^{1,2}}$ represents the matrix multiplication of the first TL with the inverse of the second

$$\mathbf{T^{1,2}} = \mathbf{T^{1}}(\mathbf{T^{2}})^{-1} \tag{B.4}$$

and likewise, matrix $\mathbf{T_{DUT}^{1,2}}$ represents the matrix multiplication of the first DUT with the inverse of the second

$$\mathbf{T_{DUT}^{1,2}} = \mathbf{T_{DUT}^{1}}\left(\mathbf{T_{DUT}^{2}}\right)^{-1}. \tag{B.5}$$

As defined above in (B.2), the matrix $\mathbf{T_{DUT}^{1,2}}$ is diagonal. Therefore, the eigenvalues of $\mathbf{T^{1,2}}$ correspond to the elements of $\mathbf{T_{DUT}^{1,2}}$, and the complex propagation constant can be extracted by

$$e^{\gamma \Delta L} = \lambda \tag{B.6}$$

where λ is the eigenvalue of the matrix $\mathbf{T^{1,2}}$, and $\Delta L = L_2 - L_1$ is the difference in length between the two DUT sections. The attenuation constant and phase constant are then found using

$$\alpha = \ln|\lambda|/\Delta L \tag{B.7}$$

$$\beta = \angle\lambda/\Delta L \tag{B.8}$$

In Fig. B.2, pictures of two HMSIW (chosen to clearly illustrate the similarity of the feeding structure) designed and fabricated in Section 3.3 with DUT line

lengths $L_1 = 40$ mm and $L_2 = 80$ mm are shown. By employing the multiline method, the effect of the SMA connectors and microstrip to HMSIW transitions represented by error box A and error box B are removed. The complex propagation constant of the HMSIW section with length $L_2 - L_1 = 40$ mm is then extracted, giving information on the attenuation constant and phase constant of the waveguide component alone.

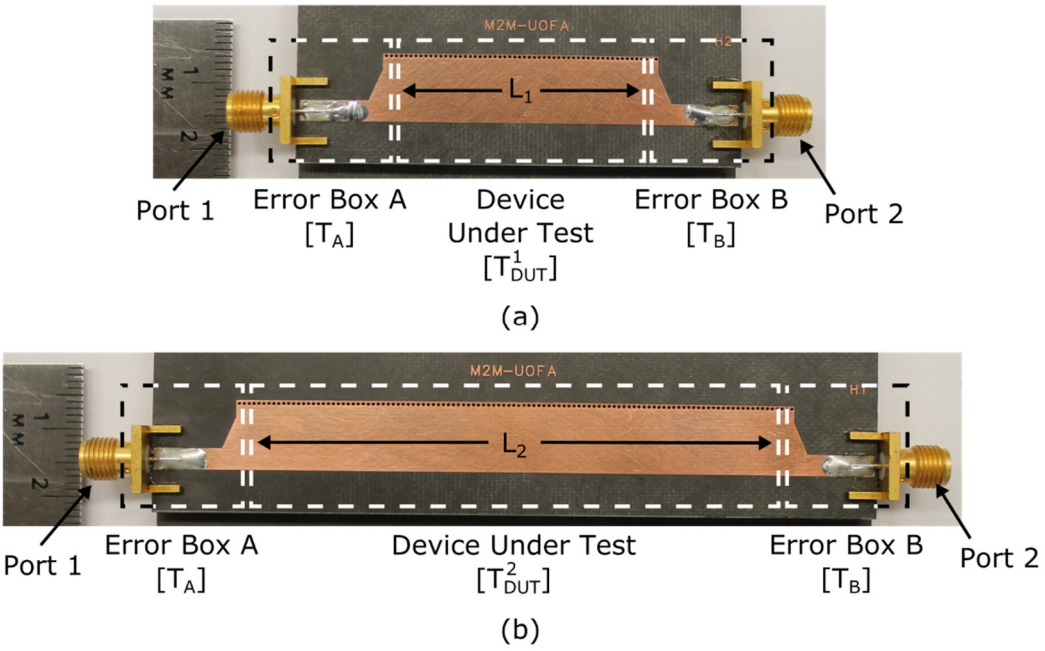

Fig. B.2. Pictures of the fabricated HMSIWs from Section 3.3 with DUT lengths (a) $L_1 = 40$ mm and (b) $L_2 = 80$ mm including error boxes A and B for extraction of the complex propagation constant using the multiline method.

The multiline method presented here can also be expanded to extract higher order modes of transmission line structures [27]. Furthermore, it is generally recommended that one line be of length $\lambda_g/4$ and the other three times as long at the center of the band, covering no more than 1:8 in bandwidth [102].

Since measurements are more commonly in the form of scattering parameters, the equations to transform the individual components from the scattering matrix to the transmission matrix are provide below for completeness [158].

$$T_{11} = 1/S_{12} \tag{B.7}$$

$$T_{12} = -S_{22}/S_{12} \tag{B.8}$$

$$T_{21} = S_{11}/S_{12} \tag{B.9}$$

$$T_{22} = (S_{12}^2 - S_{11}S_{22})/S_{12} \tag{B.10}$$